Using Non-Linear Vibration Techniques to Detect Damage in Concrete Bridges

S.A. Neild

Department of Engineering Science,

University of Oxford.

July, 2001

Abstract

There has been much work published in recent years on the use of vibration characteristics to detect damage in bridges. Almost all of this work has been based on the assumption that the vibration is linear, i.e. the natural frequencies are not dependent on the amplitude of oscillation. The aim of the work presented here was to investigate the possibility of using changes in the non-linear vibration characteristics to detect damage in reinforced concrete bridges.

These changes in the non-linear vibration characteristics were studied by conducting impact excitation vibration tests on reinforced concrete beams. The non-linearities were detected by examining the changes in fundamental frequency over time (and hence over amplitude of vibration). Several time-frequency distribution estimation tools are discussed including the discrete Fourier transform moving window, the auto-regressive model moving window, harmonic wavelets and examples of the Cohen class of bilinear time-frequency distributions. A detailed investigation into these various distribution predictors was conducted to assess which is most suitable for analysing the vibration signals to detect changes in frequency with time.

To understand the non-linearities in the vibration characteristics, a time-stepping model was described. The model is capable of including damage in the form of a moment-rotation relationship over the cracked region. It was validated for linear vibrations against theoretical values and the representation of a non-linear mechanism using the model was compared with experimental data.

Static load tests were also conducted on the beams at various damage levels. They involved the use of vibrating wire strain gauges to investigate the moment-rotation behaviour over the cracked region. Several possible non-linear crack mechanisms are discussed and two of them are assessed using the vibration and the static load tests. Future experimental work is proposed to study the possible non-linear mechanisms further.

The beam tests demonstrated that there is a change in non-linear vibration behaviour with damage. The change is greatest at low levels of damage and after the beam has been loaded to 30% of the failure load in three-point loading there is a reversal in the trend and a slight reduction in non-linearity with further damage.

Acknowledgements

I wish to thank my supervisors, Dr. P.D. McFadden and Dr. M.S. Williams, for their support and guidance throughout this work and their patience with proof-reading this thesis.

I also would like to thank A. Goldsmith for the experimental testing she conducted at the start of this project, C. Baker for making the loading rig and beam supports and R. Sawala for his help casting the beams.

I gratefully acknowledge the Lubbock fund for their grant to cover experimental costs and the EPSRC for providing me with a postgraduate studentship award.

Finally, I wish to thank my partner Jill for her patience, support and encouragement.

Contents

Chapter 1

Introduction

There is a great interest in detecting damage within a structure at an early stage of its development. Current detection methods are either visual or localised experimental methods, e.g. acoustic or ultrasonic methods. These methods require that the damage location is known and that it is readily accessible. The need for a more global damage detection method has led to the development of methods that investigate changes in the vibration properties of the structure.

In the UK, the Highways Agency is responsible for maintaining over 10,000 bridges, of which over 50% are reinforced concrete, 28% are prestressed concrete and a further 13% are steel-concrete composite structures. There are also many more bridges maintained by local authorities, most of which are concrete. The Highways Agency has become increasingly interested in vibration methods due to an increase in maximum service weight of heavy goods vehicles [76], which was introduced in 1999. This weight increase has led to more demand for testing which in turn has exposed weaknesses within the current assessment methods [30]. In addition, there is a demand to move to a "pass, fail or monitor" type of bridge assessment rather than the existing pass or fail system. If the monitor option is selected, the bridge will be subject to more frequent testing and therefore a global damage detection method would be far more convenient and cheaper than a series of localised damage detection tests [25].

For many years, work has been done to investigate the possibility of using vibration techniques to detect damage in bridges. Almost all of this work has assumed that the modal properties of the bridge do not vary with amplitude of oscillation (i.e. the vibra-

tion is linear). The work has ranged from looking at changes in natural frequencies and mode shapes due to damage to using finite element models to assess changes in modal properties. One of the major problems with this work is that a baseline undamaged set of modal parameters is required to assess any changes in the parameters due to damage. Clearly, the best that can be done for an existing structure is to compare future results with a present day baseline but for this to be meaningful the present day damage must be accurately known. A further problem is that the modal properties are affected by environmental factors such as temperature and humidity [94].

In contrast to the large amount of work on developing methods of detecting damage assuming linear vibration, there has been very little research on the feasibility of using the vibration non-linearities to assess the condition of structures. Most of the non-linear vibration damage detection work has centred on fatigue cracks in metals. Significant progress has been made in detecting damage in, for example, aeroplane wings [109]. On the whole, one of two possible ways of detecting non-linearities in the vibration characteristics is employed; either using forced vibration tests at a natural frequency and inspecting how the response deviates from a pure sine wave at the forcing frequency, or using impact excitation and inspecting the change in natural frequencies as the vibration decays. Very little work, however, has been conducted on the non-linear testing and analysis of damaged concrete beams.

The aim of the work presented here is to assess the feasibility of using non-linearities in the vibration characteristics of damaged concrete beams to detect the damage. Firstly a literature review is presented, the main conclusion of which was to conduct impulse excitation tests on concrete beams at various levels of over-load damage to assess the effect of damage on the non-linear vibration characteristics of a beam. In chapter 3, various time-frequency analysis methods are assessed using synthetic signals to find the optimum technique for analysing the non-linear vibration signals generated by impact excitation tests. A time-stepping model which is capable of including different types of crack mechanisms by specifying a moment-rotation relationship in the cracked region is derived in chapter 4. Then, in chapter 5, four possible crack mechanisms which result in amplitude dependent natural frequencies are discussed. Chapters 6 gives details of the theory and construction of a vibrating wire strain gauge, developed to allow measure-

ment of strain during static load tests. Chapter 7 contains details of the experiments conducted on two reinforced concrete beam at increasing levels of overload damage. Impact excitation tests are used to assess the change in natural frequencies as the vibration decays and a method of using static load tests to calculate the moment-rotation relationship over the cracked region is developed. In chapter 8 details of the signal processing of the experimental data are given and the results are presented. Finally in chapter 9, the experimental data is used to assess two of the possible crack mechanisms identified in chapter 5.

Chapter 2

Literature Review

The vibration testing literature may be divided into two sections: those papers that assume that the vibration is linear and those that are concerned with the non-linearities in the vibration response. Firstly, the linear and then the non-linear methods will be explored, followed by a brief review of the possible testing methods presented. Finally, an explanation of the motivation behind the work presented here is given.

2.1 Linear Modal Methods

The idea of using vibration measurements to detect damage was proposed by Cawley and Adams [14]. It is based on the fact that damage will reduce the local stiffness of the structure, which in turn reduces the natural frequencies of the whole structure. Most studies into using vibration measurements to detect damage examine changes in modal properties and assume that these properties are linear, i.e. they are not related to the amplitude of oscillation. The types of indicators can be split into several main groups, each of which is briefly described below with some examples of their application. For further details there are several review papers on vibration damage detection methods, for example Doebling *et al.* [28] and Salawu [96].

2.1.1 Natural Frequencies

It is clear from the literature that looking for changes in natural frequency is a very insensitive method of detecting damage.

Farrar and Jauregui [35] conducted tests on a steel plate girder bridge and reported only minimal changes in frequency even at extreme damage states. When the stiffness of one of the main plate girders had been reduced by 96.4% (reducing the local bending stiffness of the bridge by 21%) the maximum change in natural frequency was just 7%. At lower damage levels no significant change in frequency could be observed.

Maguire and Severn [56] conducted tests on four simply-supported pre-cast post-tensioned concrete bridge beams with a span of 27.6 m. They reported a drop in frequency when the cover concrete was removed exposing the pre-stressing tendons. However, the changes were very small (in the order of 2%) and comparable to their frequency resolution.

Salawu [97] conducted tests on a concrete bridge before and after the support bearings had been replaced and reported an average change in frequency of only 1.7% for the first six modes of vibration.

There have also been a large number of laboratory tests reported. For example, Eccles *et al.* [30] found that for concrete beams that were damaged by four-point loading, the fundamental frequency dropped initially by around 12% but for greater damage (between 20% and 80% of the final load) the additional change in frequency was only 2.5%.

It is clear from the few papers selected here that the frequency does change with the scale of damage and that as stiffness decreases so does the frequency. However, these changes in frequency are small in comparison to fluctuations due to environmental conditions, in particular changes in temperature. Abdel Wahab and De Roeck [1] measured the natural frequency of a prestressed concrete bridge twice, when the ambient temperature was 0°C and when it was 15°C. The resulting change in natural frequency due to the increase in temperature was a decrease of about 4-5%. Roberts [94] measured the natural frequencies of a box girder bridge for a year to investigate the effects of temperature and found that temperature was the primary cause of frequency change,

accounting for up to 4% of the overall change, whereas a finite element model suggested that changes resulting from damage could be expected to be in the region of 1%. A second important finding reported was that mode shapes were not affected significantly by the temperature changes.

2.1.2 Damping Ratios

There have been some attempts to use damping ratios as a measure of damage but they have proven to be unsuccessful. Salane and Baldwin [95] tested a steel girder bridge with concrete decking and concluded that, although damping ratios were affected by deterioration, they were unsuitable indicators as they initially increased and then fell with increasing damage. This finding is supported by Farrar and Jauregui [35], who also found that damping of a steel plate girder bridge did not consistently increase or decrease with increasing damage.

Tests before and after structural repairs to a reinforced concrete bridge were conducted by Salawu and Williams [98] and it was reported that the changes in damping for different modes were inconsistent. Casas and Aparicio [15] conducted tests on small concrete beams and reported no clear relationship between damage and changes in damping.

2.1.3 Modal Shapes

Conclusions drawn in the literature about detecting damage using modal shapes have been generally, but not exclusively, far more positive than for damping ratios or natural frequencies. A large number of methods of interpreting the mode shape data have been suggested.

MAC and COMAC numbers

Most of the work on mode shapes has concentrated on looking at the Modal Assurance Criterion (MAC). This compares the damaged mode shape for mode j against the undamaged reference mode shape for mode k, for all the modes j and k measured, and produces a correlation value between each damaged mode shape and each reference mode

shape. For an undamaged structure it would be expected that for all $j = k$ the MAC is 1 and for all $j \neq k$ it is 0. The Co-Ordinate Modal Assurance Criterion (COMAC) is also commonly used. This is an extension to the MAC, intended to identify the location where two sets of mode shape data disagree and hence to find the location of the damage (see, for example, Alampalli *et al.* [2] for more details).

Alampalli *et al.* [2] found that for a steel bridge no clear trend was detectable for increasing damage states when looking at the modal properties averaged over several tests for each of the first 12 modes. However, when statistical methods were applied to the results some success was reported although only at high damage levels. Salawu and Williams [98] also reported some success when using mode shape data taken before and after repairs to a reinforced concrete bridge. They reported that although nothing could be concluded from inspection of the mode shapes directly, the MAC values did indicate some damage and the COMAC indicated four locations for damage, of which two were correct and two incorrect once a suitable threshold value for damage had been selected. A third actual damage site was not detected.

In contrast, Das *et al.* [26] conducted tests on reinforced concrete beams damaged by static four-point loading and found that for lower modes the change in MAC number was extremely small, the greatest difference being when the damage was very localised, i.e. at first cracking and at the point where the steel first yielded. They also found that when the damage became more uniform the mode shape returned to a similar one to its undamaged state.

Curvature

Possibly a better method of using mode shape data is to calculate the curvature at points along the structure since small changes in mode shape are likely to be more obvious when looking at differentials than the raw shape. If a crack is introduced there is a reduction in stiffness, EI, and this should cause a local increase in curvature, which is equal to bending moment divided by stiffness. Pandey *et al.* [78] used a finite element model of a simply-supported beam with a reduction in E of 50% at the one-third span point over a region of 0.05 of the total span. They found that modal curvature was a far more sensitive damage indicator than the MAC or COMAC methods. The changes

in MAC and COMAC numbers were less that 0.5%, but using curvature a fairly clear damage region could be seen. This method was tested on a bridge and a finite element model of a bridge by Farrar and Jauregui [35, 36]. They found that damage could be detected and that the location could be narrowed down to two or three sites. However, they noted that their damage sites were extremely localised and that the method was unlikely to be as successful in locating a larger damaged region. Also, to calculate curvature accurately, a large number of measurement points were needed.

This method of detecting damage was extended by Ratcliffe [91], who proposed a method of studying the curvature of only the damaged beam rather than those of both the damaged and undamaged beams. The method uses the Laplace operator to estimate the change in slope of the beam from the mode shape. The presence of severe damage is detectable in the form of a noticeable step in the Laplacian. For less severe damage, the effect on the Laplacian is less obvious and a comparison between the Laplacian at each point and a cubic fit to the Laplacian using the two points either side of the point in question is suggested. The method was reasonably successful in predicting damage location in a steel beam.

Flexibility

Maeck *et al.* [55] extended the use of curvature to detect damage by using it to calculate the local beam stiffness. A smoothed version of the curvature was calculated from the mode shape data then the stiffness was calculated using the curvature and the moment distribution along the beam (which may be derived using the mode shapes). Maeck *et al.* [54] looked at using this method along with changes in natural frequency firstly to establish the state of a concrete beam and then to locate any damage that was present. The method is reasonably successful for a distributed damage region. It does, however, require a dense measurement grid and an accurate undamaged stiffness profile. Raghavendrachar and Aktan [89] also calculated flexibility using the mode shapes and concluded that it was a superior indicator to examining the raw mode shape data. They noted that higher modes would reveal local damage but that these higher modes would be difficult to identify experimentally on an aged bridge.

2.1.4 Finite Element Models and Model Updating Methods

There has been a large quantity of work investigating the use of a numerical model of a structure in conjunction with test data to detect damage, a few examples of which are outlined below.

The method of combining frequency information with a numerical model has largely been extended from a method proposed by Cawley and Adams [14], who looked at the change in the stiffness matrices necessary for two natural frequencies to match the corresponding natural frequencies in the damaged specimen. They then used this change in the stiffness matrix to find a locus of possible damage sites. By looking at several pairs of frequencies, several sets of loci of damage sites were calculated and a damage probability map could be generated. The tests they conducted were quite successful, although they were examining a sheet of aluminium with a saw cut representing the damage, which is relatively easy to model in comparison to a bridge.

Thyagarajan *et al.* [106] used a finite element model of a bridge to calculate the nodes at which damage may be present. Firstly, the model was adjusted so that the measured undamaged frequencies matched the predicted ones. Then using the mass, stiffness and damping matrices of the undamaged model and the damaged mode shapes, a damage vector was calculated. This is turn indicated the degrees of freedom at which damage had occurred. This method was tested by generating a damaged frequency response function for a simply-supported truss bridge using the model of the bridge. Using this frequency response function for a few of the nodes along with the undamaged model of the bridge, a prediction of the damage location was derived. The damage detection was successful even when some noise had been added to the damaged input signal. However, the damaged data were generated using the same model that was used to detect the damage in the testing of the method. The problem of how robust such a technique is when trying to model a real structure was therefore not addressed. Messina *et al.* [61] investigated the possibility of detecting damage using a comparison between the vector of measured changes in natural frequency due to damage and the vector of predicted changes in natural frequency due to damage at a known location. By making this comparison for various locations the most probable location for damage may be found.

This method was also quite successful when tested using a pin-jointed truss model, but, as with Thyagarajan *et al.* [106], the same model was used to generate the damaged frequency response and then to detect the damage.

Several authors have reported methods which use the natural frequencies of a structure in conjunction with a theoretical model to find damage location and severity. For example, Rizos *et al.* [93] reported a method of measuring the amplitude of a steel beam at two points during forced vibration at a natural frequency, then using a model of the beam to predict the crack length and position by fitting the amplitudes to the equations of motion at the natural frequency. Morassi [64] used the equations of motion of a simple beam to calculate the position and the size of a crack using the frequencies of the m^{th} and $2m^{th}$ modes. Armon *et al.* [3] used a system of rank ordering the change in natural frequencies of a structure and then related this to the damage using a finite element model. A further problem with these methods is that an accurate model of the undamaged structure is required before using the model to assess the damaged structure.

Eilbracht and Link [32] investigated the modelling of reinforced concrete. They suggested a simple finite element for the cracked region based on the length and position of the region of cracks and the height of the largest crack. The heights of the other cracks within the region were assumed to be governed by a parabolic relationship with distance from the largest crack. Using experimental modal data and parameter identification methods the location and severity of the cracking could be found. The method successfully identified the damage inflicted on a beam with free boundary conditions.

Owen and Choo [76] stated that the problem with the application of this type of method to a civil engineering structure is that the model will not predict the behaviour of the structure as accurately as for a mechanical engineering application. Salawu [96] held the same view and stated that methods that rely only on measured data would be more appropriate to large civil engineering structures.

2.1.5 Problems to Overcome

The review of previous work employing linear methods indicates that some substantial progress has been made in detecting damage using vibration techniques. There are however some major problems to overcome.

The relationship between the modal properties and environmental conditions needs further investigation. The effect of temperature on natural frequencies has already been mentioned and is believed to be the most influential factor but other factors such as humidity and rainfall must also be investigated. More detailed work on the environmental effects is being conducted. For example, Krämer *et al.* [50] reported testing a bridge for a nine-month period, recording the environmental conditions and frequency response.

A second factor which must also be overcome is the need, in almost all of the methods mentioned above, to have a set of undamaged test data or an accurate model of the undamaged structure. For a method to be useful in detecting damage in an existing bridge, this need for undamaged data must be relaxed. At best these methods might offer an assessment of deterioration between the current condition and a future condition, but this would require testing the structure to form a baseline set of data and having a good knowledge of the current defects of the structure.

Since reinforced concrete structures are non-linear in behaviour, important information is lost when the linear assumption is made. If non-linear behaviour, i.e. the effects of amplitude of oscillation on the frequencies, can be used to detect damage it might be possible to test the structure just once and from examining the non-linearities assess whether the structure is damaged so eliminating the need for a baseline measurement.

2.2 Non-Linear Modal Methods

In contrast to the vast quantity of work reported on linear damage detection techniques, little has been done to investigate non-linear time-dependent vibrational properties of civil engineering structures.

2.2.1 Modelling Cracked Beams

There has been interest for many years in the vibrational behaviour of cracked beams in the condition-monitoring field. Numerous models of beams with cracks have been developed. These generally include either a crack that is permanently open or a "breathing" crack which opens and closes during vibration.

Many models represent the cracked beam as a series of undamaged beam finite elements, with the crack represented as either a reduced stiffness in one element or a massless rotational spring at the joint between two of the beam elements. Rizos *et al.* [93] modelled a beam with an open crack as two undamaged beams connected by a spring. They used the general form of the modal shapes of the two undamaged beams, along with the boundary conditions at the crack location, to develop equations for the displacements either side of the crack. The spring compliance was found using the strain energy function of the crack (see Dimarogonas and Paipetis [27]). A similar approach was used by Narkis [67] to relate the natural frequency of a beam with a double-edged crack to the crack position and depth. The method was extended to a beam with a series of cracks by Shifrin and Ruotolo [101] and to a crack in a beam with variable cross-section by Nandwana and Maiti [66]. A variation on this approach was suggested by Fernández-Sáez *et al.* [38], who calculated the displaced shapes by adding a polynomial function in terms of distance away from the crack to the undamaged displaced shapes either side of the crack. The coefficients in the polynomials were calculated using the boundary conditions and slope discontinuity (caused by the spring representing the damage) at the crack position. Chaudhari and Maiti [16] derived equations for the mode shape of a tapered beam either side of a crack and went on to demonstrate how the crack location and size might be calculated from the first three natural frequencies.

An alternative method was proposed by Mahmoud *et al.* [57]. They divided the beam along its length into many elements and, after lumping the mass of each element at its centre, derived a matrix equation relating the forces and displacements of one end of an element to the other. The open crack was included as a reduced stiffness of one of the elements. A root searching technique was then used to find the natural frequencies using the matrix equations and boundary conditions.

For most applications, applying a simple stiffness reduction is unrealistic, since most cracks open and close during oscillations unless a static load is also applied. Gudmundson [41] noted that although the model he proposed, based on a spring representing a permanently open crack, was a good representation of the behaviour of a cantilever beam with a notch cut out but it over-predicted the change in frequency when considering a beam with a fatigue crack. Ballo [6] modelled a cracked rotating shaft with the breathing crack represented by a rotational spring element which had different properties depending on whether the curvature was positive or negative. Cheng *et al.* [19] also modelled the breathing crack as a non-linear spring, but their model was limited to the fundamental mode, as they had to assume that the changes in the spring properties occurred at the fundamental frequency to enable the equation of motion for the beam to be solved. Kisa and Brandon [48] developed a finite element model of a steel beam with a fatigue crack with varying degrees of closure. They then used modal superposition to model the transition region and calculate the natural frequency of the cracked beam. These models include crack non-linearities to enable a better prediction of the natural frequency of a cracked beam but do not investigate any changes in frequency due to a change in amplitude of oscillation. Instead, the vibration was assumed to be linear with amplitude.

Qian *et al.* [88] used a beam finite element formulation in which different EI values for positive and negative curvature were used to represent crack opening and closure. Rotational inertia and shear effects were not included in the formulation, though the approach could be modified to include these terms (see, for example, Petyt [83]). The crack mechanism assumed was very simple, since it assumed complete opening and closure always occurred at zero curvature. A more general approach would allow the stiffness change to occur at some non-zero curvature, but this would be considerably more complex to implement.

2.2.2 Non-Linear Vibration

Sundermeyer and Weaver [104] demonstrated the potential use of the non-linear behaviour of a breathing crack in detecting the existence of the crack. They used a model

with a bilinear spring representing the crack to show that, in theory, for a beam that is excited at two frequencies simultaneously the steady state signal consists not only of the two driving frequencies, as expected, but also of a component at a frequency equal to the difference between the two driving frequencies. This was thought to be due to the bilinear stiffness properties of the spring. They concluded that this additional frequency component could be a useful indicator of bilinear behaviour that resulted from damage.

Pugno *et al.* [87] developed a method of calculating the response of a beam with several breathing fatigue cracks to periodic excitation. The method used harmonic balancing to calculate the frequency components of the response. They concluded that the non-linear dynamic behaviour leads to the presence of super-harmonics in the response spectrum which could in theory be used to detect damage. A super-harmonic is a harmonic which is at a frequency that is an integer multiple of one of the modal frequencies and results from the motion not being perfectly sinusoidal but taking the form of a distorted sinusoid at the same frequency (see section 5.1). This was demonstrated by Bovsunovsky and Matveev [9] who conducted experiments on and modelled a steel beam with a fatigue crack. They presented experimental data comparing the sinusoidal vibration of the uncracked beam to the periodic vibration at a slightly lower frequency of the cracked beam, which takes the shape of a distorted sinusoid. They then investigated how the amplitudes of the super-harmonics changed with damage. Tsyfansky and Beresnevich [109] also made use of super-harmonics to detect cracks. They conducted forced vibration tests on aircraft wings. To ensure that any cracks present opened and closed during the test the wing was supported close to its tip to counteract the effects of self-weight. Without this support cracks on the upper surface would act as notches remaining open throughout the vibration tests and cracks in the lower surface would remain closed unless the vibration test was of very high amplitude. They concluded that, with this support condition, fatigue cracks lead to excitation of super-harmonics. Their work stressed the important point that non-linearities due to fatigue cracks will only be present if the fatigue crack is opening and closing during the excitation.

Rivola and White [92] investigated the possibility of using the auto-bispectrum to detect non-linearities in a bilinear system using a simple model. The auto-bispectrum detects coherence between the phases of the signal at different resonant frequencies. If

a non-linearity is present there will be some relationship between the phases causing a peak in the auto-bispectrum (see, for example, Nikias and Petropulu [73] or Collis *et al.* [23]). They concluded that the auto-bispectrum was more sensitive to changes in behaviour than the power spectral density, but it was far more difficult to interpret. Worden and Tomlinson [115] also used the auto-bispectrum to analyse a non-linear three degree of freedom model.

2.2.3 Non-Linear Testing of Concrete Beams

There is very little published work which examines the non-linear amplitude-dependent modal properties of concrete beams. Eccles *et al.* [30] conducted impact excitation tests on several beams. They showed that, initially, when the amplitude of oscillation is largest the frequency is lower than that when the amplitude of oscillation is small. The frequency increases approximately linearly with time until the amplitude of oscillation is small, at which point the frequency stabilises and no further amplitude dependence can be detected. The gradient at which the frequency increases with time is larger for higher levels of damage. However the beams tested had a fundamental frequency far higher than would be expected for a bridge and the excitation decayed away extremely quickly.

These findings have been backed up by small scale beam tests conducted by Goldsmith [40] who found that, although there was some amplitude dependence when the beam was undamaged, this increased when the beam was damaged up to the point where the reinforcing bars started to yield. After steel yield, the strength of the amplitude dependence stopped increasing and only a drop in the overall frequency was noted. Figure 2.1 shows a plot of frequency against time for increasing damage. The frequency data are based on the measured response to an impulse at time $t = 0$. The plot with the highest natural frequency is the undamaged case and as damage increases the mean frequency consistently decreases. The initial fall in frequency up to about 0.025 s is due to a window effect within the modified exponential distribution used in the data analysis (see section 3.8.2) rather than an actual phenomenon.

Forced vibration tests were conducted by Van Den Abeele and Visscher [111]. They

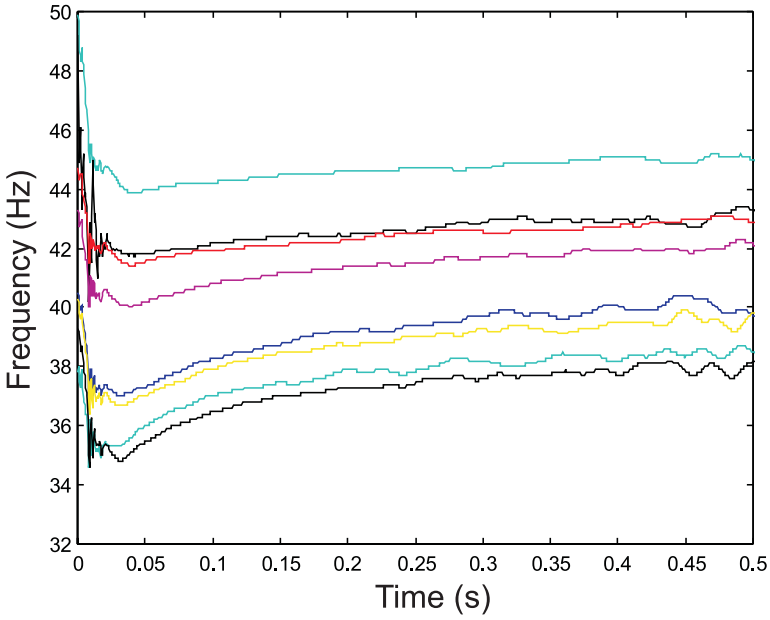

Figure 2.1: Time-frequency plot for a small reinforced concrete beam with varying amounts of cracking [40]

used continuous wave excitation at various amplitudes to build up a picture of the natural frequencies at different amplitudes of oscillation. The tests demonstrated that although the beam did not behave linearly when undamaged, once the beam was damaged using four-point loading the non-linearities became far more pronounced. This approach was also explored by Owen [75]. Van Den Abeele and Visscher also demonstrated similar trends using time domain tests. Before the test commenced the beam was subjected to steady-state excitation close to its natural frequency and then at the start of the test the excitation was stopped and the natural frequency and decay of the beam could be monitored. This type of test is similar to the impact excitation tests conducted by Eccles *et al.* [30], but with the possible advantage of exciting only one mode; that with a frequency approximately the same as the excitation frequency prior to the test beginning. However, there is the disadvantage that the tests required shaker equipment, which adds to the complexity, especially if the method were to be employed on a large structure.

Eccles *et al.* [29] presented a further possible method which could be used to detect damage. They excited the beam at a natural frequency and measured acceleration for

a fixed excitation energy. By integrating the acceleration data twice (with a moving window averaged baseline to reduce the effects of cumulative errors) a phase-plane plot could be found. For a linear system, the path taken in the phase-plane is a circle (provided the phase-plane has been normalised for both the displacement and the velocity axes). The degree to which the path calculated differs from a circle is a measure of the non-linearity of the system. However, these non-linearities would also appear in the signal when plotted in the frequency domain at integer multiples of the excitation frequency (as super-harmonics) which would possibly be easier to interpret.

2.3 Testing Methods

There has been much work published on the advantages and disadvantages of the three types of tests including sizeable reviews conducted by Salawu and Williams [99] and Prakash Rao *et al.* [85]. Test methods may be split into three main categories;

- Forced vibration
- Impact excitation
- Ambient excitation

Forced vibration tests consist of exciting the bridge using a shaker over either a broad band of frequencies, at one frequency or at a gradually changing frequency. The main benefit of forced vibration tests is that the amplitude of the bridge vibration may be held at a certain level which allows averaging of the periodic response over many cycles giving a cleaner shape of the response (see, for example, Eccles *et al.* [29]). Other advantages of forced vibration tests are that the input excitation is known and that the frequency range may be controlled. A disadvantage is that for a bridge to be excited at a reasonable amplitude a large shaker is required, which increases the cost of the tests. Also the bridge must be closed so that vehicle excitation does not affect the tests. Tests on bridges using forced excitation tests include Salawu and Williams [98] and Krämer *et al.* [50], who reported the need for two shakers at different locations on the bridge to minimise the effect of traffic vibration from the road beneath the bridge.

Tests on a bridge using impact excitation have been conducted by, for example, Raghavendrachar and Aktan [89], who constructed a bump on the road surface and drove a truck over it. Although, as with forced vibration tests, the bridge must be closed for the duration of the test, it is reported that the disruption to traffic is less as each test is quicker and traffic can be allowed over the bridge between tests. A problem with this type of excitation is that the truck movement over the bridge results in a change of mass distribution. Theoretical work has been done to assess the effect of a truck moving along a bridge by Humar and Kashif [44]. Another test method was employed by Krämer *et al.* [50], that of dropping a weight onto the bridge. Although this is more complex than truck excitation and may prevent reopening of the bridge between tests, it is easier to measure the input force. Mazurek and DeWolf [60] compared the two types of impact excitation on a small scale steel box section beam. They found that the natural frequencies differed by up to 3% due to the weight of the vehicle and that the damping properties were affected by the changing weight distribution as the model vehicle traversed the beam. Krämer *et al.* [51] compared the three types of test and concluded that since drop-weight excitation gave the same modal characteristics as forced excitation tests for the bridge they tested, it was the most suitable excitation method despite the lower levels of excitation.

Ambient excitation tests are the easiest and cheapest to perform, relying simply on traffic or other environmental excitation. There is no need for expensive excitation equipment or to disrupt traffic flow and it would be possible to record the bridge vibration remotely using permanently installed accelerometers and data acquisition equipment [50]. However, it is the most difficult excitation method to interpret. There is a continously changing mass distribution on the bridge and vibration due to interaction with the vehicle suspensions [44]. The input excitation is unknown and must be assumed to be white noise (Farrar and James [34] and Felber *et al.* [37]), although some work to overcome this problem has been conducted by Ward [112]. He suggested measuring the vibration response of the approach road and using this to normalise the response of the bridge. A further problem is that of whether ambient excitation will be sufficiently large to allow the modal properties to be measured. Roberts [94] reported that traffic excitation was sufficient to measure the first 12 modes of a multi-span steel box girder

bridge and Krämer *et al.* [50] reported sufficient excitation to measure modal properties of a short-span concrete bridge.

The suitability of the various sorts of tests for detecting non-linearities has not been established in field trials.

2.4 Conclusions Drawn from the Literature Review

From an examination of the literature, it is clear that, although some promising work has been reported on damage detection in concrete bridges using linear methods, there are still major problems to overcome, particularly those of sensitivity and the effect of environmental conditions. Non-linear methods that detect any amplitude dependence of the natural frequencies should therefore be further investigated. The amplitude-frequency dependence reported by Eccles *et al.* [30] and Goldsmith [40] provides a good starting point for the work. Further impact tests conducted on simply-supported beams of lower natural frequencies than those used by Eccles *et al.* [30] and larger geometry than those used by Goldsmith [40], to simulate drop-weight tests on bridges, are presented here. This was felt to be preferable to forced vibration excitation as it would allow a direct measurement of the frequency of the beam during the decaying vibration induced by the impact. The work presented here consists of three main parts:

Time-Frequency Distributions

To detect non-linearities present in impact tests, the change in natural frequencies of the beam over time must be estimated. A detailed study of time-frequency distribution tools was conducted to assess the best method of analysing the data.

Modelling

To further understand the reason for the non-linearity, a mathematical model of a beam capable of testing different possible crack mechanisms would be useful. The modelling of non-linear cracks in homogenous materials has been achieved using the types of model discussed in section 2.2.1. However, those models are complex and use fracture mechanics to calculate the stress distribution in the crack region which is then converted

into a spring stiffness. This type of method would be extremely difficult to apply to a reinforced concrete beam. It was therefore decided that a simple model of a vibrating beam, which allowed the inclusion of the moment-rotation relationship over a cracked region, would be a useful addition to the work that has already been performed.

Experimental Work

Impact excitation tests on beams with a low natural frequency were conducted. The changing relationship between frequency and amplitude with increasing damage was investigated and a method of measuring the moment-rotation relationship over the cracked region was developed. This, it is anticipated, will be used in conjunction with the model to further aid understanding of the vibration behaviour of cracked concrete beams.

Chapter 3

Time-Frequency Analysis

3.1 Introduction

In order to study the non-linear effects of a vibrating beam it is necessary to be able to calculate an approximation of the instantaneous frequency content of the vibration signal at any time so that a time-frequency relationship may be found. In this chapter several approaches will be examined. First, it is necessary to discuss the estimation of the frequency content of a discrete finite time signal using the discrete Fourier transform and modifications that can be made to it including the auto-regressive method of predicting the frequency content. Then the evaluation of a time-frequency relationship for a time signal using the moving-window method will be presented. The use of harmonic wavelets in estimating the time-frequency relationship will also be investigated. Finally, the calculation of time-frequency relationships using the Cohen class of bilinear distributions will be examined.

3.2 The Discrete Fourier Transform

The discrete Fourier transform (DFT) is used to calculate the frequency content of a discrete, finite-length time signal. It assumes that the frequency content remains unchanged during the time span of the signal. Despite this, the DFT may be used to predict the time-frequency properties of a signal by using the moving-window method (section 3.6.1).

The Fourier series (FS) representation of a cyclic signal with time period T may be written as:

$$x(t) = C_0 + C_1 \mathrm{e}^{\mathrm{j}2\pi t/T} + C_2 \mathrm{e}^{\mathrm{j}4\pi t/T} + \cdots = \sum_{m=0}^{\infty} C_m \mathrm{e}^{\mathrm{j}2\pi mt/T} \tag{3.1}$$

where the constants C_m are the amplitudes of the sinusoids at each frequency m/T. These values may be found using the equation:

$$C_m = \frac{1}{T} \int_{-T/2}^{T/2} x(t) \mathrm{e}^{-\mathrm{j}2\pi mt/T} \mathrm{d}t \tag{3.2}$$

The Fourier transform (FT) of a continuous infinite signal $x(t)$ may be written as:

$$X(f) = \int_{-\infty}^{\infty} \mathrm{e}^{-\mathrm{j}2\pi ft} x(t) \mathrm{d}t \tag{3.3}$$

The finite discrete form of the Fourier transform may be derived from considering either the frequency content of the Fourier series representation, equation 3.2, or a discretised version of the Fourier transform, equation 3.3, multiplied by a finite-length window (see, for example, Randall [90] or Papoulis [79]).

3.2.1 Using the Fourier Series

The Fourier series representation of a cyclic signal enables the calculation of frequencies in steps of $1/T$ using equation 3.2, where T is the inverse of the repetition frequency of the signal (see for example Brigham [12]). With the DFT, the time signal is known only at discrete time-points $(-N/2+1)T/N,\ \ldots,\ -T/N,\ 0,\ T/N,\ \ldots,\ nT/N,\ \ldots,\ (N/2)T/N$ (i.e. the signal has finite duration T and sample frequency N/T) so C_m must be approximated by calculating the summation:

$$C_m = \frac{1}{T} \sum_{n=-N/2+1}^{N/2} x_n \mathrm{e}^{-\mathrm{j}2\pi mn/N} \tag{3.4}$$

However, because of the limited number of data points, the maximum frequency that can be calculated is limited to $(N-1)/T$, when $m = N-1$. This can be shown by making the substitution $m = N + m^*$ in equation 3.4:

$$C_{N+m^*} = \frac{1}{T} \sum_{n=-N/2+1}^{N/2} x_n \mathrm{e}^{-\mathrm{j}2\pi m^* n/N} \mathrm{e}^{-\mathrm{j}2\pi n} \tag{3.5}$$

Since n is an integer, the last term always equals unity so $C_{N+m^*} = C_{m^*}$, which is the amplitude at frequency m^*/T rather than $(N+m^*)/T$. Extending the same argument

it is usual to assume the frequency information for points $m > N/2$ as actually for the negative frequency points $m - N$. Therefore, by using the DFT, the frequency content in the range of $m = -N/2 + 1$ to $m = N/2$ may be found. Thus the discrete transform is only a true representation of the signal if the signal has no frequency content for $|m| > N/2$ or there is no frequency content above half the sampling frequency (the Nyquist frequency). If higher frequencies are present then the calculation for C_m will contain not only the signal content at frequency m/T but also for all frequencies $(m + Nk)/T$, where k is an integer.

The Fourier series is valid for a signal that is periodic with period T. Therefore the signal used in the DFT may be thought of as repeating outside the known range with period T. The only difference between the FS and the DFT analysis methods is that with the FS the time period is selected to match exactly one cycle of the fundamental frequency, a selection which is not possible for the DFT of a signal since the frequency content is unknown. The result of not matching the period of the time window with the repeating period of the signal is that, when the signal is thought of as a repeating signal, there will be a step change at $t = (k+1/2)T$ where k is an integer. This leads to unexpected frequency components. This can be seen in figures 3.1 and 3.2. Figure 3.1a shows the real component of a time signal to be transformed and the repeating signal which may be thought of as the signal used in the DFT. In this case the signal is the complex exponential of $10\pi t/T$, so that the frequency of the signal is $5/T$ and the DFT is performed over $t = -T/2$ to $t = T/2$. Figure 3.1b shows the calculated values of the frequency content which is non-zero only at frequency $5/T$. Figure 3.2 is the same except that the frequency of the signal is $5.2/T$, so the repeating signal has steps in it. Here the DFT incorrectly predicts the frequency content.

3.2.2 Using the Fourier Transform and Windowing

It is possibly more useful to think of the DFT, equation 3.4, as the transform of an infinitely long signal which is zero outside the range $-T/2 < t \leq T/2$. This is the same as a continuous signal (not necessarily repeating at frequency $1/T$ so therefore not having steps at time-points $t = (k+1/2)T$) which has been multiplied by a box window

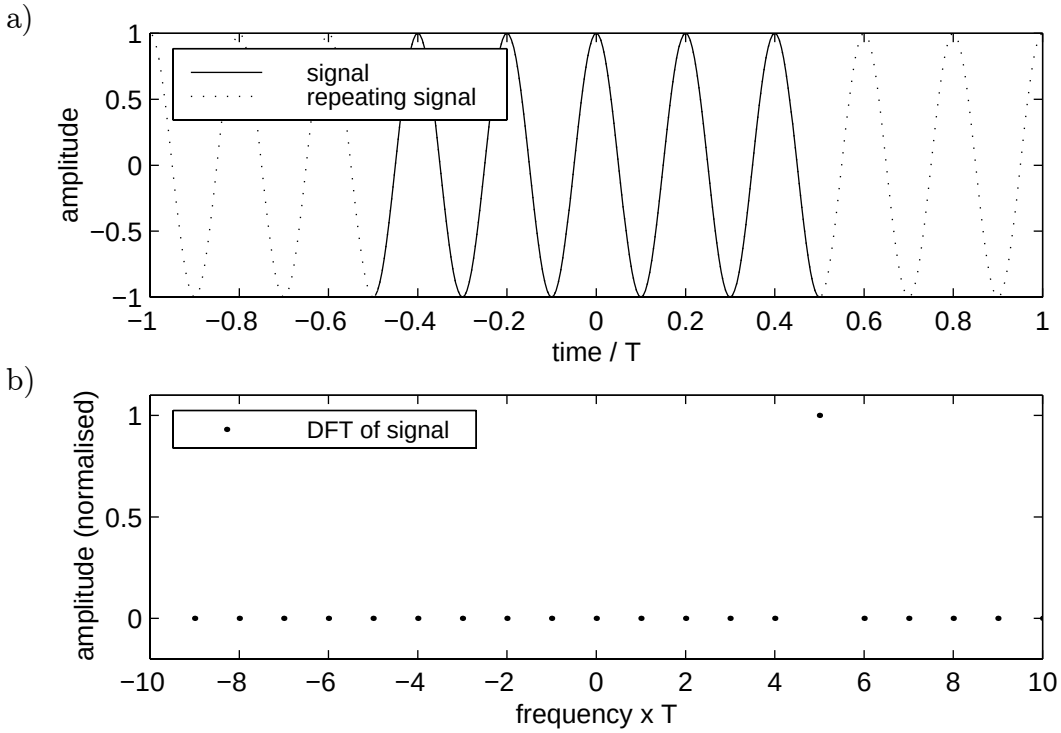

Figure 3.1: The DFT: a signal of frequency $5/T$ in a) the time and b) the frequency domain

that takes the value 1 over the range $-T/2 < t \leq T/2$ and is zero elsewhere. The FT of a non-sampled signal multiplied by a box window is the convolution of the signal in the frequency domain with a "sinc" function, defined as:

$$\text{sinc}(x) = \frac{\sin(x)}{x} \tag{3.6}$$

For the DFT of a sampled signal the result is the same, a convolution of the expected frequency content with a sinc function, explaining the unexpected frequencies in the previous example. This can be seen in figure 3.3, which shows the frequency content of a) the $5/T$ signal and b) the $5.2/T$ signal of length T using the DFT and the continuous FT with a box window applied to the signal, called the windowed Fourier transform (WFT). The case where a whole number of cycles exactly fits into the window (for example the $5/T$ signal in figure 3.3a) is a special case where the sinc function takes the value zero at the frequency points calculated by the DFT other than frequency $5/T$. The additional peaks due to the convolution with the sinc function are termed "side-lobes".

The effect of discretising the signal can be seen by multiplying the continuous signal

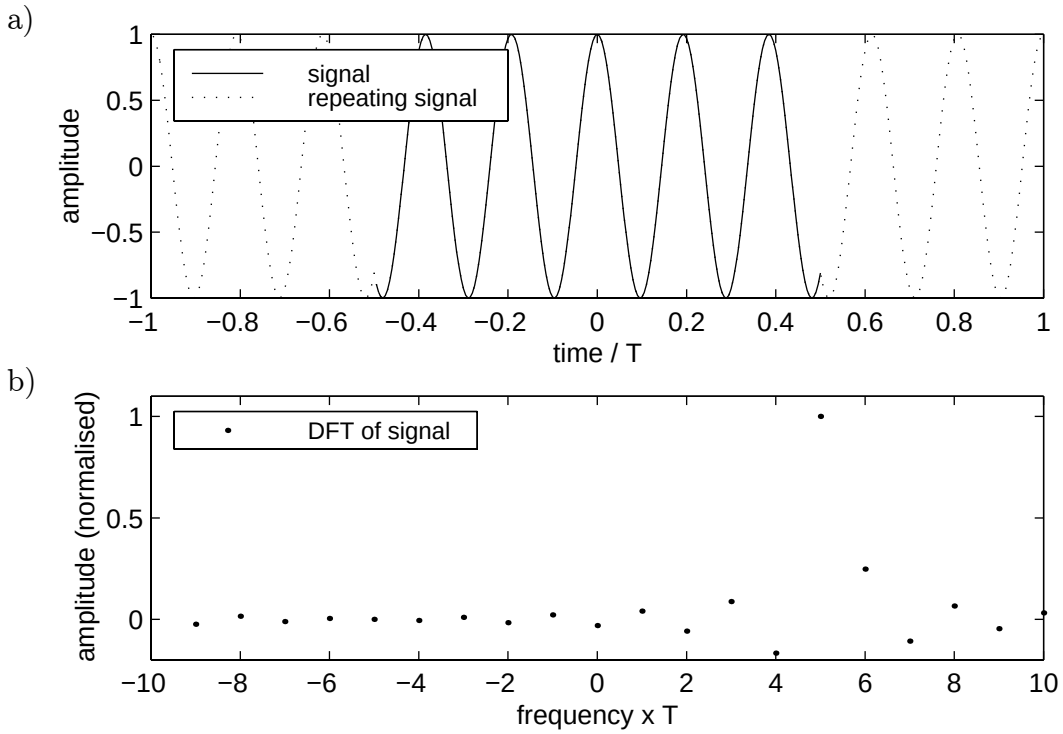

Figure 3.2: The DFT: a signal of frequency $5.2/T$ in a) the time and b) the frequency domain

by a pulse train with a frequency equal to the sampling frequency of the discrete signal. The FT of the discretised signal is, therefore, the same as for the continuous signal convolved with the transform of the pulse train (which is a pulse train in the frequency domain with a pulse frequency the same as the sampling frequency). This results in alias frequency spectra centred at integer multiples of the sample frequency. Therefore, as with the discrete Fourier series equation, a true representation of the signal is only possible if the signal has no frequency content greater than half the sampling frequency.

It can be seen that the FT (equation 3.3) is the same as a continuous version of the DFT (equation 3.4) for the signal (albeit multiplied by a scaling factor); the summation over the range $n = -N/2 + 1$ to $n = N/2$ is the same as the integration over the range $n = -\infty$ to $n = \infty$, because the signal is zero outside the range $-T/2 < t \leq T/2$ (or $-N/2 + 1 \leq n \leq N/2$). The complex exponential term $\mathrm{e}^{-\mathrm{j}2\pi ft}$ may be written as $\mathrm{e}^{-\mathrm{j}2\pi mn/N}$ in discrete form, since the frequency at bin m is m/T and the time at bin n is nT/N. The only effect of the discretisation is to add alias terms which are unimportant

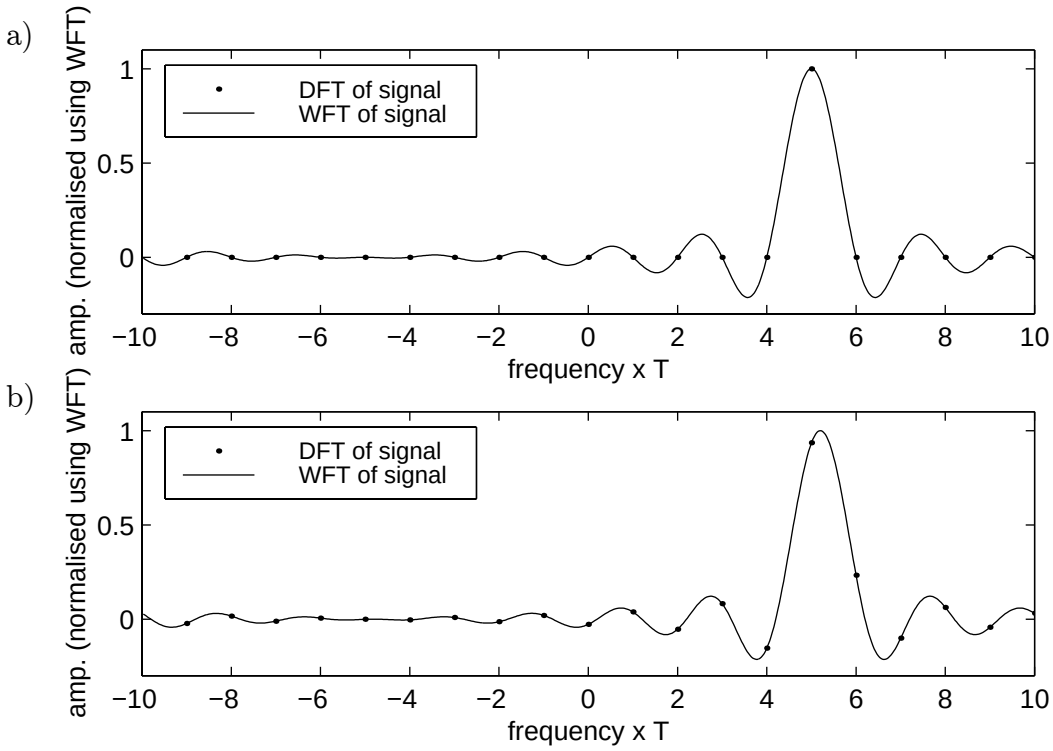

Figure 3.3: DFT and WFT of the signals with frequency a) $5/T$ and b) $5.2/T$

provided the sampling frequency is at least twice the highest frequency component of the signal. This leads to the question:

> "why does the discrete Fourier transform calculate the frequency for only integer values of m between $-N/2+1$ and $N/2$?"

The answer is that non-integer values of m within the range $-N/2+1$ to $N/2$ can be calculated as explained in subsection 3.2.3 on zero-padding. It is only the comparison between the discrete Fourier transform and the Fourier series and the idea of having a repeating signal which leads to the artificial limitation that m may only be an integer number.

At this stage, it is worth commenting on the DFT of a signal which lasts for time T in the range $0 < t \leq T$ (or $1 \leq n \leq N$). Using the WFT approach, the signal may be thought of as a signal in the range $-N/2+1 \leq n' \leq N/2$ where n' is time bin n shifted by $N/2$. The effect of shifting the time axis before applying the FT is to multiply the frequency domain function of the signal before the time-shift by a complex exponential

term:

$$x(t') = x(t - T/2) \overset{\mathcal{F}}{\leftrightarrow} \mathrm{e}^{\mathrm{j}\pi fT} X(f) \tag{3.7}$$

where $X(f)$ is the FT of $x(t)$. It is, therefore, possible to treat the signal as being in the range $-T/2 < t' \leq T/2$ (corresponding to bins $-N/2 + 1 \leq n \leq N/2$) when applying the DFT, provided the signal in every frequency-domain bin m is then multiplied by $\mathrm{e}^{\mathrm{j}\pi mn/N}$. The effect of this is to ensure the phase of the signal in the frequency-domain refers to the signal at time $t = 0$ rather than $t = T/2$. However, it is possibly neater to look at the problem from the Fourier series approach. The DFT may be thought of as the transform of a repeating signal, with period T. It follows that the signal at bin n is the same as at bin $n + N$. Therefore, it is possible to reproduce the signal sampled over $0 < t \leq T$ as a signal over $-T/2 < t \leq T/2$ by shifting the signal in the range $T/2 < t \leq T$ to the range $-T/2 < t \leq 0$. This may be expressed algebraically for a discrete signal $y(n)$ over the range $1 \leq n \leq N$ by calculating the DFT of signal $x(n)$ over the range $-N/2 + 1 \leq n \leq N/2$ where:

$$\{x\} = \begin{bmatrix} x(-N/2+1) \\ x(-N/2+2) \\ \vdots \\ x(-1) \\ x(0) \\ x(1) \\ \vdots \\ x(N/2-1) \\ x(N/2) \end{bmatrix} = \begin{bmatrix} y(N/2+1) \\ y(N/2+2) \\ \vdots \\ y(N-1) \\ y(N) \\ y(1) \\ \vdots \\ y(N/2-1) \\ y(N/2) \end{bmatrix} \tag{3.8}$$

3.2.3 Zero-Padding

The Fourier transform is the transform of an infinitely-long time signal giving infinite frequency resolution. For a discrete signal the frequency content is approximated by transforming a signal of finite length T to a series of discrete values in the frequency domain, with resolution of $1/T$. Zero-padding is a technique which allows a better approximation to the FT of a signal to be calculated using the DFT. Before the DFT

of the time signal is calculated, a string of zeros is added to the beginning and end of the signal.

The effect of adding these zeros may be seen as calculating the DFT for non-integer values of m. If the signal is zero-padded to length αN, then the DFT equation (equation 3.4) becomes:

$$C_{m^*} = \frac{1}{\alpha T} \sum_{n=-\alpha N/2+1}^{\alpha N/2} x_n \mathrm{e}^{-\mathrm{j}2\pi m^* n/(\alpha N)} \tag{3.9}$$

where m^* takes the integer values $-\alpha N/2+1$ to $\alpha N/2$ and the time period of the signal is increased from T to αT. This can be simplified, since the signal is zero outside the range $-N/2+1 \leq n < N/2$:

$$C_{m^*} = \frac{1}{\alpha T} \sum_{n=-N/2+1}^{N/2} x_n \mathrm{e}^{-\mathrm{j}(2\pi n/N)(m^*/\alpha)} \tag{3.10}$$

This is the same as the original equation before zero-padding (albeit scaled by $1/\alpha$), except that now m takes values from $-N/2+1/\alpha$ to $N/2$ in steps of $1/\alpha$ rather than steps of one. Thus the frequency steps are $1/(\alpha T)$ rather than $1/T$.

Figure 3.4 shows the DFT (normalised using the maximum value of the WFT) of a complex exponential signal with frequency $5/T$ lasting time T, sampled at a frequency $20/T$. There are 20 points in the time domain and so 20 points in the frequency domain. The range of frequencies calculated is $-9/T$ to $10/T$, with resolution between points of $1/T$ (as the signal lasted time T). This figure also shows the effect of zero-padding the signal to double its length, which leads to a frequency resolution of $0.5/T$ and a frequency range of $-9.5/T$ to $10/T$, and the effect of zero-padding to four times its original length, resulting in $0.25/T$ resolution and a frequency range of $-9.75/T$ to $10/T$. Infinite zero-padding results in the same estimation as a windowed continuous FT.

In this example, the zero-padding of the signal appears to lead to a loss of accuracy of the frequency content of the signal. With no zero-padding, no frequency content other than at $5/T$ was predicted. However, this example is a special case where the frequency of the signal is exactly the same as one of the frequency bins. So, although the increase in zero-padding highlights the underlying sinc function caused by windowing the time signal to a finite length, it does not affect the predicted frequencies.

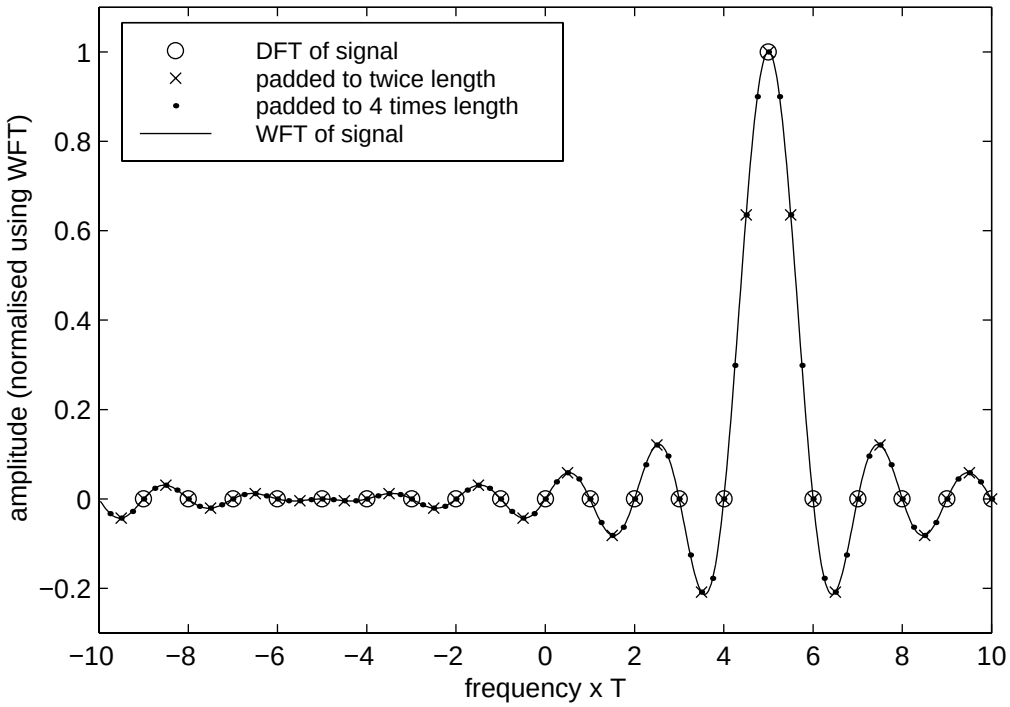

Figure 3.4: Zero-padded DFT of $5/T$ frequency complex exponential signal

If the frequency is not the same as one of the frequency bins for the unpadded signal, then zero-padding will improve the frequency estimation. Figure 3.5 shows the Fourier transform for the $5.2/T$ complex exponential signal lasting for time T. With no zero-padding the predicted frequency is $5/T$. However, with increased resolution the frequency estimate is improved, as the underlying sinc function is exposed in more detail.

It should be noted that zero-padding is not a true improvement in the frequency estimation, as it is only capable of showing a better discrete approximation to the continuous FT of the windowed signal. A true improvement in resolution can only be achieved by increasing the length of the time signal and so reducing the width of the peaks of the sinc function. This is illustrated in figure 3.6, which shows the frequency content predicted for the $5/T$ frequency signal compared with the frequency estimation when the signal is zero-padded to twice its original length and when the signal is recorded over twice the original length. The solid and dotted lines are infinitely padded signals of length T and $2T$ respectively, exposing the full details of the underlying sinc function

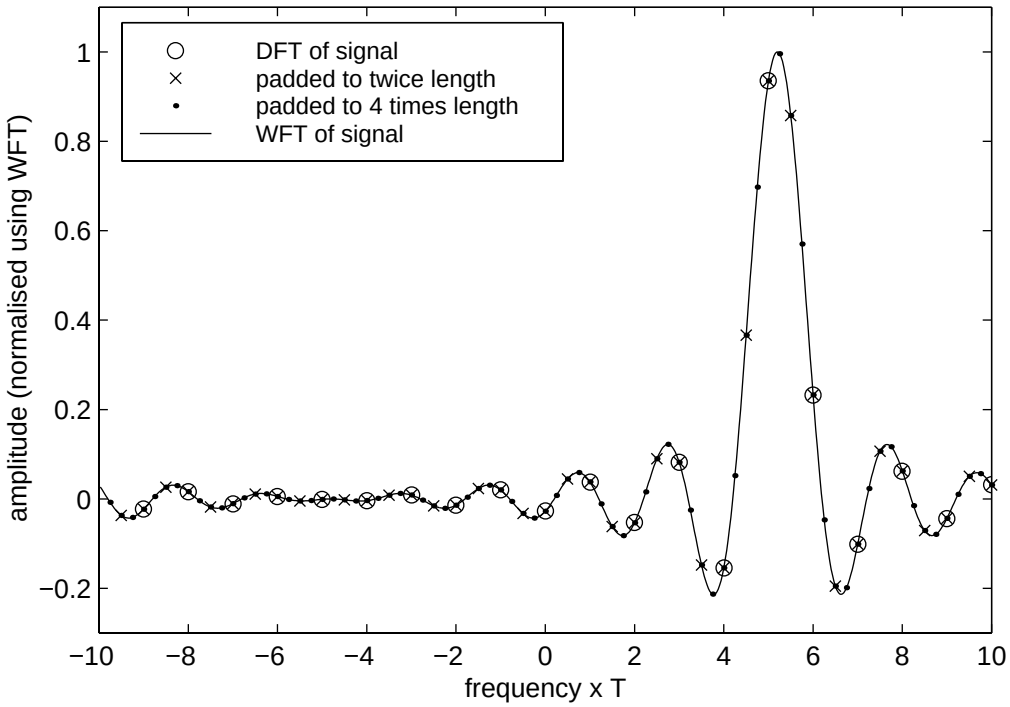

Figure 3.5: Zero-padded DFT of $5.2/T$ frequency complex exponential signal

caused by the windowing in time.

Clearly, by zero-padding to a sufficient length, the frequency of the signal can be found accurately by looking for the frequency bin with the largest frequency content. However, when there are two or more modes, the sinc functions corresponding to each mode interfere and can lead to incorrect estimations of the frequencies of the modes, as discussed in section 3.3.

If a signal of length T in the range $0 < t \leq T$ is considered, to maintain the correct phase relationship it is necessary to ensure the repeating signal (using the Fourier series approach) contains the true signal over the range $0 < t \leq T$. The DFT may then be calculated using the signal over the range $-T/2 < t \leq T/2$. For example, if the signal is to be zero-padded to four times its original length, the repeating signal takes the value 0 over the range $-2T < t \leq 0$, the original signal over the range $0 < t \leq T$ and 0 over the range $T < t \leq 2T$.

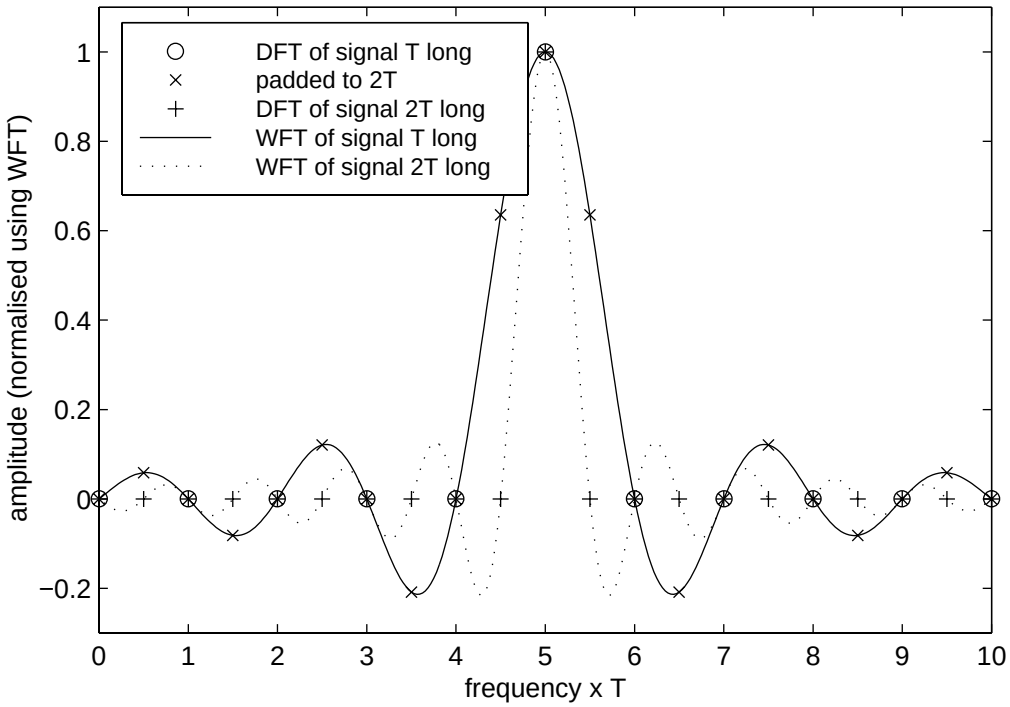

Figure 3.6: A comparison between zero-padding and an increase in sample time

3.2.4 Decimation

It is sometimes useful to reduce the sample frequency of a signal to speed up analysis of data. The cost of this operation is the loss of information relating to higher frequency components. In order to avoid aliasing, it is necessary to filter the signal while skipping data points to remove these higher frequency components, a process called decimation (although the process skips data points rather than removing every tenth element). The decimation routine used here is a standard Matlab function using a Chebyshev low-pass filter.

3.2.5 Windowing

To reduce the side-lobes, windowing is sometimes used. This is where the signal is multiplied by a window the same length as the signal before the DFT is calculated. If the windowed Fourier transform is considered, the effect of using the window is that it replaces the rectangular window applied to the signal. Therefore, rather than the frequency content being convolved with a sinc function it is convolved with the transform

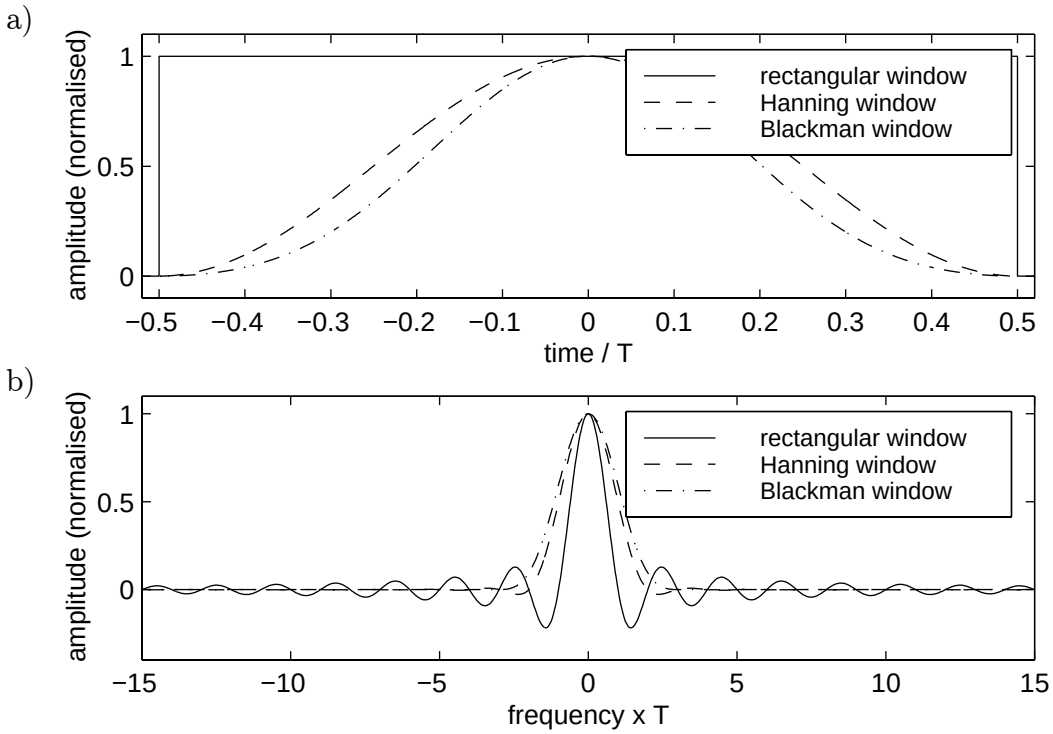

Figure 3.7: Windows, in a) the time and b) the frequency domain, applied in the time domain to reduce side-lobes in the frequency domain

of the window. There are numerous windows, of which two popular ones implemented in Matlab are the Hanning and the Blackman windows. Figures 3.7a and 3.7b show these windows in the time and frequency domains respectively, along with the rectangular window for comparison. It can be seen that the drawback of reducing the side-lobes is that the true frequency peak is wider. Windowing is not used in the work presented here because correct frequency estimation is more important than reduction in side-lobes, as it will be seen that the fundamental frequency dominates the signal.

3.3 Auto-Regressive Model

The auto-regressive (AR) model is a way of calculating the frequency content of a discrete, finite-duration signal, without introducing a convolution of the true frequency content of the signal with a sinc function as is done when using the DFT. As with the DFT, a time-frequency estimation may be calculated using the moving window method (section 3.6.2).

3.3.1 The z-Transform

Before the AR model can be explained, it is first necessary to summarise the properties of the z-transform. The z-transform is defined as:

$$x_n \leftrightarrow X(z) = \sum_{n=-\infty}^{\infty} x_n z^{-n} \tag{3.11}$$

where z is the complex variable. If z is expressed in polar form:

$$z = r\mathrm{e}^{\mathrm{j}2\pi f} \tag{3.12}$$

then the z-transform may be written as:

$$X\left(r\mathrm{e}^{\mathrm{j}2\pi f}\right) = \sum_{n=-\infty}^{\infty} \left(x_n r^{-n}\right) \mathrm{e}^{-\mathrm{j}2\pi f n} \tag{3.13}$$

From this equation it can be seen that if r is set to unity then the z-transform of x_n reduces to the FT of x_n. Therefore, to assess the frequency content of the series x_n using the z-transform, the value of $X(z)$ on the unit circle should be considered [74].

From the definition of the z-transform (equation 3.11) it is possible to calculate the z-transform of x_{n-1}:

$$x_{n-1} \leftrightarrow \sum_{n=-\infty}^{\infty} x_{n-1} z^{-n} = \sum_{m=-\infty}^{\infty} x_m z^{-m} z^{-1} = z^{-1} X(z) \tag{3.14}$$

where $X(z)$ is the z-transform of x_n (see for example Oppenheim *et al.* [74]).

3.3.2 The ARMA Function

In general, a process may be modelled using a transfer function. The most general model is the auto-regressive moving average (ARMA) model and can be written as:

$$x_n = \sum_{i=0}^{q} b_i n_{n-i} - \sum_{k=1}^{p} a_k x_{n-k} \tag{3.15}$$

where the input sequence is n_n and the output sequence is x_n (see Kay and Marple [47] or Gutowski *et al.* [42]). This can be transformed into the z-domain using the z-transform, equation 3.14:

$$X(z) \sum_{k=0}^{p} a_k z^{-k} = N(z) \sum_{i=0}^{q} b_i z^{-i} \tag{3.16}$$

where $a_0 = 1$. Therefore, the transfer function from the input sequence n_n to the output sequence x_n can be written as:

$$H(z) = \frac{\sum_{i=0}^{q} b_i z^{-i}}{\sum_{k=0}^{p} a_k z^{-k}} = \frac{B(z)}{A(z)} \tag{3.17}$$

where $B(z)$ is the z-transform of b_i and $A(z)$ is the z-transform of a_k. If the input driving sequence n_n is assumed to be white noise of zero mean and variance σ^2, then the power spectral density of the input is $\sigma^2 \Delta t$, where Δt is the sampling time step. It can be shown (Kay and Marple [47]) that the power spectral density of the resulting signal using the ARMA method is:

$$\mathcal{P}_{\mathrm{ARMA}}(f) = \sigma^2 \Delta t \left| \frac{B(f)}{A(f)} \right|^2 \tag{3.18}$$

where $B(f)$ is the special case of the z-transform of b_n when $z = \mathrm{e}^{\mathrm{j}2\pi f \Delta t}$:

$$B(f) = \sum_{i=-\infty}^{\infty} b_n \mathrm{e}^{-\mathrm{j}2\pi f \Delta t i} \tag{3.19}$$

If the sample time step is written not as Δt but as T/N, where T is the length of the time signal and N is the number of samples in the time signal, and it is accepted that $q \leq N - 1$ (otherwise over-fitting of the signal will occur), then the equation may be rewritten as:

$$B(f) = \sum_{i=0}^{q-1} b_i \mathrm{e}^{-\mathrm{j}2\pi f T i/q} \tag{3.20}$$

This is the same as the discrete Fourier transform equation (equation 3.4), except for a scaling factor of $1/T$, the range being 0 to $q - 1$ rather than $-q/2 + 1 \leq i \leq q/2$ (but this may be overcome using equation 3.8) and that it is usual to calculate the DFT for integer values of m, i.e. in frequency steps of $1/T$, whereas the equation for $B(f)$ can be calculated for any frequency. This limitation in the implementation of the DFT can be overcome by zero-padding (see section 3.2.3). Therefore, the easiest (although not the most computationally efficient) way of calculating $B(f)$ for a range of values of f is to use the DFT of b_i, zero-padded sufficiently to give the desired frequency resolution.

It can be seen from equation 3.17 that the b_i coefficients result in poles in the transfer function and the a_k coefficients result in zeros. If all the a_k terms are set to zero, with the exception of $a_0 = 1$, then equation 3.15 becomes:

$$x_n = \sum_{i=0}^{q} b_i n_{n-i} \tag{3.21}$$

which is a moving average of order q, sometimes termed the all-zero model. Alternatively, if the b_i terms are zero except $b_0 = 1$:

$$x_n = -\sum_{k=1}^{p} a_k x_{n-k} + n_n \tag{3.22}$$

which is called the auto-regressive (AR) model or all-pole model, since x_n is a linear regression on itself with n_n being the error terms. This model allows estimation of the current x_n term as a weighted sum of the past terms and a noise term n_n [58].

3.3.3 The Auto-Regressive Model

The auto-regressive model is arguably more useful than the moving average model, as it is usually the frequency peaks which are of interest. These are determined by the poles in the z-domain, rather than the zeros which affect the frequency troughs [58].

Noting that $a_0 = 1$, equation 3.22 may be written as:

$$n_n = \sum_{k=0}^{p} a_k x_{n-k} \tag{3.23}$$

Therefore, n is the discrete convolution of a with x, with the condition that $a_k = 0$ where $k < 0$ and $k > p$:

$$n_n = a_n * x_n \tag{3.24}$$

A convolution in the time domain is the same as multiplication in the frequency domain:

$$N_m = A_m \times X_m \tag{3.25}$$

where m is a frequency coefficient. Since n_n is the error term which is minimised with the restriction that $a_k = 0$ where $k < 0$ and $k > p$, then a_k may be thought of as having very small frequency content at the frequency where x_n has large frequency content and vice versa. Therefore, loosely speaking, if the frequency content of a_k is inverted, then the peaks in frequency will correspond to the peaks in the frequency content of x_n.

The advantage with a_k is that it is fitted to x_n with the condition that it is zero outside the range $0 \leq k \leq p$. It has been shown that the DFT can be thought of as the discrete form of a continuous FT multiplied by a window in the time domain (see section 3.2.2). If this window is applied to a_k, a_k will not be altered, so the convolution

with a sinc function in the frequency domain, present in the DFT, will not occur. The DFT of a_k will be the same as a FT of a_k over infinite time. As discussed in section 3.2.3, the transform may be calculated at any frequency, not just the frequencies corresponding to integer values of m. Therefore, it is possible to find the exact frequencies where a_k has minima, which correspond to the frequencies where x_n has peaks (provided the error term n_n has been minimised to an acceptable level). The drawback is that when calculating a_k, a suitable number of poles must be selected to ensure the error signal n_n is reduced to an acceptable level in order that the inverse of the frequency content of a_k matches the frequency content of x_n. This is normally done on a trial-and-error basis.

The routine to calculate the time signal a_k used here is the Burg algorithm along with the Levinson-Durbin recursive algorithm (see Appendix A for the equations, Press *et al.* [86] for an implementation in C^{++} or [59] for the implementation in Matlab). There are several methods for selecting a suitable number of non-zero values in a_k, or poles. Some of these are explained in Kay and Marple [47], however they are all for the case where the number of points N in the time signal is large. When the time signal is "short" there is a rule of thumb that the number of poles should be in the range $N/3 \leq p \leq N/2$ (see, for example, the paper by Ulrych and Ooe in Haykin [43]). Ulrych and Bishop [110] suggest "short" means a signal which contains only a few cycles of the lowest frequency of interest.

Once a_k has been calculated in the range $1 \leq k \leq p$, the frequency content of x_n may be examined by calculating its power spectral density. Putting $q = 0$, to eliminate the zeros in the ARMA model gives $B(f) = 1$ (the Fourier transform of a Dirac-delta function). Hence equation 3.18 becomes:

$$\mathcal{P}_{\mathrm{AR}}(f) = \sigma^2 \Delta t \left| \frac{1}{A(f)} \right|^2 \tag{3.26}$$

where $A(f)$ may be calculated for a series of frequencies using the discrete Fourier transform and zero-padding.

It is now possible to compare the normalised power spectral density using the discrete Fourier transform and the auto-regressive model. Considering a complex exponential signal at frequency $5.2/T$ sampled at frequency $20/T$ for time T, figure 3.8 shows the power spectral density using the DFT of the signal, zero-padded to 32 times its original

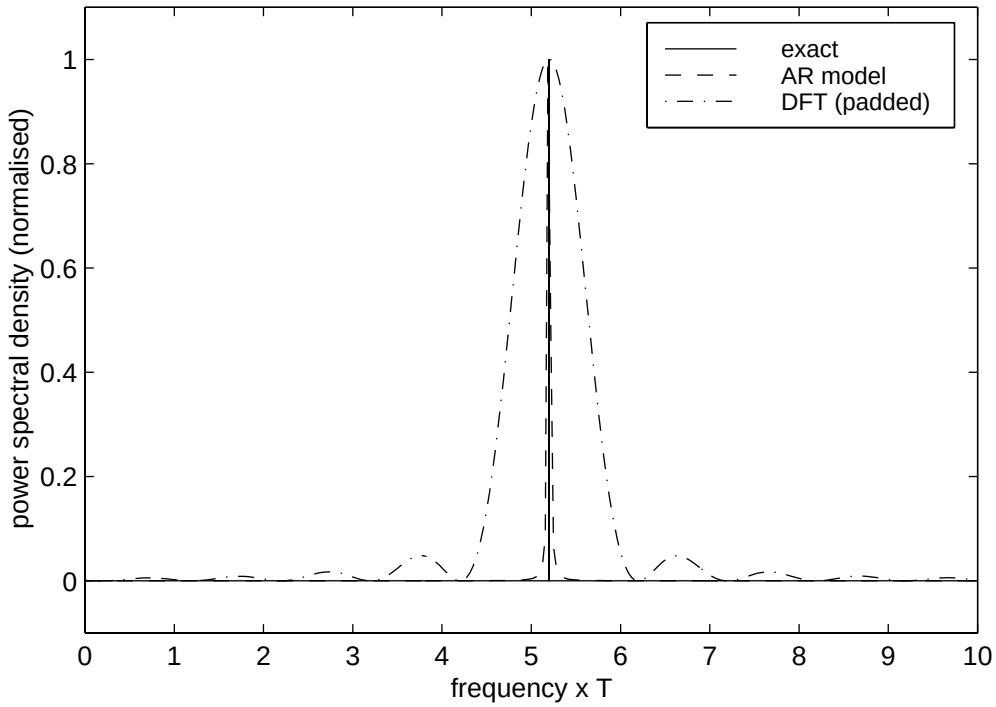

Figure 3.8: Comparison of the AR model and the DFT methods on a complex exponential signal with frequency $5.2/T$

length, and the auto-regressive model using one pole, with the frequencies calculated to the same resolution (i.e. the a_k coefficient vector zero-padded to the same length as the signal after zero-padding in the DFT). As expected, the DFT exhibits the sinc function due to the windowing in time, which is avoided when using the auto-regressive model. However, if the frequency at which there is maximum amplitude is all that is of interest, the result using either method is the same. The advantage of the auto-regressive model becomes apparent when the signal contains multiple closely-spaced modes, as will be shown.

When more complicated synthetic signals were used to test the auto-regressive model, it was found that rounding errors were affecting the location of the predicted frequencies. This can be avoided by adding a small amount of noise to the signal. It is thought that without noise all the poles congregate close together near the signal frequency and interfere with each other. The noise adds additional small amplitude frequency peaks which are picked up by the "excess" poles in the model leaving one pole at the correct

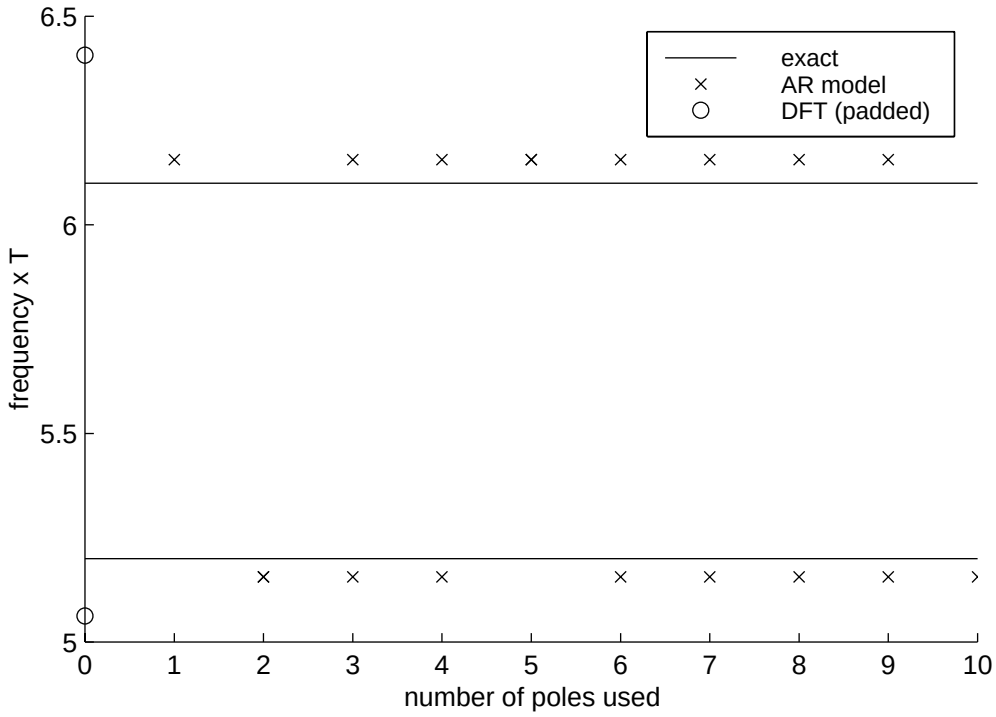

Figure 3.9: Frequency estimation using the AR model with increasing numbers of poles

frequency.

To demonstrate the advantage of using the auto-regressive model, the case of a signal with two closely-spaced modes is considered. The signal consists of the sum of two complex exponentials, one at frequency $5.2/T$ and one of half the amplitude at $6.1/T$, and some added noise (maximum of 1% of the signal amplitude) sampled at $20/T$ for time T. Figure 3.9 shows the location of the two largest frequency peaks for the auto-regressive model with increasing numbers of poles and the peaks for the DFT (zero-padded to 32 times the original length). Note that the number of poles to be used in an AR model must be chosen by a trial-and-error basis. In this case, the peaks in frequency remain unchanged for greater than six poles suggesting that this is likely to be close to the acceptable number of poles. Figure 3.10 compares the power spectral density for the AR model using six poles to that for the DFT, both plotted with a frequency resolution of $1/(32T)$ using zero-padding. It shows that although there is still an error with the frequency estimation using the auto-regressive model, it is a better predictor of the power spectral density than the discrete Fourier transform.

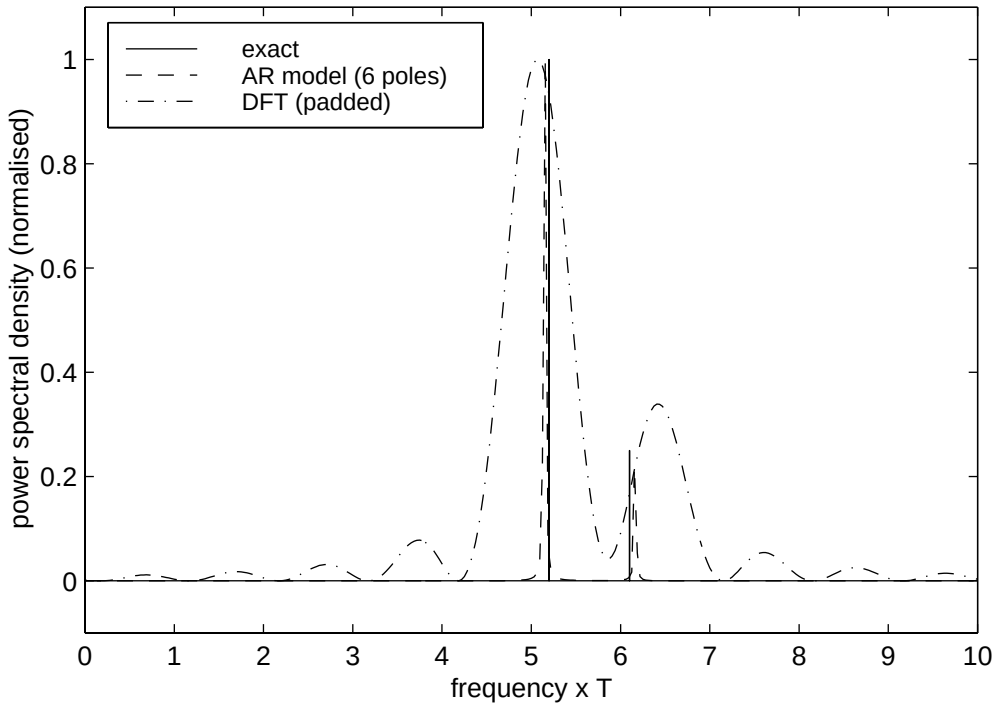

Figure 3.10: Power spectral density for a signal with two modes sampled at a frequency of $20/T$, 6 poles

A complication with the AR approach is that it is sensitive to the sampling frequency. With the DFT, the sampling frequency only affects the maximum frequency content that can be calculated. Hence decimating to a slower sampling frequency leaves the frequency content estimations below half this rate unchanged. When using the AR model this rule does not apply. By decimating the signal to half the sample frequency, if the window width in time and the number of poles used remains the same, the number of data points in the window will halve. However, this will lead to the a_k fit spanning twice the time and so the properties of the frequency estimation will be altered. At first sight, it seems that when decimating the signal to half the sample frequency, the number of poles should be halved so that the time span of a is the same as before decimation. However, when the signal is decimated it is also filtered to remove frequencies above half the new sample frequency to avoid aliasing, so the number of poles required to model the signal satisfactorily will reduce as there will be fewer frequency peaks in the signal. A lower sample frequency will then lead to fewer a_k coefficients spanning a longer time.

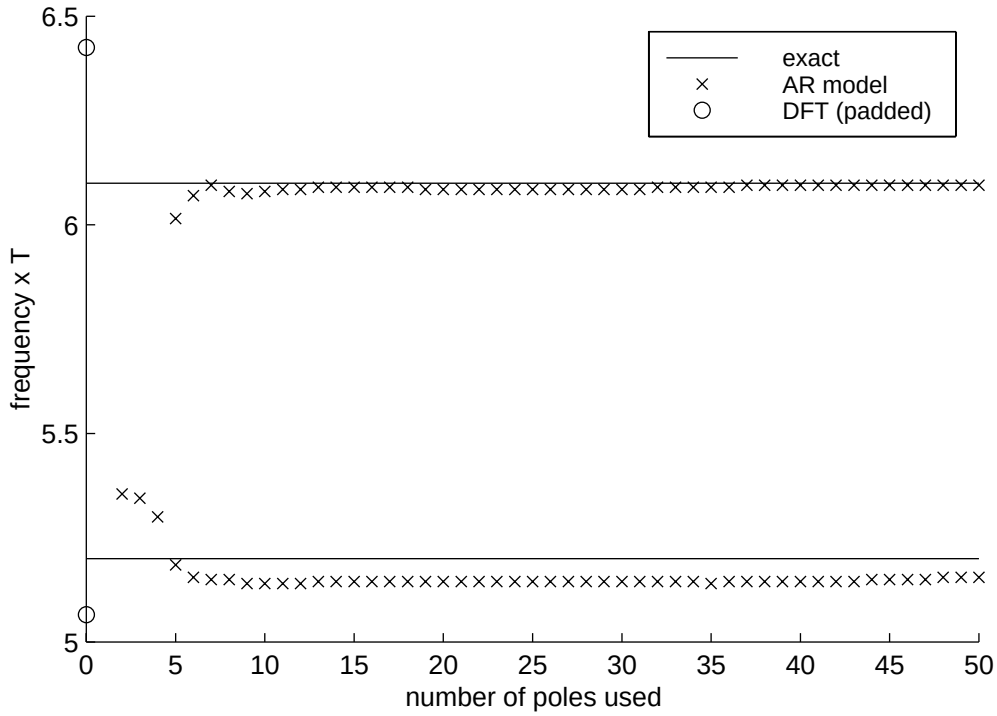

Figure 3.11: Frequency estimation using the AR model with increasing numbers of poles

The frequency estimation is therefore a function of not only the length of the signal in time and the number of poles selected but also the sample frequency. This may be demonstrated if the signal containing two modes is generated at a sampling frequency of $200/T$ for time T. Figure 3.11 shows the location of the two largest frequency peaks for the auto-regressive model and the DFT. If the number of poles remains unchanged from that used for the signal sampled at $20/T$, the model fails to predict the frequency of the second mode with any confidence, as shown in figure 3.12. If, however, 11 poles are used (see figure 3.13) the resulting power spectral density is similar to that using six poles on the signal sampled at a frequency of $20/T$. It can be seen that the frequency estimation using the auto-regressive model has changed due to the change in sampling frequency.

In summary, the auto-regressive model calculates a better estimation of the frequency peaks for a signal of two or more modes. However, the drawbacks are that the optimal number of poles for the model must be selected and a change in sampling frequency affects both the frequency estimation and the optimum number of poles.

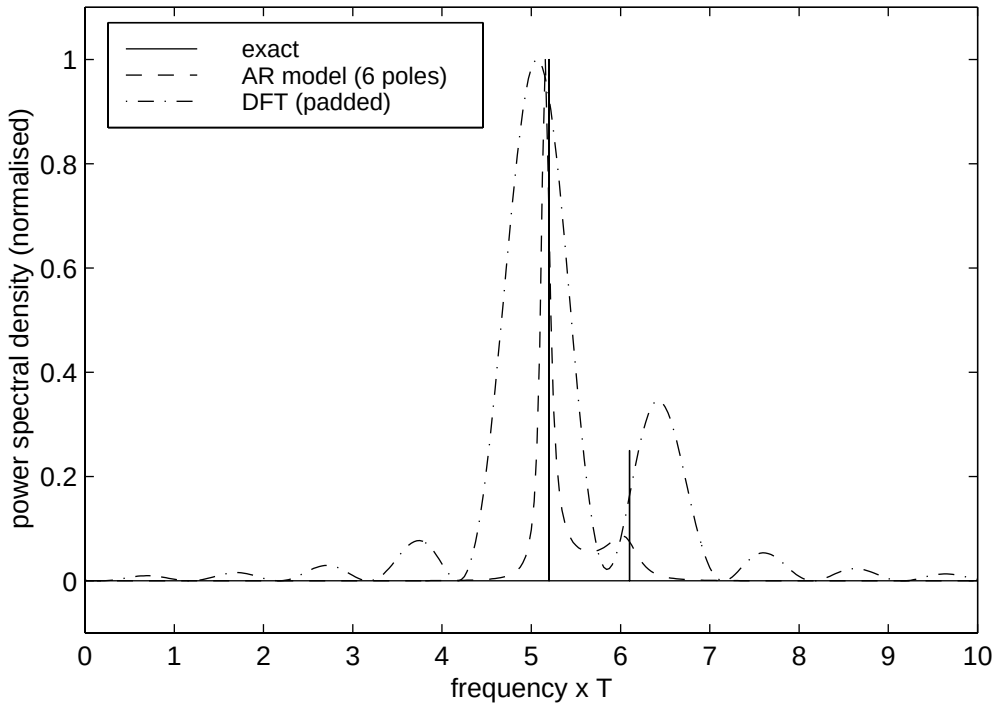

Figure 3.12: Power spectral density for a signal with two modes sampled at a frequency of $200/T$, 6 poles

3.4 The Analytic Signal

So far, the only signals considered have been in complex exponential form. Experimental signals are always real. An analytic signal is a complex version of a signal created by applying the Hilbert transform to the signal (see, for example, Randall [90] or Bracewell [10]). The real part of an analytic signal is the same as the original signal and the imaginary part is the Hilbert transform of the signal. The analytic signal is a rotating phasor with an instantaneous amplitude the same as the maximum amplitude of the signal at the time in question.

The analytic signal $s(t)$ is given by:

$$s(t) = x(t) + \mathrm{j}\hat{x}(t) \tag{3.27}$$

where $x(t)$ is the real signal and $\hat{x}(t)$ is the Hilbert transform of $x(t)$, which in the frequency domain is defined as:

$$\hat{X}(\omega) = -\mathrm{j}\,\mathrm{sign}(\omega)X(\omega) \tag{3.28}$$

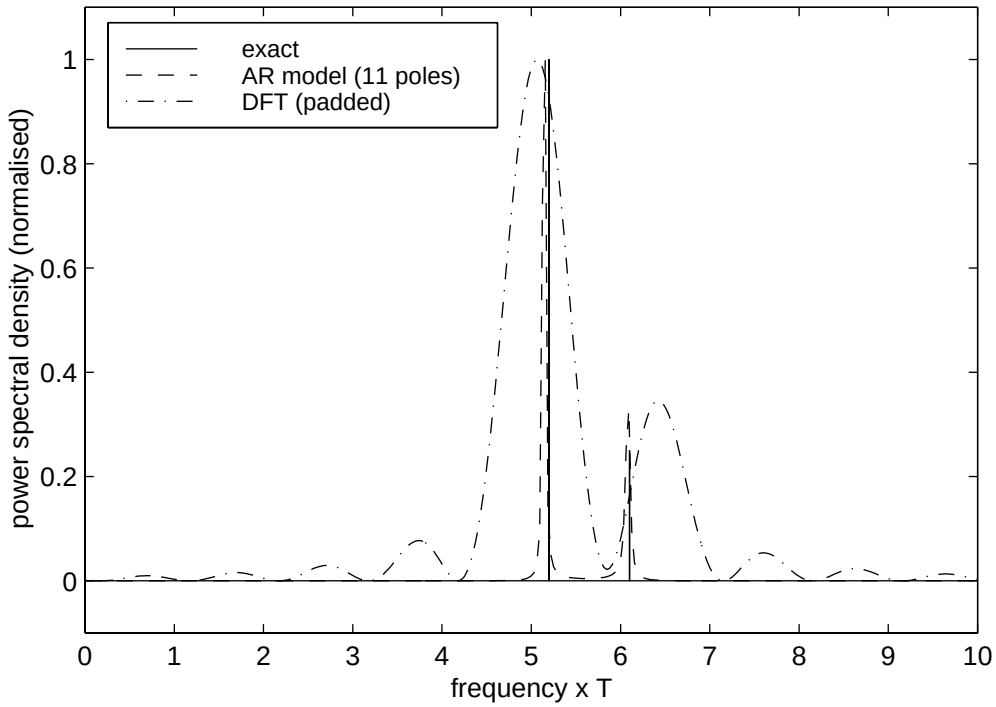

Figure 3.13: Power spectral density for a signal with two modes sampled at a frequency of $200/T$, 11 poles

noting that $\text{sign}(0) = 0$. If a constant frequency signal is considered, the analytic version is a helix of constant amplitude at the same frequency as the original signal:

$$x(t) = A\cos(\omega_0 t) + B\sin(\omega_0 t) \qquad \leftrightarrow \qquad s(t) = (A - \mathrm{j}B)\mathrm{e}^{\mathrm{j}\omega_0 t} \tag{3.29}$$

This transform is useful because the amplitude of each frequency component is constant with time with only the phase changing. Therefore, by taking the absolute value of the analytic signal, the amplitude envelope of the signal can be calculated. More importantly, it will be seen that it reduces any phase difference effects in moving-window time-frequency estimations (section 3.6), using discrete Fourier or auto-regression (see section 3.3) transforms. A further advantage is that it helps to reduce cross-terms when using the bilinear form of the signal to calculate the time-frequency relationship.

3.5 A Non-Linear Signal

Before proceeding to a discussion of methods of calculating time-frequency relationships, it is helpful to describe how to generate a non-linear test signal (that is, a test signal with a time-dependent frequency). A non-linear test signal can be generated by using the equation:

$$y = A\sin(2\pi g(t)t) \tag{3.30}$$

where $g(t)$ must be related to the instantaneous frequency at time t. At any time t, the signal will be equivalent to a phase-shifted sine wave with a frequency matching the instantaneous frequency f_t:

$$y = A\sin(2\pi f_t t + \phi) \tag{3.31}$$

Equating the values and the gradients of the two signals at time t, the relationship between the function $g(t)$ and the instantaneous frequency f_t is given by:

$$f_t = \frac{\mathrm{d}\left(g(t)t\right)}{\mathrm{d}t} \tag{3.32}$$

and the phase, ϕ, of the signal of frequency f_t required to match the signal of time-varying frequency at time t can be written:

$$\phi = -2\pi t^2 \frac{\mathrm{d}g(t)}{\mathrm{d}t} \tag{3.33}$$

These relationships can be used to generate test signals of known instantaneous frequency to allow assessment of various time-frequency analysis tools.

3.6 The Moving Window

3.6.1 Moving Window using the Discrete Fourier Transform

The Fourier transform enables the frequency content of a time signal to be calculated. If a small section of the time signal is taken, the Fourier transform of this small section gives an approximation to the instantaneous frequency content at the time in the centre of the window. A time-frequency relationship may then be built up by repeating the windowed Fourier transform with the window centred at each time-point in turn. At time-point k

the frequency content $M(k,l)$ of the signal using the moving window approach is given by:

$$M(k,l) = \sum_{n=-N/2+1}^{N/2} \mathrm{e}^{-\mathrm{j}2\pi nl/N} x(k+n) \tag{3.34}$$

This is the basis for the moving-window and Gabor transform methods. There are, however, problems with this method. Firstly, the frequency content is only approximated as it is based on the assumption that it remains constant within the window. This leads to a second problem. To minimise the effect of this assumption, it is desirable to have as short a window in time as possible, but because the frequency resolution of the DFT is the inverse of the length of the time signal, there is a direct trade-off between time resolution and frequency resolution. The frequency resolution of the windowed signal can be improved by zero-padding. However, as mentioned before, this is not a true improvement in resolution as it does not lead to a narrowing of the sinc function peaks.

Due to the width of the time window, the instantaneous frequency estimation may only be calculated in the range $T/2$ to $T_s - T/2$, where T is the length of the time window and T_s is the length of the signal. A technique for overcoming this restriction is to zero-pad the signal by $T/2$ at either end, so that the first calculable frequency estimation is at the start of the real signal. It must be recognised, however, that the uncertainty in the estimation is larger at the beginning and end of the signal, as there are fewer non-zero data points and so the frequency content is convolved with a sinc function of wider peaks due to the windowing.

3.6.2 Moving Window using the Auto-Regressive Model

In an effort to reduce the window width, or to get a better frequency estimation for the same length window, the auto-regressive model is sometimes used in the moving window. As with the fixed-window version, the benefits are only likely to be significant where there are closely-spaced modes, when the DFT suffers from interference between the sinc functions associated with the adjacent modes.

3.6.3 A Comparison of the Two Moving Window Methods

The benefit of using the Analytic Signal

Firstly, a sine wave signal will be considered to demonstrate the effect of using the Hilbert transform to convert the real signal into a complex one. Figure 3.14 shows the estimation of the frequency content based on the peaks in the power spectral density using the moving window with the auto-regressive model and with the discrete Fourier transform for a sine wave of frequency $5.2/T$ sampled at $100/T$ with added noise (maximum 1% signal amplitude). The signal lasts $2T$ and a time window of length T is selected, giving instantaneous frequency estimations in the range $T/2$ to $3T/2$. The discrete Fourier transform time window is zero-padded to 100 times its original length and the auto-regressive model frequencies are calculated to the same resolution, $1/(100T)$. The number of poles used was 20. Figure 3.15 shows the peak frequency estimations for the signal with a window width T centred at $T/2$. It should be noted that the frequency predicted by the auto-regressive model over this time window is incorrect. From figure 3.14, it can clearly be seen that there is periodic oscillation in the instantaneous frequency estimation using the DFT, and using the auto-regressive moving window (using the largest frequency peak of the transform).

For the discrete Fourier transform, the reason for this oscillatory behaviour may be seen if the Fourier transform of a sine wave is considered:

$$x(t) = \sin(2\pi f_0 t) \Longleftrightarrow X(f) = \frac{\mathrm{j}}{2}\left(-\delta(f - f_0) + \delta(f + f_0)\right) \tag{3.35}$$

where δ is the Dirac-delta function. If the Fourier transform of the signal centred at some point τ later in time is now considered, using the relationship for the Fourier transform of a time-shifted signal:

$$x(t - \tau) \Longleftrightarrow \mathrm{e}^{-\mathrm{j}2\pi f\tau} X(f) \tag{3.36}$$

the Fourier transform may be written as:

$$x(t-\tau) = \sin(2\pi f_0(t-\tau)) \Longleftrightarrow \mathcal{F}\{x(t-\tau)\} = \frac{\mathrm{j}}{2}\left(-\delta(f - f_0)\mathrm{e}^{-\mathrm{j}2\pi f\tau} + \delta(f + f_0)\mathrm{e}^{\mathrm{j}2\pi f\tau}\right) \tag{3.37}$$

This shows that the amplitude of the Fourier transform is a function of the location in the signal that time is taken to be zero. Therefore, when a windowed time signal

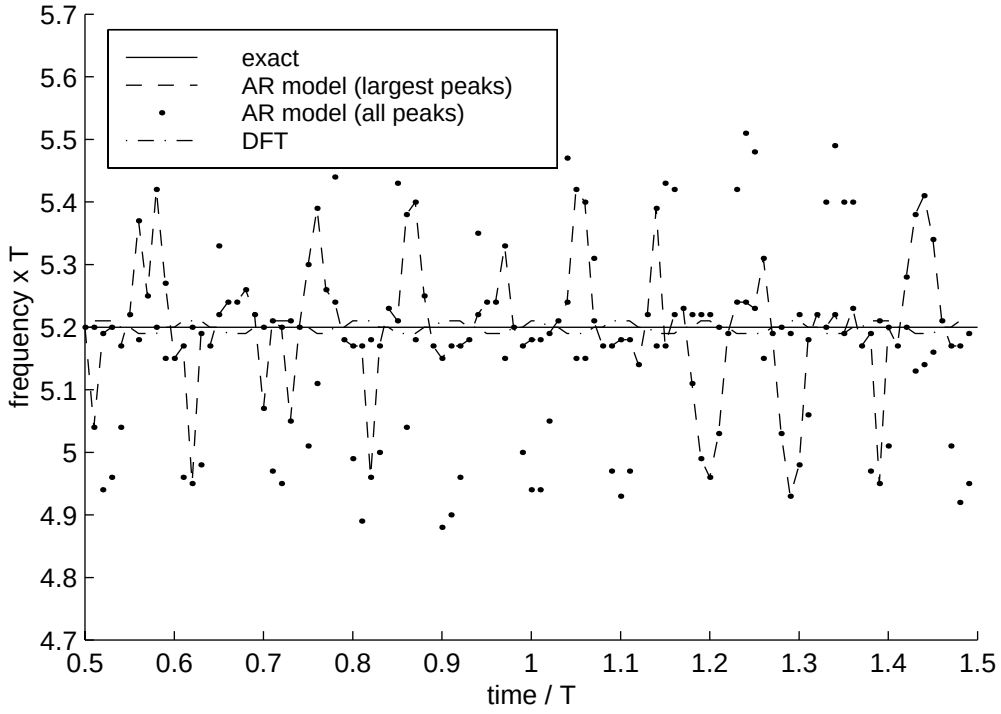

Figure 3.14: The moving window frequency estimation using the real signal

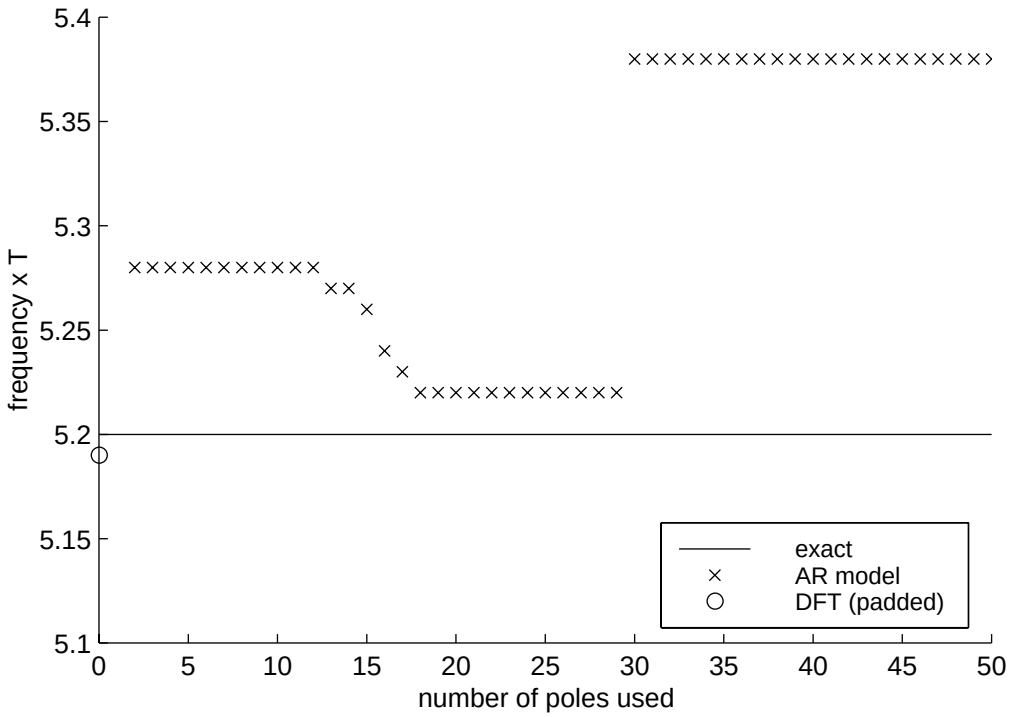

Figure 3.15: Selecting the number of poles to be used in the AR model of a real signal

is considered, resulting in a convolution of equation 3.37 with a sinc function in the frequency domain, the Fourier transform will vary with the position of the centre of the time window. This variation of the estimated frequency over time is itself periodic, with a frequency equal to twice the frequency of the signal since the absolute value of the DFT is considered. This leads to a change in the location of the maximum positive peaks in frequency due to the varying degree of interaction between the side-lobes of the sinc function centred at frequencies $-f_0$ and f_0. The amplitude of the oscillations in the frequency estimation will be minimised if, at frequency f_0, the gradient of the side-lobe corresponding to the sinc function centred at frequency $-f_0$ is zero. The reason for the behaviour in the auto-regressive model is less clear, but is reported to be due to the phase difference of the signal at the beginning and end of the window (Owen *et al.* [77] and Chen and Stegen [18]). This may be demonstrated using the sinusoidal signal with frequency $5.2/T$. Figure 3.16a shows the frequency estimation using the AR model with 20 poles and a time window of length T, corresponding to 5.2 cycles over the window. This may be compared to figure 3.16b which is the estimation using a time window of length $0.96T$ corresponding to 4.992 cycles over the window. The effect of reducing the time window width to approximately a whole number of cycles has, as expected, reduced the variation in the frequency estimation with time. However, this approach would be difficult for a non-linear signal of unknown frequency.

To overcome this problem the analytic version of the signal should be used. Figure 3.17 shows the results of using the two moving window methods on the signal after it has been converted to analytic form. The reason for the improvement in the DFT is that since the signal now contains only the positive frequency component, there is no interaction between sinc functions in the frequency domain.

A signal with two modes

A signal consisting of a sum of two complex exponentials, one at frequency $5.2/T$ and one of half the amplitude at $6.1/T$, and some added noise (maximum of 1% of the signal amplitude) using a sample frequency of $100/T$ for time T, is considered. Figures 3.18a and 3.18b show the variation in the estimation of the frequency content using the AR model with increasing numbers of poles for the real signal and the analytic version of

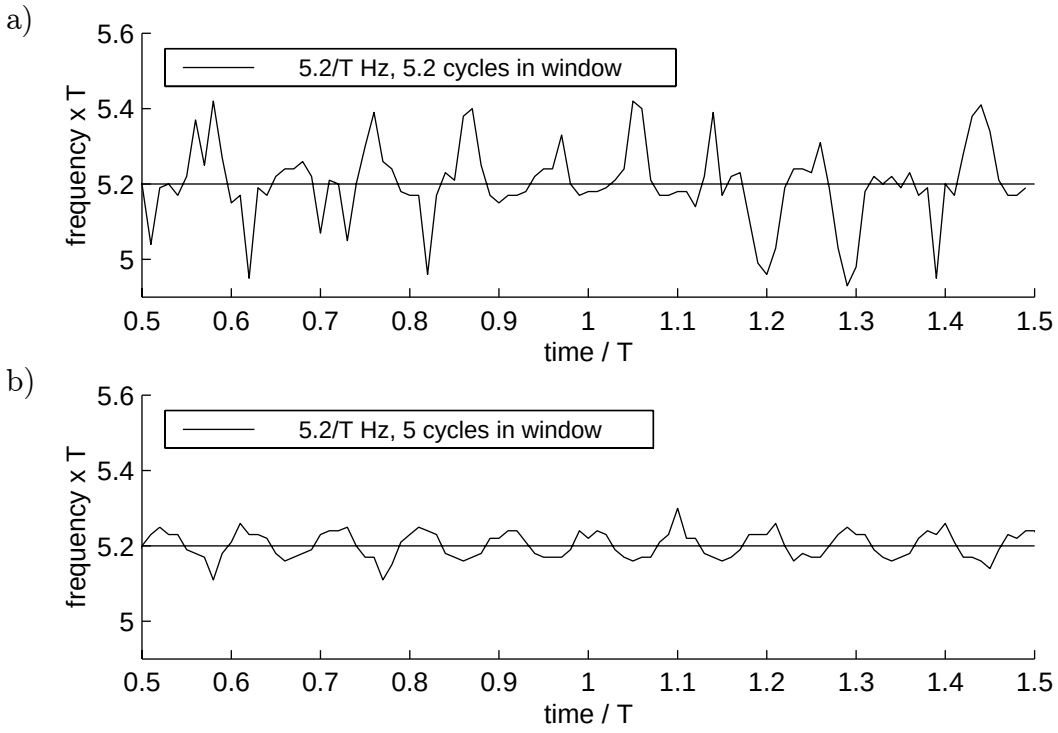

Figure 3.16: Moving window AR model; the effect of an incomplete number of cycles within the window, a) 5.2 cycles and b) 5 cycles within the window

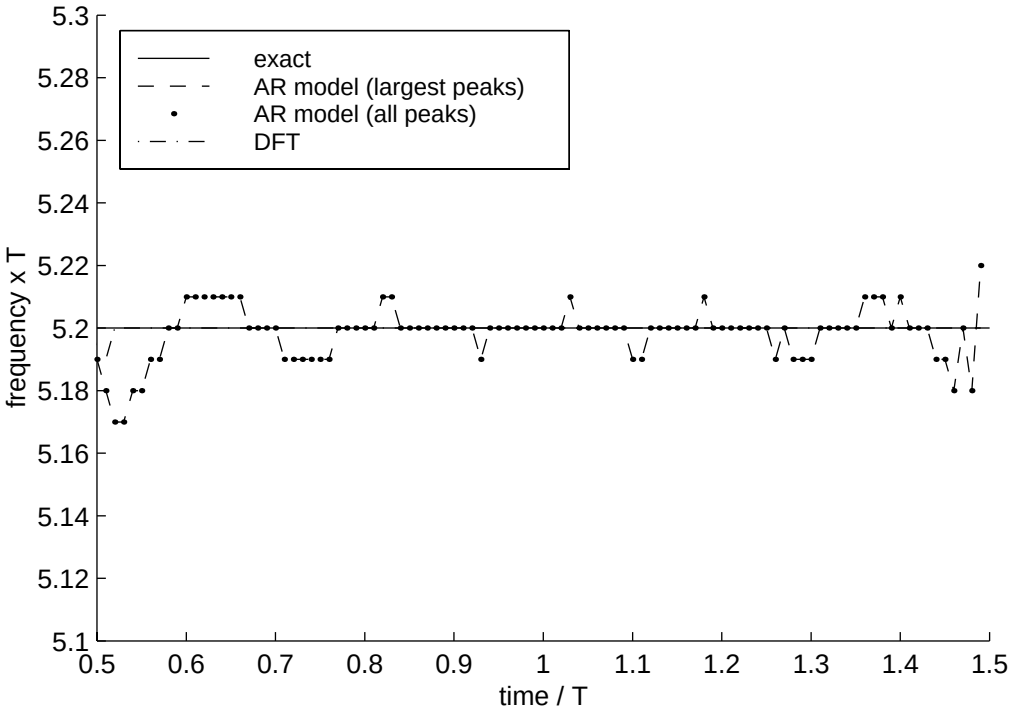

Figure 3.17: The moving window frequency estimation of the analytic signal

the signal respectively, for a window T long centred at time $0.49T$. From figure 3.18b it would seem that 40 poles would be required to detect the second mode for the analytic signal using the auto-regressive model. However, this results in a large number of peaks around the $t/T = 1$ point, indicating over-fitting of poles. It was found that 20 poles resulted in a better overall estimation of the signal frequencies over time. The reason for this inaccurate estimation of the number of poles required is that the estimation is based on only one position in time. Since the performance of the model differs depending on the time (as has been seen in figure 3.17) it is possible that, as has occurred with this example, occasionally the time selected does not represent the performance of the model at other times. The peaks in the power spectral density for the auto-regressive model with 20 poles and the DFT moving windows are shown in figures 3.19a and 3.19b, for the real and the analytic signal respectively. It can be seen that the improvements using the analytic signal are no longer as pronounced. For the DFT, this is because the interference due to the overlap of the sinc functions at $5.2/T$ and $6.1/T$ has a far larger effect on the resultant frequency estimation than the interference due to the sinc functions centred at the negative frequencies. Since the phase of one mode relative to the other will change with time, this interaction of the sinc functions will vary with time. This results in the disappearance of the smaller peak of the power spectral density estimations in the region $0.8T < t \leq 1.4T$, combined with oscillations in the peaks at a frequency equal to the difference between the frequencies of the two modes. This problem is not present in the auto-regressive model, which displays some improvements using the analytic signal where the time variation in the estimation of the fundamental frequency is reduced significantly.

A non-linear signal

Now, a non-linear signal similar to the vibration data recorded during impact tests on damaged concrete beams is considered. A linear increase in frequency from $5.2/T$ to $6.1/T$ over the first $1.5T$ is followed by a region of constant frequency for $1.5T$. The signal is generated using equations 3.32 and 3.33. An auto-regressive model with 10 poles was chosen for the moving window. Figures 3.20a and 3.20b show the frequency estimations based on the maximum peak of the power spectral density using the moving

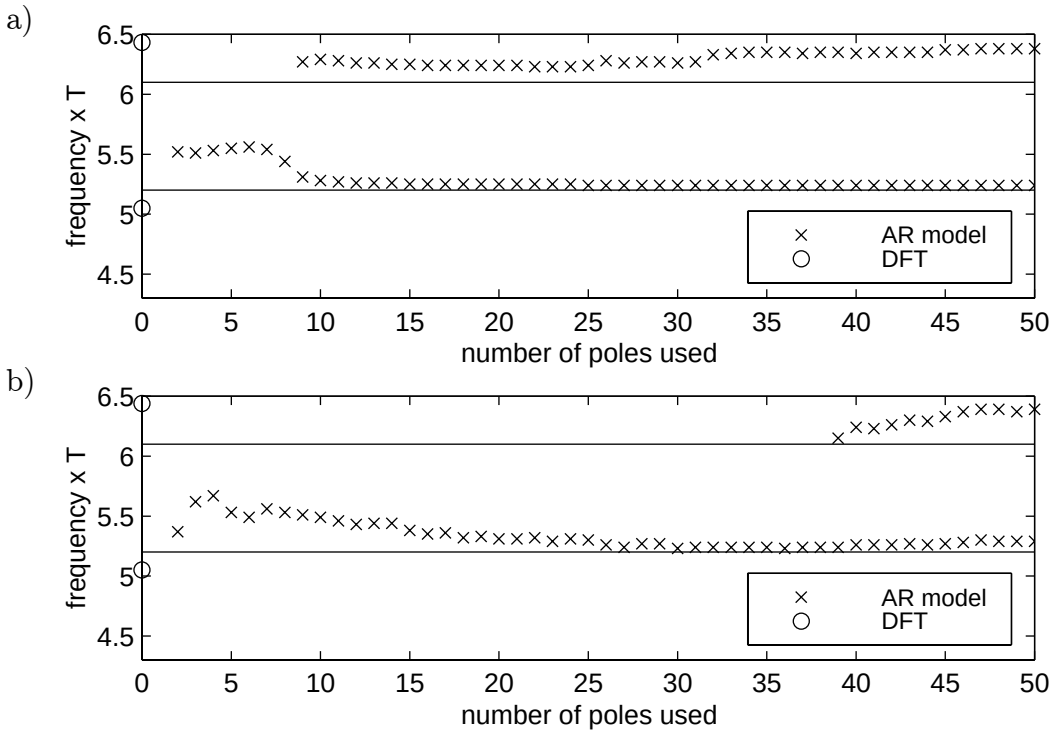

Figure 3.18: Optimising the number of poles used in the AR model using a) the real and b) analytic signal

window for the real and analytic signal respectively. It shows that both the DFT and the AR model track the frequency reasonably well and that both estimations are improved when the analytic signal is used. However, near the region of the step change in gradient of the instantaneous frequency, both methods underestimate the frequency because they are calculating an average frequency over a window T long rather than the true instantaneous value. This error may be reduced by reducing the width of the time window. Figure 3.21 shows the estimations for the case where the window width is $T/2$ rather than T and six poles are used for the auto-regressive model. For both the real and the analytic signals the estimation of the step has improved. However, for the case of the real signal this improvement is masked by an increase in the amplitude of the erroneous frequency oscillation over time.

The error due to calculating the frequency over a window of length T rather than the instantaneous frequency is better illustrated if a phase-modulated signal is considered. Figure 3.22a shows the predicted frequencies for the analytic version of a sine wave with

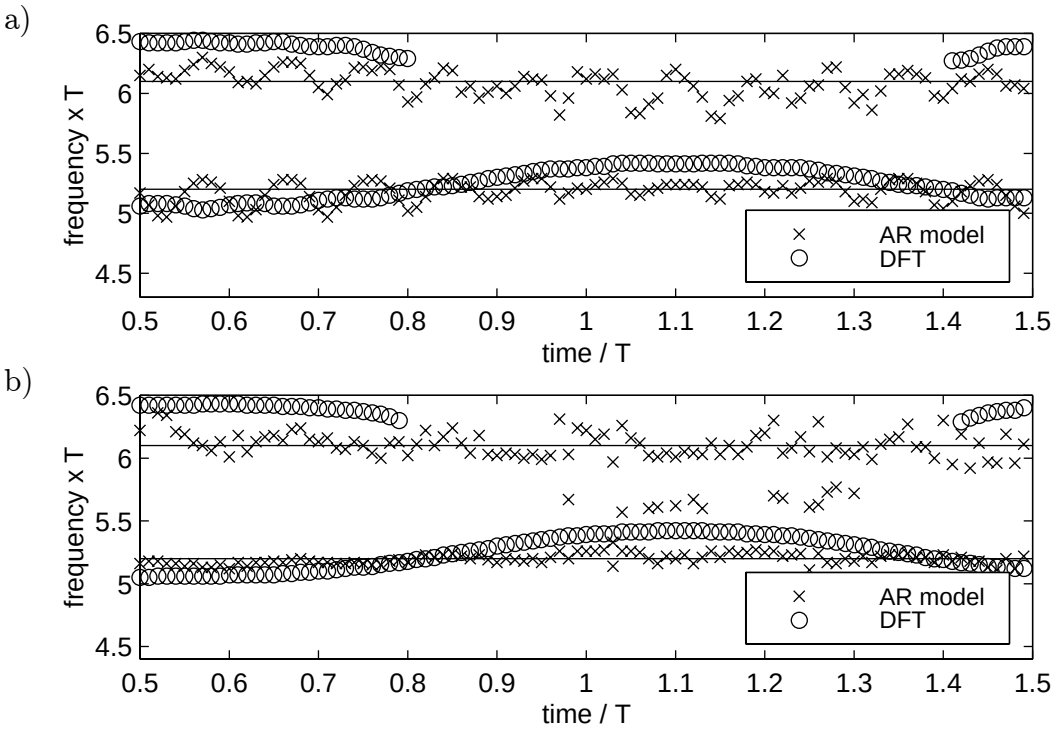

Figure 3.19: The moving window frequency estimation of a) the real and b) the analytic signal

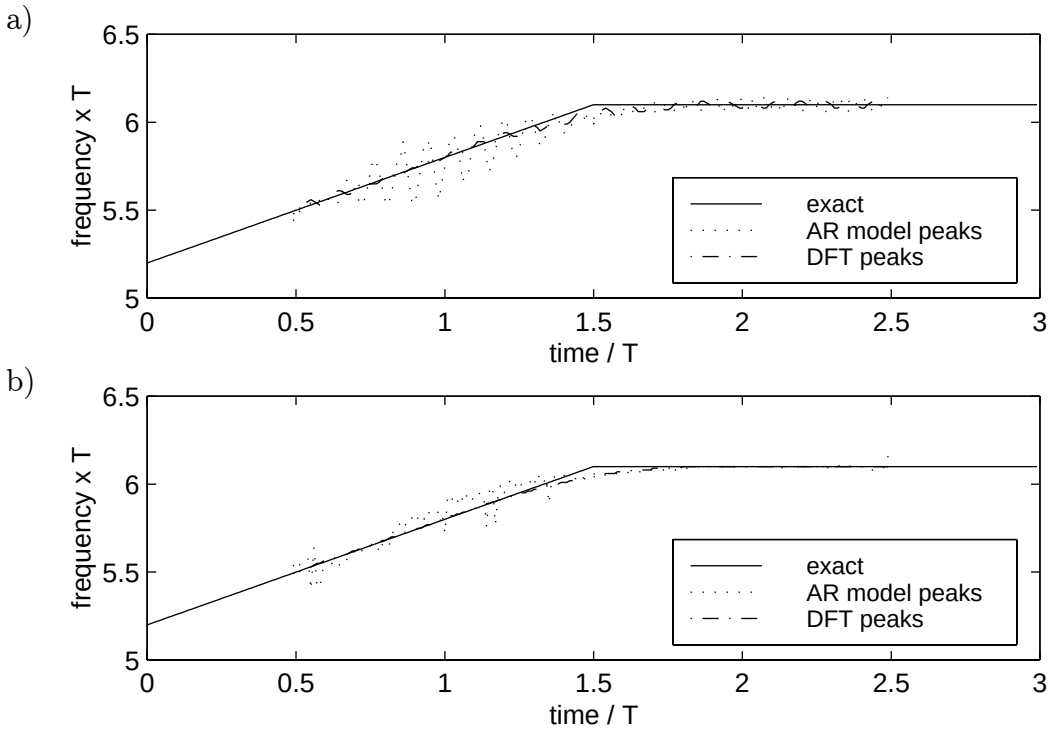

Figure 3.20: Comparison of the AR model and DFT methods with window width T using a) the real and b) the analytic non-linear signal

instantaneous frequency:

$$f_t = \frac{5.2}{T} + \frac{0.1}{T} \sin\left(2\pi \frac{0.7}{T}\ t\right) \tag{3.38}$$

The signal lasts $3T$, the moving window width is T and 16 poles are used in the auto-regressive model. As expected, the frequency estimation oscillates less than the instantaneous frequency due to the averaging over the window width. If a moving window of half the length is used (using an eight pole AR model) the estimation is far better, as shown in figure 3.22b. In both cases the discrete Fourier transform performs better than the auto-regressive model. However, there is a cost attached to reducing the time window length. For the DFT, there is an increase in the width of the sinc function involved in the convolution and, for the AR model, fewer points are available for the fitting of the poles, both of which will lead to less certain frequency estimations.

There is therefore a compromise; for improved instantaneous frequency estimation a short time window is desirable, but to limit the width of the sinc function or to maintain an acceptable number of data points for pole-fitting, a long time window is desirable.

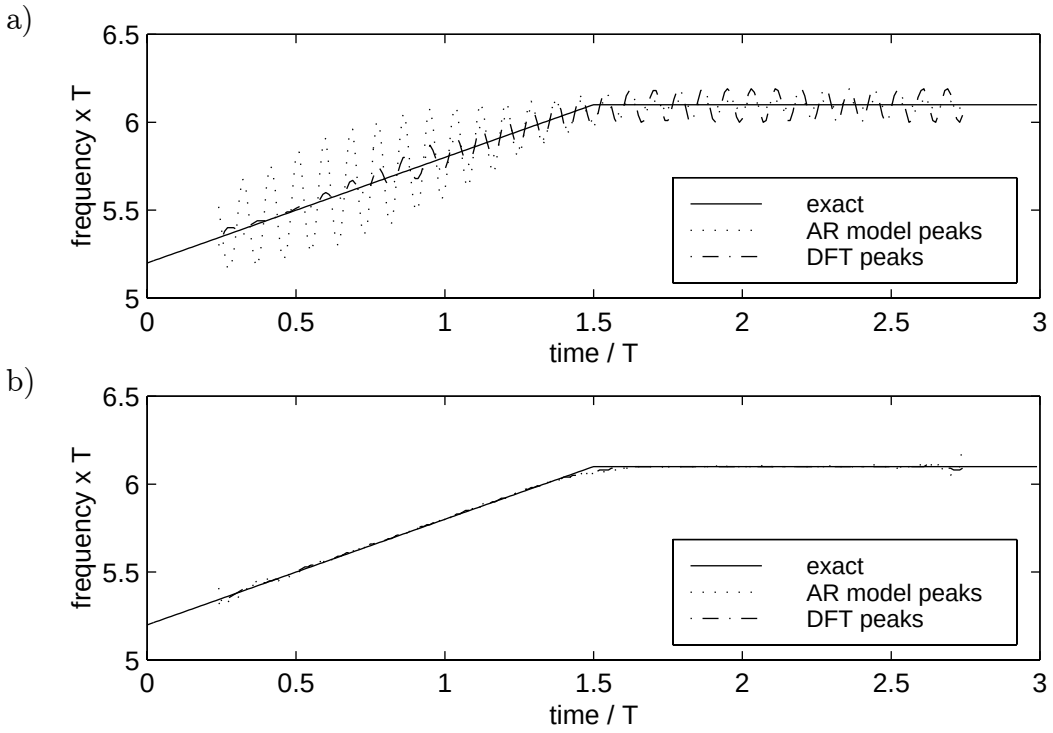

Figure 3.21: Comparison of the AR model and DFT methods with window width $T/2$ using a) the real and b) the analytic non-linear signal

In summary, the analytic version of the signal improves the estimation of the frequency content for most signals. For a single mode signal the DFT moving window performs slightly better than the AR model. However, for closely-spaced modes the moving window using the AR model displays some advantages over the DFT. For non-linear signals a compromise window width is required to ensure an acceptable sinc function width or number of points for accurate pole-fitting as well as to minimise the effect of calculating an averaged frequency over the window rather than the true instantaneous frequency. One clear disadvantage with the AR model is that it requires a suitable number of poles to be chosen as well as the width of the time window, whereas the DFT only requires the window width.

3.7 Harmonic Wavelet Transform

Wavelet analysis is a method of decomposing the time signal into constituent parts. The shape and magnitude of these constituent parts depends on the selected wavelet (see,

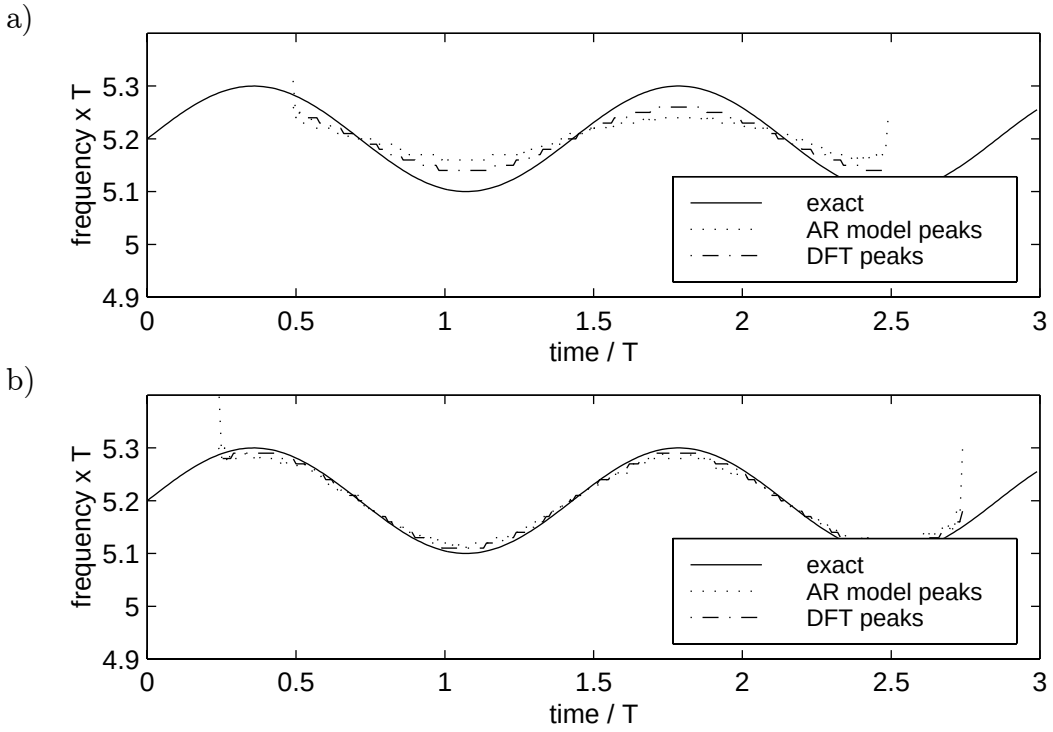

Figure 3.22: Comparison of the AR model and DFT methods using a non-linear phase-modulated signal with a time window of a) T and b) $T/2$

for example, Newland [71]). The wavelet can take any form provided it is localised in time but for computational simplicity tends to be limited to a function which leads to the signal being decomposed into orthogonal parts.

Recently, there has been increased interest in using harmonic wavelet transforms to analyse dynamic systems, for example Staszewski [102], [103] and Piombo *et al.* [84]. Harmonic wavelets lend themselves to vibration analysis where time-frequency relationships are required (Newland [72]) and so the study of wavelets presented here will be limited to these.

The harmonic wavelet transform is very similar to the moving window DFT except that the window is applied in the frequency domain rather than in the time domain. Consider the phase-modulated complex exponential signal:

$$s = \mathrm{e}^{\mathrm{j}200\cos(2\pi 0.04t/T)} \tag{3.39}$$

over the range $-10T < t \leq 10T$ with a sampling frequency of $0.05/T$. The instantaneous frequency is $-8\sin(2\pi 0.04t/T)$, calculated using equation 3.32. The DFT moving

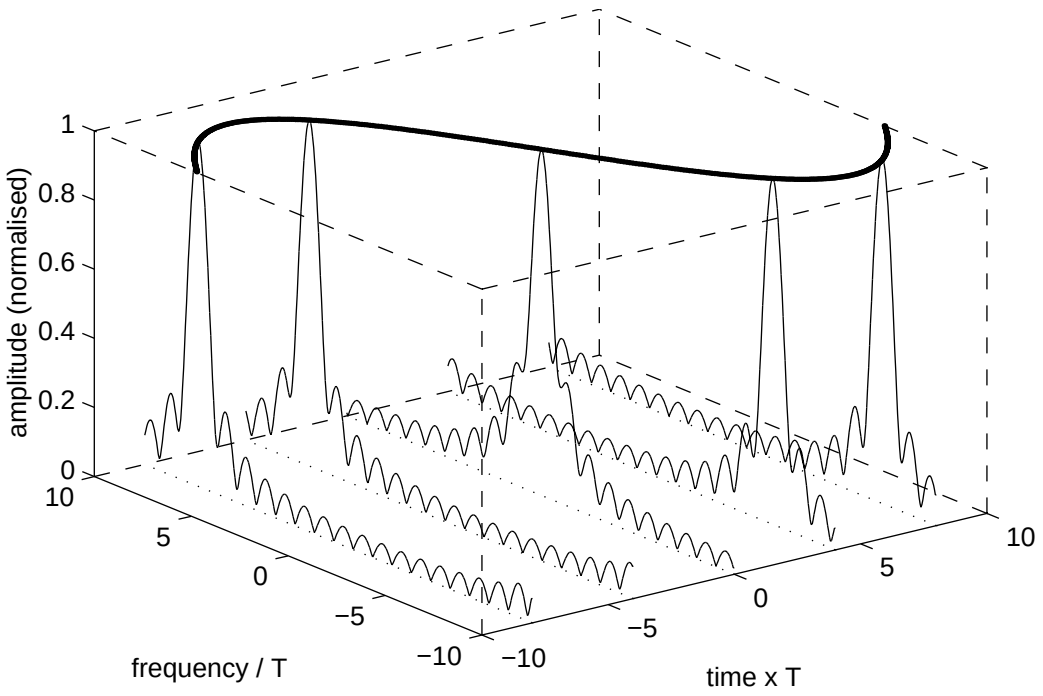

Figure 3.23: Calculating an approximate time-frequency spectrum using the DFT moving window

window builds up an approximate time-frequency distribution time-point by time-point. At each time-point in turn, an approximate frequency spectrum is calculated by applying the DFT to a short section of the signal (length T) centred at the time-point. The result of this is shown in figure 3.23, which is a plot of the normalised magnitude of the signal across the frequency spectrum for the time-points $-8T$, $-4T$, 0, $4T$ and $8T$. The frequency spectra for all the other time-points have been omitted for clarity. The actual instantaneous frequency is indicated with a thick line.

On the other hand, if the initial signal is first converted into the frequency domain using the DFT (applied to the whole signal), an approximate time-frequency distribution may be calculated using the wavelet transform. Using the frequency domain version of the signal, at each frequency point in turn an approximate time spectrum is calculated by applying the inverse DFT to a short section of this signal centred at the frequency point. Figure 3.24 shows the normalised magnitude of the signal across the time spectrum for the frequency points $-8/T$, $-4/T$, 0, $4/T$ and $8/T$. As with the DFT moving window, time spectra may be calculated for the other frequency points but have been omitted

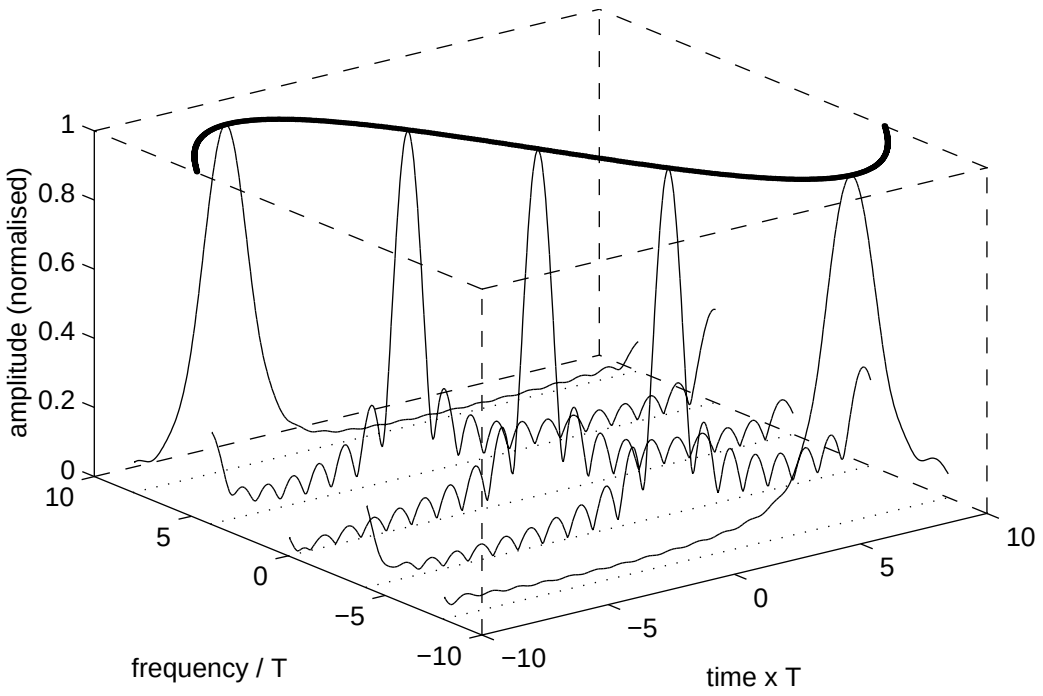

Figure 3.24: Calculating an approximate time-frequency spectrum using the wavelet transform

for clarity. The width of the frequency window used was $1/T$.

Algebraically the wavelet transform may be written, for frequency point l:

$$W(k,l) = \sum_{m=-M/2+1}^{M/2} \mathrm{e}^{\mathrm{j}2\pi mk/M} S(l+m) \tag{3.40}$$

where M is the width of the window in the frequency domain and S is the DFT of the signal s, using the whole length of the signal, not just a windowed portion [72]. Contour plots of the absolute values of the wavelet transform will be used to plot the relationship.

3.7.1 Decimation and Zero-Padding

With the DFT moving window, the signal may be decimated to reduce the sample frequency so that the computation time is reduced. The effect is to increase the step between the time-points and so at first sight reduce the time resolution. However, as the instantaneous frequency estimation at any time-point is based on an averaged frequency over a short window of time, the step between the time-points in the time-frequency distribution is not the limiting factor for the resolution in time. Decimation requires

the filtering out of higher frequencies to maintain the Nyquist criterion. To reduce the steps between frequency points, the signal can be zero-padded once the time window has been applied. This does not improve the true resolution in the frequency domain, since the accuracy of the frequency estimation is dependent on the width of the window in time, which itself affects the width of the sinc function involved in the convolution.

The effect of decimating the time signal before applying the wavelet transform is that when the signal is then converted to the frequency domain the maximum frequency will be reduced. Once windowing is applied in the frequency domain and the signal is transformed back to the time domain, the time-step will be that of the decimated signal. However, the limiting factor in the resolution in time will be the width of the window applied in frequency which determines the width of the sinc function involved in the convolution in time (resulting from the windowing in frequency). The effect of zero-padding the original signal before conversion to the frequency domain is that the steps between frequency points will be smaller. However, the resolution in frequency will be determined by the averaging over the width of the window of the time domain information at a certain frequency. As with the DFT moving window there is a compromise between time and frequency resolution when choosing the width of the window.

There appear to be two opportunities to zero-pad the signal when using the wavelet transform. The initial time domain signal may be zero-padded so as to increase the number of frequency bins once the signal is converted to the frequency domain. zero-padding may also be used on the frequency domain signal once windowing has occurred; the effect of this padding is to reduce the time-steps in the time-frequency distribution. The process adopted here assumes that the signal is sampled at a frequency sufficient to give an acceptable time-step in the time-frequency distribution, or has been sampled at a higher frequency and decimated to an acceptable level. The signal is then zero-padded to ensure an acceptable frequency step before the whole signal is transformed using the DFT into the frequency domain. The frequency window is applied resulting in a short length of frequency domain signal. This signal is zero-padded to the length of the full frequency domain signal before the inverse DFT is applied in order to transform it back to the time domain. Thus the zero-padding in the frequency domain simply maintains the time resolution in the original signal.

For example, take a signal of length T_s with a sample frequency of N/T_s after decimation, for which an estimation of the time-frequency distribution with steps in frequency of $1/(BT_s)$ is desired. For the DFT moving window with a window size of T, the resulting windowed signal would contain NT/T_s points. Without zero-padding the resulting frequency step would be $1/T$. To reduce the frequency steps to $1/(BT_s)$ the windowed signal must be zero-padded to BT_s/T times its original length, i.e. to BN points. For the wavelet transform with a frequency window of F, the initial signal (of N points) must be zero-padded to BN points or to a time span of BT_s. It is then transformed into the frequency domain resulting in frequency steps of $1/(BT_s)$. The windowing is then applied, giving a signal FBT_s points long spanning a frequency F. If this is not zero-padded, when transformed back to the time domain the signal time-step would be $1/F$, spanning a time BT_s. To maintain the time-step of T_s/N, it is necessary to zero-pad to $N/(FT_s)$ times the length in the frequency domain after windowing, resulting in a windowed signal of length NB with FBT_s non-zero points. After transforming back into the time domain, the signal will span BT_s time with time-steps of T_s/N. Of these, the first N points correspond to the time-points of the original signal. The rest are due to the initial zero-padding before transforming to the frequency domain and consequently may be discarded.

3.7.2 Limitations due to Window Width

With the DFT moving window, because of the finite width of the window, it is necessary to add a half window width of zeros to the beginning and end of the signal to allow an estimate of the frequency content during the first half window width and last half window width of time to be calculated (see section 3.6.1). In the case of the wavelet distribution, the finite width window is in frequency, therefore without any addition of zeros the time-frequency estimation may be calculated within the frequency range $F/2 \leq f < F_n - F/2$ where F_n is the Nyquist frequency. To expand the range to $0 \leq f < F_n$, addition of zeros within the frequency window is necessary. If the analytic version of the signal is used, there is no negative frequency content and if filtering is applied to ensure no aliasing there is no frequency content above the Nyquist frequency. Therefore the addition of

zeros to windows within the ranges $0 \leq f < F/2$ and $F_n - F/2 \leq f < F_n$ will correctly represent the signal. This method of allowing the frequency estimation over the full range will be employed here.

3.7.3 Windowing

Consider the complex exponential signal of frequency $5.2/T$ lasting $2T$ sampled at a frequency of $1/(100T)$. Figure 3.25a shows a contour plot of the absolute values of the wavelet time-frequency estimation using a frequency window width of $3/T$. The signal is padded such that the frequency resolution is $1/(10T)$. The thick black lines show peaks in frequency. It can be seen that the frequency resolution is very poor, with several peaks between approximately $3.9/T$ to $6.4/T$. This can be overcome by using a different window in frequency, analogous to using, for example, a Hanning window in the time domain when applying the DFT moving window. As with the DFT moving window, numerous windows have been proposed; the Gaussian window or Morlet wavelet (see Staszewski [102]) and the Hanning window (see Newland [72]) are both popular choices. Figure 3.25b shows the contour plot if a Hanning window, rather than a rectangular one, is applied in the frequency domain. It is clear that the performance is much improved. Figure 3.26 shows a cross-section through both contour plots at time T to highlight this improvement.

The reason for the improvement can be seen if the signal is considered in the frequency domain. Figures 3.27a, 3.27b and 3.27c show the absolute values of the signal in the frequency domain, along with the rectangular window applied to the signal to calculate the time-frequency distribution at frequencies $4.7/T$, $5.2/T$ and $5.7/T$ respectively. It can be seen that the windowed signal is broadly the same for all frequencies, albeit with a frequency shift and some difference in the side-lobes. However, the frequency shift (due to the fact that the windowed signal is treated as centred at frequency zero) will not affect the contour plot. This is because the contour plot uses the absolute values of the distribution and the only effect of applying a frequency shift before an inverse FT is to multiply the result by a complex exponential of constant amplitude. If a Hanning window is applied in place of the rectangular window, the amplitude of the peak at

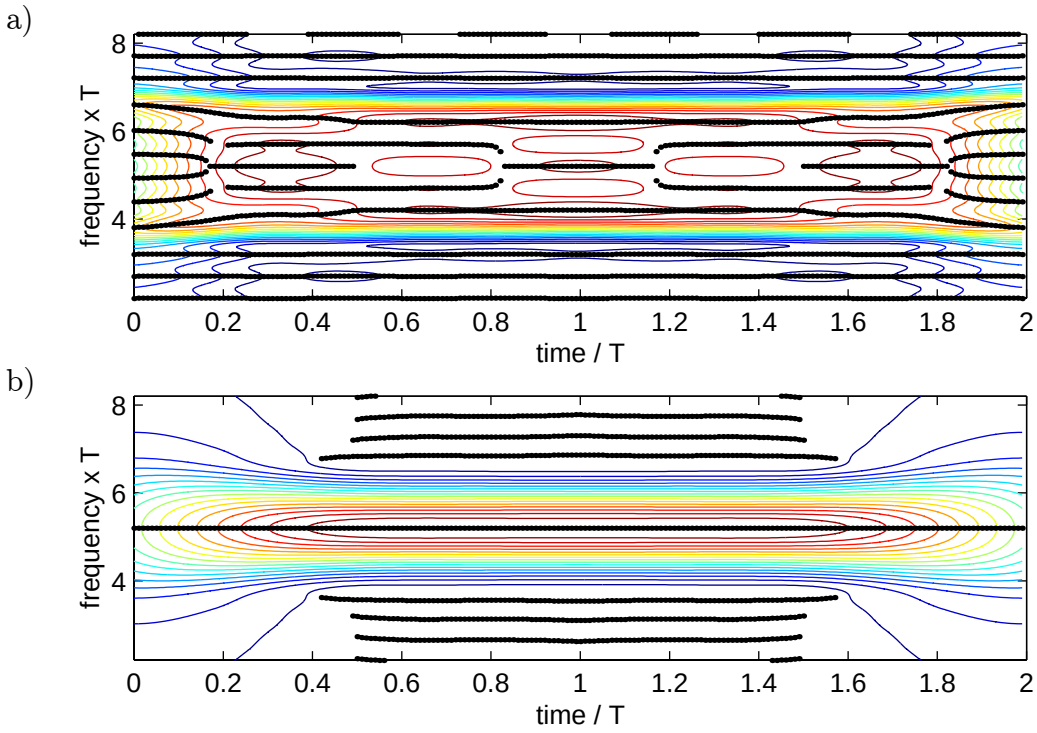

Figure 3.25: The wavelet distribution using a) a rectangular window and b) a Hanning window

frequency 5.2/T is dependent on the centre frequency of the window. This results in a larger amplitude signal when converted back to the time domain for the frequencies closest to $5.2/T$, as shown in figure 3.28.

This effect is clearer if an infinite signal is considered. In the frequency domain the result would be a Dirac-delta function at $5.2/T$. When a rectangular window is applied in the frequency domain, then if the window does not include $5.2/T$, the resulting signal will be zero. If, on the other hand, the window covers frequency $5.2/T$, then the Dirac-delta would not be windowed out and the absolute inverse FT would be a constant amplitude over time not dependent on the centre frequency of the window. However, if the Hanning window is applied, this amplitude will be dependent on the centre frequency, resulting in a peak in frequency in the time-frequency estimation. The Hanning window will therefore be used in the wavelet transform. Equally, other windows could be used, which would lead to slightly different results. However the Hanning window will allow a broad study of the wavelet transform without the added complication of altering the window properties.

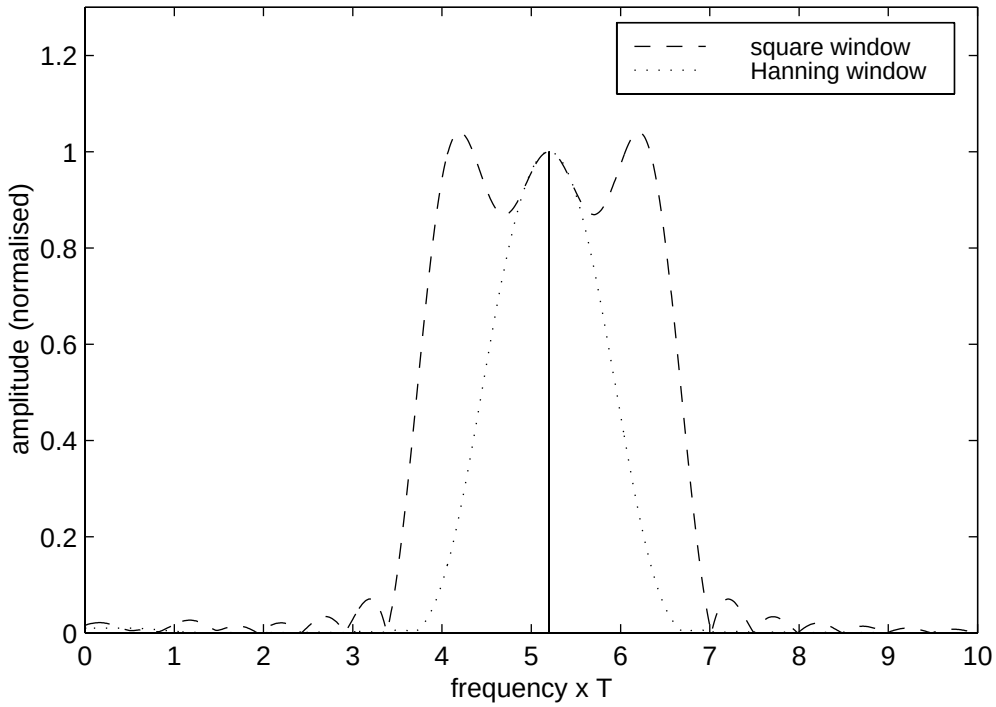

Figure 3.26: Cross-section of the wavelet distribution in the frequency domain at time T

The signal shown in figures 3.23 and 3.24 is an exception. Here the rectangular window works well because the signal frequency varies widely, leading to a broad signal in both time and frequency.

Figure 3.25 also demonstrates that the wavelet transform incorrectly predicts the amplitude of oscillation at the start and end of the time signal. This is because, if the amplitude estimation over time at frequency $5.2/T$ is considered, the windowing in frequency has the effect of removing the outer side-lobes of the sinc function as shown in figure 3.27b. As already stated, in the time domain the signal may be seen as a continuous exponential signal multiplied by a rectangular window, which results in the Dirac-delta function at $5.2/T$ being convolved with a sinc function in the frequency domain. The outer side-lobes of the sinc function contain the higher frequency information of the window. If these side-lobes are removed, the window will be rounded at its ends, just as a truncated Fourier series fit of a periodic step wave results in a less crisp step from one of the levels to the other.

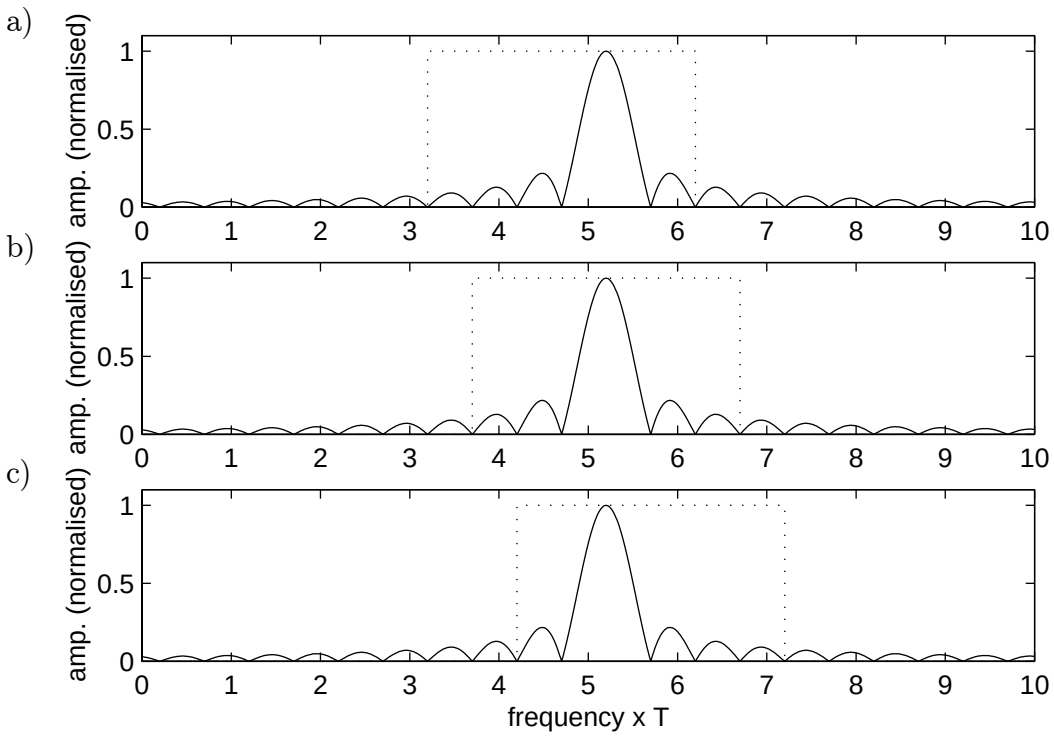

Figure 3.27: The rectangular window applied to the signal in the frequency domain at frequencies a) $4.7/T$, b) $5.2/T$ and c) $5.7/T$

3.7.4 Using the Wavelet Transform on Non-Linear Signals

Considering the non-linear signal introduced in figure 3.20, the DFT moving window and wavelet transforms may be compared. Figures 3.29a and 3.29b show contour plots of the absolute values of the amplitude of the signal using the DFT moving window and wavelet transforms respectively. For the DFT moving window, the time window width used was T and the frequency window width used in the wavelet transform was $3/T$. Direct comparison of the two methods is difficult since the windows are applied in different domains and the optimum window width is dependent on the signal properties within that domain. It can be seen that the two methods produce very similar peak frequency estimations. Examining the contour lines, the wavelet transform seems to perform slightly better at the start and the end of the signal as the width of the peak in frequency seems to grow at a slower rate when approaching these points. It is thought that this is because, to the left of the first vertical line and to the right of the second vertical line in figure 3.29a, the time window spans times outside the signal span and

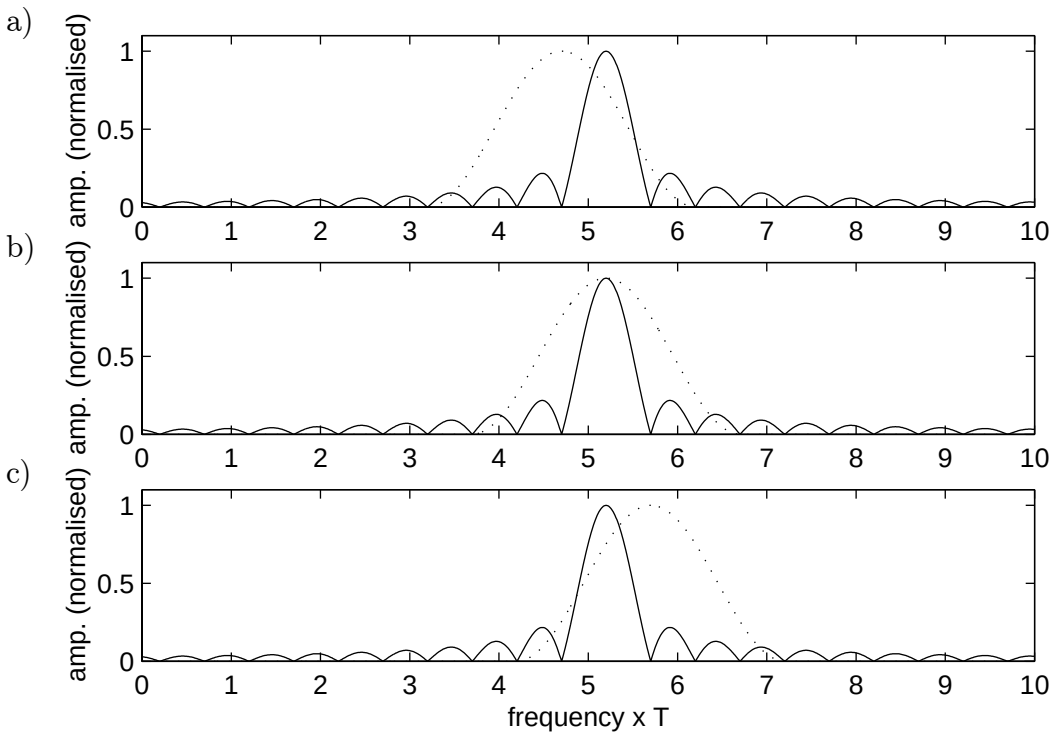

Figure 3.28: The Hanning window applied to the signal in the frequency domain at frequencies a) $4.7/T$, b) $5.2/T$ and c) $5.7/T$

so part of the window is filled with zeros, which leads to a wider peak. The wavelet transform overcomes this as the window is in frequency as discussed in section 3.7.2.

The performance of the wavelet transform on a real signal will be discussed in section 8.2.

3.8 The Cohen Class

To overcome the compromise between time and frequency resolution, work has been done on an alternative method of studying time-varying frequency spectra which involves ways of calculating joint time-frequency distributions. With Fourier analysis, the instantaneous energy of the signal is given by $|s(t)|^2$ and the energy density spectrum is given by $|S(f)|^2$, where $S(f)$ is the Fourier transform of $s(t)$. Ideally, the joint distribution, $P(t, f)$, would provide information on the energy intensity for each time and frequency. The instantaneous energy would then be calculated by integrating $P(t, f)$

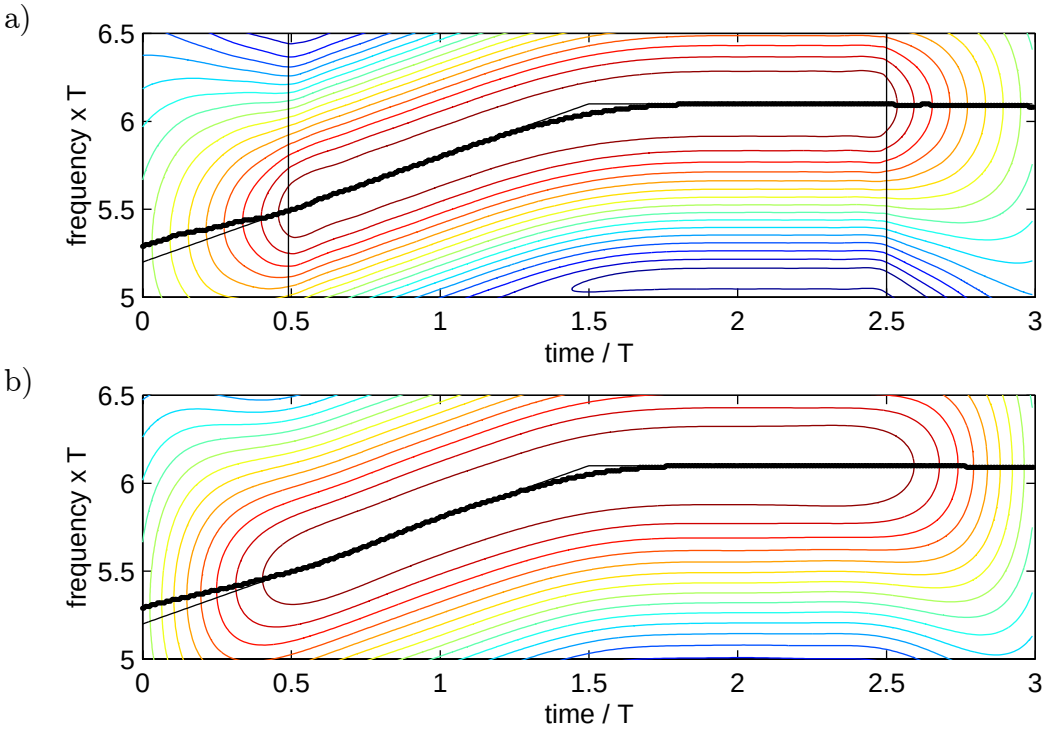

Figure 3.29: The time-frequency distribution of the analytic non-linear signal using a) the moving window DFT and b) the wavelet transform method

over all frequency and the energy density spectrum by integrating over all time:

$$|s(t)|^2 = \int_{-\infty}^{\infty} P(t,f)\mathrm{d}f \tag{3.41}$$

$$|S(f)|^2 = \int_{-\infty}^{\infty} P(t,f)\mathrm{d}t \tag{3.42}$$

These conditions are termed "marginals". Marginals are conditions derived from the joint distribution by integrating out all the other variables, giving equations which ideally should be satisfied in order for the distribution to be valid.

Ville derived such a distribution which was mathematically (but not physically) analogous to a derivation reported by Wigner in the field of quantum statistical mechanics (see for example Cohen [22]). The Wigner-Ville distribution is:

$$P_{wv}(t,f) = \frac{1}{2\pi}\int_{-\infty}^{\infty} \mathrm{e}^{-\mathrm{j}\tau 2\pi f} s\left(t+\frac{\tau}{2}\right) s^*\left(t-\frac{\tau}{2}\right)\mathrm{d}\tau \tag{3.43}$$

where s is the analytic data signal and s^* is the conjugate of s. Others obtained different distributions using the derivation and it was later shown by Cohen [21] that there is an infinite number of such distributions which can all be generated using the equation:

$$P(t,f) = \frac{1}{4\pi^2}\int_{-\infty}^{\infty}\int_{-\infty}^{\infty}\int_{-\infty}^{\infty} \mathrm{e}^{-\mathrm{j}\theta t-\mathrm{j}\tau 2\pi f+\mathrm{j}\theta u}\phi(\theta,\tau)s\left(u+\frac{\tau}{2}\right) s^*\left(u-\frac{\tau}{2}\right)\mathrm{d}u\mathrm{d}\tau\mathrm{d}\theta \tag{3.44}$$

where $\phi(\theta,\tau)$ is an arbitrary function called the kernel. These distributions are referred to as the Cohen Class of joint time-frequency distributions. All the distributions within this class have the property that they are invariant to time and frequency shifts [8]. If the kernel is independent of the signal then the distribution is termed "bilinear" because the signal is entered into the equation only twice. The Wigner-Ville distribution may be derived from equation 3.44 by setting the kernel to 1 for all τ and θ. There have been many other kernels proposed, each resulting in a slightly different joint distribution. Kernels include, for example, the Choi-Williams exponential kernel [20] and the modified exponential kernel [117].

The marginals result in conditions that should be satisfied by the kernel. For example, if $P(t,f)$ is to be a measure of energy intensity, then the result of integrating the joint distribution over all t should be equal to the energy density spectrum. From Fourier analysis it can be shown that the energy density spectrum is given by $|S(f)|^2$.

Equating the two equations for the energy density spectrum gives:

$$\int_{-\infty}^{\infty} P(t,f)\mathrm{d}t = \left| \frac{1}{\sqrt{2\pi}} \int_{-\infty}^{\infty} s(t)\mathrm{e}^{-\mathrm{j}2\pi f t}\mathrm{d}t \right|^2 \tag{3.45}$$

which results in the condition that:

$$\phi(0,\tau) = 1 \tag{3.46}$$

Cohen's generalised equation [22] may be written as three separate equations:

$$P(t,f) = \frac{1}{2\pi} \int_{-\infty}^{\infty} \mathrm{e}^{\mathrm{j}2\pi f \tau} R(t,\tau)\mathrm{d}\tau \tag{3.47}$$

$$R(t,\tau) = \int_{-\infty}^{\infty} \frac{1}{2\pi} \psi(t-u,\tau) s\left(u+\frac{\tau}{2}\right) s^*\left(u-\frac{\tau}{2}\right) \mathrm{d}u \tag{3.48}$$

$$\psi(v,\tau) = \int_{-\infty}^{\infty} \mathrm{e}^{-\mathrm{j}\theta v} \phi(\theta,\tau)\mathrm{d}\theta \tag{3.49}$$

At $t = t'$ equation 3.47 relating $R(t',\tau)$ to $P(t',f)$ is a Fourier transform from a pseudo-time τ to the frequency f scaled by $1/(2\pi)$. Therefore, for a given time t', $R(t',\tau)$ may be thought of as a generated "time" signal. Equation 3.48 may be rewritten in terms of the bilinear version of the signal:

$$R(t,\tau) = \int_{-\infty}^{\infty} \frac{1}{2\pi} \psi(t-u,\tau) b(u,\tau)\mathrm{d}u \tag{3.50}$$

where the bilinear signal is defined as:

$$b(u,\tau) = s\left(u+\frac{\tau}{2}\right) s^*\left(u-\frac{\tau}{2}\right) \tag{3.51}$$

It can now be seen that equation 3.50 is a convolution with respect to time:

$$R(t,\tau) = \frac{1}{2\pi} \psi(t,\tau) *_t b(t,\tau) \tag{3.52}$$

where $*_t$ indicates a convolution with respect to variable t. The effect of this may be thought of as a time-averaging of the signal for a given pseudo-time-point, or as a filter of the time signal at a given pseudo-time-point. This can be seen by considering equation 3.49 and using the substitution $\theta = -2\pi f'$:

$$\frac{1}{2\pi} \psi(t,\tau) = \int_{-\infty}^{\infty} \mathrm{e}^{\mathrm{j}2\pi f' t} \phi(-2\pi f',\tau)\mathrm{d}f' \tag{3.53}$$

which may be rewritten as:

$$\phi(-2\pi f',\tau) = \mathcal{F}_t\left[\frac{1}{2\pi}\psi(t,\tau)\right] \tag{3.54}$$

where $\mathcal{F}_t$ is the Fourier transform with respect to t. Therefore equation 3.52 may be rewritten as the following multiplication in the frequency domain:

$$R(t,\tau) = \mathcal{F}_t^{-1}\left[\phi(-2\pi f',\tau)B(f,\tau)\right] \tag{3.55}$$

where $B(f,\tau)$ is the Fourier transform of $b(t,\tau)$ with respect to time. The kernel is often represented in the "ambiguity" plane (see for example Bonato *et al.* [8]). This plane has angular frequency, θ, in one axis and pseudo-time, τ in the other. For a given pseudo-time-point, it may be thought of as a representation of the shape of the filter applied to the bilinear signal in the time domain.

In summary, Cohen's generalised equation may therefore be broken down into two main steps:

- Conversion of the signal into pseudo-time.
- Transformation from pseudo-time to time-frequency domain.

The first step must be performed for each pseudo-time-point, τ, in turn. For each pseudo-time-point the step may be subdivided into two operations. First is the conversion of the time signal into its bilinear form using equation 3.51. Then comes the convolution with respect to time (as opposed to pseudo-time) of the bilinear signal with the function $\psi(t,\tau)$ to generate the pseudo-time signal, $R(t,\tau)$, using equation 3.52. This convolution is equivalent to a filtering applied in the frequency domain, equation 3.55. The kernel at the given value of τ may be seen as the frequency domain representation of the filter, equation 3.54. It should be noted that the filter applied to the bilinear version of the signal for a given value of pseudo-time τ is dependent on the value of τ. The second step is performed for each time-point, t, in turn, and is simply a Fourier transform of the pseudo-time signal at the given time t into the frequency domain, to give a estimation of the frequency content of the signal at that time.

The Wigner-Ville distribution will now be discussed, followed by the modified exponential distribution proposed by Zheng and McFadden [117] as an example of a distribution with a non-unity kernel.

3.8.1 The Wigner-Ville Distribution

As stated above, the Wigner-Ville distribution (WV) uses the kernel $\phi(\theta, \tau) = 1$ and may be written in the form:

$$P_{\mathrm{wv}}(t, f) = \frac{1}{2\pi} \int_{-\infty}^{\infty} \mathrm{e}^{-\mathrm{j}\tau 2\pi f} R_{\mathrm{wv}}(t, \tau) \mathrm{d}\tau \tag{3.56}$$

where:

$$R_{\mathrm{wv}}(t, \tau) = s\left(t + \frac{\tau}{2}\right) s^*\left(t - \frac{\tau}{2}\right) \tag{3.57}$$

As discussed above, the equation converting $R_{\mathrm{wv}}(t, \tau)$ to $P_{\mathrm{wv}}(t, f)$ is a Fourier transform from pseudo-time τ to frequency f. There are two differences between the WV distribution and a moving window calculation. The bilinear version of the signal is used and the FT is evaluated over infinite pseudo-time rather than over the width of the moving window.

It is possible to examine the theoretical advantage of the WV distribution over the moving window calculation by considering a signal with a frequency which varies quadratically with time:

$$x(t) = \cos\left(2\pi t \left[\alpha + \frac{\beta t}{2} + \frac{\gamma t^2}{3}\right]\right) \tag{3.58}$$

where the frequency at time t is given by $\alpha + \beta t + \gamma t^2$. Converting to analytic form and inserting in equation 3.57 gives:

$$R_{\mathrm{wv}}(t, \tau) = \mathrm{e}^{\mathrm{j}2\pi\tau(\alpha+\beta t+\gamma t^2)} \mathrm{e}^{\mathrm{j}2\pi\gamma\tau^3/24} \tag{3.59}$$

The first complex exponential term has frequency $\alpha+\beta t+\gamma t^2$ which is the instantaneous frequency of the signal at time t, in pseudo-time space τ. If only the first term were present, $R_{\mathrm{wv}}(t, \tau)$ would be a linear signal at the instantaneous frequency of the signal x at time t, for all τ. When this is inserted into equation 3.56 the resulting frequency estimation will be a spike at the instantaneous frequency at all time-points. The second term is an error term which results in a less clean frequency estimation. However, if the signal has a frequency which is only linearly dependent on time (i.e. $\gamma = 0$), the frequency estimation is correct. This is an improvement on the Fourier transform of the signal which is only correct if the frequency of the signal is a constant.

The disadvantage with using the bilinear form of the signal is that spurious "cross-terms" are added to the frequency estimation. If an analytic signal consisting of two complex exponential terms is considered:

$$s(t) = \mathrm{e}^{\mathrm{j}2\pi ft} + A\mathrm{e}^{\mathrm{j}2\pi\alpha ft} \tag{3.60}$$

then substituting into equation 3.57 transforms the signal into its bilinear form in terms of pseudo-time τ for the time-point t:

$$R_{\mathrm{wv}}(t,\tau) = \mathrm{e}^{\mathrm{j}2\pi f\tau} + A^2\mathrm{e}^{\mathrm{j}2\pi\alpha f\tau} + 2A\mathrm{e}^{\mathrm{j}2\pi(1+\alpha)f\tau/2} \tag{3.61}$$

As well as predicting correctly the peaks at frequencies f and αf, a third peak at a frequency $1+\alpha f/2$ will be present, known as a "cross-term".

In order to implement the WV distribution on real signals, it must be converted to discrete form. This is not straightforward, since, to calculate R_{wv}, knowledge of the signal at half time-steps is needed. To overcome this it is necessary to skip every second term in R_{wv} so that only frequencies up to half the Nyquist frequency may be calculated. However, this does have the advantage of doubling the frequency resolution. The discrete version of the pseudo-time signal at time t (or bin k) in terms of pseudo-time τ (or bin n') is:

$$R'_{\mathrm{wv}}(k,n') = s\left(k+\frac{n'}{2}\right)s^*\left(k-\frac{n'}{2}\right) \tag{3.62}$$

The time-frequency relationship at time t (or bin k) and frequency f (or bin m') can also be written in discrete form, by analogy with the discretisation of the FT:

$$P_{\mathrm{wv}}(k,m') = \sum_{n'=-\mathcal{N}/2+1}^{\mathcal{N}/2} \mathrm{e}^{-\mathrm{j}2\pi n'm'/\mathcal{N}} R'_{\mathrm{wv}}(k,n') \tag{3.63}$$

where $\mathcal{N}$ is the number of bins for which the pseudo-time signal is non-zero. Since the pseudo-time signal is only known at each bin, the odd values of n' must be skipped. This is done by writing $n = n'/2$ and $m = 2m'$ giving:

$$R_{\mathrm{wv}}(k,n) = s\left(k+n\right)s^*\left(k-n\right) \tag{3.64}$$

$$P_{\mathrm{wv}}(k,m/2) = \sum_{n=-\mathcal{N}/2+1}^{\mathcal{N}/2} \mathrm{e}^{-\mathrm{j}2\pi nm/\mathcal{N}} R_{\mathrm{wv}}(k,n) \tag{3.65}$$

Now the equation for $P_{\mathrm{wv}}(k, m/2)$ is the DFT of $R_{\mathrm{wv}}(k, n)$. However, the frequency calculated for bin m in the DFT corresponds to bin $m/2$ in the time-frequency distribution. Hence the frequency resolution of P_{wv} is doubled and the maximum frequency that can be calculated is half the Nyquist frequency. Therefore, to avoid aliasing, the signal must be filtered at half the Nyquist frequency. In discretising the FT equation, an artificial limit on the resolution in frequency has been imposed which may be overcome by zero-padding.

If the signal lasts for time T_s and is sampled at frequency f_s, leading to $N_s = T_s f_s$ data points, then at sample k, corresponding to time $T_s k/N_s$, the length of the pseudo-time signal used in the DFT $\mathcal{N}$ is $2k - 1$ if $k \leq N_s/2$ and $2(N_s - k) + 1$ if $k > N_s/2$. This means that, in the frequency domain, the sinc function in the convolution with the true frequency content of the signal will have peaks whose width varies with time. At either end of the signal the peaks will be at their widest and in the middle at their narrowest. This can be demonstrated using the analytic version of the non-linear signal shown in figures 3.20 and 3.21. Figure 3.30a is a contour plot of the absolute values of the WV distribution for this signal, with the peaks highlighted as thick black lines. There is a clear narrowing of the contour lines towards the centre of the time range. Around the centre of the time range there is a worsening of the frequency estimation. This is because equation 3.64 only converts the signal into a pseudo-time signal of the correct frequency if the frequency of the original signal changes linearly with time. In this case the signal is bilinear, with a step change in gradient at $t = 1.5T$.

To overcome both these problems, windowing may be applied to the pseudo-time signal before the time-frequency distribution is calculated. By limiting the range of the pseudo-time over which the DFT is calculated, the width of the sinc function will remain constant and the frequency of the pseudo-time signal will be closer to the instantaneous frequency, since a linear estimation of the frequency will be more accurate over the window rather than over infinite pseudo-time. Figure 3.30b shows the contour plot if the maximum window width is set to T, i.e. the condition that the maximum size of $\mathcal{N}$ is limited to N is applied. The vertical lines indicate the region where the windowing affects the calculation of $P_{\mathrm{wv}}(k, m/2)$. Within this region the width of the maximum peak remains approximately constant and there is an improvement in the frequency

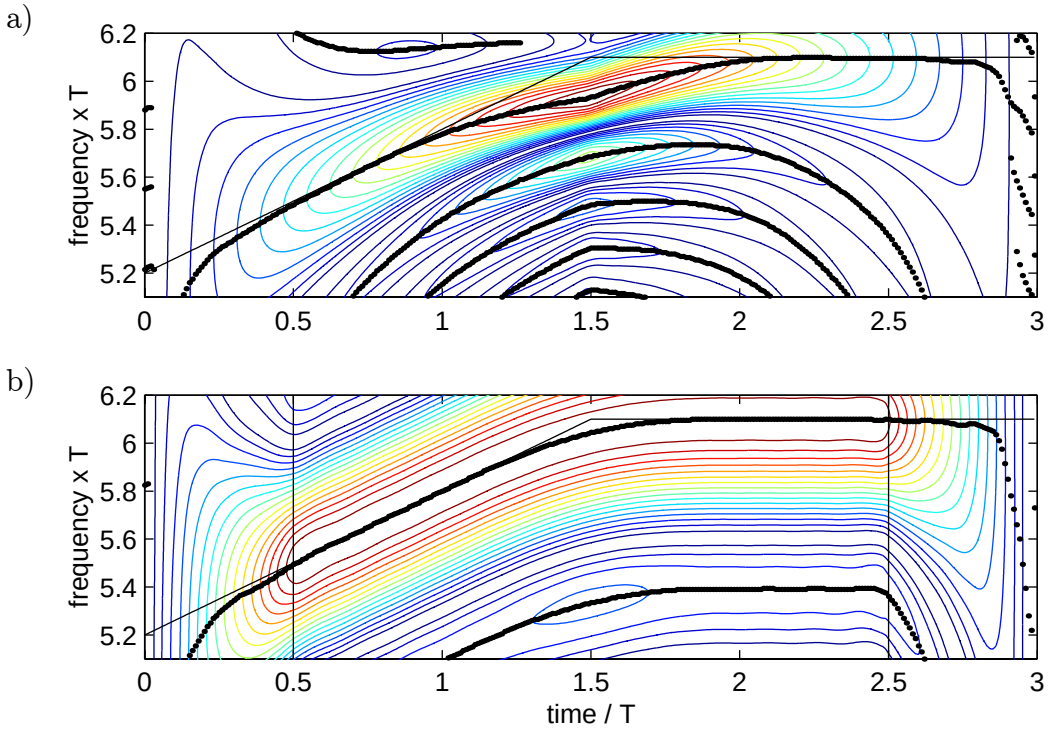

Figure 3.30: The time-frequency distribution of the analytic non-linear signal using a) the WV and b) the WWV distribution

estimation.

The discrete-windowed Wigner-Ville distribution (WWV) may be summarised by the equations:

$$P_{\text{wwv}}(k, m/2) = \sum_{-N/2+1}^{N/2} \mathrm{e}^{-\mathrm{j}2\pi nm/N} R_{\text{wwv}}(k, n) \tag{3.66}$$

where the pseudo-time series is:

$$R_{\text{wwv}}(k, n) = s(k+n)s^*(k-n) \tag{3.67}$$

where, for the points at which $k+n$ or $k-n$ is less than 0 or greater than the number of bins in the signal, $s = 0$.

3.8.2 The Modified Exponential Distribution

In order to reduce cross-terms and side-lobe interference many other kernels have been suggested. As an example, the modified exponential distribution (ME) suggested by

Zheng and McFadden [117] is examined. They suggest using the kernel:

$$\phi(\theta,\tau) = \mathrm{e}^{-\theta^2/\left(\sigma\cos^2(\alpha\tau)\right)} \tag{3.68}$$

where α and σ are parameters for controlling the time and frequency domain windows. Using equation 3.49 gives an equation for ψ:

$$\psi(t,\tau) = \sqrt{\frac{\sigma}{4\pi}}\cos(\alpha\tau)\mathrm{e}^{-\sigma t^2\cos^2(\alpha\tau)/4} \tag{3.69}$$

They also suggest the use of the anti-alias version of the bilinear signal, proposed by Jeong and Williams [46], giving the equation for the pseudo-time series to be:

$$R_{\mathrm{me}}(t,\tau) = \int_{-\infty}^{\infty}\psi(t-u,\tau)s\left(u\right)s^*\left(u-\tau\right)\mathrm{d}u \tag{3.70}$$

The pseudo-time signal is generated using a windowed version of the signal. The window is a step function which is zero outside the range $-U/2 < u \leq U/2$. As with the WWV distribution, the ME distribution is also windowed in pseudo-time so the time-frequency distribution may be written as:

$$P_{\mathrm{me}}(t,f) = \frac{1}{4\pi^2}\int_{-T/2}^{T/2}\mathrm{e}^{\mathrm{j}2\pi f\tau}R_{\mathrm{me}}(t,\tau)\mathrm{d}\tau \tag{3.71}$$

Using this kernel and the anti-alias version of the bilinear signal, taking the windowing into account and ignoring scaling factors, a discrete form of the distribution may be written in two parts as:

$$P_{\mathrm{me}}(k,m) = \sum_{n=-N/2+1}^{N/2}\mathrm{e}^{-\mathrm{j}2\pi nm/N}R_{\mathrm{me}}(k,n) \tag{3.72}$$

$$R_{\mathrm{me}}(k,n) = \cos(\alpha n)\sum_{l=-L/2+1}^{L/2}\mathrm{e}^{-\sigma l^2\cos^2(\alpha n)/4}s(k+l)s^*(k+l-n) \tag{3.73}$$

where m is the frequency bin and N and L are the lengths in bins of the windows in pseudo-time, τ, and u respectively. It is recommended to set $\alpha = \pi/N$ so that $\cos(\alpha n) = 0$ at the start and end of the pseudo-time window and so that (looking at the discrete Fourier transform in terms of the Fourier series) there is no step change between the repeating units. It is possibly more useful to rewrite equation 3.72 as:

$$P_{\mathrm{me}}(k,m) = \sum_{n=-N/2+1}^{N/2}\mathrm{e}^{-\mathrm{j}2\pi nm/N}R'_{\mathrm{me}}(k,n)t(n)\cos\left(\frac{\pi n}{N}\right) \tag{3.74}$$

where $t(n)$ is defined as:

$$t(n) = \sum_{l=-L/2+1}^{L/2} \mathrm{e}^{-\sigma l^2 \cos^2(\pi n/N)/4} \tag{3.75}$$

and the equation for $R'_{\mathrm{me}}(k,n)$ is now a weighted average over l and may be derived from equation 3.73:

$$R'_{\mathrm{me}}(k,n) = \frac{1}{t(n)} \sum_{l=-L/2+1}^{L/2} \mathrm{e}^{-\sigma l^2 \cos^2(\pi n/N)/4} s(k+l)s^*(k+l-n) \tag{3.76}$$

It can now be seen that the $t(n)\cos(\pi n/N)$ multiplier is simply a window applied to the pseudo-time series $R'_{\mathrm{me}}(k,n)$ before the DFT is calculated. This has an effect similar to using, for example, the Hanning window (see section 3.2.5). The window is shown in the pseudo-time and frequency domains in figures 3.31a and 3.31b respectively. Figure 3.31b also shows the sinc function resulting from a rectangular window applied in the pseudo-time domain for comparison. It is clear that this window has, in the frequency domain, smaller amplitude side-lobes at the cost of slightly wider peaks than the sinc function. However this is a secondary effect of having a kernel which is not unity; this window could be applied within the WWV distribution before the DFT is performed. The important effect of the new kernel is the weighting of the bilinear signal used to calculate the pseudo-time series for each time-point k.

To understand the effect of the weighted average over l, it is first necessary to consider the WWV distribution again. The anti-alias version of the WWV distribution, the pseudo-time signal $R^{\mathrm{aa}}_{\mathrm{wwv}}(k,n)$, may be written as:

$$R^{\mathrm{aa}}_{\mathrm{wwv}}(k,n) = s(k)s^*(k-n) = b^{aa}(k,n) \tag{3.77}$$

where $b^{aa}(k,n)$ is the anti-alias bilinear version of the signal.

A plane is now considered with the x-axis being time bins (centred at time k) and the y-axis being pseudo-time bins n. Over this plane the bilinear version of the signal may be plotted. If this plane is used, the pseudo-time signal for a certain time k may be generated for each pseudo-time bin n in turn. At a certain pseudo-time bin this is done by taking the values of the bilinear signal and performing a weighted average over the x-axis. The weightings are shown in figure 3.32. For the case of the WWV distribution, at each pseudo-time bin n it is simply a matter of taking the corresponding value of

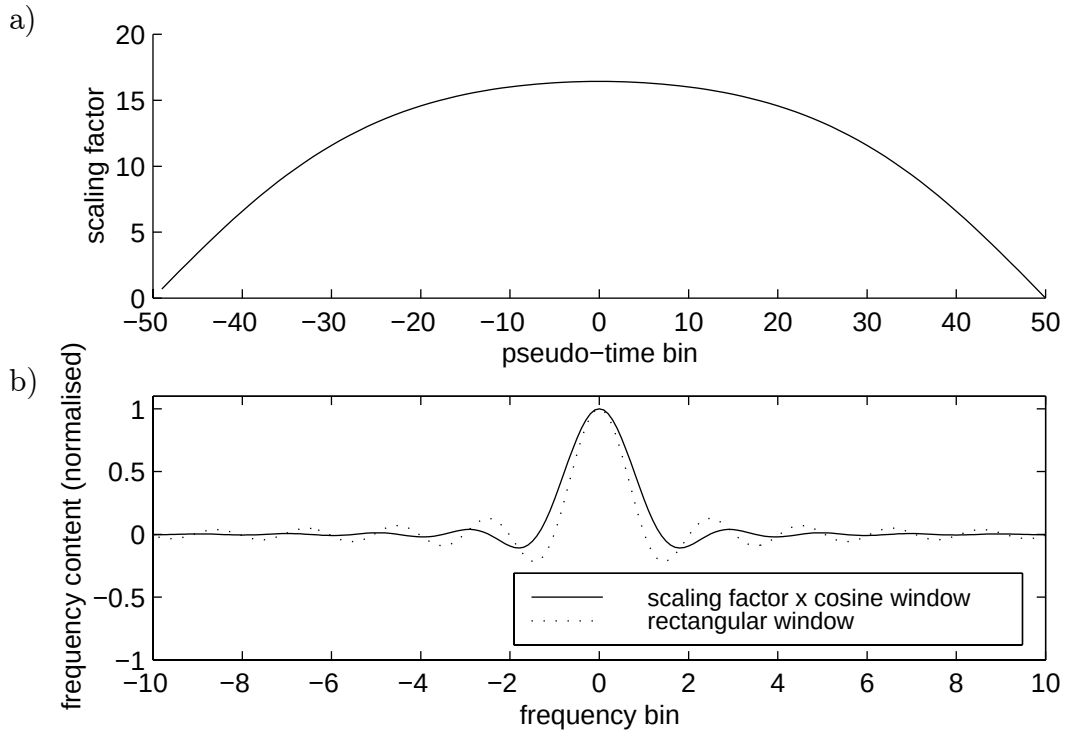

Figure 3.31: The window applied to the pseudo-time series before the DFT, in a) the pseudo-time and b) the frequency domain

the bilinear signal at time k (i.e. the value of the bilinear signal at co-ordinate $[0, n]$ in the time-pseudo-time plane). It should be noted that, in figure 3.32, the pseudo-time signal width is taken to be $N = 100$ bins and for clarity only the values $n = -55, -50, -49, -40, -30, \ldots 30, 40, 50, 51, 55$ are plotted. For the ME distribution the pseudo-time signal R'_{me} may be rewritten as:

$$R'_{\text{me}}(k, n) = \sum_{l=-L/2+1}^{L/2} \mathrm{e}^{-\sigma l^2 \cos^2(\pi n/N)/4} b^{aa}(k + l, n) \tag{3.78}$$

As with the WWV distribution, at a specific time bin k the pseudo-time signal used in the ME distribution may be generated at each pseudo-time bin n by performing a weighted average of the values of the bilinear signal $b(k + l, n)$ using the weighting over the x-axis for bin n in the y-axis and summing over time. The weightings for various pseudo-time-points, n, are shown in figure 3.33. As with figure 3.32, to aid clarity the windows are only shown for certain n bins. The window parameters used are $N = 100$, $L = 22$ and $\sigma = 0.075$ (see below).

It is reported that the negative and imaginary parts of the function $P_{\text{me}}(k, m)$ are

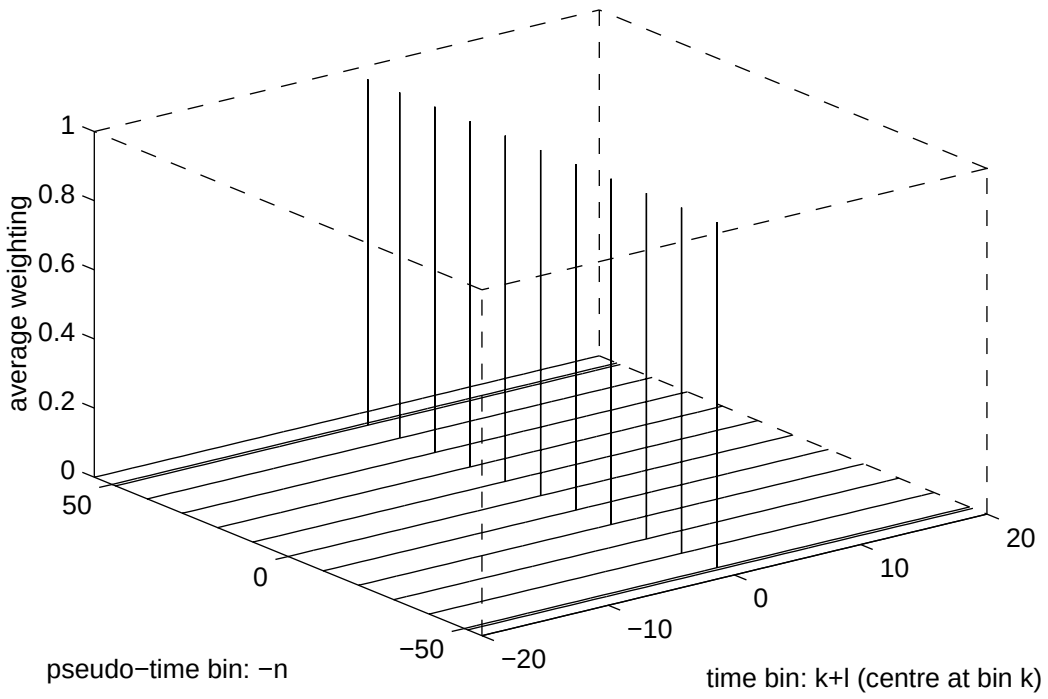

Figure 3.32: The time averaging windows applied in the WWV distribution to the bilinear signal for certain pseudo-time-points

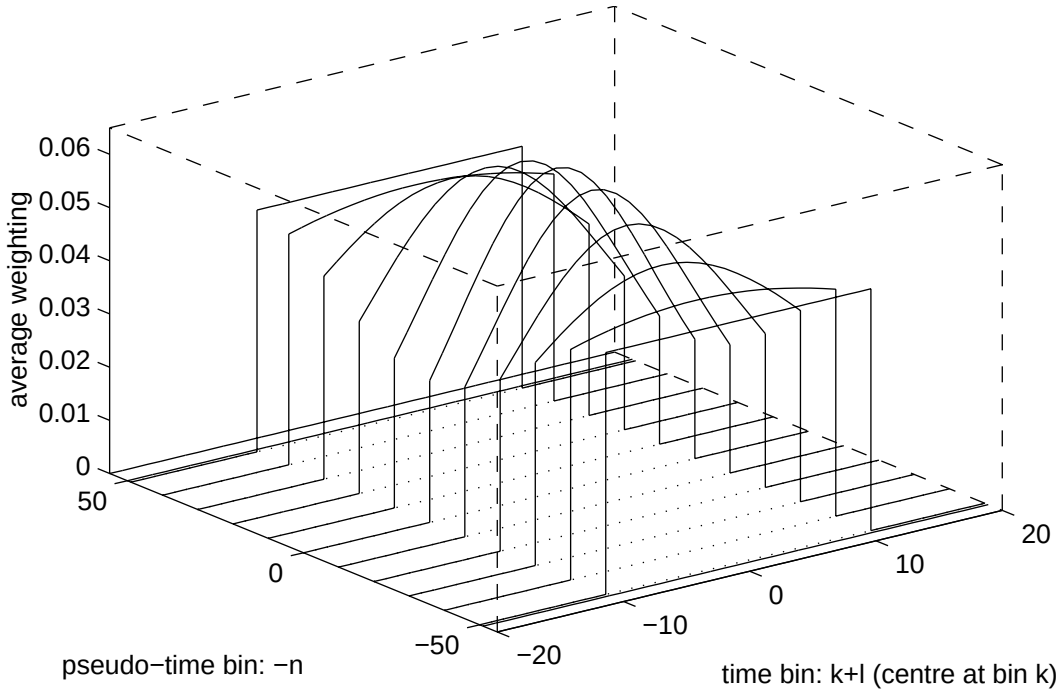

Figure 3.33: The time averaging windows applied in the ME distribution to the bilinear signal for certain pseudo-time-points

due to cross-terms so they may be set to zero [117], based on the assumption that the signal is linear over the pseudo-time window N (an assumption that is not made with the WWV distribution). The ME distribution can now be calculated for each time-point (value of k) in turn.

For a time window T long, sampled at f_s, resulting in $N = Tf_s$, it was found that a suitable relationship for the window constant is $\sigma \approx 330/N^2$ and for the range of the window in the u-domain is $L \approx 0.22N$, which is consistent with optimal values supplied by Zheng and McFadden [117]. Figure 3.34a shows the same signal using the modified exponential distribution kernel, but without using the anti-alias version of the bilinear signal. This allows direct comparison with the WWV distribution to assess the effect of the new kernel. The contour plot using the anti-alias version of the bilinear signal is given in figure 3.34b. It demonstrates that the result of using the anti-alias signal is to widen the frequency peak. This is due to the fact that it calculates $P_{\mathrm{me}}(k, m)$ using a zero-padded discrete Fourier transform of $R_{\mathrm{me}}(k, n)$ rather than calculating $P_{\mathrm{me}}(k, m/2)$. However, it should be remembered that the cost of using the bilinear signal is that the maximum frequency of the signal must be half the Nyquist frequency, a problem which is overcome using the anti-alias version of the signal.

The application of these various methods on the vibration data recorded from concrete beam tests will be discussed in section 8.2.

3.9 Summary

An assessment of the performance of the various time-frequency methods using synthetic signals has been presented. The problem with the DFT of a finite signal is that it is equivalent to a convolution of an infinite signal with a sinc function in the frequency domain. The auto-regressive model, which is capable of estimating the frequency content of a finite signal as if it were an infinite signal, overcomes this limitation. However, the additional step of calculating the model parameters may add noise to the prediction. It was also shown that for a single mode signal the analytic version of the signal is likely to improve the prediction by reducing periodic fluctuations in the estimation. When selecting a window width for a non-linear signal, a compromise is required to balance

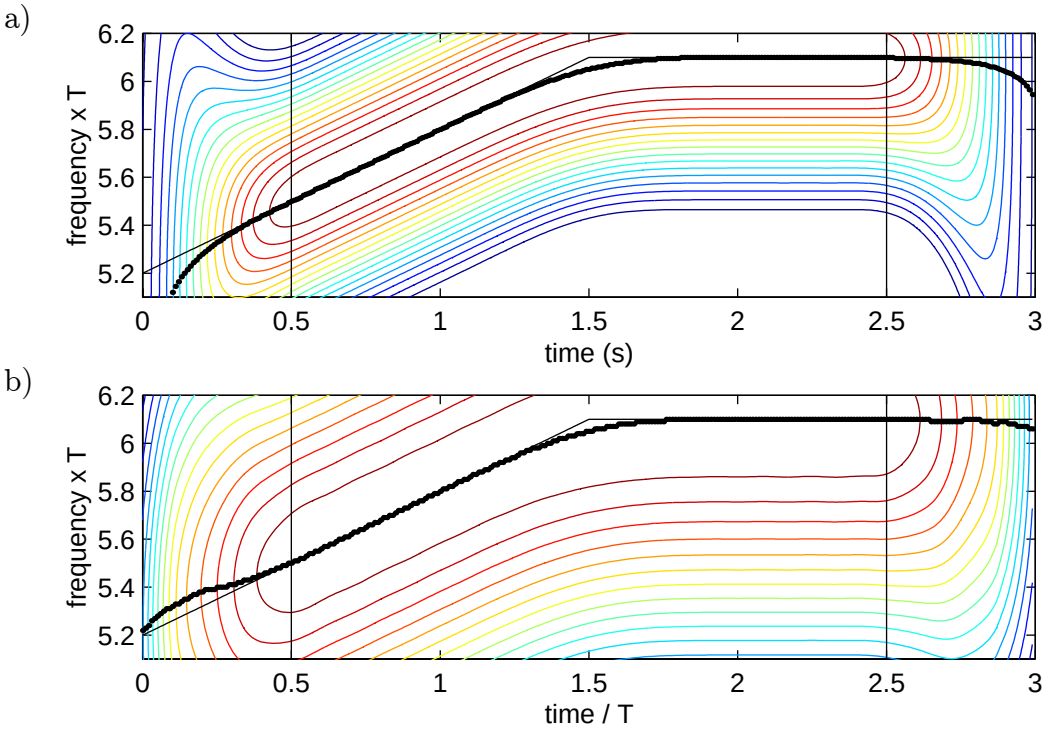

Figure 3.34: The time-frequency distribution using the ME distribution, with a) the standard representation and b) the anti-alias representation of the bilinear signal

the sinc function width (for the DFT) or number of data points for accurate pole-fitting (for the AR model) with the effect of calculating an average frequency over the length of the window rather than the true instantaneous frequency. One clear disadvantage with the AR model is that it requires a suitable number of poles to be chosen as well as the width of the time window, whereas the DFT only requires the window width. The problem with applying a time (or pseudo-time) window at the start and end of the signal is that it will be partly filled with zeros reducing the frequency resolution. This can be overcome by using the harmonic wavelet transform which applies the window in the frequency rather than the time domain.

The Cohen class of distributions use the bilinear version of the windowed signal. The advantage of transforming the signal into its bilinear form is that a signal with a linear time-frequency relationship is transformed to a signal of constant frequency equal to the instantaneous frequency at the centre of the window. With the Wigner-Ville distribution, the influence of an event at a certain time influences the frequency estimation over a large region of time, which can result in a poor estimation if the time-frequency relationship is more complex than a linear dependence. This may be overcome by using the windowed Wigner-Ville distribution which applies a window to the pseudo-time signal before transforming to the frequency domain and so limits the extent of the influence of any event in time. The anti-alias version of the bilinear signal, used in the modified exponential distribution, overcomes the condition that the maximum frequency of the bilinear signal must be limited to half the Nyquist frequency.

Chapter 4

Modelling a Vibrating Beam

The derivation of a time-stepping model of a transversely vibrating simply-supported beam which allows the inclusion of non-linear damage such as a breathing crack is now presented. This model allows inclusion of damage in the form of a moment-relative rotation relationship over a region of the beam spanning the crack, and will allow a better understanding of the non-linear behaviour exhibited by the beam during vibration.

The idea of representing a crack as a spring has been mentioned in the literature review, section 2.2.2. Existing methods use a rotational spring to represent damage combined with Timoshenko or Euler-Bernoulli beams between cracks to represent bending and shear deformation present if the beam was undamaged (see for example Gudmundson [41], Rizos *et al.* [93] or Narkis [67]). This idea is extended here, with the intention of representing the bending and shear deformation of the undamaged sections using springs, as well as the damaged regions. The beam is divided into short rigid blocks joined using rotational and transverse springs which represent bending and shear deformation respectively. Any stiffness reduction due to a crack is represented by adjusting the rotational spring stiffness at that spring position. It is then possible to derive equations for the displacement and rotation of each rigid block in terms of the accelerations (both transverse and rotational) of the blocks and use these equations in a time-stepping method to find the response of the beam to a set of initial conditions. The advantage of this approach is that, as well as being capable of including rotational inertia and shear deformation, the spring stiffness equation at the crack position may be easily altered between time-steps, allowing a bilinear breathing crack or a more complex fatigue crack

to be modelled.

Firstly, the model for a simply-supported beam ignoring shear distortion is derived. The predicted natural frequencies using the model for a varying number of blocks are compared to the theoretical frequencies based on the differential equation of motion for the beam. Then the model is extended to include shear distortion and the predicted natural frequencies are compared to theoretical values. The model's accuracy in predicting the natural frequencies is also compared to a numerical solution for a simply-supported truncated conical beam [17]. Finally, a cantilever beam version of the model including damping (represented as dash-pots at each spring position) is used to predict the dynamic response of a beam with a stiffness non-linearity and the results are compared to a simple experiment.

4.1 A Discrete Approximation to the Beam

The model of the beam is based on the idea of representing the bending and shear stiffnesses in discrete form. The beam is represented as a series of rigid blocks connected by rotational and transverse springs. The rotational spring approximates the bending of the beam and the transverse spring approximates the shear.

Firstly, the mass and inertia of the beam are approximated in lumped form. The beam is split into N blocks, those at either end being half the length of the other blocks as shown in figure 4.1a. The mass and rotational moment of inertia of each block are then lumped at its centre as shown in figure 4.1b. For blocks of rectangular cross-section the mass and rotational inertia of block n are given by:

$$m_n = \rho b h l_n \tag{4.1}$$

$$J_n = \frac{m_n}{12}(h^2 + l_n^2) \tag{4.2}$$

where b is the width of the beam, h is the depth and l_n is the length of the block (equal to $L/(N-1)$ where L is the total beam length, except for the two end blocks which have length $L/2(N-1)$).

Secondly, the light flexible elements between the lumped masses and inertias are

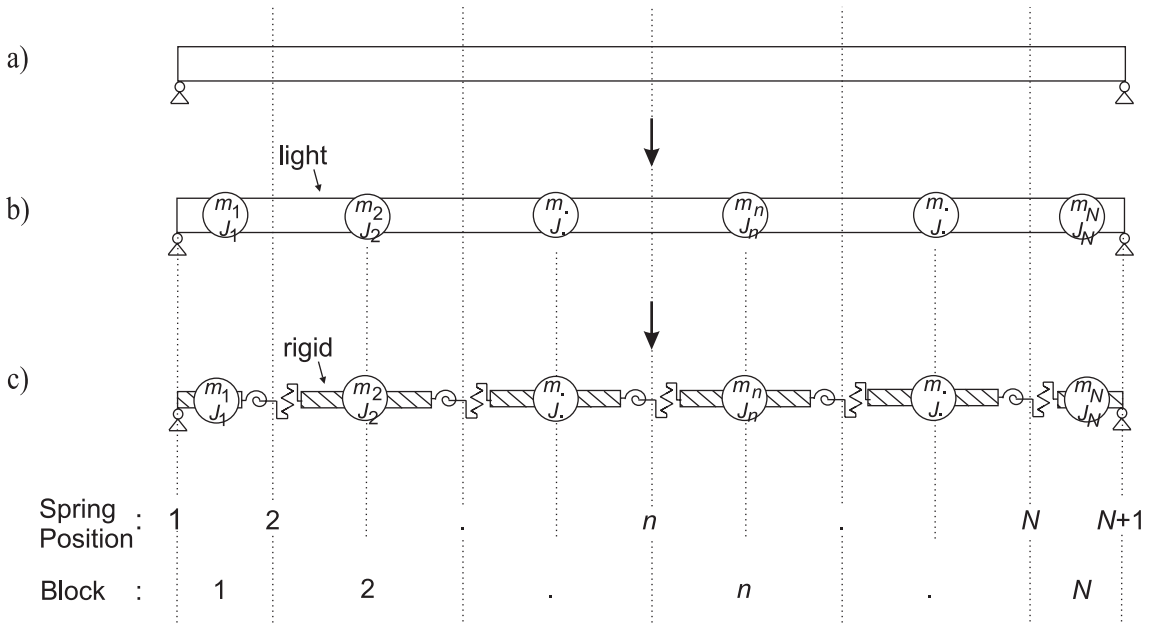

Figure 4.1: Modelling of the beam as discrete blocks

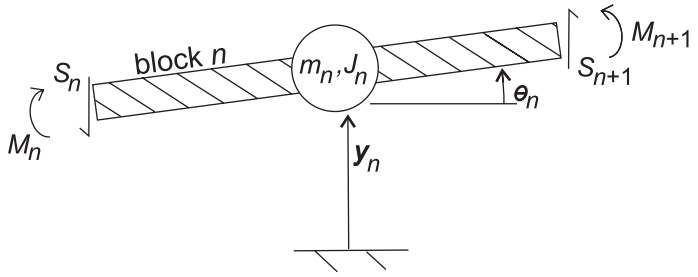

Figure 4.2: Forces and displacements at block n

approximated by rigid elements connected by rotational and transverse springs. For the end elements, the compliance due to the half-length element in contact with the support and half of the next element is lumped at the block boundary between the end and the second element, as shown in figure 4.1c. The notation for the spring positions and the rigid blocks is defined in figure 4.1c. The displacement and rotation of the rigid block n are defined in figure 4.2, where the forces acting on the block due to the springs at either end are also shown. It should be noted that as there are no springs at the supports and as the beam is simply-supported, the moments at the supports (M_1 and M_{N+1}) are zero.

It is now necessary to calculate the required rotational and transverse spring stiffnesses at spring position n (K_n and V_n respectively) to model the bending and shear

distortion. In the lumped model, the springs at position n are subjected to moment M_n and shear force S_n, representing the bending and shear distortion over a length l from the centre of block $n-1$ to the centre of block n, as shown in figure 4.3a (with the exception of the end springs which represent the distortions from the support to the block position 2 or $N-1$, which is still length l.) Now consider the intermediate stage where the mass and inertia have been lumped but the compliance is distributed, as in figure 4.1b. The only forces and moments on the beam element are applied at the ends. If the moment and shear at the centre of the beam element take values M_n and S_n, then the end moments are as shown in figure 4.3b. The relative end rotation of this beam is given by:

$$\theta_n - \theta_{n-1} = \frac{1}{EI}\left(\left(M_n + \frac{l}{2}S_n\right)l - \frac{l^2}{2}S_n\right) = \frac{l}{EI}M_n \tag{4.3}$$

where I is the second moment of area for the element and E is the Young's modulus. The relative end deflection (including shear distortion) is given by:

$$\begin{aligned} y_n - y_{n-1} &= l\,\theta_{n-1} + \frac{l^2}{2EI}\left(M_n + \frac{l}{2}S_n\right) - \frac{l^3}{6EI}S_n + \frac{l}{kAG}S_n \\ &= l\,\theta_{n-1} + \frac{l^2}{2EI}M_n + \left(\frac{l}{kAG} + \frac{l^3}{12EI}\right)S_n \end{aligned} \tag{4.4}$$

where kA is the effective shear area and G is the shear modulus. These equations may be compared to the relative rotation and deflection equations for the beam with the lumped compliance:

$$\theta_n - \theta_{n-1} = \frac{M_n}{K_n} \tag{4.5}$$

$$y_n - y_{n-1} = l\,\theta_{n-1} + \frac{l}{2}\frac{M_n}{K_n} + \frac{S_n}{V_n} \tag{4.6}$$

to give the spring stiffnesses:

$$K_n = \frac{EI}{l} \tag{4.7}$$

$$V_n = \frac{kAG}{l}\,\frac{1}{1 + \dfrac{kAGl^2}{12EI}} \tag{4.8}$$

Shear distortion has only a minor effect on the vibration of a beam. Later it will be shown that for a stocky rectangular beam the effect on the frequency of the third mode is about 8% and far less for the first and second modes. It is a common assumption that

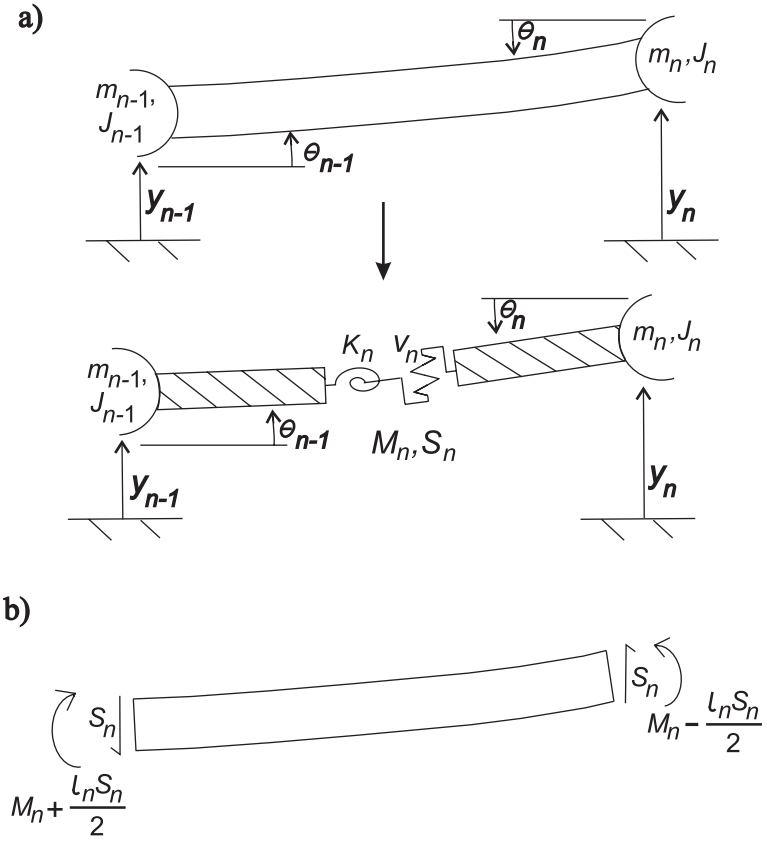

Figure 4.3: Spring at position n

shear distortion can be ignored, as for example in the Euler-Bernoulli approximation to a beam. If a rectangular cross-section beam is considered, taking $E/kG = 3$ (a typical value quoted by Clough and Penzien [24]), and noting that $(N-1)l = L$ where L is the total length of the beam, the transverse spring constant may be written as:

$$V_n = \frac{kAG}{l} \frac{1}{1 + \frac{1}{3\lambda^2(N-1)^2}} \tag{4.9}$$

where $\lambda = h/L$, the depth to length ratio for the whole beam. It can be seen that the contribution to the transverse spring stiffness due to bending is small compared to that made by the shear distortion, which in turn only has a small effect on the overall behaviour of the beam. As the effect decreases with increasing numbers of blocks, it was decided to ignore the contribution of the bending distortion to the transverse spring, which gives:

$$V_n = \frac{kAG}{l} \tag{4.10}$$

This approximation allows bending and shear effects to be represented entirely in the form of rotational and transverse springs respectively.

4.1.1 The Time-Stepping Routine

A time-stepping routine is necessary to solve the equations governing the motion of the blocks. These equations will be arranged such that a vector of acceleration terms may be calculated from a vector of displacement terms. The time-stepping routine then uses the accelerations along with the displacements to calculate the displacement terms at the next time-point. It is therefore necessary to use a second-order multiple degree of freedom time-stepping routine.

The model was derived in two stages; initially shear distortion was ignored for simplicity then the model was extended to include it. Without shear distortion the time-stepping routine employed was the Modified Euler method (or Heun's Method) and when shear distortion was included in the model a Runge-Kutta fourth-order time-stepping routine was used.

The Modified Euler method, a predictor-corrector method (see for example Kreyszig [52])

is defined in two stages. For a first-order differential equation:

$$\dot{y} = f(y, t) \tag{4.11}$$

firstly, the predictor step must be performed:

$$y^*_{n+1} = y_n + hf(y_n, t_n) \tag{4.12}$$

where h is the time-step length and y^*_{n+1} is the predicted value of the displacement at time-step $n+1$, and then the corrector step:

$$y_{n+1} = y_n + \frac{h}{2}\left[f(y_n, t_n) + f(y^*_{n+1}, t_{n+1})\right] \tag{4.13}$$

where y_{n+1} is the displacement at time-step $n+1$.

This method may be extended to a second-order differential equation by splitting the differential equation into two simultaneous first-order equations (see Todd [107], for example). The second-order equation:

$$\ddot{y} = g(y, \dot{y}, t) \tag{4.14}$$

can be written as:

$$\dot{y} = y' \tag{4.15}$$

$$\dot{y'} = g(y, y', t) \tag{4.16}$$

The predicted velocity and acceleration terms may now be calculated by applying the first step of the time-step method to the two first-order equations, then the corrected velocity and acceleration terms may be calculated using the second step. Therefore the resulting method for the second-order differential equation is given by:

$$y^*_{n+1} = y_n + h\dot{y}_n \tag{4.17}$$

$$\dot{y}^*_{n+1} = \dot{y}_n + h\ddot{y}_n \tag{4.18}$$

$$\ddot{y}^*_{n+1} = f(y^*_n, \dot{y}^*_n, t_n) \tag{4.19}$$

$$y_{n+1} = y_n + \frac{h}{2}\left(\dot{y}_n + \dot{y}^*_{n+1}\right) \tag{4.20}$$

$$\dot{y}_{n+1} = \dot{y}_n + \frac{h}{2}\left(\ddot{y}_n + \ddot{y}^*_{n+1}\right) \tag{4.21}$$

$$\ddot{y}_{n+1} = f(y_{n+1}, \dot{y}_{n+1}, t_{n+1}) \tag{4.22}$$

To start this time-stepping method both the displacements and velocities are required at the start time. In the model there are i degrees of freedom relating to the i blocks, so the variable y must be seen as a vector of all the degrees of freedom.

If the time-step is too large, errors are introduced into the prediction of the displacement. These errors are cumulative over each time-step and lead to a growth in the overall energy of the system. To ensure that this did not happen the ratio of the current energy to the initial energy of the beam was calculated every 5000 time-steps. For the case where damping was included in the model (see section 4.2.2) the model was run twice, the second time with a time-step half the size of the first. The time signals generated from these two runs were then compared to check the stability of the time-step.

For the later model which includes the shear distortions, the computation time increased by approximately a factor of four as the model required a smaller time-step to remain stable. This also led to far larger data files for a required length (in time) of a signal, which consequently slowed down the signal processing. To overcome these problems a fourth-order Runge-Kutta method was used instead of the Modified Euler method. This involves three intermediate values of y being calculated at each time-step, two at time-point $n + \frac{1}{2}$ and the third at time-point $n + 1$ before the actual y_{n+1} value is estimated, rather than the one intermediate value y^*_{n+1} as used in the Modified Euler method. It therefore takes approximately twice as long to calculate one time-step since the equation relating accelerations to displacements must be evaluated four times rather than twice. However, each time-step can be considerably larger as the prediction of the new displacement based on the old displacement is far superior to that using the Modified Euler Method. It was found that, typically when using the model, the time-step could be increased by a factor of 16 when employing the Runge-Kutta technique rather than the modified Euler method, so reducing the computation time by roughly a factor of eight. The equations used to implement the Runge-Kutta technique are not given here as they may be found in Todd [107] or Press *et al.* [86] and the technique of using them to solve a second-order differential equation follows the same lines as for the

Modified Euler method.

The computation time can be reduced further still if an adaptive step size is used for the Runge-Kutta method (see, for example, Press *et al.* [86]). This can be achieved by a technique called step doubling, which involves calculating each step twice, once as a full step and then as two half time-steps. The difference between these two predicted values can be used to judge the error in the calculation and also to scale the step size to be used in the next time-step. If the difference is too large, then the step size used for the current time-step was too great and the step must be recalculated using a smaller step size. However, if this method is used, difficulties will arise with taking Fourier transforms of the signal due to the varying sampling rate caused by the varying step size. It is possible to overcome this problem by generating a signal of constant sampling frequency from the signal with a varying step size using curve fitting techniques, but this will introduce new errors and complexity. A second way of improving the computational efficiency is to use the Adams-Bashforth (or a related) method. This method first predicts a current value of y using several past values of $\dot{y}$ and then evaluates its derivative, $\dot{y}$, which in turn is used with past values of $\dot{y}$ to correct the value of the current y. The problem with using this type of method in the model is that non-linearities in the stiffness of the damaged spring may lead to sudden changes in the displacements of the blocks and so the predictor step using the velocities would not work well.

4.1.2 Model Ignoring Shear Effects

A discrete model of a beam ignoring shear distortion is derived below. Shear distortion does affect the natural frequencies of a beam and so is included in the model in the next section, however it is worth deriving the model excluding shear distortion first as it is significantly easier. Ignoring shear distortion allows the spring representation of the deflection to be reduced to simply a rotational spring at each location and so it is possible to express the displacements purely in terms of the rotations.

Derivation of the Model

The forces acting on block n are shown in figure 4.2, where M_n is the moment due to deflection of the spring at position n, l_n is the length of block n, m_n is its mass and J_n is its moment of inertia. It follows that the equations of motion of the block are:

$$J_n\ddot{\theta}_n = M_{n+1} - M_n + \frac{l_n}{2}(S_{n+1} + S_n) \tag{4.23}$$

$$m_n\ddot{y}_n = S_{n+1} - S_n \tag{4.24}$$

The moment at position n can be expressed in terms of block rotations and spring stiffness:

$$M_n = K_n(\theta_n - \theta_{n-1}) \tag{4.25}$$

except for M_1 and M_{N+1} at either end of the beam, where the moments are zero as the beam is simply-supported. If the beam is damaged this relationship between block rotation and resulting spring moments can be altered easily. For example, the spring stiffness K_n could be altered at each time-step. An expression for displacement y_n may be written in terms of rotations and the displacement y_{n-1} and then by differentiating twice with respect to time the rotational and linear accelerations may also be related:

$$y_n = y_{n-1} + \frac{l_{n-1}}{2}\theta_{n-1} + \frac{l_n}{2}\theta_n \tag{4.26}$$

$$\ddot{y}_n = \ddot{y}_{n-1} + \frac{l_{n-1}}{2}\ddot{\theta}_{n-1} + \frac{l_n}{2}\ddot{\theta}_n \tag{4.27}$$

The final equation to be derived is the boundary condition that the displacement of one end with respect to the other end of the beam is zero. This may be expressed as:

$$\sum_{n=1}^{N} l_n\theta_n = 0 \tag{4.28}$$

From these equations, it is possible to express the rotational accelerations in terms of the rotations of each block and so, using the Modified Euler time-stepping method (see section 4.1.1), solve the equations for given initial conditions. Before this can be attempted, the equations must be written in matrix form. The derivation shown here is for the case where there are four blocks in the model. This is an unrealistically small number but the derivation for larger numbers of blocks is identical.

The linear equations of motion for all the blocks may be expressed in matrix form. Since there are $N+1$ shear forces but only N equations relating shear forces to accelerations $\ddot{y}_n$, it is only possible to eliminate N of the shear forces using the vertical equations of motion and so the shear force S_1 is kept out of the shear vector and included as a separate vector:

$$\begin{pmatrix} m_1 & 0 & 0 & 0 \\ 0 & m_2 & 0 & 0 \\ 0 & 0 & m_3 & 0 \\ 0 & 0 & 0 & m_4 \end{pmatrix} \begin{pmatrix} \ddot{y}_1 \\ \ddot{y}_2 \\ \ddot{y}_3 \\ \ddot{y}_4 \end{pmatrix} = \begin{pmatrix} 1 & 0 & 0 & 0 \\ -1 & 1 & 0 & 0 \\ 0 & -1 & 1 & 0 \\ 0 & 0 & -1 & 1 \end{pmatrix} \begin{pmatrix} S_2 \\ S_3 \\ S_4 \\ S_5 \end{pmatrix} - \begin{pmatrix} 1 \\ 0 \\ 0 \\ 0 \end{pmatrix} S_1 \quad (4.29)$$

$$\mathbf{m}\{\ddot{y}\} = \mathbf{A}\{S\} - \{a\}S_1 \quad (4.30)$$

Similarly, the rotational equations of motion may be expressed in matrix form as:

$$\begin{pmatrix} J_1 & 0 & 0 & 0 \\ 0 & J_2 & 0 & 0 \\ 0 & 0 & J_3 & 0 \\ 0 & 0 & 0 & J_4 \end{pmatrix} \begin{pmatrix} \ddot{\theta}_1 \\ \ddot{\theta}_2 \\ \ddot{\theta}_3 \\ \ddot{\theta}_4 \end{pmatrix} = \begin{pmatrix} 1 & 0 & 0 \\ -1 & 1 & 0 \\ 0 & -1 & 1 \\ 0 & 0 & -1 \end{pmatrix} \begin{pmatrix} M_2 \\ M_3 \\ M_4 \end{pmatrix} + \frac{1}{2} \begin{pmatrix} l_1 & 0 & 0 & 0 \\ 0 & l_2 & 0 & 0 \\ 0 & 0 & l_3 & 0 \\ 0 & 0 & 0 & l_4 \end{pmatrix} \left[\begin{pmatrix} 1 & 0 & 0 & 0 \\ 1 & 1 & 0 & 0 \\ 0 & 1 & 1 & 0 \\ 0 & 0 & 1 & 1 \end{pmatrix} \begin{pmatrix} S_2 \\ S_3 \\ S_4 \\ S_5 \end{pmatrix} + \begin{pmatrix} 1 \\ 0 \\ 0 \\ 0 \end{pmatrix} S_1 \right] \quad (4.31)$$

$$\mathbf{J}\{\ddot{\theta}\} = \mathbf{C}\{M\} + \frac{1}{2}\mathbf{L}(\mathbf{B}\{S\} + \{a\}S_1) \quad (4.32)$$

The $N-1$ rotational spring equations may be expressed as:

$$\begin{pmatrix} M_2 \\ M_3 \\ M_4 \end{pmatrix} = \begin{pmatrix} K_2 & 0 & 0 \\ 0 & K_3 & 0 \\ 0 & 0 & K_4 \end{pmatrix} \begin{pmatrix} -1 & 1 & 0 & 0 \\ 0 & -1 & 1 & 0 \\ 0 & 0 & -1 & 1 \end{pmatrix} \begin{pmatrix} \theta_1 \\ \theta_2 \\ \theta_3 \\ \theta_4 \end{pmatrix} \quad (4.33)$$

$$\{M\} = \mathbf{KD}\{\theta\} \quad (4.34)$$

The compatibility equations may be written in matrix form as:

$$\begin{pmatrix} 1 & 0 & 0 & 0 \\ -1 & 1 & 0 & 0 \\ 0 & -1 & 1 & 0 \\ 0 & 0 & -1 & 1 \end{pmatrix} \begin{pmatrix} y_1 \\ y_2 \\ y_3 \\ y_4 \end{pmatrix} = \frac{1}{2} \begin{pmatrix} 1 & 0 & 0 & 0 \\ 1 & 1 & 0 & 0 \\ 0 & 1 & 1 & 0 \\ 0 & 0 & 1 & 1 \end{pmatrix} \begin{pmatrix} l_1 & 0 & 0 & 0 \\ 0 & l_2 & 0 & 0 \\ 0 & 0 & l_3 & 0 \\ 0 & 0 & 0 & l_4 \end{pmatrix} \begin{pmatrix} \theta_1 \\ \theta_2 \\ \theta_3 \\ \theta_4 \end{pmatrix} \tag{4.35}$$

$$\mathbf{A}\{y\} = \frac{1}{2}\mathbf{BL}\{\theta\} \tag{4.36}$$

Finally, the boundary condition equation is:

$$\begin{pmatrix} l_1 & l_2 & l_3 & l_4 \end{pmatrix} \begin{pmatrix} \theta_1 \\ \theta_2 \\ \theta_3 \\ \theta_4 \end{pmatrix} = 0 \tag{4.37}$$

$$\{l\}^T\{\theta\} = 0 \tag{4.38}$$

where $\{l\}^T$ is the transpose of $\{l\}$.

These matrix equations may be rearranged to enable the calculation of the rotational accelerations for a given set of rotations, and so may be used in a time-stepping method. Firstly, equations 4.34 and 4.30 may be used to eliminate $\{M\}$ and $\{S\}$ in equation 4.32. Then the $\{\ddot{y}\}$ vector may be eliminated using equation 4.36 differentiated twice with respect to time. The resulting equation is:

$$\left(\mathbf{J} - \frac{1}{4}\mathbf{LBA}^{-1}\mathbf{mA}^{-1}\mathbf{BL}\right)\{\ddot{\theta}\} = \mathbf{CKD}\{\theta\} + \frac{1}{2}\mathbf{L}\left(\{a\} + \mathbf{BA}^{-1}\{a\}\right)S_1 \tag{4.39}$$

This is simplified by defining $\mathbf{E}^{-1} = \mathbf{J} - \frac{1}{4}\mathbf{LBA}^{-1}\mathbf{mA}^{-1}\mathbf{BL}$ and noting that $\frac{1}{2}\ \mathbf{L}(\{a\} + \mathbf{BA}^{-1}\{a\})$ is the same as a column vector $\{l\}$ of the lengths of each block, giving:

$$\{\ddot{\theta}\} = \mathbf{ECKD}\{\theta\} + \mathbf{E}\{l\}S_1 \tag{4.40}$$

This equation along with the boundary condition equation may be used to find the rotational accelerations in terms of the rotations in two steps:

1. Calculate the shear force S_1 from the rotations, using the boundary condition, equation 4.38, differentiated twice with respect to time, and equation 4.40, resulting in the relationship:

$$\{l\}^T\{\ddot{\theta}\} = \{l\}^T\mathbf{ECKD}\{\theta\} + \{l\}^T\mathbf{E}\{l\}S_1 = 0 \tag{4.41}$$

2. Calculate the rotational accelerations by substituting the shear force S_1, calculated in step 1, into equation 4.40 above.

The resulting rotational accelerations and the rotations may be used in conjunction with the time-stepping method to predict the rotations at the next time-step.

Checking the Validity of the Model

In the case of an undamaged beam of uniform cross-section, it is possible to solve the continuous equation of motion of the beam to find the natural frequencies and so check the validity of the discrete model. The continuous equation of motion (see, for example, Tse *et al.* [108] or Clough and Penzien [24]) is:

$$EI\frac{\partial^4 y}{\partial x^4} + \bar{m}\frac{\partial^2 y}{\partial t^2} - \bar{m}r^2\frac{\partial^4 y}{\partial t^2 \partial x^2} - \frac{E\bar{m}r^2}{kG}\frac{\partial^4 y}{\partial t^2 \partial x^2} + \frac{\bar{m}^2 r^2}{kAG}\frac{\partial^4 y}{\partial t^4} = 0 \qquad (4.42)$$

where kA is the effective shear area of a cross-section, $\bar{m}$ is the mass per unit length and r is the radius of gyration, i.e. $r^2 = I/A$, where I is the second moment of area. The first two terms in the equation are the terms found in the elementary case where neither rotational inertia nor shear distortion are taken into account, the third term is due to rotational inertia, the fourth due to shear distortions and the last term due to a combination of rotational inertia and shear distortion. Therefore, if shear effects are ignored the left-hand side of the equation is reduced to the first three terms only. Weaver *et al.* [113] state that for a simply-supported beam, with or without the inclusion of rotational inertia and shear distortion, the deformed shape will take the form:

$$y = \sum_{i=1}^{\infty} \sin\left(\frac{i\pi x}{L}\right)\left(A_i \cos(\omega_i t) + B_i \sin(\omega_i t)\right) \qquad (4.43)$$

where i is the mode number $1, 2, 3, \ldots$, and ω_i is the natural frequency of mode i. Therefore the natural frequency of mode i ignoring shear distortion, ω_{ai}, may be expressed as:

$$\omega_{ai} = \frac{\omega_{oi}}{\sqrt{1 + \left(\frac{i\pi r}{L}\right)^2}} \qquad (4.44)$$

where ω_{oi} is the natural frequency of the elementary case ignoring both the rotational inertia and the shear distortions:

$$\omega_{oi} = i^2\pi^2\sqrt{\frac{EI}{\bar{m}L^4}} \qquad (4.45)$$

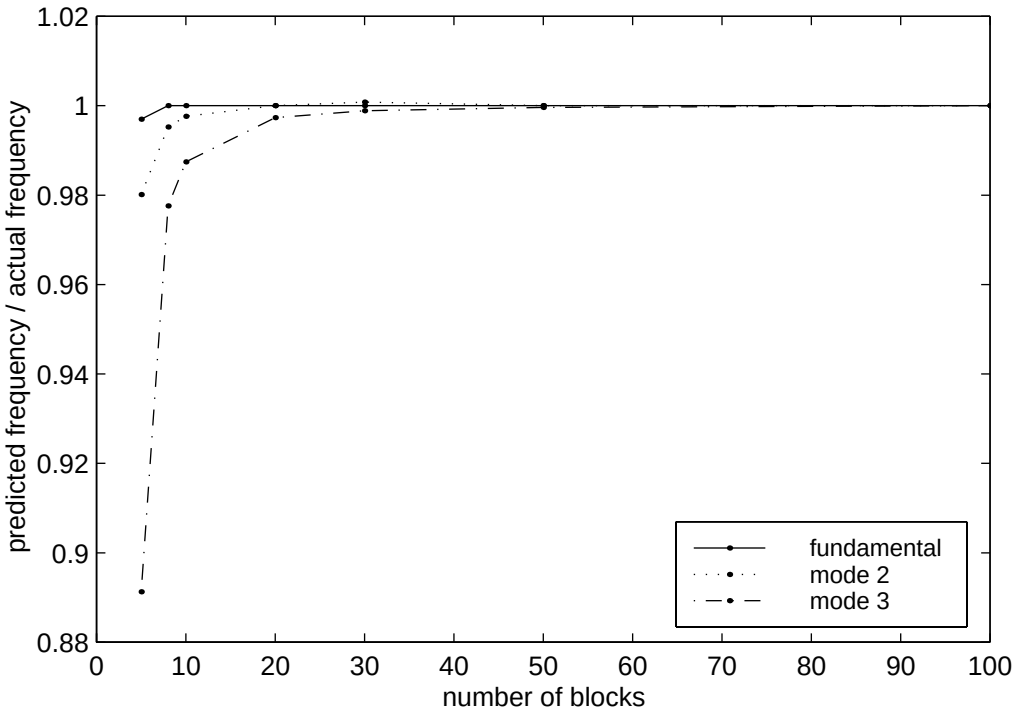

Figure 4.4: Frequencies predicted by the model which excludes shear deformation for varying numbers of blocks (the frequencies are normalised using ω_{ai}, the theoretical frequency of mode i ignoring shear deformation)

The discrete model can now be tested. The choice of time-step was checked by monitoring the energy of the system. The time-step used was in the order of 1×10^{-5} s, the precise value depending on the number of blocks in the model. The natural frequencies predicted by the model can be calculated by using the discrete Fourier transform of the displacement signal and these can be compared to the theoretical values. Figure 4.4 shows the first three natural frequencies predicted by the model using varying numbers of blocks for a rectangular cross-section beam with a depth to length ratio of 0.21. The frequency values are normalised using the theoretical frequencies calculated from equations 4.44 and 4.45. It shows that the model performs very well even with a reasonably small number of blocks for the first two modes and if 20 or more blocks are used there is less than 0.5% error in predicting the frequencies of the first three modes.

Figure 4.5 shows the corresponding mode shapes calculated from the time signal generated by the model when 20 blocks are used, plotted as points at each block centre,

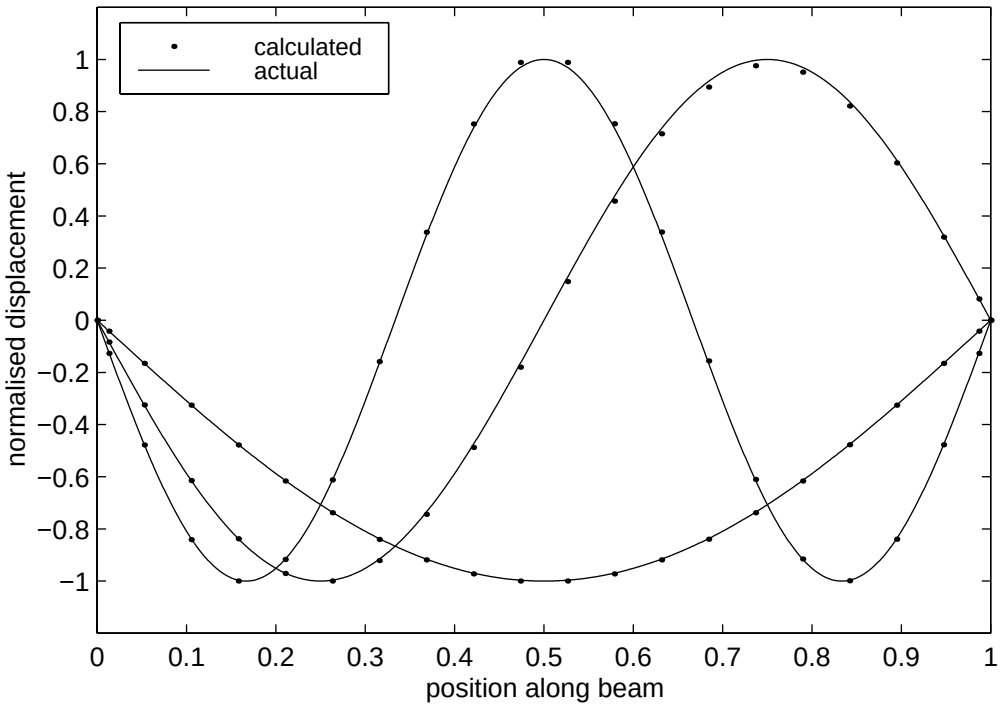

Figure 4.5: Mode shapes calculated using the model which excludes shear deformation

compared with the expected sinusoidal mode shapes. There is very good agreement between the calculated model values and the actual values for the first three modes here too.

4.1.3 Model Including Shear Distortion

Effect of Shear Distortion on Natural Frequencies

In reality, a beam will be subject to both bending and shear deflections. Although these additional shear effects only make a relatively small difference in the natural frequencies, they should not be ignored because the changes in natural frequency due to damage are also expected to be small. The effect of the shear distortions on the natural frequencies may be examined by looking again at the equation of motion of a beam, equation 4.42. If the expected mode shape equation (equation 4.43) is substituted into the equation of motion, an equation for the natural frequencies may be found in two stages.

Firstly, if the last term on the left hand side of the equation of motion (the term due to a combination of shear and inertial effects) is ignored, an equation for the resulting

natural frequency may be derived using the mode shape equation:

$$\omega_{bi} = \frac{\omega_{oi}}{\sqrt{1 + \left(\frac{r\pi i}{L}\right)^2 \left(1 + \frac{E}{kG}\right)}} \tag{4.46}$$

where ω_{bi} is the natural frequency of mode i for the case where only the term due to the combination of shear and inertial effects is ignored.

Now the effect of the last term can be examined. If a correction term κ_i, for mode i, is defined to relate ω_{bi} to the actual natural frequency ω_{ci} (which includes all the terms in equation 4.42) by:

$$\omega_{ci}^2 = (1 + \kappa_i)\omega_{bi}^2 \tag{4.47}$$

then by substituting the mode shape into the equation of motion it can be shown that:

$$\kappa_i = \frac{1}{2\alpha_i^2} - 1 - \frac{1}{2\alpha_i^2}\sqrt{1 - 4\alpha_i^2} \tag{4.48}$$

where α_i is defined as:

$$\alpha_i^2 = \frac{\bar{m}r^2}{kAG}\frac{\omega_{bi}^4}{\omega_{oi}^2} = \frac{\left(\frac{\pi ir}{L}\right)^4 \frac{E}{kG}}{\left(1 + \left(\frac{\pi ir}{L}\right)^2 \left(1 + \frac{E}{kG}\right)\right)^2} \tag{4.49}$$

Except when the slenderness is very low or a high mode number is being considered, α_i is small and so the expression for κ_i may be simplified to:

$$\kappa_i = \alpha_i^2(1 + 2\alpha_i^2) \tag{4.50}$$

Table 4.1 shows the natural frequencies including shear deformation (ω_{ci}) and excluding shear deformation (ω_{ai}) non-dimensionalised using ω_{oi} (the natural frequency if both shear distortions and rotational inertia are ignored), for a range of values of r/L. For a rectangular section of uniform material properties, the depth to length ratio $h/L = \sqrt{12}(r/L)$. A value of $E/kG = 3$ was used as suggested by Clough and Penzien [24] as a typical value for a rectangular cross-section.

This shows that the shear effects can be significant when predicting the natural frequencies of a beam. For example, if $r/L = 0.04$, the error in the predicted frequency of mode three is 16%. Therefore, to represent the actual beam accurately, the shear distortions must be included in the model.

r/l	ω_a/ω_o			ω_c/ω_o		
	mode 1	mode 2	mode 3	mode 1	mode 2	mode 3
0.005	1.000	1.000	0.999	1.000	0.998	0.996
0.010	1.000	0.998	0.996	0.998	0.992	0.983
0.015	0.999	0.996	0.990	0.996	0.983	0.963
0.020	0.998	0.992	0.983	0.992	0.970	0.937
0.025	0.997	0.988	0.973	0.988	0.955	0.907
0.030	0.996	0.983	0.962	0.983	0.937	0.875
0.035	0.994	0.977	0.950	0.977	0.918	0.842
0.040	0.992	0.970	0.936	0.970	0.897	0.809
0.045	0.990	0.962	0.921	0.963	0.875	0.776
0.050	0.988	0.954	0.905	0.955	0.853	0.744
0.055	0.985	0.945	0.888	0.946	0.831	0.713

Table 4.1: Normalised natural frequencies with and without shear distortions, where ω_a is ignoring shear deformation, ω_c is including shear deformation and ω_o is ignoring shear deformation and inertia

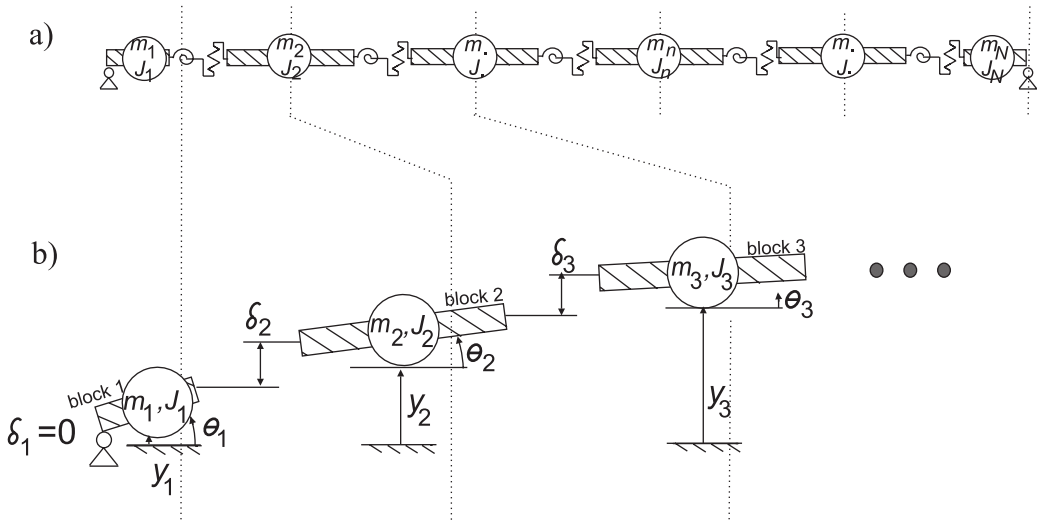

Figure 4.6: Diagrammatic representation of the model which includes shear deformation

Derivation of the Model

The major advantage in ignoring shear deformation in the previous section is that the deflections y_n of the centre of block n can be expressed as a function of the rotations of each block using equation 4.36. Figure 4.6 shows the additional shear springs included in the model of a beam, which give rise to additional deflections, δ_n. There are no shear springs at the supports so δ_1 and δ_{N+1} are zero.

Due to the deformation of the shear springs, it is now not possible to express the block deflections only in terms of the rotations of each block as the δ deflection values are also needed. This means that the number of degrees of freedom has increased from N to $2N-1$, i.e. there are now degrees of freedom δ_2 to δ_N in addition to the rotational degrees of freedom θ_1 to θ_N. It should be noted that there is one less shear degree of freedom than rotational degree of freedom as there are N blocks with $N-1$ joins between them.

The equations of motion for block n are the same as for the model with no shear distortions (equations 4.23 and 4.24), as is the equation using the rotational spring stiffness to give the moments from rotations at spring position n (equation 4.25). There is an additional set of equations relating extension of the shear springs with shear force for each spring position:

$$S_n = V_n \delta_n \tag{4.51}$$

type of unknown	number	type of equation	number
S	$N+1$	Vertical Equations of Motion	N
M	$N-1$	Rotational Equations of Motion	N
$\ddot{\theta}$	N	Equations for Rotational Springs	$N-1$
$\ddot{\delta}$	$N-1$	Equations for Shear Springs	$N-1$
$\ddot{y}$	N	Compatibility of Displacements ($y = f(\theta, \delta)$)	N
θ	N	Compatibility of Accelerations ($\ddot{y} = f(\ddot{\theta}, \ddot{\delta})$)	N
		Boundary Condition	1

Table 4.2: Numbers of equations and unknowns

where V_n is the stiffness of the shear spring (equation 4.10). Equation 4.26 relating deflection to block rotations and the equation relating accelerations (equation 4.27) must be modified to take into account the shear deflections. They become:

$$y_n = y_{n-1} + \frac{l_{n-1}}{2}\theta_{n-1} + \frac{l_n}{2}\theta_n + \delta_n \tag{4.52}$$

$$\ddot{y}_n = \ddot{y}_{n-1} + \frac{l_{n-1}}{2}\ddot{\theta}_{n-1} + \frac{l_n}{2}\ddot{\theta}_n + \ddot{\delta}_n \tag{4.53}$$

Finally the boundary condition that one end of the beam may not move relative to the other (equation 4.28) must be altered to include shear deflections:

$$\sum_{n=1}^{N} l_n\theta_n + \sum_{n=2}^{N} \delta_n = 0 \tag{4.54}$$

As before these equations are used in a time-stepping routine. To do this it is necessary to calculate the accelerations of the $2N-1$ degrees of freedom given the displacements of those degrees of freedom. It was chosen to take the displacements of the block centres $(y_1, \ldots, y_N)$ and the shear displacements $(\delta_2, \ldots, \delta_N)$ to be the degrees of freedom, although it would have been equally valid to use the rotations of the block centres $(\theta_1, \ldots, \theta_N)$ and shear displacements instead. The difficulty in using these equations to find the $\ddot{y}$ and $\ddot{\delta}$ values, if values for y and δ are known, is that there are both varying numbers of the different sets of equations and of different sets of unknowns, as shown in table 4.2.

The easiest way to solve this problem is to express the equations in matrix form with vectors of values of unknowns 2 to N and additional vectors of the other unknowns

S_1, S_{N+1}, $\ddot{\theta_1}$, $\ddot{y_1}$ and θ_1. Where there are more than $N-1$ equations in a set then the additional equations must be expressed separately. This approach ensures that all the matrices are invertible and so allows the equations to be manipulated easily. As with the previous model, the last step before calculating the accelerations is to eliminate a final unknown, this time the shear force S_{N+1}, using the boundary condition.

The derivation shown here is again for the case where there are only four blocks in the model. Firstly, the linear equations of motion for blocks two to four may be expressed in matrix form:

$$\begin{pmatrix} m_2 & 0 & 0 \\ 0 & m_3 & 0 \\ 0 & 0 & m_4 \end{pmatrix} \begin{pmatrix} \ddot{y}_2 \\ \ddot{y}_3 \\ \ddot{y}_4 \end{pmatrix} = \begin{pmatrix} -1 & 1 & 0 \\ 0 & -1 & 1 \\ 0 & 0 & -1 \end{pmatrix} \begin{pmatrix} S_2 \\ S_3 \\ S_4 \end{pmatrix} + \begin{pmatrix} 0 \\ 0 \\ 1 \end{pmatrix} S_5 \tag{4.55}$$

$$\mathbf{m}'\{\ddot{y'}\} = \mathbf{A}'\{S'\} + \{a'\}S_5 \tag{4.56}$$

where the prime notation is used to distinguish the vectors and matrices shown here from those used in the model excluding shear distortions, and the equation of motion for block 1 is written separately:

$$m_1\ddot{y}_1 = S_2 - S_1 \tag{4.57}$$

Similarly, the rotational equations of motion are expressed as:

$$\begin{pmatrix} J_2 & 0 & 0 \\ 0 & J_3 & 0 \\ 0 & 0 & J_4 \end{pmatrix} \begin{pmatrix} \ddot{\theta}_2 \\ \ddot{\theta}_3 \\ \ddot{\theta}_4 \end{pmatrix} = \begin{pmatrix} -1 & 1 & 0 \\ 0 & -1 & 1 \\ 0 & 0 & -1 \end{pmatrix} \begin{pmatrix} M_2 \\ M_3 \\ M_4 \end{pmatrix} + \frac{l_4}{2} \begin{pmatrix} 0 \\ 0 \\ 1 \end{pmatrix} S_5 + \frac{1}{2} \begin{pmatrix} l_2 & 0 & 0 \\ 0 & l_3 & 0 \\ 0 & 0 & l_4 \end{pmatrix} \begin{pmatrix} 1 & 1 & 0 \\ 0 & 1 & 1 \\ 0 & 0 & 1 \end{pmatrix} \begin{pmatrix} S_2 \\ S_3 \\ S_4 \end{pmatrix} \tag{4.58}$$

$$\mathbf{J}'\{\ddot{\theta'}\} = \mathbf{A}'\{M'\} + \frac{l_4}{2}\{a'\}S_5 + \frac{1}{2}\mathbf{L}'\mathbf{B}'\{S'\} \tag{4.59}$$

and for block 1:

$$J_1\ddot{\theta}_1 = M_2 + \frac{l_1}{2}(S_1 + S_2) \tag{4.60}$$

There are only $N-1$ rotational spring equations, so they may be written as matrix equations without the need for an additional equation:

$$\begin{pmatrix} M_2 \\ M_3 \\ M_4 \end{pmatrix} = \begin{pmatrix} K_2 & 0 & 0 \\ 0 & K_3 & 0 \\ 0 & 0 & K_4 \end{pmatrix} \begin{pmatrix} 1 & 0 & 0 \\ -1 & 1 & 0 \\ 0 & -1 & 1 \end{pmatrix} \begin{pmatrix} \theta_2 \\ \theta_3 \\ \theta_4 \end{pmatrix} - K_2 \begin{pmatrix} 1 \\ 0 \\ 0 \end{pmatrix} \theta_1 \tag{4.61}$$

$$\{M'\} = \mathbf{K'C'}\{\theta'\} - K_2\{b'\}\theta_1 \tag{4.62}$$

and similarly for the linear spring equations:

$$\begin{pmatrix} S_2 \\ S_3 \\ S_4 \end{pmatrix} = \begin{pmatrix} V_2 & 0 & 0 \\ 0 & V_3 & 0 \\ 0 & 0 & V_4 \end{pmatrix} \begin{pmatrix} \delta_2 \\ \delta_3 \\ \delta_4 \end{pmatrix} \tag{4.63}$$

$$\{S'\} = \mathbf{V'}\{\delta'\} \tag{4.64}$$

The compatibility equation may be written in matrix form:

$$\begin{pmatrix} 1 & 0 & 0 \\ -1 & 1 & 0 \\ 0 & -1 & 1 \end{pmatrix} \begin{pmatrix} y_2 \\ y_3 \\ y_4 \end{pmatrix} = \frac{1}{2} \begin{pmatrix} 1 & 0 & 0 \\ 1 & 1 & 0 \\ 0 & 1 & 1 \end{pmatrix} \begin{pmatrix} l_2 & 0 & 0 \\ 0 & l_3 & 0 \\ 0 & 0 & l_4 \end{pmatrix} \begin{pmatrix} \theta_2 \\ \theta_3 \\ \theta_4 \end{pmatrix} + \begin{pmatrix} \delta_2 \\ \delta_3 \\ \delta_4 \end{pmatrix} + 2 \begin{pmatrix} 1 \\ 0 \\ 0 \end{pmatrix} y_1 \tag{4.65}$$

$$\mathbf{C'}\{y'\} = \frac{1}{2}\mathbf{D'L'}\{\theta'\} + \{\delta'\} + 2\{b'\}y_1 \tag{4.66}$$

with an additional equation for block 1:

$$y_1 = \frac{l_1}{2}\theta_1 \tag{4.67}$$

Finally, the boundary condition may be written as:

$$l_1\theta_1 + \begin{pmatrix} 1 & 1 & 1 \end{pmatrix} \begin{pmatrix} l_2 & 0 & 0 \\ 0 & l_3 & 0 \\ 0 & 0 & l_4 \end{pmatrix} \begin{pmatrix} \theta_2 \\ \theta_3 \\ \theta_4 \end{pmatrix} + \begin{pmatrix} 1 & 1 & 1 \end{pmatrix} \begin{pmatrix} \delta_2 \\ \delta_3 \\ \delta_4 \end{pmatrix} = 0 \tag{4.68}$$

$$l_1\theta_1 + \{c'\}^T\mathbf{L'}\{\theta'\} + \{c'\}^T\{\delta'\} = 0 \tag{4.69}$$

As stated earlier, there are $2N-1$ degrees of freedom (7 in this case), namely the displacements of the block centres $(y_1, \ldots, y_N)$ and the shear displacements $(\delta_2, \ldots, \delta_N)$.

For a time-stepping method, equations relating the accelerations of the degrees of freedom in terms of the displacements are required. The time-stepping method then predicts the displacements for the next time-point. There are five steps to calculating the accelerations from the displacements:

1. Calculate the rotations using the compatibility equations 4.66 and 4.67:

$$\theta_1 = \frac{2y_1}{l_1} \tag{4.70}$$

$$\{\theta'\} = 2\mathbf{L'}^{-1}\mathbf{D'}^{-1}(\mathbf{C'}\{y'\} - \{\delta'\} - 2\{b'\}y_1) \tag{4.71}$$

2. Calculate the bending moments and shear forces between the blocks using equations 4.62 and 4.64. Note that the shear forces at either end of the beam, S_1 and S_{N+1}, are still unknowns (M_1 and M_{N+1} are both zero as the beam is simply-supported).

3. Calculate the accelerations for block 1 using equations 4.57 and 4.60 and the compatibility equation 4.67, differentiated twice with respect to time. The shear force S_1 at the end of the beam may be eliminated giving:

$$\ddot{\theta}_1 = \frac{4(M_2 + l_1 S_2)}{4J_1 + m_1 l_1^2} \tag{4.72}$$

$$\ddot{y}_1 = \frac{l_1 \ddot{\theta}_1}{2} \tag{4.73}$$

4. Calculate the shear force at the end of the beam S_{N+1} using equations 4.56 and 4.59 and equations 4.66, 4.67 and 4.69 differentiated twice with respect to time:

$$S_5 = \frac{1}{m_4 l_4^2 + 4J_4}\left(2m_4 l_4 M_4 + (4J_4 - m_4 l_4^2)S_4\right) \tag{4.74}$$

5. Calculate the accelerations using equations 4.56, 4.59 and 4.66 differentiated twice with respect to time, and the shear force S_{N+1}:

$$\{\ddot{\theta'}\} = \mathbf{J'}^{-1}\left(\mathbf{A'}\{M'\} + \frac{1}{2}\mathbf{L'B'}\{S'\} + \frac{l_4}{2}\{a'\}S_5\right) \tag{4.75}$$

$$\{\ddot{y'}\} = \mathbf{m}^{-1}\left(\mathbf{A'}\{S'\} + \{a'\}S_5\right) \tag{4.76}$$

$$\{\ddot{\delta'}\} = \mathbf{C'}\{\ddot{y'}\} - \frac{1}{2}\mathbf{D'L'}\{\ddot{\theta'}\} - 2\{b'\}\ddot{y}_1 \tag{4.77}$$

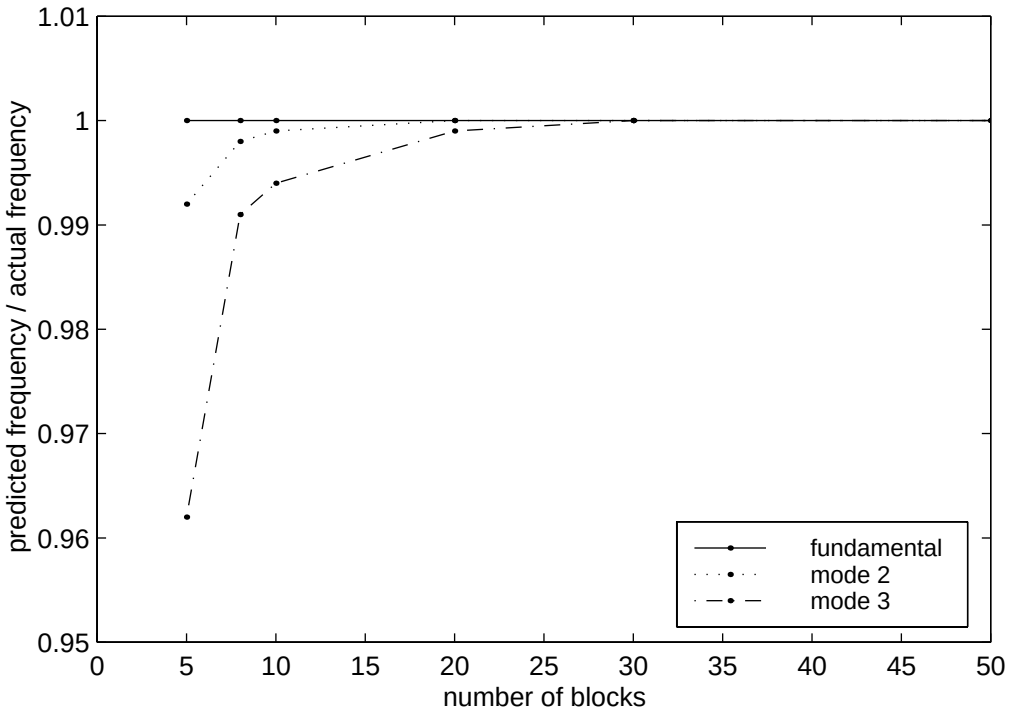

Figure 4.7: Frequencies predicted by the model including shear deformation for varying numbers of blocks (depth to length ratio= 0.127, normalised using ω_{ci}, the natural frequency including shear deformation and rotational inertia)

Checking the Validity of the Model

As with the model excluding shear deformation, it is possible to check the validity of the model for a range of numbers of blocks using the continuous equation of motion and the sinusoidal expected mode shapes [113]. For a beam of rectangular cross-section with uniform material properties, a depth to length ratio of 0.127 and $E/kG = 3$, figure 4.7 shows the variation of the predicted frequency with number of blocks. Figure 4.8 shows the same relationship for a beam with a depth to length ratio of 0.1. The figures show very good agreement between the model and the expected frequency values if more than 20 blocks are used.

For the case where the depth to length ratio is 0.1, the mode shapes for the first three modes were calculated. These are plotted for 8, 10 and 20 blocks in figures 4.9, 4.10 and 4.11 respectively. The mode shapes are plotted in the form of the actual block positions, the centres of which are marked with dots. The vertical gaps between the

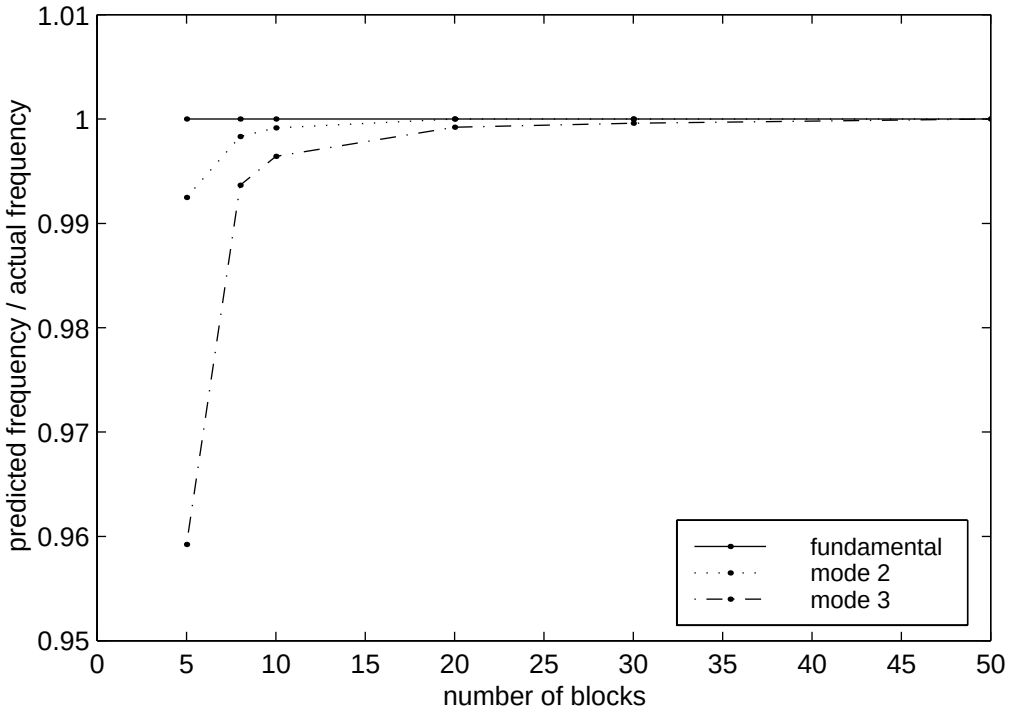

Figure 4.8: Frequencies predicted by the model including shear deformation for varying numbers of blocks (depth to length ratio= 0.1, normalised using ω_{ci}, the natural frequency including shear deformation and rotational inertia)

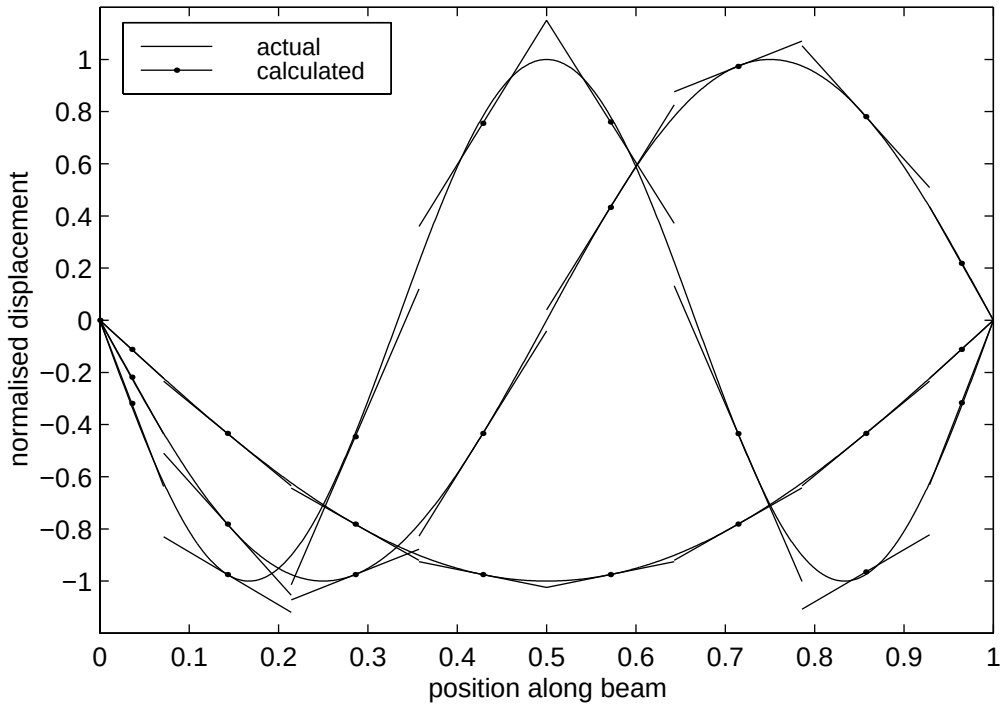

Figure 4.9: Mode shapes calculated using the model including shear deformation with 8 blocks (depth to length ratio= 0.1)

ends of the blocks are due to the deformation of the shear springs. The true sinusoidal mode shapes are also plotted for comparison.

Rather than substituting an equation for the sinusoidal mode shape into the continuous equation of motion to find the natural frequencies, it is also possible to solve the equation for the natural frequencies numerically without using the mode shapes, although this is limited to linear vibrations. This has been done by Chen [17], who considered the vibration of a simply-supported tapered cylinder. When the taper is zero, the results from this numerical solution may be compared to the results of substituting the sinusoidal mode shape into the continuous equation of motion and to the results using the model. If the ratio of the radius of the cylinder to the length is taken to be 0.1 and the value $E/kG = 2.93$ used by Chen [17] is taken, then results using the numerical method agree well with the results using the sinusoidal mode shapes, confirming that the mode shape used in the substitution is the correct one. The agreement with the block model is also good, with less than 0.1% error in the prediction of the frequencies

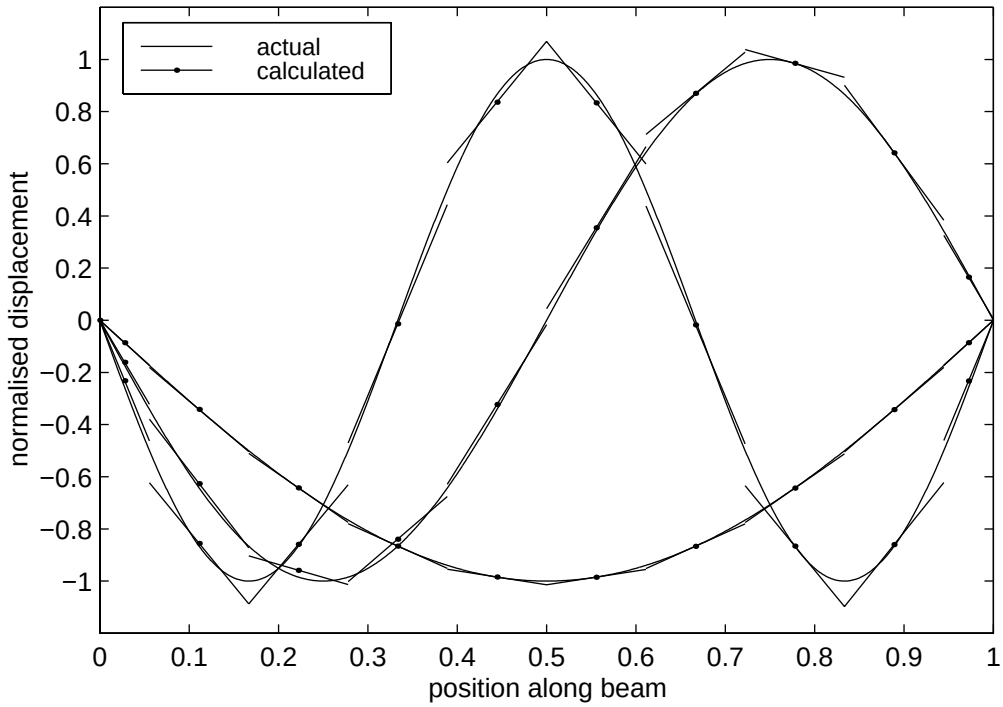

Figure 4.10: Mode shapes calculated using the model including shear deformation with 10 blocks (depth to length ratio= 0.1)

of the first five modes if 50 blocks are used and an error of only 1.2% if 20 blocks are used.

For the case where the taper is non-zero, the mode shapes are not sinusoidal. If the radius of the beam at one end is twice the radius at the other end and the ratio between the radius at the thinner end and the length of the beam is 0.1, the agreement between the numerical method and the block model is good with the error in the first four modes being less than 0.3% with 30 blocks. Figure 4.12 shows the first four mode shapes calculated using the model with 30 blocks. It should be noted that the numerical method of solving the equation of motion proposed by Chen [17] is incapable of including any non-linear damage as the method requires an expression for the stiffness which is independent of time.

These tests show that the block model is an accurate predictor of the behaviour of a simply-supported beam subject to free vibration.

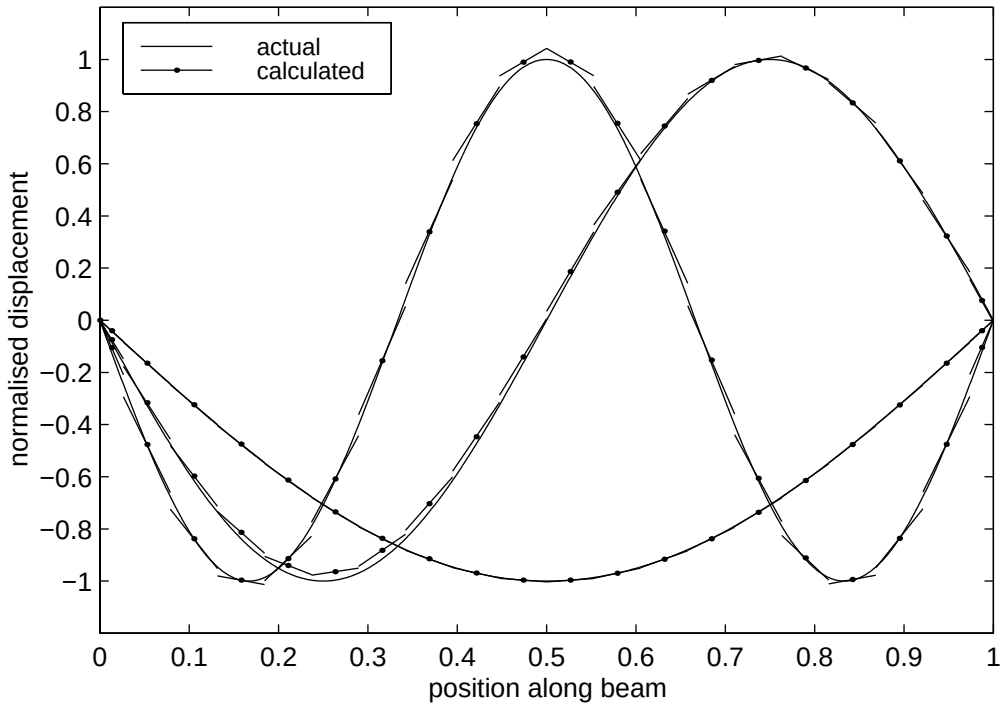

Figure 4.11: Mode shapes calculated using the model including shear deformation with 20 blocks (depth to length ratio= 0.1)

4.2 Modelling Non-Linear Damage

The model has been shown to predict to a high degree of accuracy the frequencies and mode shapes of an undamaged beam when compared to theoretical values. Now it is used to predict the behaviour of a beam with a non-linear element which is then compared to experimental results.

4.2.1 Experimental Set-up

One end of an aluminium bar was clamped tightly to a rigid base to form a cantilever. The bar was 25 mm wide and 6.4 mm deep and the length of the cantilever was 0.5 m. Close to the root, a non-linear section of beam was created by bonding, using Araldite Precision glue, two blocks onto the beam with a bolt protruding out of one and almost in contact with the other (as shown in figure 4.13), so that when the beam bends the blocks move closer together and the bolt comes into contact with the second block, increasing the stiffness of that region of the beam. The curvature at which contact occurs was

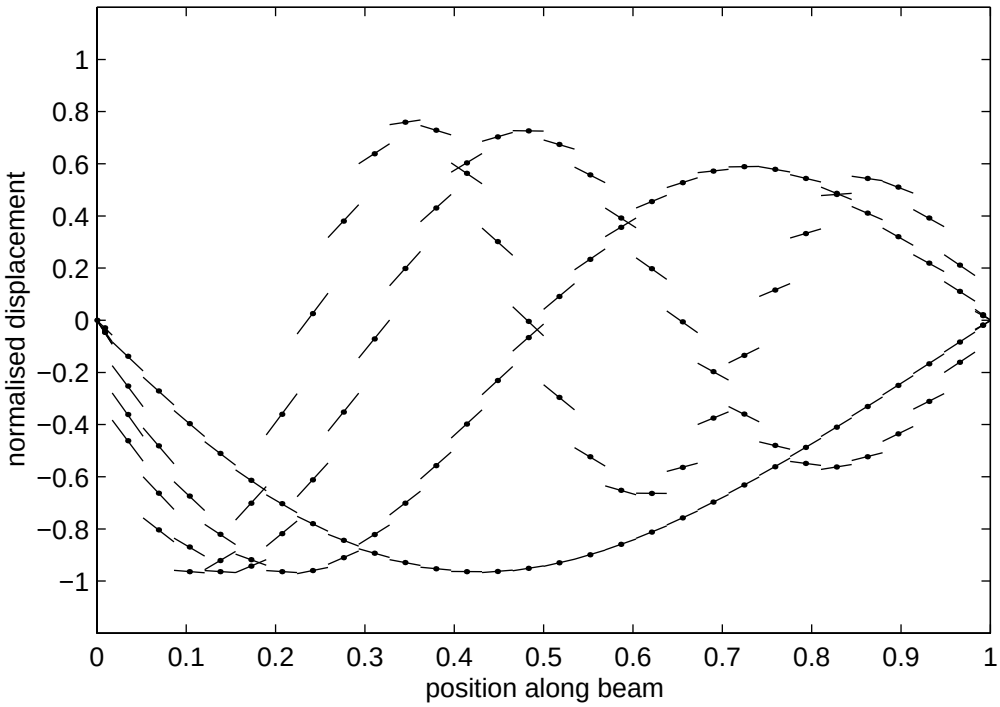

Figure 4.12: Mode shapes for a tapered cylindrical beam calculated using the model including shear deformation with 30 blocks

adjusted using the bolt. One of the blocks was electrically isolated from the beam so that a voltage signal could be generated indicating when contact has occurred.

The non-linear element was attached in a position which corresponded to spring position 2 in a 10 block model (the numbering system started at the root) and affected the stiffness over one block length. An 21 g accelerometer was attached to the cantilever at the mid-point of block 2. The cantilever was given an initial tip deflection of 15.5 mm and then released. The accelerometer output and the voltage across the blocks were recorded for 10 s at a sampling frequency of 8192 Hz per channel.

4.2.2 Model Set-up

For a cantilever beam, it is necessary to adjust the model to account for the different boundary conditions. As the beam is fixed at one end, the rotation and hence displacement of the half-length block at the end are always zero, since the deflection of the first beam element is represented by the rotational and shear springs positioned

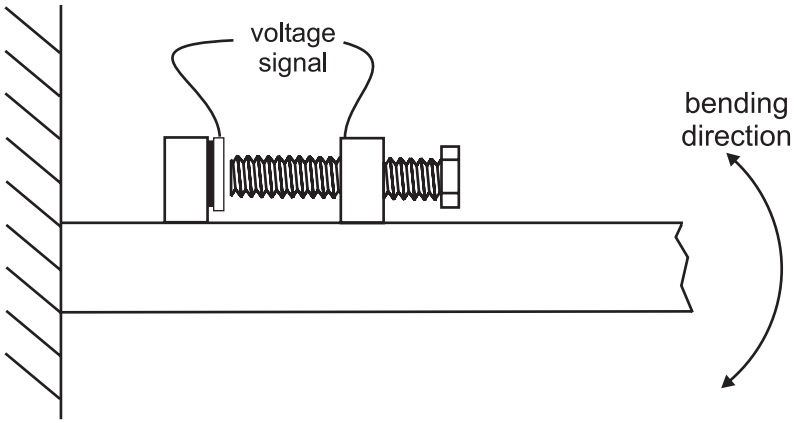

Figure 4.13: The non-linear stiffening beam element

between the first and second rigid blocks. The boundary condition used previously is no longer true as it ensured that the relative displacement of the ends of the beam remained zero. Instead the shear force at the free end of the beam is now zero. With these new conditions, the derivation of the model proceeds along much the same lines as for the simply-supported beam. To model the non-linearity, the rotation of the spring at position 2 was checked at each time-point and if it exceeded a threshold value $\Delta\theta_{th}$ the stiffness of the spring used for subsequent time-steps was increased by a factor β, so the moment curvature equation for the spring was:

$$M_2 = K_2\left(\beta(\theta_2 - \theta_1) - (\beta - 1)\Delta\theta_{th}\right) \tag{4.78}$$

until the rotation was found to be less than the threshold value.

In addition to the springs representing the beam compliance, damping was added at the spring positions in the form of rotational dash-pots (damping due to shear deformation was ignored as the effect of shear deformation is small for the slender beam). This was included by modifying equation 4.62 to:

$$\{M'\} = \mathbf{K'C'}\{\theta'\} - K_2\{b'\}\theta_1 + \mathbf{P'C'}\{\dot{\theta'}\} - P\{b'\}\dot{\theta}_1 \tag{4.79}$$

where $\mathbf{P'}$ is the dash-pot coefficient P multiplied by the identity matrix.

The model beam was excited using the theoretical statically-deformed shape (assuming no shear distortions) due to a load at the tip sufficient to deflect the tip by 15.5 mm. A 10 block model implemented in Matlab with a fourth-order Runge-Kutta

routine was run for a 5 s time period with a time increment between steps of 1×10^{-5} s, taking approximately 2.5 hours on a 200 MHz PC with a Pentium Pro processor. The rotational inertia of the bolt assembly was ignored as the assembly was close to the root of the cantilever and the cantilever was slender so rotational inertia effects are small.

4.2.3 Processing Data from either the Model or the Beam

Data were generated for the acceleration at position 2 and the voltage signal (indicating whether the element is open or shut) for both the beam and the model. From these data three types of graph may be plotted.

Firstly, a time-frequency graph may be calculated for the first mode. This was done using the modified exponential joint time-frequency distribution (see section 3.8.2 or Zheng and McFadden [117]). Zero padding was used to improve the frequency resolution (see section 3.2.3).

Secondly, the acceleration envelope for the first mode can be calculated. This was done by applying an ideal low-pass filter to the analytic version of the signal (see section 3.4) in the frequency domain and then using the inverse Fourier transform to calculate the low frequency acceleration envelope.

Thirdly, the proportion of time the non-linear element was closed may be calculated, using the voltage signal across the blocks of the element, by setting a suitable threshold below which the blocks are in contact and the element was considered shut.

4.2.4 Comparison between the Model and the Beam

Several unknowns must be established by fitting the model results to the beam results, namely the Young's modulus, the damping coefficient, the stiffening factor β for the non-linear element and the threshold curvature $\Delta\theta_{th}$ at which the non-linear element becomes stiffer.

Initially, a linear oscillation of the beam was recorded and the Young's modulus and the damping (dash-pot coefficient P) values in the model were adjusted, so that the first natural frequency and the decay envelope of the acceleration of the first mode were equal in the model and the beam. Values of $E = 76.6$ GPa and $P = 0.046$ Nms were

found to give the best fit. The effect of shear deflection is only slight, so a value of $E/kG = 3$ was used. The model over-predicted the acceleration by about 3%.

A second linear test was used to set the stiffening parameter β. In this test the bolt was tightened onto the block, so ensuring that for small amplitudes the mechanism remained in the closed position for the whole cycle. The stiffness of the spring nearest the root in the model was then adjusted so that the frequency of the time signal generated in the model matched the experimental frequency. β was then simply the ratio of that stiffness to the stiffness when the bolt was not in contact. The value $\beta = 2.0$ was found to be optimal.

Both the voltage across the non-linear element and the acceleration at block position 2 were then recorded for the non-linear test. The gap between the bolt and the block was set to 0.025 mm. The threshold rotation value was set so that the initial percentage of each cycle the non-linear element was open was the same in the beam and the model. The value $\Delta\theta_{th} = 0.004$ rads was used.

Three experimental tests were used here. Two were non-linear tests (s50 and s51) conducted under identical conditions. The third test (s52) was a linear test (the bolt in the non-linear element was retracted so the bolts never came in contact). The non-linear tests are compared to the model's simulation (run 15). Figure 4.14 shows the time-frequency plot for experimental tests s50 and s51 (the frequencies being normalised using the linear test s52), and the model run 15 using the values of β and $\Delta\theta_{th}$ stated above. The fundamental frequency was approximatly 21 Hz. Linear tests where the bolt does not come in contact with the block during the oscillation are referred to as baseline tests. Figure 4.15 compares the acceleration envelopes for the first mode for all four tests, the experimental non-linear tests s50 and s51, the baseline linear test s52, and the model run 15. Figure 4.16 is a plot of the percentage of each cycle for which the element was open against the time at which that cycle occurs. The spikes in the experimental data in this figure are due to bouncing of the bolt against the block as the element closes. The figures show good agreement between the model and the experimental test. The agreement is expected to be very good at the beginning of figure 4.16 as this was ensured when selecting the $\Delta\theta_{th}$ value. However the model also agrees well with the experimental data for the rest of the oscillations, demonstrating its ability to model

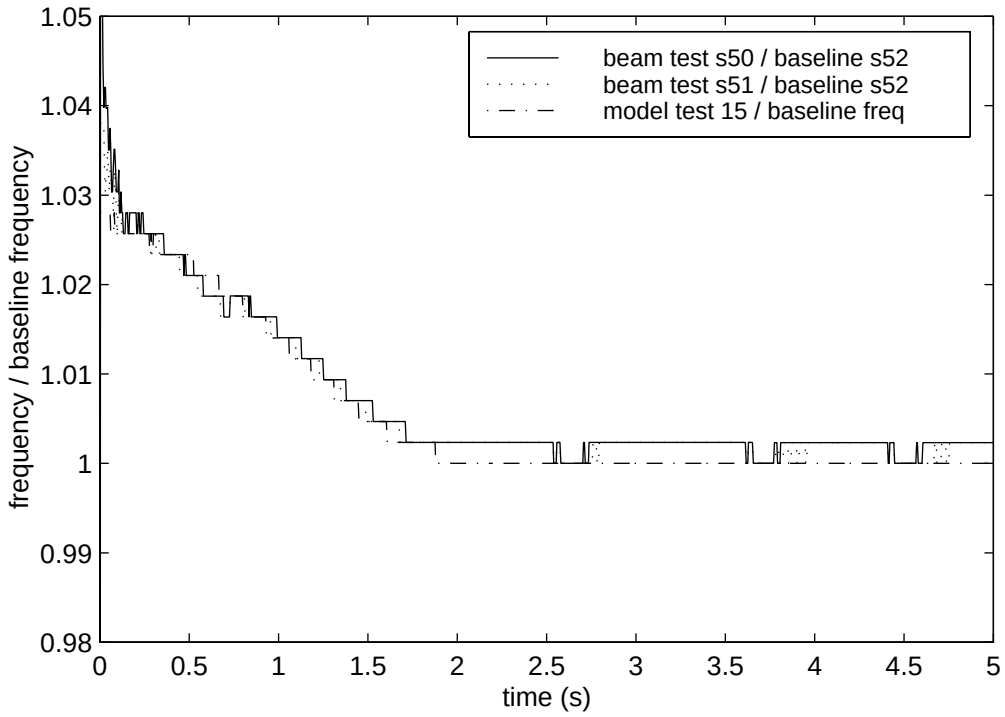

Figure 4.14: Time-frequency plots for the vibration of the cantilever

non-linear mechanisms.

4.3 Summary

In this chapter a time-stepping model of a transversely vibrating simply-supported beam has been proposed. It is based on the idea that the mass and inertia of the beam may be approximated by point masses and inertias at discrete points, and shear distortion and bending stiffness may be represented using rotational and transverse springs between rigid blocks. Two models were devised, firstly a simple one ignoring shear distortion (and hence the linear springs) and then one including the shear distortion. For the model including shear distortion, the natural frequencies and mode shapes for the first three modes, derived from acceleration data generated using the model, compared well to theoretical values with less than a 0.1% error if 20 or more blocks were used and only a 0.6% error when a 10 block representation was used.

The advantage of this method over other methods of modelling cracked vibrating beams is that it is capable of modelling breathing cracks without the assumption that

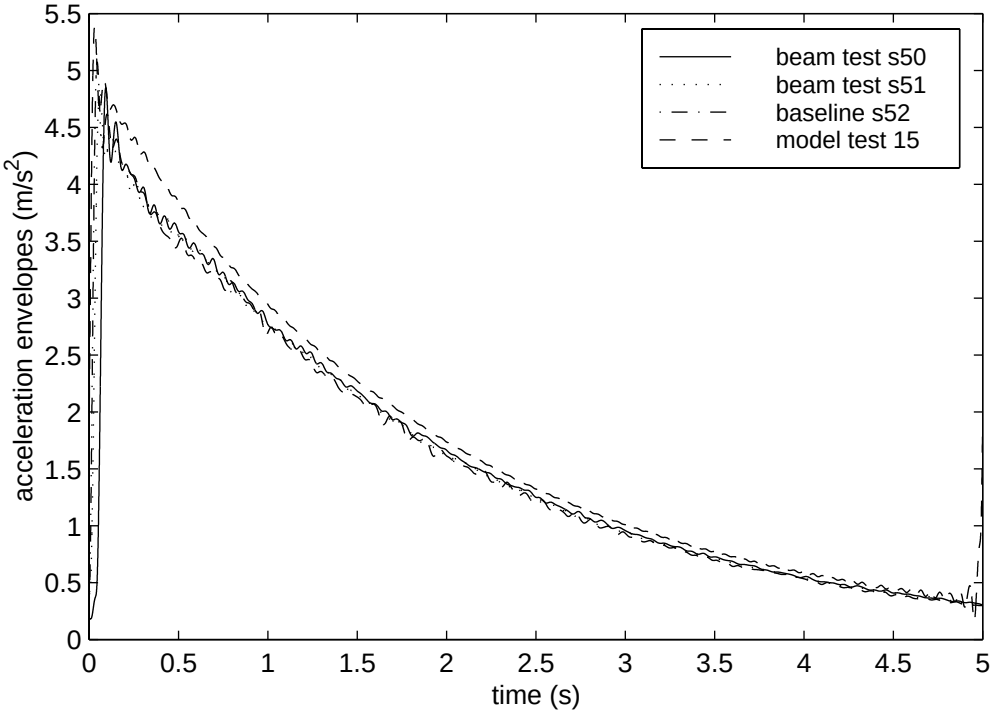

Figure 4.15: Fundamental mode acceleration envelopes for the vibration of the cantilever

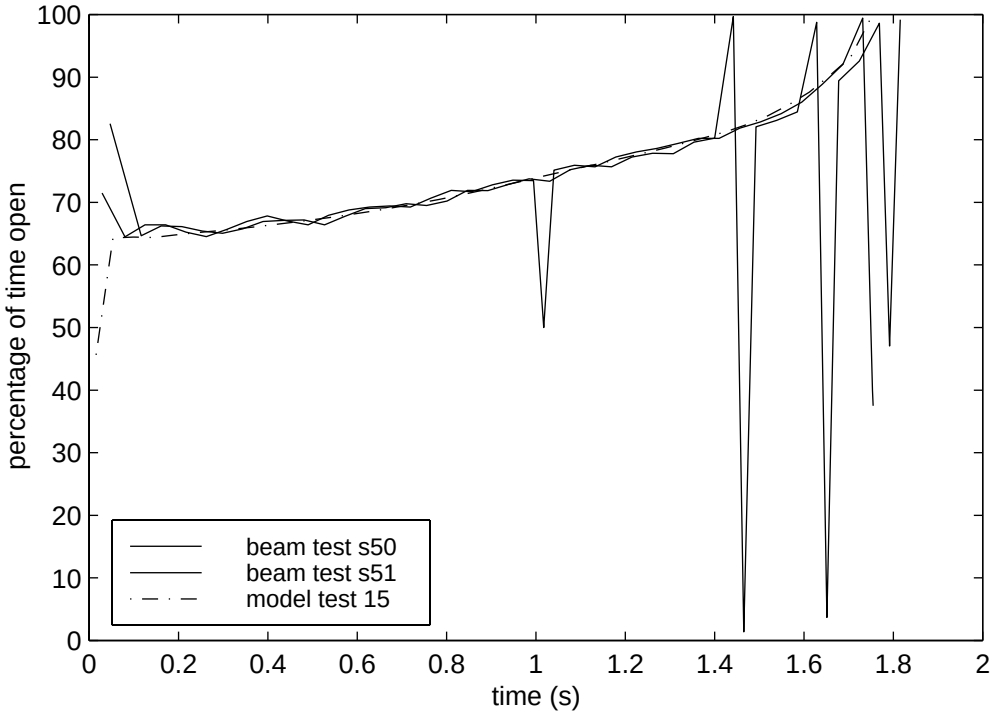

Figure 4.16: Plots of percentage of time the non-linear mechanism remained open during the vibration of the cantilever

the vibration is dominated by the fundamental mode and so the crack compliance will cycle at the same frequency. Non-linear damage is modelled by altering the spring stiffness at each time-step depending on the curvature of the beam at that time. The model's capabilities of predicting the non-linear behaviour have been demonstrated using a cantilever beam with a non-linear element which resulted in a localised stiffening of the beam when the curvature exceeded a threshold value [68].

Chapter 5

Non-Linear Mechanisms

In this chapter some possible non-linear crack mechanisms are considered. The likelihood of these mechanisms contributing to the non-linear behaviour of concrete beams during vibration tests is discussed in chapter 9 using the experimental results from the tests described in chapter 7. Firstly, however, there is a brief description of the methods of detecting non-linear damage.

5.1 Detection of Non-Linearities

For completeness it is necessary to examine how non-linearities may be detected. The literature review indicated three main methods of doing this, which involved either super-harmonics or examining how the frequency changes with the amplitude of oscillation (see section 2.2.2).

As stated in section 2.4, impact excitation tests were selected for the experimental work presented here. Since the oscillation decays during the test, an examination of the change of frequency with time (which may be related to amplitude of oscillation) will be conducted to detect any non-linearities. The time-frequency relationship will be estimated using one of the distributions described in chapter 3 and then converted to an amplitude-frequency relationship.

This method of studying the amplitude-frequency relationship can also be used on forced vibration tests by employing a sine sweep over a small frequency range spanning the natural frequency of interest. If this is repeated at many amplitudes, an

amplitude-frequency relationship may be found (see, for example, Van Den Abeele and Visscher [111]).

The third method of detecting non-linearities is to examine the super-harmonics of the vibration signal (see, for example, Bovsunovsky and Matveev [9] or Pugno *et al.* [87]). If a forced vibration test for a linear system with a forcing frequency equal to a natural frequency is considered, the expected response is a sinusoid at the forcing frequency. The effect of a slight non-linearity in the system will be that, when excited at a natural frequency, the repeating frequency will remain the same as the forcing frequency, but the shape of the response will not be a pure sinusoid. This distortion of the response may be assessed by examining the Fourier series of the repeating signal. The higher frequency terms (all integer multiples of the natural frequency) are termed super-harmonics. As the non-linearity of the system increases the magnitude of these super-harmonics will rise indicating an increase in the distortion of the sinusoidal response. This method can also be applied to an impact excitation test. However, since the non-linearity will affect the natural frequency as the vibration decays away, averaging over many cycles is not possible. Also, since the impact test will excite many modes, the results may be more difficult to interpret.

To demonstrate the methods discussed above, consider a single degree of freedom model consisting of a mass connected to a fixed point via a non-linear spring. The spring behaves in a bilinear fashion, becoming stiffer at a certain displacement and may be considered as a combination of two linear springs as shown in figure 5.1. This is the simplest version of the type of non-linear mechanism used when considering fatigue cracks in steel beams. At a certain displacement of the beam, the crack closes and hence the stiffness increases (see section 2.2.1). From figure 5.1 it can be seen that when the displacement is less than a (region 1) the motion is linear and governed by the equation:

$$m\ddot{x} + k_1 x = 0 \tag{5.1}$$

However, once the displacement exceeds a (region 2), the second spring affects the vibration and the equation of motion is given by:

$$m\ddot{x} + k_2 x + a(k_1 - k_2) = 0 \tag{5.2}$$

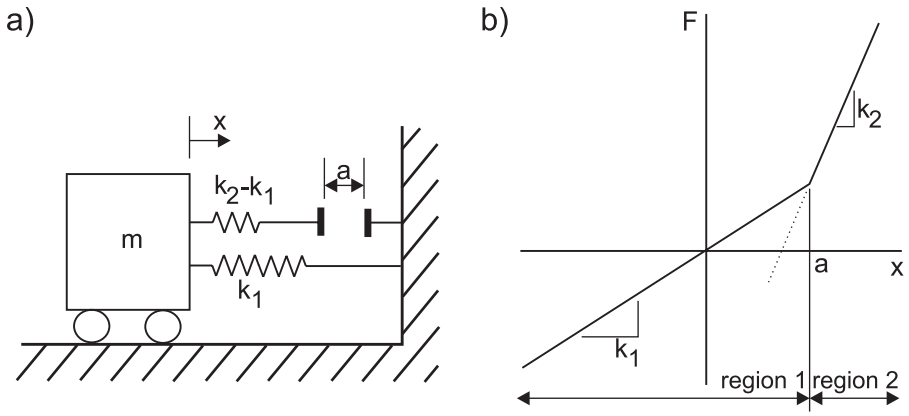

Figure 5.1: Axial representation of the bilinear system: a) a schematic and b) the force-displacement relationship

The general solution to both these equations takes the form:

$$x = C\cos\left(\sqrt{\frac{k}{m}}t + \phi\right) - \frac{K}{k} \tag{5.3}$$

where $K = 0$ and $k = k_1$ for $x \leq a$ and $K = a(k_1 - k_2)$ and $k = k_2$ for $x > a$. The value of C and ϕ change every time the motion crosses $x = a$ and may be found by equating the displacement and velocity at the change between the two regions. It should be noted that, since the spring forces exerted on the block at points just before and just after $x = a$ are the same, the acceleration either side is equated once the velocity and displacements are equated.

Initially the mass is displaced by $x = -\alpha a$ and released. The block is in region 1, where the spring is in its less-stiff state. The spring stiffness is k_1 and the displacement is governed by the equation:

$$\hat{x} = -\alpha\cos\left(2\pi\hat{t}\right) \tag{5.4}$$

where $\hat{x}$ is a dimensionless displacement, $\hat{x} = x/a$, and $\hat{t}$ is the dimensionless time variable, $\hat{t} = w_1 t/(2\pi)$, where w_1 is the angular frequency if the oscillation remains solely in region 1, i.e. $w_1 = \sqrt{k_1/m}$.

At the point $x = a$ the block moves into region 2, where the spring is in its stiffer state. This occurs at dimensionless time, $\hat{t}_a$, given by:

$$\hat{t}_a = \frac{1}{2\pi}\cos^{-1}\left(-\frac{1}{\alpha}\right) \tag{5.5}$$

Defining $t_2 = t - t_a$, then the equation for motion during the period $x > a$ is given by:

$$\hat{x} = C\cos\left(\sqrt{\frac{k_2}{k_1}}2\pi\hat{t}_2 + \phi\right) - \frac{k_1 - k_2}{k_2} \tag{5.6}$$

where $w_2 = \sqrt{k_2/m}$ and $\hat{t}_2 = w_1 t_2/(2\pi)$. The values of C and ϕ for this region may be found by equating the displacements and velocities at $t = t_a$ ($t_2 = 0$). The dimensionless amplitude of oscillation is:

$$C = \frac{k_1}{k_2}\sqrt{1 + \frac{k_2}{k_1}(\alpha^2 - 1)} \tag{5.7}$$

and the phase is:

$$\phi = \tan^{-1}\left(-\sqrt{\frac{k_2}{k_1}(\alpha^2 - 1)}\right) \tag{5.8}$$

The time at which the displacement in this region first reaches a maximum, (i.e. the first time the velocity is zero), is given by:

$$\hat{t}_{2m} = -\frac{\phi k_1}{2\pi k_2} \tag{5.9}$$

The frequency of the oscillation may then be written as:

$$f = \frac{1}{2(t_a + t_{2m})} \tag{5.10}$$

or in dimensionless form:

$$\hat{f} = \frac{1}{2(\hat{t}_a + \hat{t}_{2m})} \tag{5.11}$$

where $\hat{f} = f/f_1$ and f_1 is the frequency if the displacement remains less than a, i.e. $f_1 = w_1/(2\pi)$.

Using these equations the frequency for a range of initial amplitudes αa can be calculated, allowing the derivation of a amplitude-frequency relationship. Figure 5.2 shows this relationship for the case where $k_2/k_1 = 1.25$. The horizontal lines indicate the frequency when the amplitude of oscillation is less than a (i.e. $\alpha \leq 1$) and when $a = 0$ (i.e. as $\alpha \to \infty$). It should be noted that, if $a = 0$, the change in spring stiffness is at the origin and the frequency is not dependent on amplitude. In this special case, regardless of amplitude, during the period where the displacement is positive the frequency will be $\sqrt{k_2/m}$ and where the displacement is negative $\sqrt{k_1/m}$.

Figure 5.3 shows one cycle for the cases where $\alpha = 1$ (i.e. the system remains linear) and $\alpha = 20$ (a non-linear system). The time axis is non-dimensionalised using f_a, the

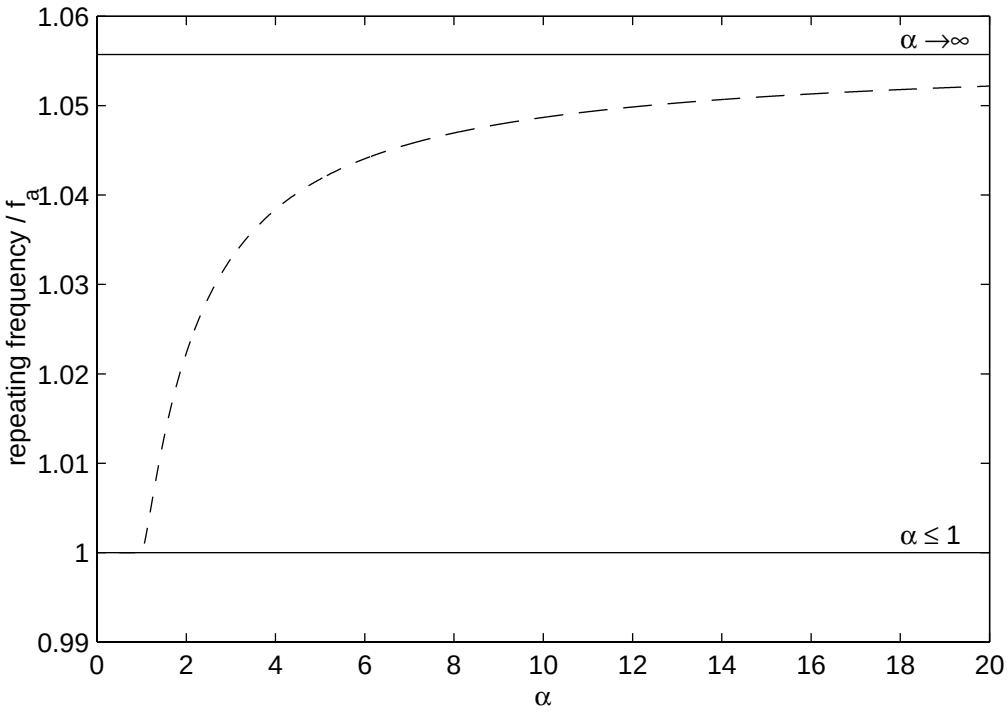

Figure 5.2: Amplitude-frequency relationship for a bilinear system

frequency if the system remains in the linear region, i.e. $\alpha \leq 1$. The frequency content of the cycle may be found using Fourier series analysis. Since the cycles were generated over a vector of time-points during one period, the discrete Fourier transform was used to transform into the frequency domain. This is the same as the discrete Fourier series provided no zero-padding is used. For a range of values of α, the amplitude of the Fourier series coefficients are plotted in Figure 5.4. The Fourier series were normalised using the amplitude of the repeating frequency. The Fourier series coefficients are a measure of how distorted the oscillation is compared to a sinusoid and the integer multiples of the repeating frequency are the super-harmonic frequencies. It is clear that in this particular example, apart from the mean of the signal, the variations in the magnitude of the super-harmonic components are small for increased amplitude of oscillation ($\alpha > 4$).

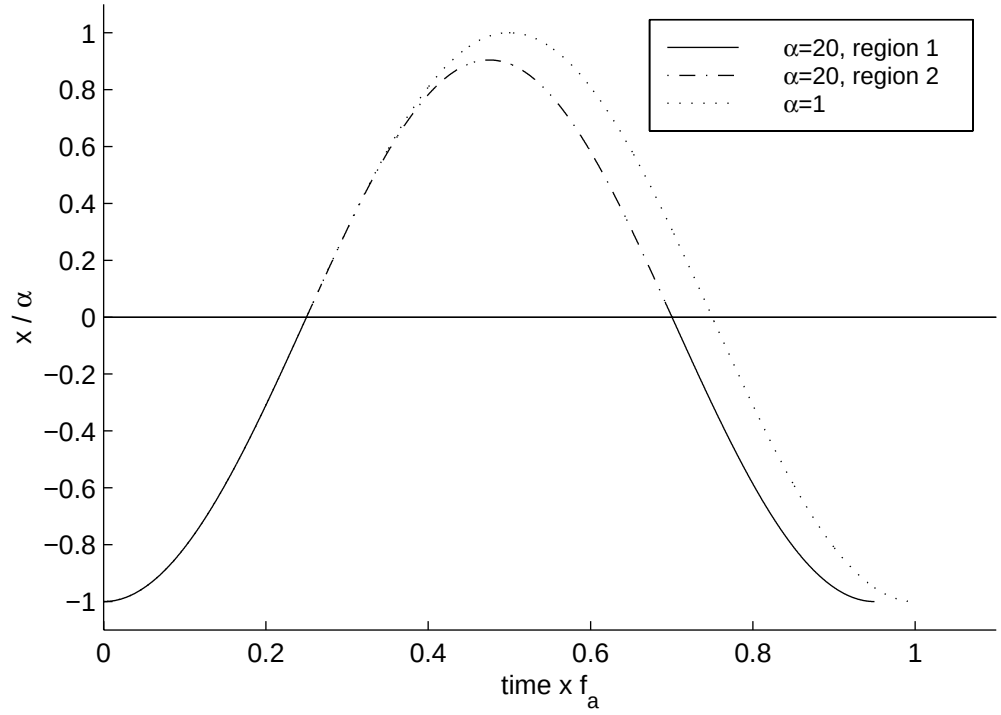

Figure 5.3: One cycle of oscillation of the single degree of freedom bilinear mechanism

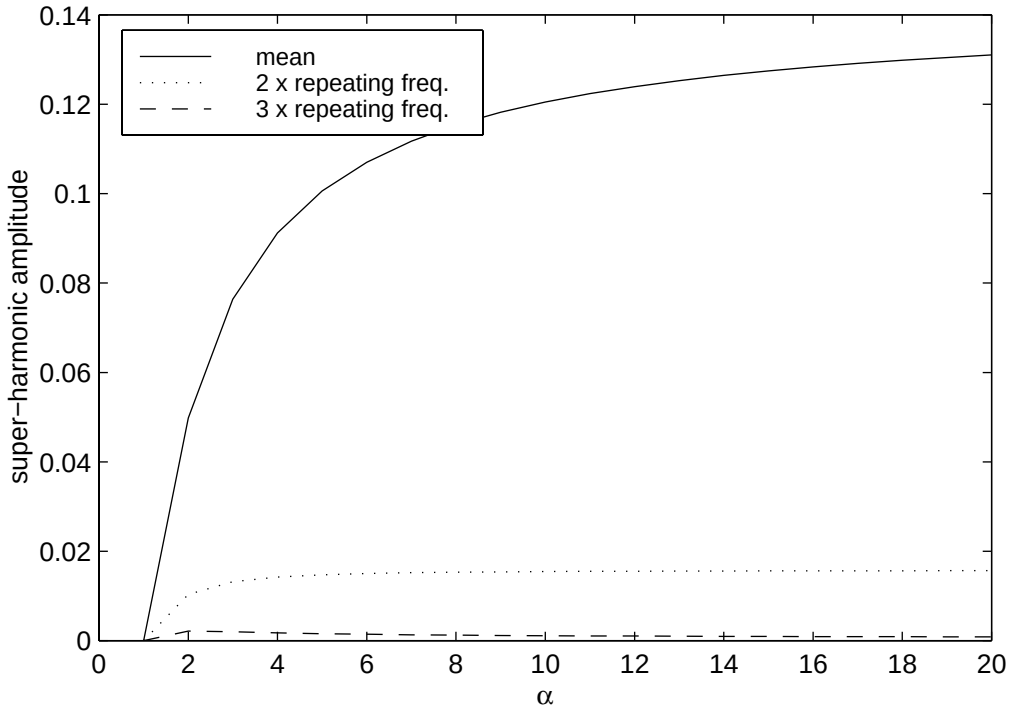

Figure 5.4: Super-harmonics of the repeating cycle for a range of α

5.2 Possible Non-Linear Mechanisms

Possible mechanisms which may cause non-linear vibration behaviour in cracked concrete beams are now discussed.

5.2.1 Crack Closure

Crack closure is usually thought of as a bilinear mechanism, that is as a spring which takes a different stiffness when its deflection exceeds a certain value. The simplest version of this mechanism was discussed in the previous section. A rotational version of this mechanism has been employed in the modelling of steel beams with fatigue cracks (see section 2.2.1). The fatigue crack is assumed to be either open or closed leading to a step change in stiffness. This means the crack stiffness takes only two values, an open value and a closed value. The position of the cross-over point is dependent on the self-weight of the beam. Some researchers (for example Ballo [6]) have assumed that the beam self-weight is small or that the beam is oriented vertically to ensure the cross-over point is at the origin. This significantly reduces the complexity of the model, since at every point the tangent to the stiffness on a force-displacement (or moment-rotation) plot goes through the origin (i.e. for the example in section 5.1, $K = 0$).

Even with fatigue cracks in metal beams, the approximation to a system where the crack is thought of as either open or closed has proved inaccurate and an intermediate stage has been suggested (see, for example, Kisa and Brandon [48]). In reinforced concrete the problem becomes more complex. Once a crack has been opened during damage loading, loose aggregate may prevent the crack from closing and the interaction between the steel and concrete must also be considered. If, at the crack, there is localised slip of the steel relative to the concrete during damage loading, it is possible that once unloaded a proportion of this relative slip will remain and the crack will stay open. In this scenario it is possible that the crack does not close during vibration as the stresses during the vibration are not great enough to overcome the residual slip. It is, therefore, unclear whether crack closure occurs in cracked concrete beams and if it does what the non-linear characteristic is.

The possibility of crack closure is discussed using experimental data in section 9.1.

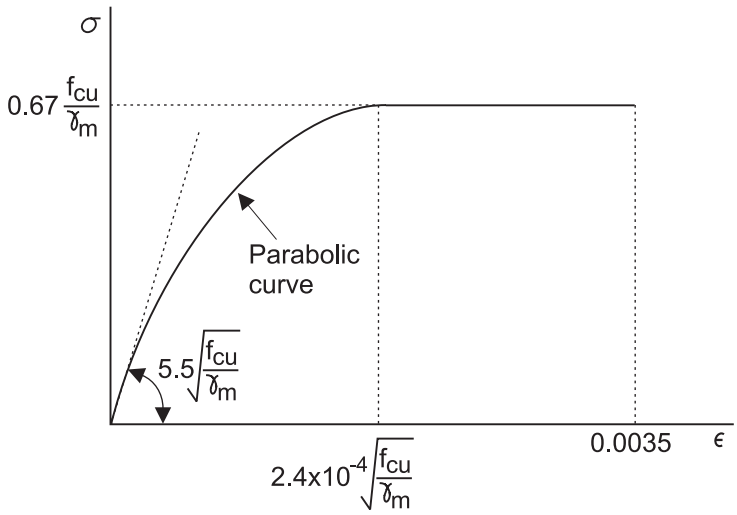

Figure 5.5: Stress-strain relationship for concrete (after [13])

5.2.2 Concrete in Compression

Concrete is a non-linear material in compression. When calculating the strength of concrete beams, the British Standard Code [13] states that the stress of concrete in compression may be thought of as initially being a parabolic function of strain followed by a region of constant stress with increasing strain before failure. This is shown in figure 5.5 where f_{cu} is the cube strength (in N/mm^2) and γ_m is the partial safety factor. When a beam has been damaged by a small overload, the concrete in compression will have behaved non-linearly but as the damage load has been removed the concrete will have returned to the approximately linear region (with stiffness $5.5\sqrt{f_{cu}/\gamma_m}$). During subsequent vibration tests, the amplitude of oscillation will be small in comparison to the deflection during overload and the concrete at the outer surface of the compression region is likely to remain in this approximately linear region. If the overload force is increased, the beam will not recover completely and the concrete may remain in compression. In this case, the concrete may not behave linearly during the vibration. However, it is likely that since the amplitude of vibration is small, the concrete stiffness curve over the stress range during vibration may be approximated very closely by a straight line.

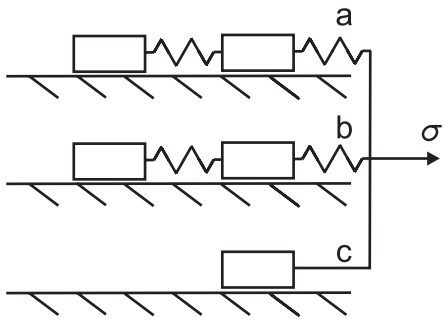

Figure 5.6: Spring mechanism representing concrete in tension

5.2.3 Cracked Concrete Strength

There are several other possibilities for the introduction of the amplitude-dependent frequency behaviour when a crack is present. Firstly, it has been shown by König and Duda [49] that cracked concrete subjected to cyclic loading may be modelled as a series of springs and friction blocks. Figure 5.6 shows the proposed mechanism. There are three sets of friction blocks connected in parallel. The frictional properties and spring stiffnesses are multiples of a variable, ϕ, related to the maximum width of the crack. This variable is needed to take into account the fact that, once the crack has opened, the mechanism will fail over some areas and will not be reactivated once the crack is closed. The springs and blocks in set "a" represent an adhesion mechanism between the matrix and aggregate and the value of ϕ_a drops rapidly with increasing maximum width. The set of springs labelled "b" represents a friction mechanism between the matrix and aggregate. Block "c" is needed to represent the small particles which separate from the surfaces of the crack when open and prevent the surfaces from fitting together again as the crack closes without additional force. It was found that this mechanism, once calibrated, was capable of predicting well the behaviour exhibited during axial cyclic tests and demonstrated the important fact that cracked concrete is capable of transmitting load. If these forces are significant, they will result in non-linear behaviour of the beam as the stiffness is far from constant when the width of the crack varies during oscillation. A simple model is derived in section 9.2 and used in conjunction with experimental data to assess the significance of the contribution of the cracked concrete strength to the overall stiffness of the cracked beam.

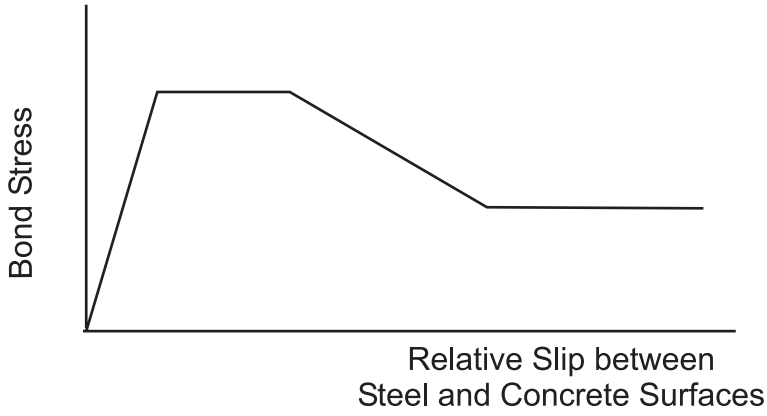

Figure 5.7: Stress-slip relationship for bond between steel reinforcement and concrete

5.2.4 Steel-Concrete Bond Slip

The bonding between the reinforcing bars and the concrete could also introduce amplitude-dependent frequency behaviour. It is possible that, once a crack has developed, the steel slips relative to the concrete as the beam vibrates and the stress in the steel fluctuates. Many authors have reported slip-stress relationships for monotonic or low-cycle loading. For example, Yankelevsky [116] proposed a stress-slip relationship between the concrete and the steel based on monotonic tests (see figure 5.7), which indicated that at a certain stress level the bond between the steel and concrete deteriorates until there is only a residual frictional force. The slip characteristics are discussed further in section 9.2. However, the loading pattern experienced by a concrete beam is very different from these bond slip tests. Firstly, the beam is damaged by overload and then once unloaded the beam is subjected to low-amplitude vibration (in comparison to the deflection during overload). The effect of this type of loading pattern has not been assessed.

5.3 Including Frictional-Type Damage in the Model

In view of the belief that there is likely to be a slip-stick type of behaviour in both the steel-concrete bond and the cracked concrete, it is useful to investigate what sort of amplitude-dependent frequency behaviour would occur from a slip-stick mechanism. This investigation is used as an example of how a friction-type damage mechanism may be included within the model developed in the previous chapter.

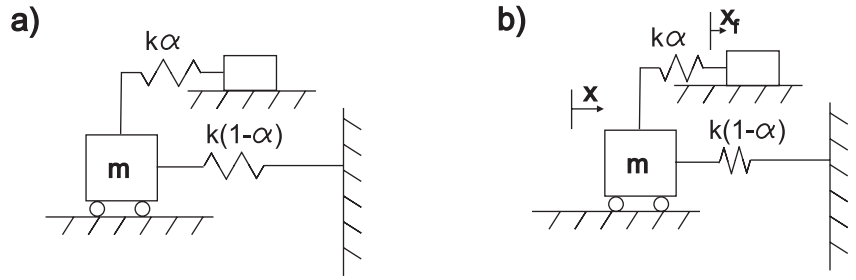

Figure 5.8: A simple axial friction slip mechanism: a) at equilibrium and b) when displaced

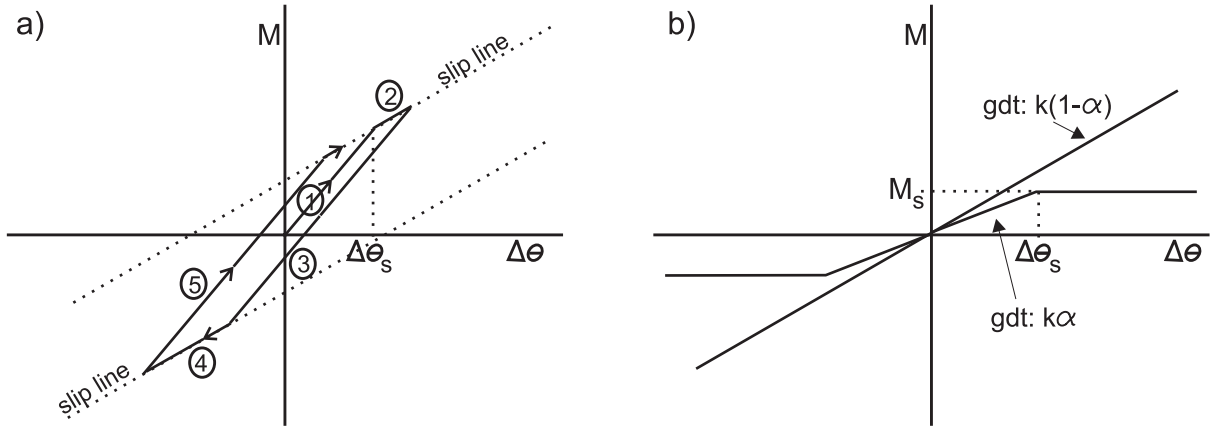

Figure 5.9: Moment-curvature relationship for a) the rotational friction-slip mechanism and b) the two spring mechanisms which make up the friction-slip mechanism

As a first step to including a slip-stick mechanism representing the slip between the reinforcing bars and concrete or one representing the frictional forces between the crack surfaces, a simple friction mechanism is considered. Figure 5.8a shows an axial single degree of freedom version of the mechanism used. The resulting moment-curvature relation takes the same form as the axial mechanism and is shown in figure 5.9a. The mechanism may be thought of as the sum of the two spring mechanisms shown in figure 5.9b, where the fraction of the spring stiffness which is subject to slip due to rotation beyond the linear $\Delta\theta$ limit ($\Delta\theta_s$) is defined as α. The effects of this type of crack mechanism on the dynamic behaviour of a beam may be assessed by including the stiffness relationship in the model derived in chapter 4.

Algebraically, three equations for the moment-curvature relationship are required,

relating to the slip in either direction and to the no-slip region. In the no-slip region, i.e. at stages 1, 3 or 5 in figure 5.9a, the equation for the moment may be expressed as:

$$M = k\Delta\theta - \Delta\theta_f \alpha k \tag{5.12}$$

where $\Delta\theta_f$ is analogous to x_f in the axial slip-stick mechanism (figure 5.8b) and is the rotational displacement of the slip-block due to rotation of the damaged spring past the linear region. This expression for the moment is valid until the boundary with either slip region is reached. The positive slip region (increasing $\Delta\theta_f$ region) is reached when:

$$\Delta\theta \geq \Delta\theta_s - \Delta\theta_f \tag{5.13}$$

and the negative slip region (decreasing $\Delta\theta_f$ region) is reached at the point when:

$$\Delta\theta \leq -\Delta\theta_s - \Delta\theta_f \tag{5.14}$$

The moment equation in the positive slip zone, stage 2 in figure 5.9a, can be expressed as:

$$M = (1-\alpha)k\Delta\theta + M_s \tag{5.15}$$

which remains valid until $\Delta\dot{\theta} \leq 0$ at which point:

$$\Delta\theta_f = -\Delta\theta + \Delta\theta_s \tag{5.16}$$

The moment equation in the negative slip zone, stage 4 in figure 5.9a, is given by:

$$M = (1-\alpha)k\Delta\theta - M_s \tag{5.17}$$

and remains valid until the rotation $\Delta\theta$ starts to increase, i.e. while $\Delta\dot{\theta} \geq 0$, at which point:

$$\Delta\theta_f = -\Delta\theta - \Delta\theta_s \tag{5.18}$$

Figure 5.10 shows the typical shape of the time-frequency distribution where the fundamental mode is shown for a beam with a crack at its mid-point. The beam was modelled as being excited by specifying initial velocities for the blocks. The initial, almost-constant, frequency region is where the duration of the no-slip behaviour is insignificant compared to the time spent in slip zones. The constant region starting at about 0.04 s is when the amplitude is small and the oscillations remain in the no-slip zone.

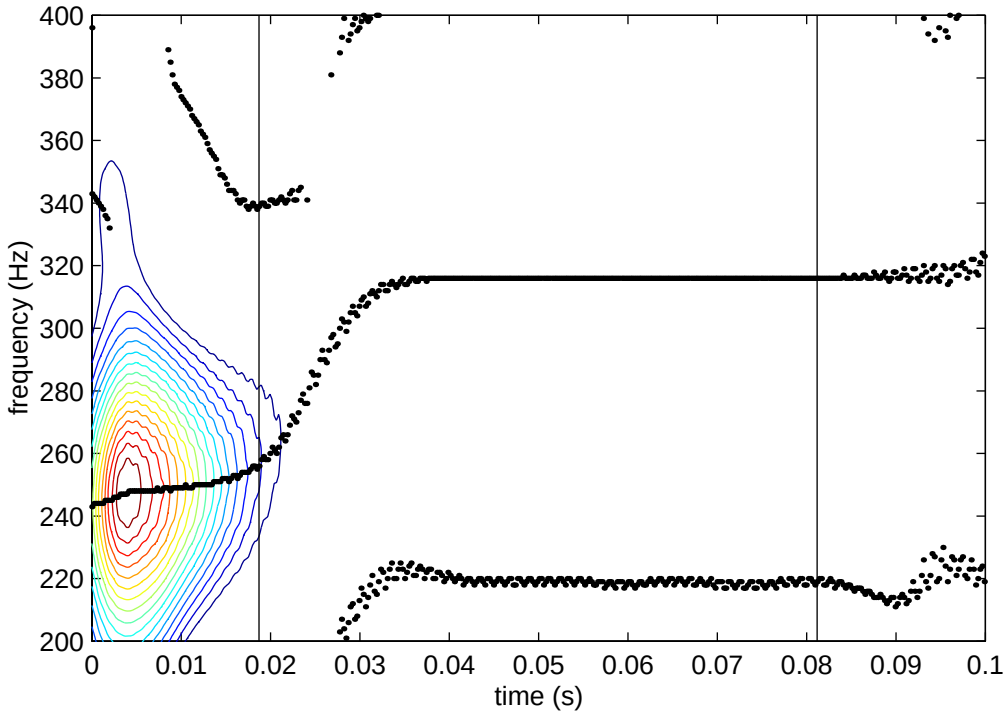

Figure 5.10: A typical time-frequency plot for a beam with a friction-slip spring

5.4 Summary

In this chapter, after an examination of various methods of detect non-linear vibration behaviour, four possible mechanisms to explain the non-linear behaviour have been identified. These mechanisms are based on:

- Crack closure
- The non-linear behaviour of concrete in compression
- The frictional forces over the crack surface due to matrix-aggregate interaction
- The slip between the reinforcing bars and the concrete either side of the crack

Finally, the implementation of an example friction based non-linear mechanism within the vibrating beam model was discussed.

Chapter 6

Vibrating Wire Strain Gauge

To understand the non-linear behaviour of a cracked concrete beam using the vibrating beam model developed earlier it is necessary to know the moment-rotation relationship of the beam at the crack. This may then be entered into the model at the spring closest to the damage location and an approximate time-frequency relationship can be derived from the generated vibration behaviour.

There has been a large amount of work on the cyclic behaviour of reinforced concrete. For example Bresler and Bertero [11] have reported the behaviour of reinforced concrete under axial cyclic loading. They cast a cylindrical block of concrete with a single reinforcing bar (protruding out of both ends of the concrete) and measured the strain of the bar, the elongation of the concrete block and the end slip of the bar relative to the concrete while applying loads to the ends of the reinforcing bar. Ismail and Jirsa [45] conducted similar experiments on a rectangular block of concrete and also conducted tests at the root of a cantilever measuring strain and end deflection under cyclic loading. Lutz [53] looked at the finite element modelling of the axial cyclic tests. Monti *et al.* [63] and Aoyama [4] looked at the behaviour of reinforced concrete beams under reversal of bending measuring deflection and concrete and steel strains. Unfortunately, all the work concentrated on loading to near failure with a view to using the results to predict better the behaviour during earthquake loading or under low-cycle fatigue loading.

To understand the non-linear behaviour during vibration, testing the moment-rotation relationship is required for low amplitude cyclic loading of a beam (to simulate the vibration) once loading to a certain damage level has been applied and removed. It was

decided to determine this relationship by measuring strain at the top and bottom surfaces of the beam over a region spanning a crack. It was anticipated that the magnitude of the static loading to produce curvatures similar to those present during vibration testing would require measurement of strains in the order of 10 μstrain.

Vibrating wire strain gauges were chosen to measure the strain. A vibrating wire strain gauge consists of a wire held in tension between two mountings which are fixed to the specimen. This wire is excited and its natural frequency measured, which may then be used to calculate the strain in the wire and hence the strain in the specimen. The main problem with this principle is that temperature also affects the tension in the wire and hence the frequency, with a 1^{o} C change in temperature typically leading to a 20 μstrain change in the wire strain. Gauges with an electronic resolution (as opposed to measurement precision) of down to 1 μstrain are available commercially ([39] and [62]). An optional thermistor allows for temperature correction. However, the cost of the measurement electronics was prohibitive for this work, so it was necessary to develop a gauge using existing measurement and recording equipment. This chapter describes the theory behind the gauges and the methods employed to find the frequency and hence the strain using the gauges.

6.1 Vibrating Wire Strain Gauge Theory

If a wire is held rigidly at both ends, its first natural frequency is:

$$f = \frac{1}{2l}\sqrt{\frac{\sigma}{\rho}} \tag{6.1}$$

where σ is the stress in the wire, ρ is the density and l is the length of the wire (see for example [69]).

6.1.1 Specimen Strain

For the case where a wire has unstressed length l_w and is held at a tension T_0 over a span of l_0 (where $l_0 \geq l_w$), the frequency may be written as:

$$f_0 = \frac{1}{2l_0}\sqrt{\frac{E\epsilon_0}{\rho}} \tag{6.2}$$

where E is the Young's modulus and the strain in the wire, ϵ_0 may be written as:

$$\epsilon_0 = \frac{l_0 - l_w}{l_w} \tag{6.3}$$

If the length of the wire is now increased to l due to extension of the specimen to which the wire is anchored, the new fundamental frequency is:

$$f = \frac{1}{2l}\sqrt{\frac{E\epsilon}{\rho}} \tag{6.4}$$

where the strain in the wire, ϵ is now given by:

$$\epsilon = \frac{l - l_w}{l_w} \tag{6.5}$$

Since the anchors have finite thickness the strain in the wire is not the same as the strain in the specimen so, defining the length between the centres of the anchors while the specimen is unstrained as l_s, the specimen strain may be expressed as:

$$\epsilon_s = \frac{l - l_0}{l_s} \tag{6.6}$$

Using the strain equations 6.3, 6.5 and 6.6, the length of the wire while the specimen is strained may be eliminated. This gives a relationship between the strains and the initial lengths:

$$\epsilon = \frac{l_s}{l_w}\epsilon_s + \epsilon_0 \tag{6.7}$$

Using equations 6.2 and 6.4, the wire material properties may be eliminated giving:

$$\frac{f}{f_0} = \frac{l_0}{l}\sqrt{\frac{\epsilon}{\epsilon_0}} \tag{6.8}$$

The length l and the strain ϵ may then be eliminated using equations 6.6 and 6.7 respectively, giving:

$$\frac{f}{f_0} = \frac{1}{1 + \frac{l_s}{l_0}\epsilon_s}\sqrt{1 + \frac{l_s}{l_w}\frac{\epsilon_s}{\epsilon_0}} \simeq \sqrt{1 + \frac{l_s}{l_w}\frac{\epsilon_s}{\epsilon_0}} \tag{6.9}$$

noting that the specimen strain is much less than unity and that the specimen and wire lengths before the specimen is strained are of the same order. Rearranging gives an equation for the strain in the specimen in terms of the frequency of the wire when the specimen is unstrained and when it is strained and a gauge factor:

$$\epsilon_s = \frac{l_0\epsilon_0}{l_s f_0^2}(f^2 - f_0^2) = G(f^2 - f_0^2) \tag{6.10}$$

In deriving this equation it is assumed that the lengths of the unstrained wire and the wire while the specimen is unstrained are equal (i.e. the tensioning strain in the wire, ϵ_0, is much less than 1). The gauge factor, G, is dependent on the wire material properties and gauge length:

$$G = \frac{l_0 \epsilon_0}{l_s f_0^2} = \frac{4 l_0^3 \rho}{l_s E} \tag{6.11}$$

It should be noted that the gauge factor is independent of initial strain in the wire when the specimen is unstrained, so it may be assumed that gauges of equal length have the same gauge factors, meaning that calibration is only necessary on one gauge at an arbitrary initial tension.

6.1.2 Temperature

The next thing to consider is the effect of changes in temperature on the measurement of strain. When attempting to measure strain to a resolution of 1 μstrain it is necessary to eliminate changes in the frequency of the wire due to changes in temperature. In commercial gauges this is typically done using a thermistor. However, this is arguably not accurate enough for such fine strain resolution since a thermistor can typically measure absolute temperature to approximately 1^o C. Temperature is eliminated here by comparing the frequency of the gauge to the frequency of a control gauge on an unstrained sample of specimen material. The control effectively measures the change in frequency due to temperature alone.

If the temperature is included in equation 6.10, the strain in the specimen may be written as:

$$\epsilon_s = \epsilon_{load} + (T - T_0)(\alpha_m - \alpha_w) = G(f^2 - f_0^2) \tag{6.12}$$

where T is the current temperature, T_0 is the temperature when the unstrained frequency measurement was taken, α_m is the coefficient of thermal expansion of the material, α_w is the coefficient of thermal expansion of the wire and ϵ_{load} is the strain in the material once thermal effects have been removed. To eliminate temperature, a control gauge is mounted on an unstressed sample of the material and its frequency is governed by:

$$(T_c - T_{c0})(\alpha_m - \alpha_w) = G(f_c^2 - f_{c0}^2) \tag{6.13}$$

where the subscript c indicates the control gauge. Equations 6.12 and 6.13 may be combined on the assumption that the gauge factor and the temperature of the control gauge are the same as those for the measurement gauge:

$$\epsilon_{load} = G(f^2 - f_0^2 - f_c^2 + f_{c0}^2) \tag{6.14}$$

6.2 Design

The design of the gauge was quite simple. The two anchors were glued onto the specimen using a jig to ensure the correct spacing between the anchors. Gluing the anchors avoided the need for holes in the specimen which might induce cracking. The wire was then attached to one anchor and the other end was threaded through the other anchor and tensioned using a spring balance (to ensure the tension in each gauge was approximately the same). The second anchor was then tightened, holding the wire in its tensioned state.

Each anchor consisted of an M8 bolt with a 2 mm hole drilled in the shaft close to the head. The heads of the anchor bolts were filed to remove any undulations and then scored to ensure a good glue bond. The surface of the concrete was also scored. Araldite Precision glue was used which was found to be strong enough to induce local concrete shear failure before bond failure. A washer was placed on the shaft, the wire was threaded through the hole and a second washer was added. Next, a well-lubricated washer and a nut were added. The wire was trapped between the two washers as the nut was tightened. The lubricated washer minimised the likelihood that the second washer would rotate as the nut was tightened, twisting the wire.

To measure the natural frequency an electric guitar pick-up was used. The pick-up consisted of six bar magnets (corresponding to the six strings on the guitar) with a coil wound around them. The outer four magnets were removed and the coil was oriented differently to that on a guitar, so that both the remaining magnets measured the vibrating wire frequency, see figure 6.1 and 6.2. As the magnets will attract the mild steel wire, so changing the tension in the wire, the frequency of the wire was dependent on the coil position. However, provided the coil was not moved, the effects would be

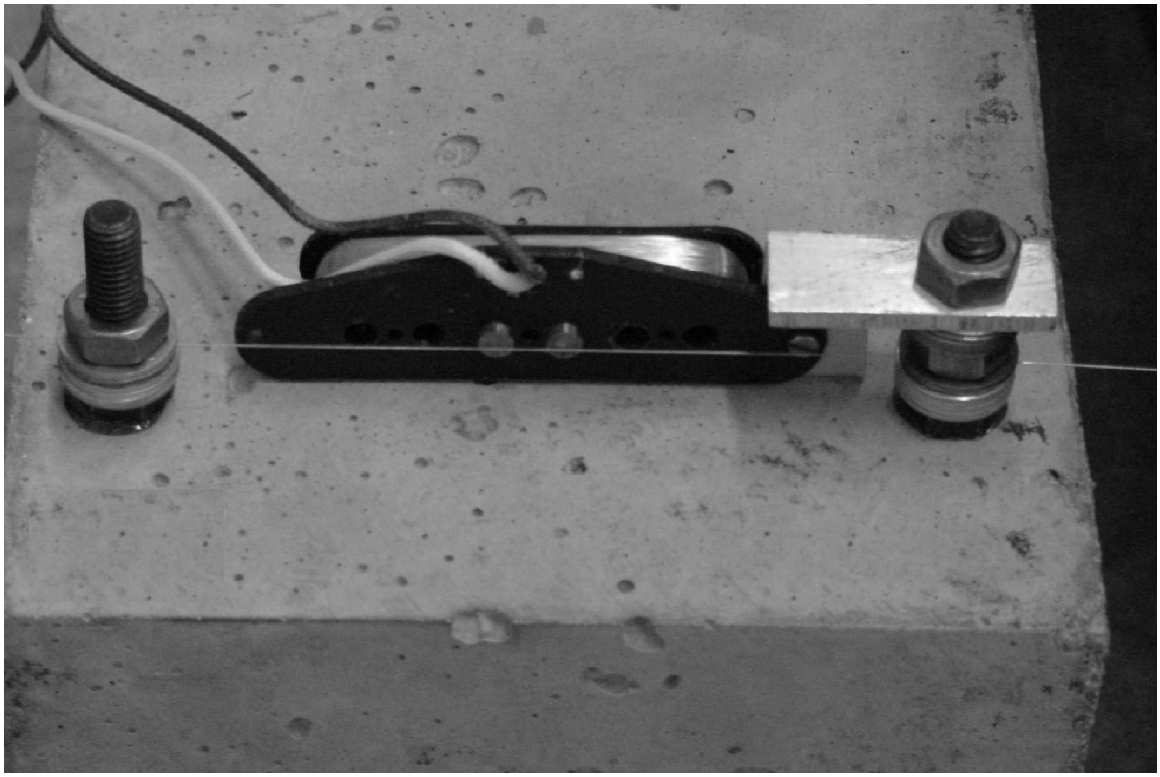

Figure 6.1: A vibrating wire strain gauge

the same for the unstrained test as for a strained test and so cancel each other out. The coil was supported by an aluminium bracket attached to one of the anchor bolts.

As the wire vibrated, a voltage was induced in the coil due to the movement of the mild steel wire causing second-order changes in magnetic field. This voltage was measured. The vibration was induced using a single Velcro hook attached to a thin rod. The hook was placed over the wire and pulled approximately in the plane of the magnets (i.e. the y-direction in figure 6.2). The amplitude of excitation varied slightly from test to test but this can be overcome in the signal analysis.

6.3 Experimental Set-Up

The gauge anchors were glued onto the specimen and the control gauge anchors to the separate unstressed specimen, such that the length l_s was 117 mm. A length of NP010 gauge guitar wire (corresponding to a diameter of 0.25 mm) was then attached to one anchor. The wire was tensioned to a force of approximately 7.8 N (corresponding

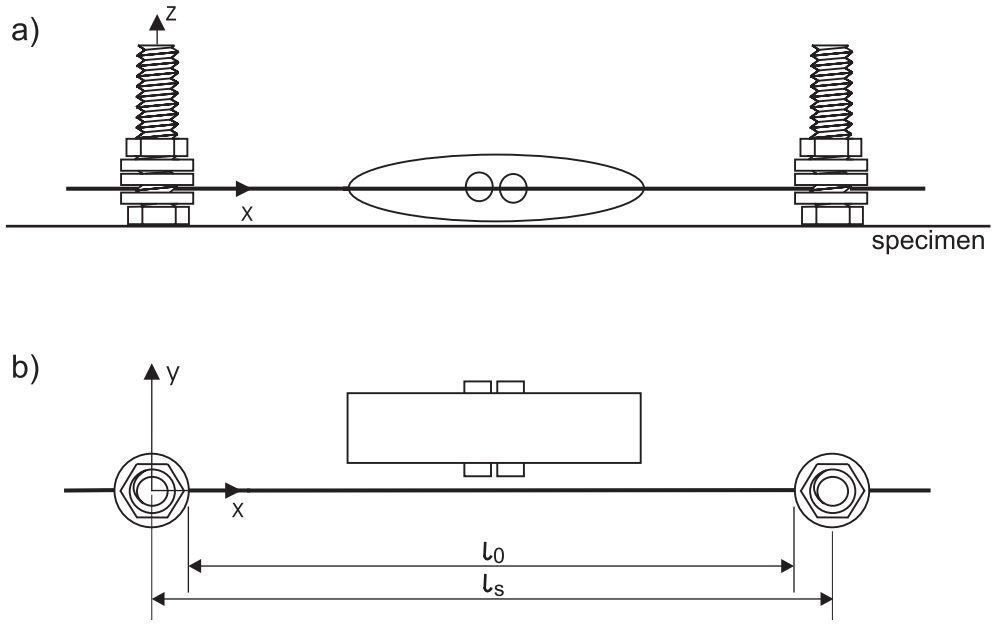

Figure 6.2: Diagram of a vibrating wire strain gauge (magnet mounting not shown, lengths shown for unstrained specimen), a) from the side and b) from above

to a stress of 154 MPa) using a spring balance before the second anchor was tightened. The coil for each gauge was fixed to one anchor ensuring that the gap between the bar magnets and the wire was approximately 1 mm. The coils were each connected via a filter with a low-pass cut-off of 2500 Hz and a times 10 gain to separate channels of a data acquisition board in a computer. The computer sampled each channel at 10 kHz. During each test, the wires of each gauge including the control gauge were excited in quick succession nine times, so that the average frequency for each wire could be calculated.

The first test was to establish the datum zero-strain frequencies and subsequent tests allowed the calculation of strain relative to the first zero-strain test, using equation 6.14. The control gauge was placed as close as possible to the other gauges to ensure the temperature differences between gauges were minimised.

6.4 Signal Analysis

Initially, it was thought that the best way of processing the data would be to calculate the time it took for a certain number of zero crossings in the time-domain signal. It was thought that the effects of noise could be minimised by ignoring all but the middle zero-crossing of a set of crossings which occurred in quick succession, the others assumed to be due to higher frequency noise superimposed on the real signal. However, it was found that, as well as noise, the fundamental frequency consisted of two closely-spaced peaks in the frequency domain, one of a much smaller amplitude than the other. A possible explanation for these two modes is that they are due to a difference in support conditions at the bolts in the y and z-directions (see figure 6.2). The excitation was mainly in the y-direction, but some excitation in the z-direction was inevitable. The supports will be stiffer in the z-direction so it is likely that the oscillation will be of slightly higher frequency.

It was therefore decided to use a zero-padded discrete Fourier transform to find the fundamental frequency in the y-direction, by taking the maximum peak of the signal in the frequency domain. There is an additional complication in that the vibration is geometrically non-linear at relatively high amplitudes. As the excitation amplitude differs from test to test, it is necessary to select an amplitude for each gauge at each damage level at which the signal may be approximated to that of a linear system. This in turn leads to a further complication, in that the signal must be band-pass filtered for the amplitude to be calculated accurately. Without filtering, the amplitude envelope was found to oscillate, which led to a less accurate positioning of the beginning of the linear vibration region.

The experimental procedure employed in concrete beam tests is explained in section 7.2.3. Briefly, sets of tests were performed for various levels of damage. Each set of tests consisted of tests during a series of cycles of loading and unloading. At each of these load conditions, nine excitations of each gauge were recorded. The processing of the data for one gauge at a certain damage level was performed in several stages, as described below.

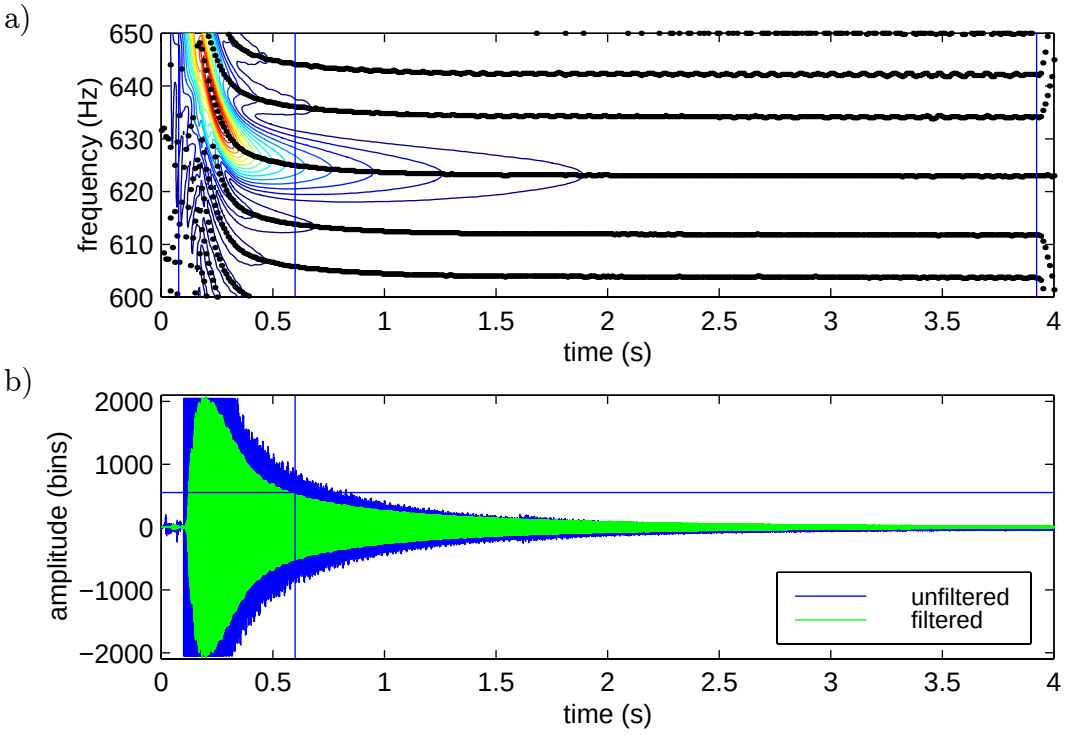

Figure 6.3: A vibrating wire signal: a) the time-frequency relationship and b) the time-amplitude relationship

Selecting a Start Point

Firstly, it was necessary to calculate the largest amplitude at which the vibration of the wire could be approximated to linear behaviour. For each gauge, this was done at each damage level using the first excitation for the unloaded case and the result was applied to all the excitations of that gauge at that damage level. The time-frequency relationship was calculated using the moving window DFT with a time window width of 0.064 s. A typical time-frequency plot is shown in figure 6.3a. The time at which the signal may be considered to be broadly linear was chosen by hand, in this case at approximately 0.61 s.

Filtering the signal

From the time-frequency plot it can be seen that the fundamental frequency was approximately 625 Hz. Therefore a band-pass filter centred at 625 Hz with band width 100 Hz was applied to the signal. A standard Matlab function implementing a finite

impulse response filter with a Hamming window was used (see [59]). The amplitude of the signal at the starting point (the threshold amplitude) was then found, as shown in figure 6.3b, in this case 550 bins. The unfiltered signal is also shown in order to demonstrate the uncertainty that would be present if the unfiltered signal was used to select the threshold amplitude. This uncertainty being due to the fluctuations in the amplitude envelope.

Calculating the Fundamental Frequency

The time at which the amplitude of the signal falls below the threshold amplitude was found for each excitation. This was done by finding the time at which the magnitude of the analytic version of the filtered signal first falls below the threshold value. The next 1.5 s of data was then converted into the frequency domain using the DFT with zero-padding to four times its original length. It was found that beyond 1.5 s after the threshold amplitude, the signal to noise ratio was too small to give reliable results. The frequency at which the amplitude of vibration was largest was then taken to be the fundamental frequency. The fundamental frequency was found for the nine excitations and the mean was taken. The maximum variation from the mean over all nine excitations for one gauge at a certain damage level with a certain static load applied was typically in the order of $\pm 0.1\%$.

Calculating the Strain

The specimen strain was now calculated using the reference and the measurement gauge frequencies for both the strained and unstrained conditions. These frequencies may be combined using equation 6.14 to calculate the strain relative to the unstrained condition in terms of the gauge factor, G.

6.5 Testing on a Length of Aluminium Bar

Tests were conducted on a short length of aluminium bar to calibrate the gauge. The bar, with a cross-section area of 121 mm^2, was suspended vertically at one end using string to ensure that there was no moment transfer at the support. The other end of

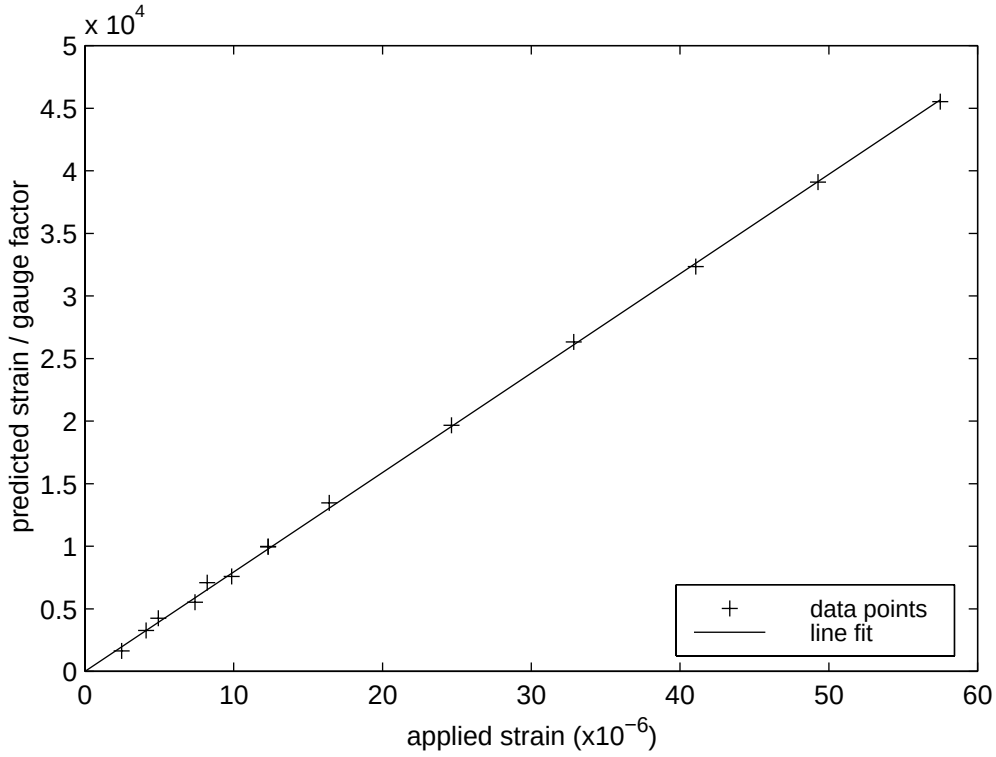

Figure 6.4: Calibration of the vibrating wire strain gauge

the bar was loaded using weights, again via a length of string to ensure no moment was applied. The strain applied to the bar was calculated using a Young's modulus of 76.6 GPa. The strain measurement was calculated using the process set out above. Figure 6.4 shows the calibration data along with a straight-line fit (forced through the origin). It is clear from the line fit that the gauge behaves linearly with increasing load. The gradient of the line fit gives a gauge factor of 1.259×10^{-9}. This is only an approximate gauge factor as the Young's modulus of the aluminium was not known exactly. However, the gauges are to be used in static load tests to investigate the shape of the hysteresis loop exhibited by the cracked concrete beam, so an exact gauge factor is not needed. What is important is that the strain estimated using the gauge changes linearly with increasing applied strain. The maximum error in the prediction is in the order of 0.5 μstrain.

6.6 Summary

To help understand the non-linear behaviour of cracked concrete, cyclic static load tests will be performed. At each load level, strain over a region of cracked concrete will be measured using vibrating wire strain gauges. In this chapter, the theory and design of the gauges has been presented including a method of removing temperature effects using a control gauge. A method of calculating the vibration frequency has then been developed. Finally, calibration of a gauge was performed to verify that it behaved linearly and to calculate a gauge factor.

Chapter 7

Testing of Concrete Beams

The aim of the experiments performed on concrete beams was to assess the change in non-linear behaviour with increasing damage and to improve understanding of the mechanisms causing the non-linearity. At levels of increasing damage, vibration responses to impact excitation were measured. This allowed the time-frequency relationship to be estimated using one of the transforms described in chapter 3. In addition to the vibration tests, static load tests were also performed using the vibrating wire strain gauges described in chapter 6. These would aid understanding of the non-linear mechanisms by assessing the resulting moment-relative rotation relationship. This moment-relative rotation relationship could in the future be used in conjunction with the model of a vibrating beam to allow modelling of the non-linear behaviour.

7.1 Beam Design

7.1.1 Testing of Short Beams

Some preliminary experiments were performed on four 1.8 m long beams. The beams were 200 mm deep and 140 mm wide with two 12 mm diameter reinforcing bars. The fundamental frequency was 120 Hz. A loading rig was used to damage the beams by means of three-point loading. Vibration testing was conducted while the beams were in the loading rig with the loading jack withdrawn.

No test results are presented here as it was found that the loading frame vibrated

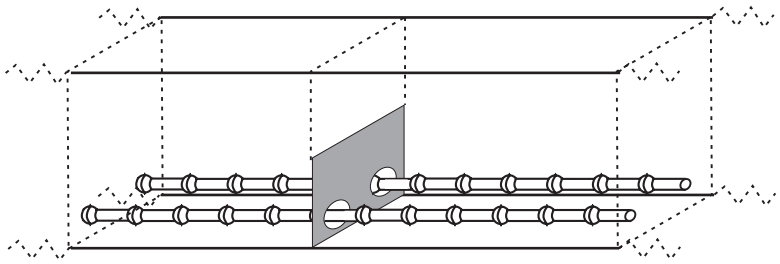

Figure 7.1: Casting a beam with a steel plate to simulate a smooth crack

at a similar frequency to the beam during the hammer excitation tests. However, it is worth mentioning a way in which an assessment of the significance of the cracked concrete strength was attempted.

In order to assess the extent to which the cracked concrete contributes to the vibration behaviour, two beams were cast using the same mix of concrete. The beams were identical with one exception; prior to casting a thin steel plate was fitted vertically at mid-span in one of the moulds. The plate covered half the depth and the whole width of the beam as shown in figure 7.1. One side of the plate was oiled to ensure no bond with the concrete while the other had short lugs welded on to ensure a good bond with the concrete. The plate had oversize holes for the reinforcing bar to fit through to ensure that it had no effect on the concrete-steel bond. With the plate cast into the beam, during testing it would act as a pre-cast smooth crack. The behaviour of this beam could then be compared to that of the beam without a plate, which after loading would develop a crack in the concrete at mid-span, to assess the effect of removing the cracked concrete strength from the mid-span crack. The lugs were required to ensure that the plate was not free to rattle during the impact tests at higher damage load levels. The results of the tests on the beam with the plate were different to those on the plain beam. However, it was unclear whether the differences were due to the plate changing the non-linear properties of the beam or due to a slight change in natural frequency, which affected the interaction between the sinc functions centred at the supports' natural frequency and the beam's natural frequency in the frequency domain. Due to time constraints this method was not pursued for the long beam tests, but there are plans for it to be employed in future work.

7.1.2 Beam Requirements

There have been many reports on typical fundamental frequencies of bridges. Shepherd and Aves [100] tested 11 concrete bridges and reported a range of fundamental frequency between 5.7 Hz and 12.5 Hz. Billing [7] and Paultre *et al.* [81] related frequency to span and found frequencies ranging from 1.5 Hz (corresponding to a span in the region of 160 m) to 12 Hz (corresponding to a span of 20 m), with the bulk of the bridges tested having a frequency in the range of 2 to 9 Hz. It is difficult to design a beam of manageable dimensions which has such a low natural frequency without it being very slender. However, if it is too slender it is unlikely to have been scaled realistically, since the size of the aggregate cannot be scaled down too much without altering the behaviour of the concrete. If the aggregate is too small, the cracked concrete behaviour will be affected, as it is believed to be caused by friction between the matrix and aggregate. It was therefore decided to make the beam as long as feasibly possible to achieve a low natural frequency.

7.1.3 Supports

To avoid the problems with support movement present in the earlier preliminary tests, the long beams were tested on a 1.8 m thick concrete floor. This led to the length of the beam being restricted to 3 m with a span of 2.8 m. The supports were made of solid sections of steel to ensure they were as rigid as possible. They consisted of a 15 mm thick plate with two M30 clearance holes to be used to bolt the plate to the floor, welded to a 50 mm square bar which in turn was welded to a 44 mm diameter cylindrical bar. The cylindrical bar provided a rounded surface for the beam to rest on. A photograph of a support is shown in figure 7.2.

The physical drawback of the supports was the point at which the steel plate rested on the concrete floor. In order to eliminate effects due to the uneven concrete surface and any twist in the beam, shimming was necessary. The rigidity of the supports is assessed in section 8.2.1.

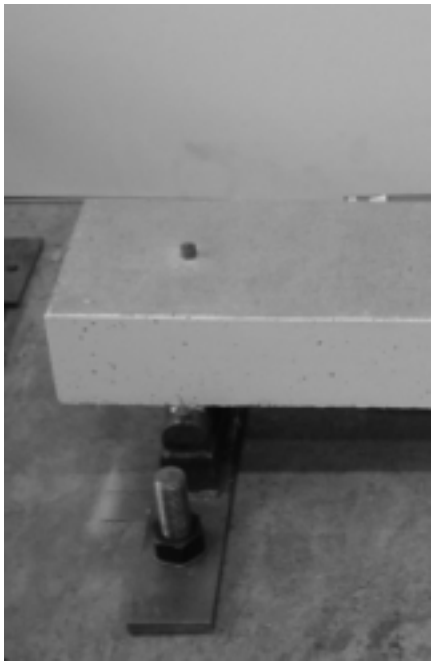

Figure 7.2: Support

7.1.4 Beam Specification

As already stated, the length of span of the beam was limited to 2.8 m. It was decided to adopt the beam design used by Williams [114] to investigate the changes in vibration characteristics of a beam using a MAC number (see section 2.1.3). The fundamental frequency of the beam was reported to be 16 Hz 14 days after casting. Ideally, this frequency should be lower to model a bridge, but this would lead to an unrealistic beam cross-section.

The beams were 0.105 m deep and 0.2 m wide to ensure that vibration due to torsional modes would not be significant. The tension reinforcement consisted of three 12 mm diameter reinforcing bars. There was no significant top reinforcing, only two 6 mm diameter mild steel bars to aid positioning of shear stirrups. The stirrups were made from 4.8 mm mild steel bar and were positioned vertically at a spacing of 0.08 m. A concrete mix giving a 7 day design cube strength of 30 MPa was used based on the Department of the Environment guidelines [105] (see for example Neville [70]). Cube compression tests 30 days after casting gave a cube strength of 46 MPa.

It was estimated that the failure moment was 9.5 kNm, corresponding to a three-

Design Properties		**Concrete Mix**		
natural frequency	16 Hz	design cube strength		30 MPa
failure moment	9.5 kNm	water		9.5%
failure load	12.6 kN	fine aggregate		34.4%
maximum shear force	7.1 kN	coarse aggregate		37.3%
Beam Dimensions		cement		18.8%
length	3 m	**Reinforcing Dimensions**		
span	2.8 m	–	**Bottom**	**Top**
depth	0.105 m	type	rebar	smooth bar
width	0.2 m	effective depth	0.079 m	0.02 m
Shear Stirrup		bar diameter	12 mm	6 mm
orientation	vertical	number of bars	3	2
spacing	0.08 m	yield strength	410 MPa	240 MPa
bar diameter	4.8 mm	rib spacing	10 mm	–

Table 7.1: Beam design

point loading force of 12.6 kN (ignoring self-weight). The full dimensions of the beams and the concrete mix details are summarised in table 7.1.

Due to the duration of the tests (each load level requiring a day of testing), the beams were cured for 28 days before testing to minimize any change in the concrete properties over the test period.

7.2 Test Methods

At each damage level, testing was split into three parts:

- Damage loading
- Vibration response to impact excitation testing
- Static strain testing using vibrating wire strain gauges

7.2.1 Damage Loading

Applying Loads

The beam was damaged using three-point loading. The damage levels were in steps of 1500 N, approximately 10% of the failure load. Failure was defined as the point where the beam could sustain no further increase in load. The load was applied using a small hydraulic jack and measured using a MIL 5000 kgf load cell.

Displacement

For the first few damage levels, the central displacement of the beam was measured before loading, at maximum load and after the load was removed, using a RDP D2 displacement transducer (LVDT). For later damage levels, the displacement exceeded the maximum travel of the transducer. The sensitivity of the transducer was such that 1 mm displacement corresponded to a voltage change of 0.308 V.

Strain

Strain was also measured at mid-span using a 100 mm Demec gauge. The strain was measured at five heights to give the strain profile over the section. It was necessary to loosen the vibrating wire strain gauge wires (see section 7.2.3) during loading to avoid yield of the wire so preventing them from being used.

7.2.2 Vibration Tests

Once the beam had been unloaded, impact response tests were performed. Measurements of impact force, acceleration and displacement were recorded using a RACAL V-Store instrumentation recorder (see below).

Impact

The impact excitation was applied 70 mm away from mid-span using an instrumented sledge hammer dropped from a height of approximately 50 mm above the beam. The hammer used was a 12 pound instrumented impulse hammer, model 5803A, made by

Dytran instruments, in conjunction with a model 4105B battery-powered gain current source. The softest impact tip (brown-MOP 6252S) was used. The impact force was recorded at two resolutions to ensure the recorder range was not exceeded. The signal was recorded at 25 kHz to ensure that the peak value was captured with an acceptable accuracy.

Acceleration

Acceleration was measured at the half and quarter span points using Brüel & Kjær type 4382 accelerometers with sensitivity 3.2 pC/ms^{-2}. The accelerometers were connected to PCB 464A charge amplifiers fitted with 10 kHz low-pass filters, with gains set such that 1 V at the output corresponded to an acceleration of 10 m/s^2. The data signal for each accelerometer was recorded at several sensitivity levels to allow reasonable resolution at all times over the exponentially decaying vibration signal. The combination of the different resolution signals is explained in section 8.2.4.

Displacement

In addition to the accelerometer data, the LVDT was used to measured displacement at the centre of the beam. The LVDT has a built-in 10 kHz low-pass filter. The output signal voltage was magnified by passing it through a Kemo type VBF/23 10 kHz low-pass elliptic filter with a times 10 gain. Before the filter, 1 V output corresponded to 3.23 mm displacement. The displacement information is required when comparing the static load test results to the vibration response.

Data Recording

Data recording involved two stages. Firstly, during testing the data was recorded onto VHS video cassette using a 16 channel RACAL V-Store instrumentation recorder. The recorder was set to 2WB1 and had a tape speed of 7.5 inch/s resulting in signals with frequencies up to 10 kHz being recorded in analogue form. The channels and voltage ranges used to record each signal are shown in figure 7.3.

The second stage was to digitise the data. The recorder was played at 1/4 speed and

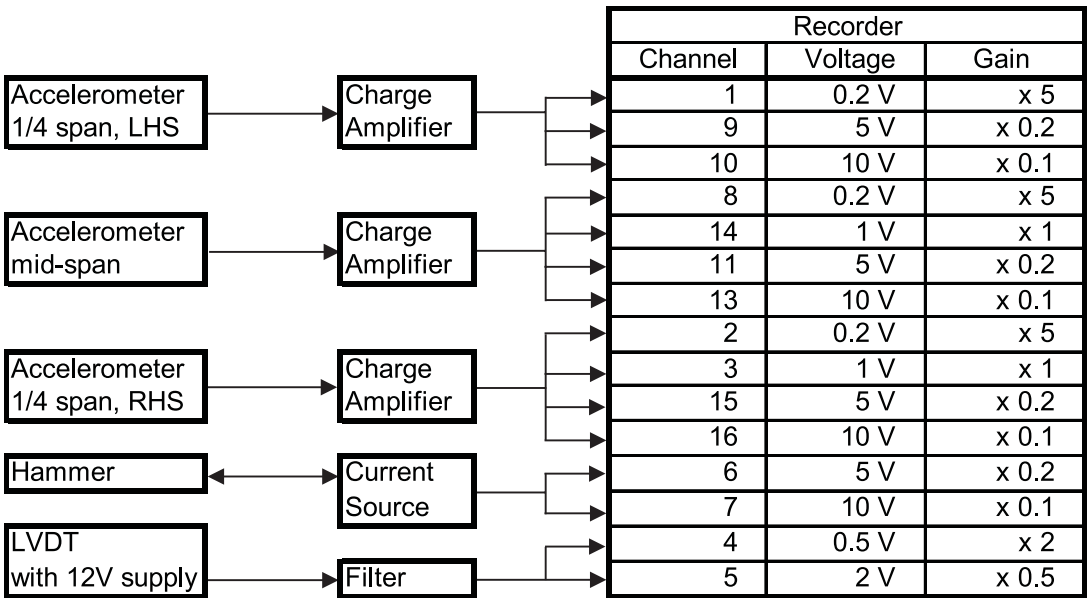

Recorder		
Channel	Voltage	Gain
1	0.2 V	x 5
9	5 V	x 0.2
10	10 V	x 0.1
8	0.2 V	x 5
14	1 V	x 1
11	5 V	x 0.2
13	10 V	x 0.1
2	0.2 V	x 5
3	1 V	x 1
15	5 V	x 0.2
16	10 V	x 0.1
6	5 V	x 0.2
7	10 V	x 0.1
4	0.5 V	x 2
5	2 V	x 0.5

Figure 7.3: Data recording during vibration testing

four channels were digitised using a MetraByte DAS-20 12-bit digitising board fitted in a 100 MHz 486 PC. The digitiser sampling frequency was set to 25 kHz over all four channels, which meant that as the signal was played at 1/4 speed, the signal sample frequency was 25 kHz for each channel. The output from the recorder was ± 1 V resulting in an effective gain through the recorder (as shown in figure 7.3). Between the recorder and the digitiser, each of the four channels was passed through a 25 kHz low-pass filter with a times 10 gain, channel 0 and 1 through Kemo type VBF/8 filters and channels 2 and 3 through Kemo VBF/23 filters. The digitiser was set such that $+2047$ and -2048 bins corresponded to ± 10 V. The digitising process was performed three times for each damage level since only four channels could be digitised at a time. To allow accurate alignment of the digitised data in the time domain, the impact hammer data (channel 6 on the analogue recorder) were recorded each time and the time axis shifted to ensure that the maximum impact force occurred at the same time bin for each test.

In the next chapter, the time-frequency relationship is based on the central accelerometer signal using three ranges, the recorder channels 11, 14 and 8, corresponding to a range of ± 50 m/s^2, ± 10 m/s^2 and ± 2 m/s^2 respectively.

Experimental Procedure

At each damage level, 30 impact tests were performed with 8 s between impacts. The recorder ran continuously over the 4 minutes that this took place. After testing, the signal was digitised three times at 1/4 speed for 8 minutes, which resulted in three files containing a signal of the hammer impact along with three other signals interlaced in each for 15 impacts. These data were separated in Matlab into separate files for each channel of interest, each stored in a matrix with 15 columns corresponding to the 15 impacts with 6 s of data in each (i.e. 150001 rows).

7.2.3 Moment-Rotation Relationship

Tests were conducted to measure the static moment-rotation hysteresis loop for different levels of loading and at different damage levels.

Loading

The beam was loaded 120 mm from the mid-span using weights. A pulley system was used to allow loading upwards. Tests were not conducted for all damage levels, but for the damage levels chosen, three hysteresis loops were measured, ± 40 kg, ± 30 kg and ± 20 kg. Figure 7.4 shows the loading arrangement. The loading loops started at 0 kg and were increased in steps of 10 kg to maximum range then reduced in steps of -10 kg to the maximum load in the upward direction, before being increased back up in steps of 10 kg to the maximum load and then reduced back to 0 kg. Between the three load loops, the beam was excited with the impact hammer to ensure that it was in the equilibrium position at the start of each load cycle.

Strain

Strain was measured using three vibrating wire strain gauges. Two gauges were positioned at mid-span, one at 7 mm and the other at 98 mm from the top of the beam. The third was used as a temperature reference and was fixed on a separate piece of concrete (cast using the same mix as the beam) that remained unloaded throughout the tests. The gauge length was 117 mm. The reference and top gauge data were passed through

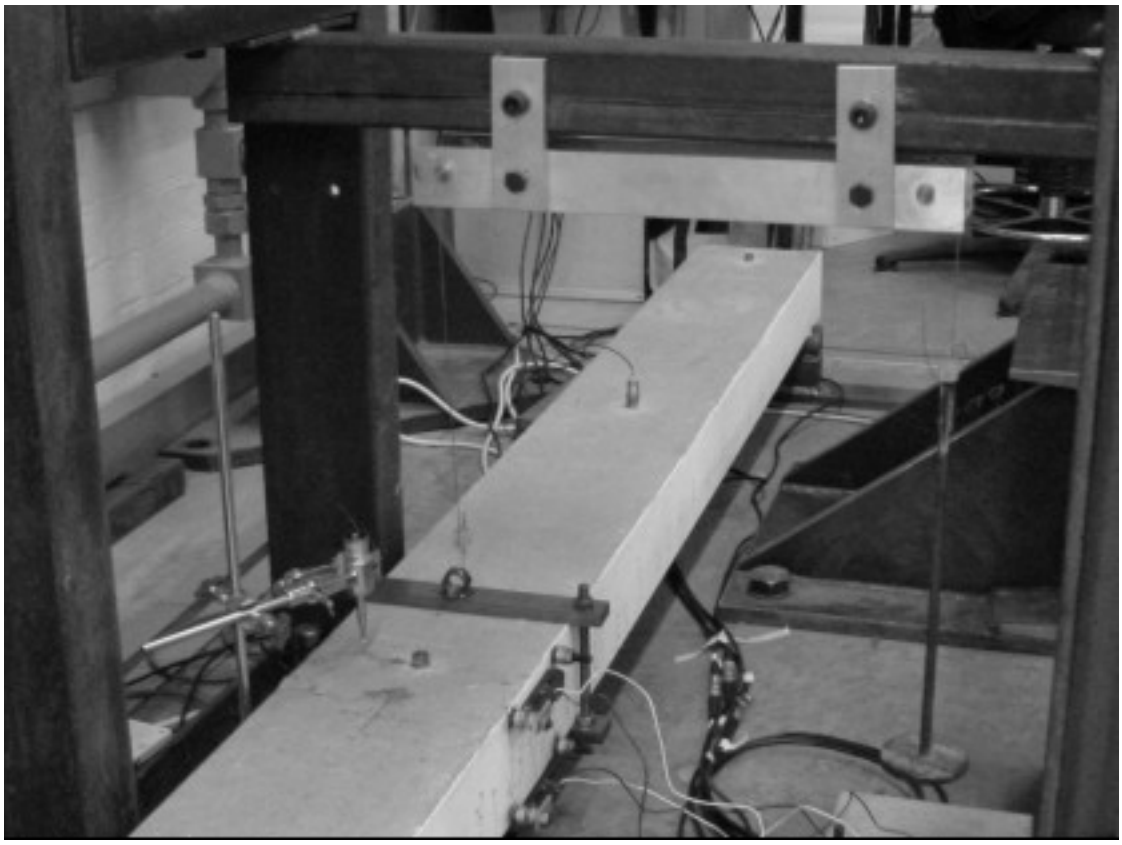

Figure 7.4: Loading pulley system

Kemo VBF/23 elliptic filters with a low-pass cut-off of 2.5 kHz and a gain of 10 and the bottom gauge data through a Kemo VBF/8 filter with the same cut-off and gain.

Displacement

In addition to the strain measurements, the LDVT was used to measure vertical displacement at mid-span.

Experimental Procedure

At each load level all three strain gauges were excited in quick succession nine times with a spacing of 10 s. The signals were recorded using three channels of the MetraByte DAS-20 digitising board with a sample frequency of 30 kHz over the three channels. The range (+2047 and −2048 bins) was set to ±0.5 V. The data were recorded for 100 s, resulting in a file containing the nine excitations of each gauge. These could be split into three matrices each with nine columns corresponding to the nine excitations and containing 4 s of data in each column, with the excitation of the wire occurring at 0.1 s. This was then processed in Matlab as described in the previous chapter.

7.2.4 Test Procedure

Initially tests were conducted to assess the support conditions. Once they were confirmed as being satisfactory, the undamaged test was performed and then the subsequent damage levels up to failure. Failure was defined as the point where the beam was no longer capable of sustaining higher loading. For each damage level the vibration tests were carried out immediately after damage loading.

For beam 5, the static load tests were conducted at varying times after the vibration tests. However, as will be seen in section 8.4.1, there is some degree of strain recovery after loading which affects the hysteresis loop predictions. For beam 6, the static load tests were conducted 16 hours after damage loading. The vibration tests were not sensitive enough to detect any change in beam properties with time.

7.3 Summary

To summarise, experiments were performed on concrete beams to assess the change in non-linear behaviour with increasing damage and to improve understanding of the mechanisms causing the non-linearity.

The experiments where performed at increasing levels of over-load damage. At each of these damage levels the measurements may be split into three parts. Strain measurements were taken using a Demec gauge both during and after damage loading. Then vibration responses to impact excitation were measured. This allowed the time-frequency relationship to be estimated using one of the transforms described in chapter 3. Finally, static load tests were performed using the vibrating wire strain gauges described in chapter 6. These will aid understanding of the non-linear mechanisms by assessing the resulting moment-relative rotation relationship.

Chapter 8

Analysis of Beam Test Results

As with the testing chapter, the analysis of results may be split into three sections:

- Damage loading
- Vibration tests: response to impact excitation
- Static strain tests using vibrating strain gauges

After the presentation of the test results, an assessment of the possible non-linear mechanisms suggested in chapter 5 is given in the next chapter.

8.1 Damage Loading

Damage levels are in steps of 1500 N ranging from UD (undamaged, no load case) to D10 the final damage level before failure. Beams 5 and 6 failed at loads of 16.4 kN and 16.5 kN respectively.

Figure 8.1 shows the strains at the mid-span of beam 6 for each damage level at the point when the maximum load was applied. The strain was measured at 5 points over the depth of the beam using a Demec gauge with gauge length of 100 mm. The strains at each damage level were with respect to the initial undamaged condition. For damage levels D6 to D9, the strain at the lowest depth position could not be measured as the Demec pips became inaccessible due to the deflection of the beam. For damage level D10, both the lowest and the second lowest position were inaccessible. The Demec

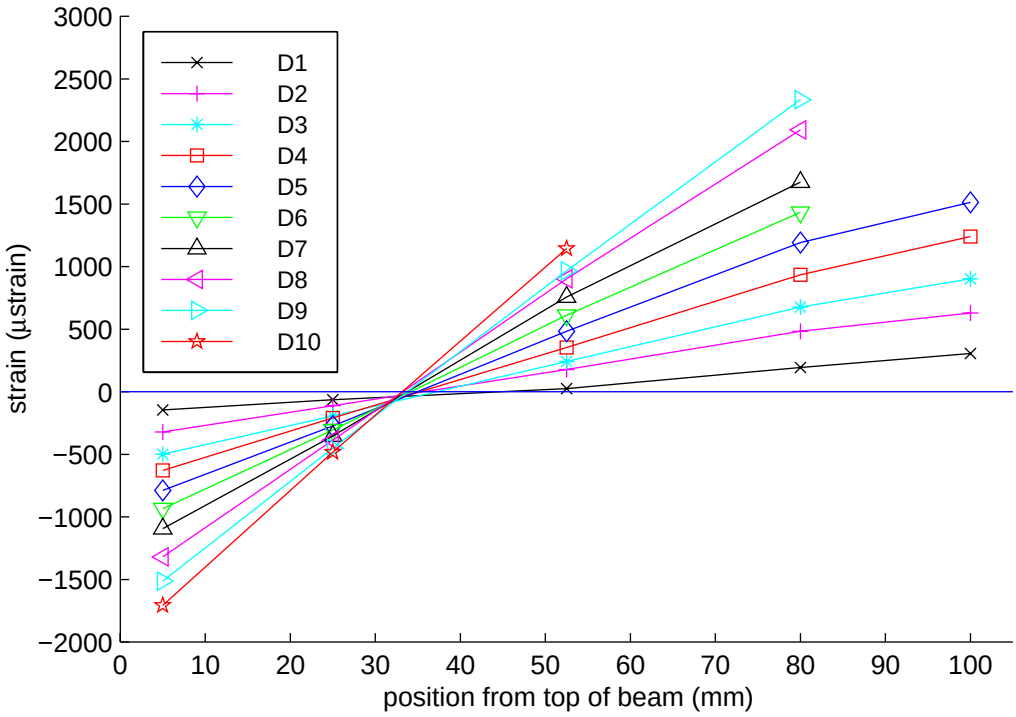

Figure 8.1: Strain during damage loading, beam 6

strain data clearly show that two plane sections 50 mm either side of mid-span may be considered to remain plane during the damage loading.

Figure 8.2 shows the residual strain after loading to each damage level. Again the strains are relative to the undamaged state. It can be seen that broadly the two planes may again be considered to be plane. More importantly, the data indicate that the residual strains after loading are approximately a fifth of the strains during damage loading.

During testing, the crack spacing was approximately 80 mm, corresponding to the stirrup separation distance. Ideally, the strain measurements would have been taken over this distance to ensure that the effect due to only one crack was measured. However a 80 mm Demec gauge was not available. For beam 6, the crack was located almost exactly at mid-span and so the effect of using a 100 mm Demec gauge was minimal. Clearly, at a crack, a vertical plane section of the beam in the undamaged state will not remain plane after damage loading as the crack does not close completely, demonstrated by the presence of the residual strain. However, as the span was large, the moment over

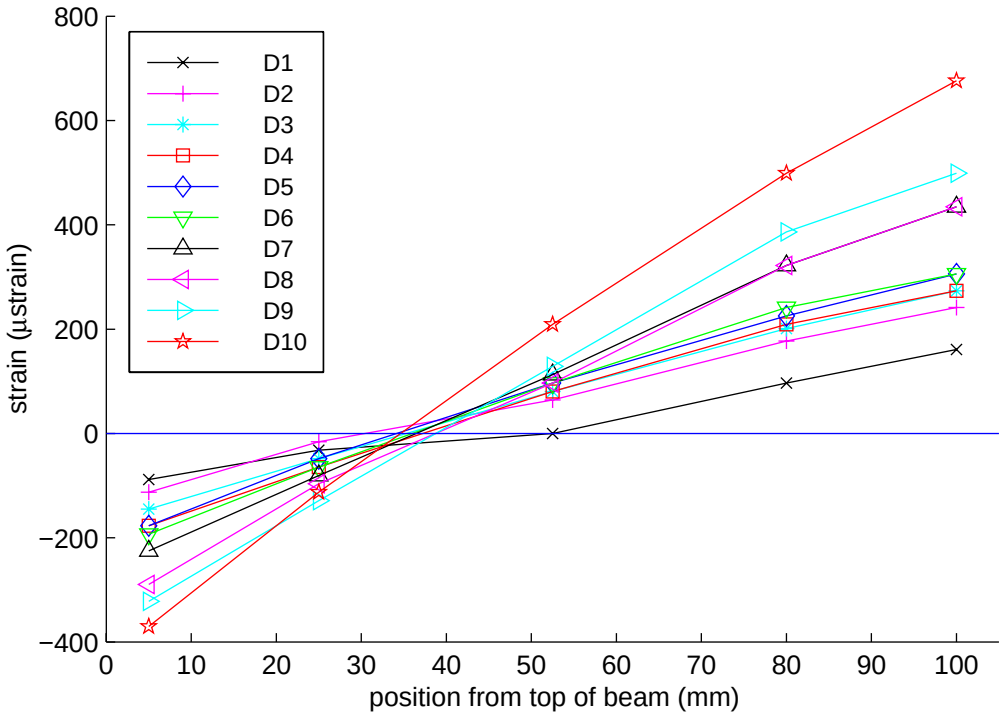

Figure 8.2: Residual strain after damage loading, beam 6

the central three cracks will be roughly constant, so it is reasonable to assume that the two plane sections (ps) 40 mm away from the central crack will remain plane, as shown in figure 8.3. The results of the Demec measurements show that these two points at which the plane section remains plane after loading are not just points 40 mm from the crack, but regions (labelled R in figure 8.3) spanning at least between 30 mm and 50 mm away for the crack.

For beam 5, the central crack was approximately 20 mm off mid-span and for higher damage levels (after D4), a second crack appeared 75 mm away, only 5 mm the other side of the Demec pips. The plane sections remaining plane behaviour exhibited by beam 6 was not present in beam 5. The probable explanation for this is that as there is a crack 5 mm away from one of the Demec pips, the section that the pips are on will not remain plane. However the other set of pips are positioned 30 mm from a crack and so they will be in the region in which plane sections remain plane.

In addition to strain measurements, crack locations and lengths were studied. Cracks were located almost exclusively at stirrup locations up to damage level 10, at which

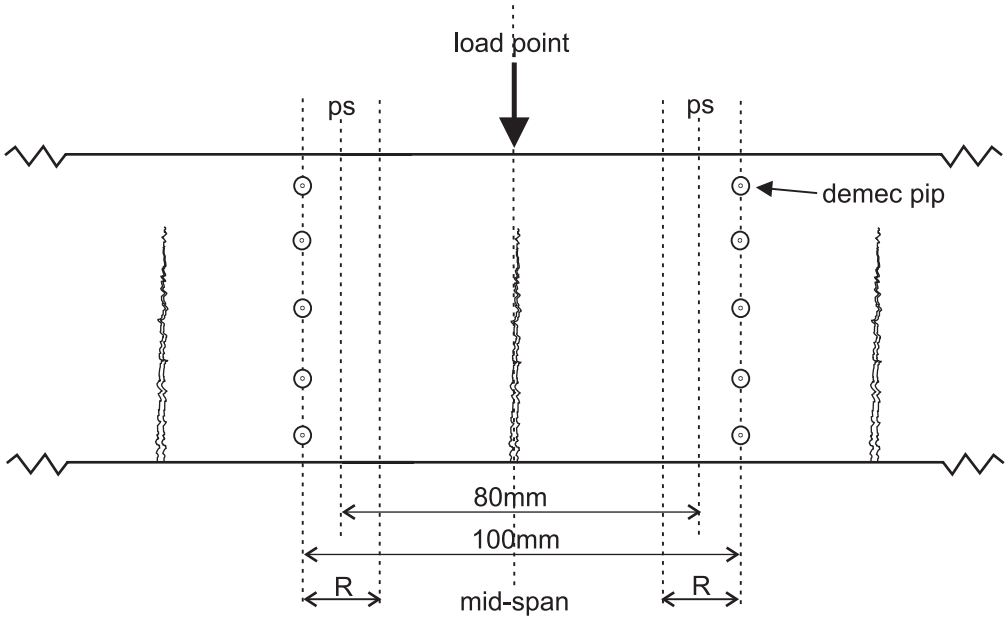

Figure 8.3: Crack and Demec pip locations

point additional cracks appeared near the mid-span. Table 8.1 gives a summary of crack growth during the damage loading.

8.2 Vibration Tests: Processing

Firstly, some linear frequency analysis will be presented in order to examine the support conditions and the modal content of the vibration signals. Then the various time-frequency distributions will be assessed using an undamaged acceleration signal. Finally, the optimum time-frequency distribution will be used to assess the effects of damage on the non-linear vibration behaviour.

8.2.1 Support Conditions

As stated in section 7.1.4, the beam supports were made out of solid steel bar so that they were as stiff as possible. The physical drawback of the supports was the tolerance of the floor surface. Shimming was necessary to ensure that the supports sat firmly on the floor and that any rotation in the supports relative to the beam was accommodated.

Some preliminary vibration tests were performed to assess the support conditions for

Damage level	Max. Load (N)	Max. Compressive Strain (μstrain)	Observed Damage
UD	0	0	No visible cracking
D1	1500	179	No visible cracking
D2	3000	382	Small single crack at mid-span
D3	4500	602	Further cracking near mid-span at stirrup locations
D4	6000	741	Mid-span crack around 34 mm long with small cracks near mid-span
D5	7500	943	Growth of cracks near mid-span
D6	9000	1102	Cracks appearing between supports and quarter-span points
D7	10500	1301	Cracks around 63 mm long near mid-span and 50 mm near quarter-span points
D8	12000	1529	Growth of cracks around quarter-span points, no significant growth of cracks near mid-span
D9	13500	1785	Further growth of cracks near quarter-span points and very slight growth of cracks near mid-span
D10	15000	2033	Additional cracks appear at mid-span between stirrup locations
Failure	16400		

Table 8.1: Observed damage during loading, beam 5

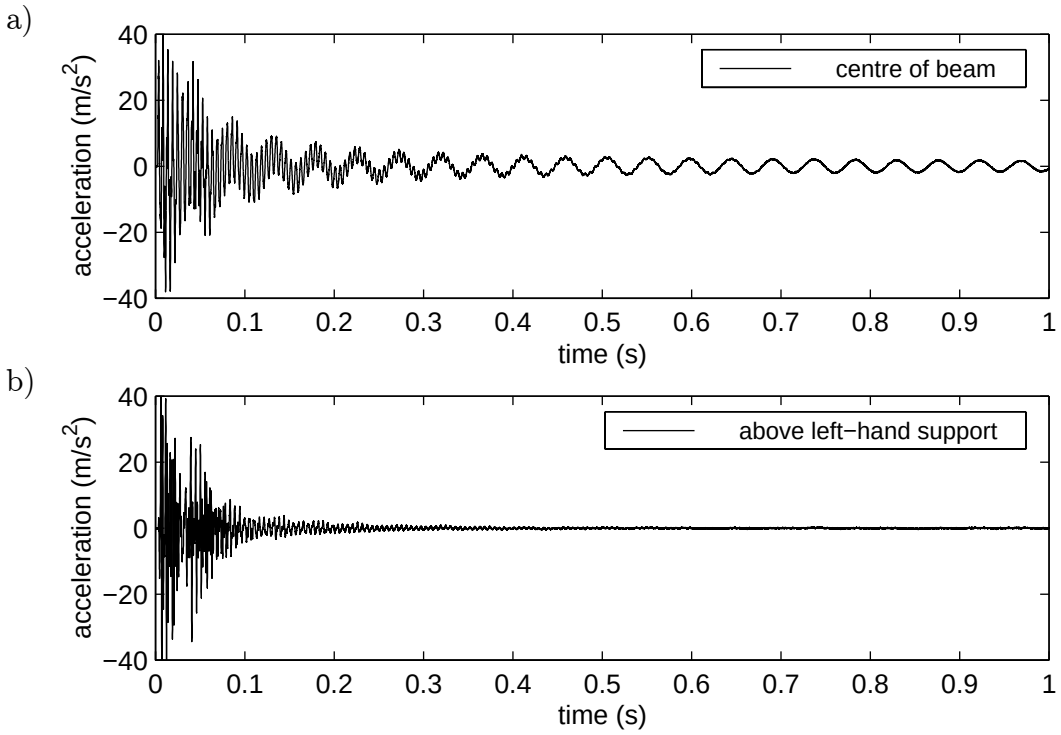

Figure 8.4: Accelerations recorded at a) mid-span, b) above left-hand support, beam 6

both beams. Figure 8.4a shows a typical acceleration signal at the centre of the beam and figure 8.4b illustrates the response at the left-hand support for beam 6. As with all the vibration data, unless otherwise stated, the time axis was defined such that the maximum impulse force occurred at 0 s. Figure 8.5 shows the corresponding plots for the right-hand support. It can be seen that, initially, the responses are of similar amplitude. However the movement at the support died away much faster than the vibration at the centre of the beam. The reason is that the majority of the response at the support is at the higher frequency end of the spectrum. This is demonstrated in figure 8.6, which shows the magnitude of the first 1 s of the vibration response of the left-hand support and the centre of the beam in the frequency domain, using the analytic signal. It can be seen that there was negligible response at the support at the fundamental frequency of the beam (approximately 21 Hz), but there was significant movement of the support at the frequency of the third mode of the beam (approximately 180 Hz). There was no significant frequency content in the response at either location above 1000 Hz.

Therefore, initially, the beam may not be considered as simply-supported, but around

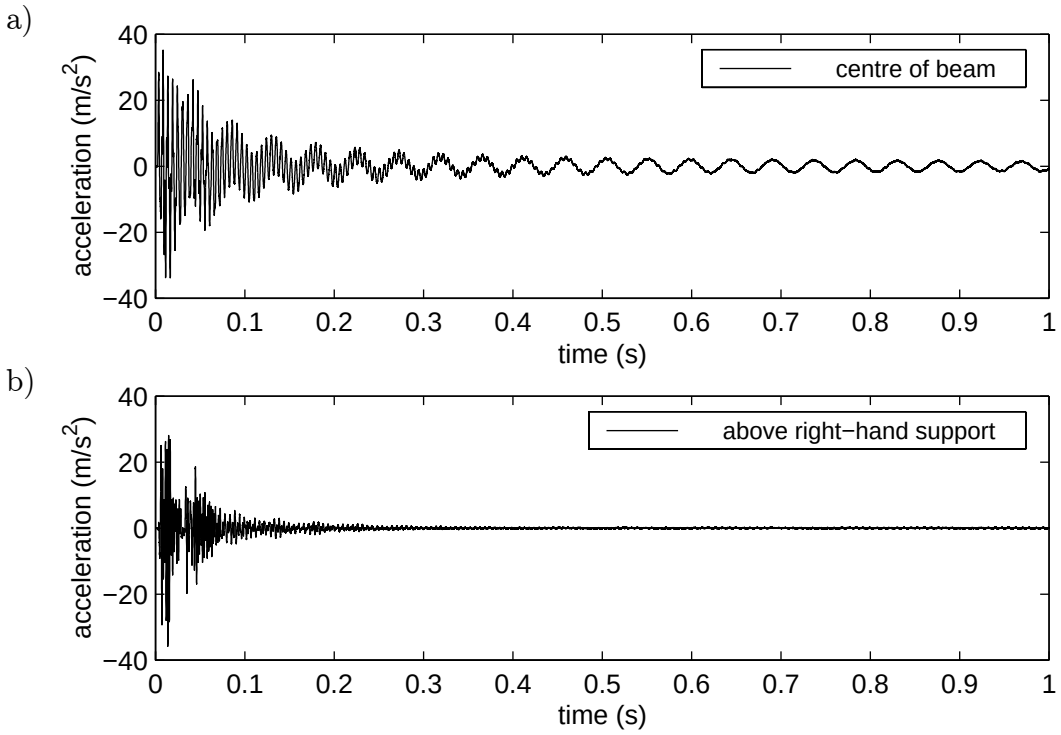

Figure 8.5: Accelerations recorded at a) mid-span, b) above right-hand support, beam 6

0.5 s after the impact, the movement at the support was far smaller than at the centre of the beam and so the beam may be considered as simply-supported.

8.2.2 Vibration Modes

It is desirable that the vibration is made up purely of the fundamental mode. This will allow easier understanding of any non-linear mechanisms involved, since it will be straightforward to calculate the amplitude of the vibration from the acceleration signals, and the amplitude directly correlates to the curvature of the beam if only the fundamental mode is present. The amplitude of each mode may be examined by filtering the signal. Firstly, the signal was converted into its analytic form and transformed to the frequency domain. Then a box window was applied to limit the signal to one mode before conversion back to the time domain. The acceleration amplitude for the mode may then be calculated by taking the magnitude of this signal. The frequency ranges applied using the box window were 0 to 50 Hz, 50 to 110 Hz and 110 to 300 Hz for the

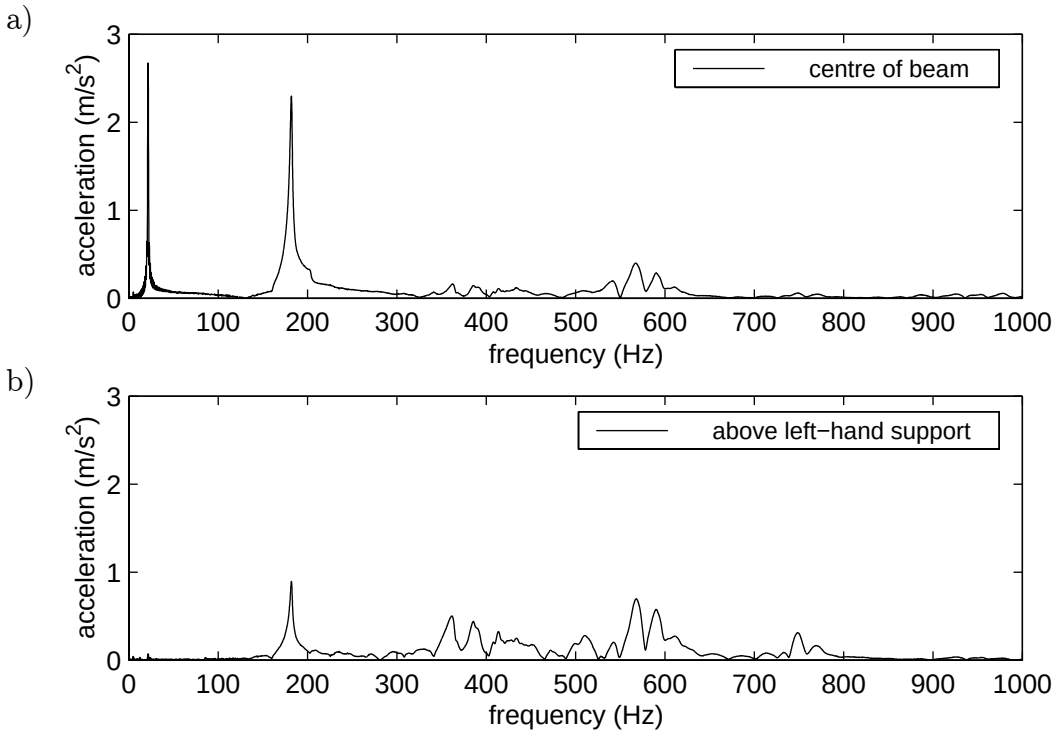

Figure 8.6: First 1 s of the response in the frequency domain at a) mid-span, b) above left-hand support, beam 6

first, second and third modes respectively. Figures 8.7a and 8.7b show the amplitude of the first three modes for the mid-span and for the quarter-span for beam 6 in its undamaged state. It can be see that 0.5 s after the impact the vibration was almost entirely at the fundamental frequency. Therefore, the time-frequency relationship for the concrete beam will be considered using the data after 0.5 s. For completeness, the plots of time-frequency relationship will continue to be from 0 s, the point of maximum impulse force.

A further implication is that the signal can be decimated without loss of useful information, which allows significant computational saving. The data were decimated such that only every 108th time-point was used, i.e. the post-decimation sample frequency was 25000/108 Hz. This means that the highest frequency at which the signal contained information was 116 Hz.

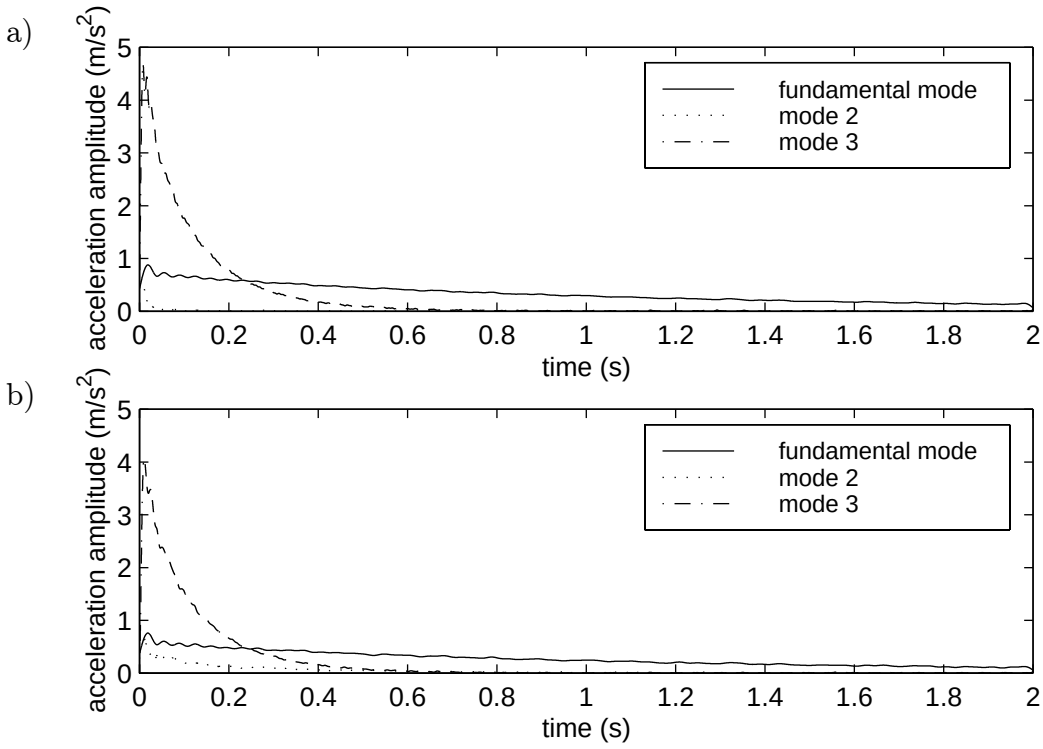

Figure 8.7: Modal content of impact response, beam 6

8.2.3 Optimum Window Width for the DFT Moving Window

Before the effects of damage on the vibration characteristics can be appraised, the optimum time-frequency distribution estimator must be found. Firstly, the effect of the size of the time window was assessed and an acceptable window width was found. This was done using the moving window with the discrete Fourier transform. Then, after an explanation of the way the three signals of different sensitivity are combined, the various time-frequency distribution estimators will be examined.

The optimum window width was assessed using a vibration data signal for damage level 2 for the central accelerometer recorded in the least sensitive range. The signal was decimated to a sample frequency of 25000/108 Hz to reduce the computation time to an acceptable level, without filtering out any useful frequency information. Then the signal was converted to the analytic form before the time-frequency distribution was calculated. Figures 8.8a, 8.8b, 8.9a and 8.9b show the DFT moving window time-frequency estimation for window widths of 1 s, 0.5 s, 0.25 s and 0.125 s respectively. Zero padding has been used to attain a frequency resolution of 0.04 Hz. At first sight

the 1 s window looks the best as the estimation is smooth for the first 5 s. However, the frequency estimation may be loosely thought of as the "average" of the instantaneous frequencies over the time window. Therefore, the effect of having a large window is to smooth the signal at the risk of losing non-linear effects as well as the undesirable effects due to noise and quantisation. This was demonstrated in section 3.6.3 using a phase-modulated signal. On the other hand, when the window is too small the width of the sinc function peak becomes too large. This results in a very rounded peak which is more susceptible to noise and quantisation errors. This is demonstrated in the 0.125 s window and to a lesser degree in the 0.25 s window distribution. The quantisation problem may be overcome to an extent by using the more sensitive range signals. After examination of various test signals, it was decided to use a window of 0.164 s corresponding to approximately 3.5 cycles of the fundamental frequency. Figures 8.10a and 8.10b show the DFT moving window estimation using a 0.164 s window for the ± 50 m/s^2 and the ± 10 m/s^2 range signals respectively. It can be seen that the oscillations in the estimation are reduced using the more sensitive range over the time period of $1 \leq t \leq 3$ due to the reduction of the quantisation error.

8.2.4 Vibration Signals

When discussing the experimental procedure in section 7.2.2, it was stated that the accelerometer signals were recorded over several voltage ranges so that a good resolution could be maintained during digitisation. The signals analysed up to now used the least sensitive range, i.e. full scale at the digitiser (bin 2047) corresponds to an acceleration of 50 m/s^2. Figure 8.4a shows that this range is needed to capture the signal initially. However, at 1 s after impact the maximum acceleration at the centre of the beam has decayed to approximately 2.8 m/s^2 which corresponds to digitised bin 68. The problem with a signal which has been digitised over a range of just ± 68 bins is that the quantisation noise introduced by the digitisation becomes significant. Therefore, it was necessary to record the accelerometer signal using several sensitivity ranges, so that the quantisation error was kept to an acceptable level over the length of the signal.

Figure 8.11 shows an impact response for the undamaged beam for the three ranges

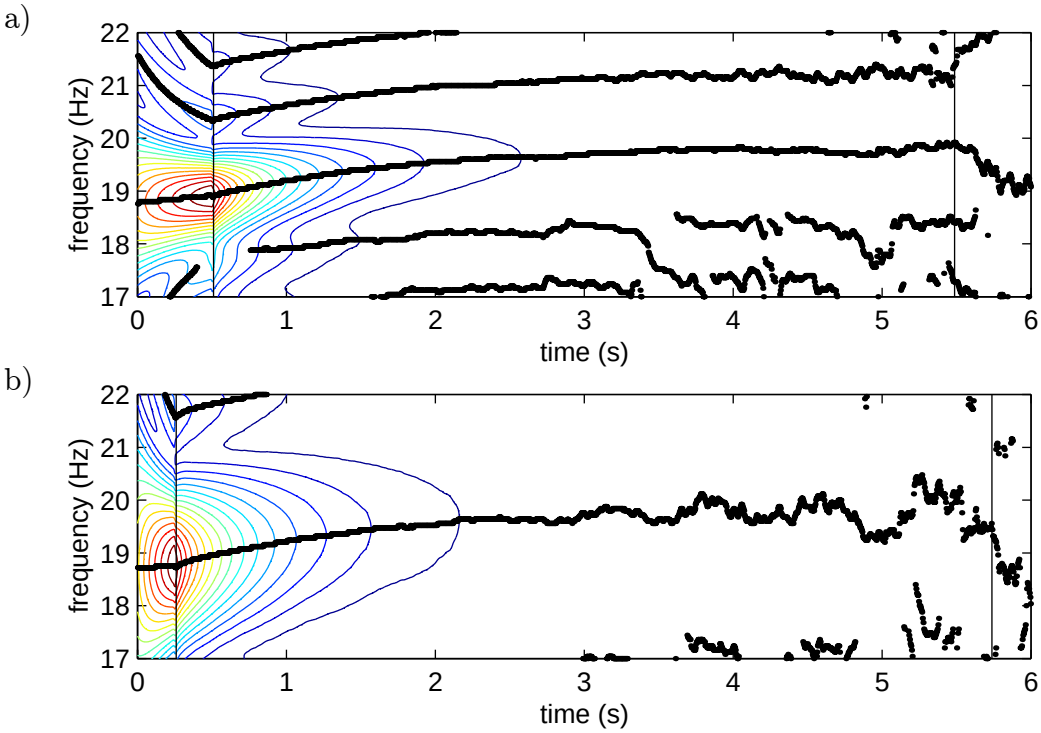

Figure 8.8: DFT moving window, a) 1 s and b) 0.5 s windows

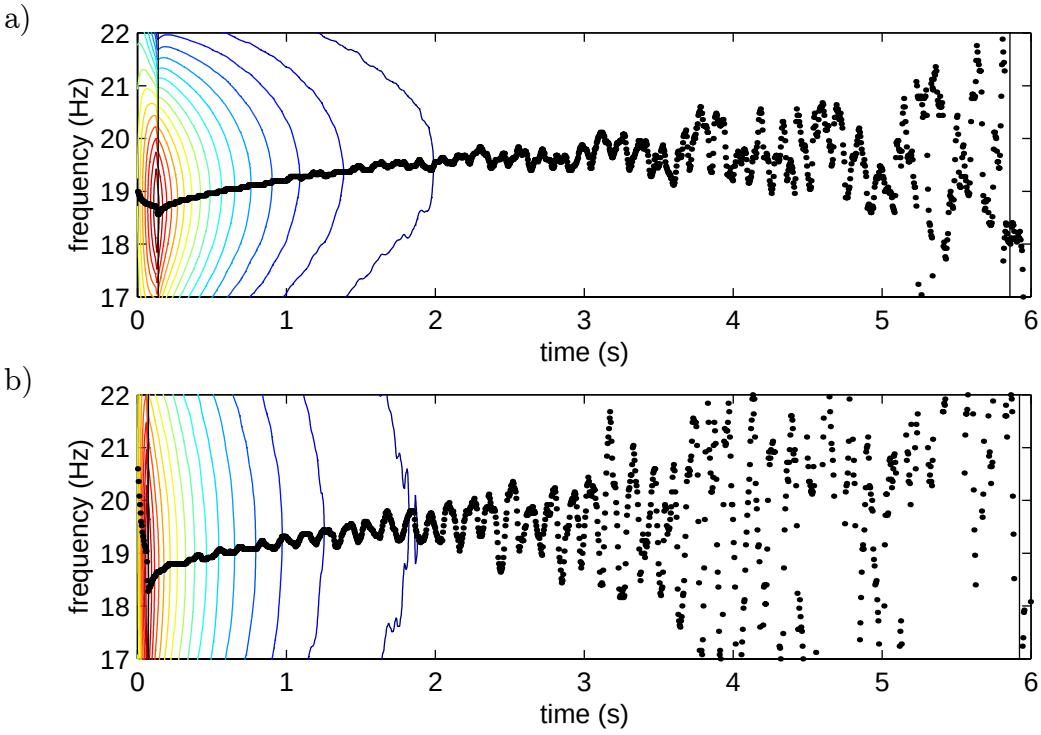

Figure 8.9: DFT moving window, a) 0.25 s and b) 0.125 s windows

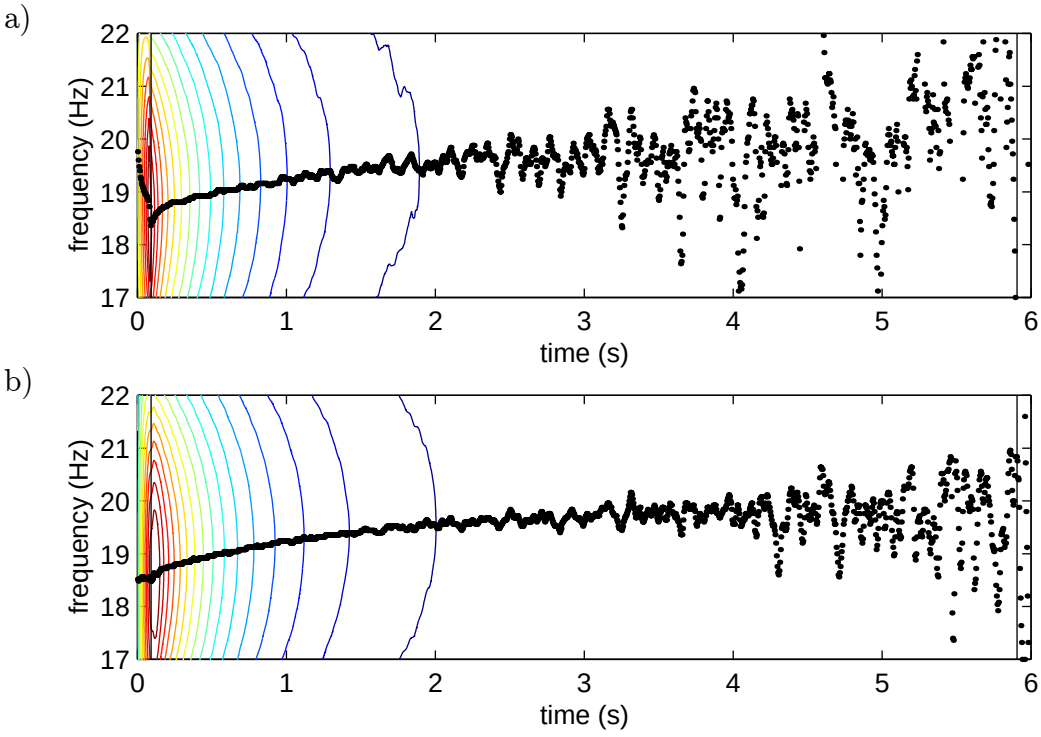

Figure 8.10: DFT moving window, 0.164 s window for a) the ± 50 m/s^2 and b) the ± 10 m/s^2 sensitivity ranges

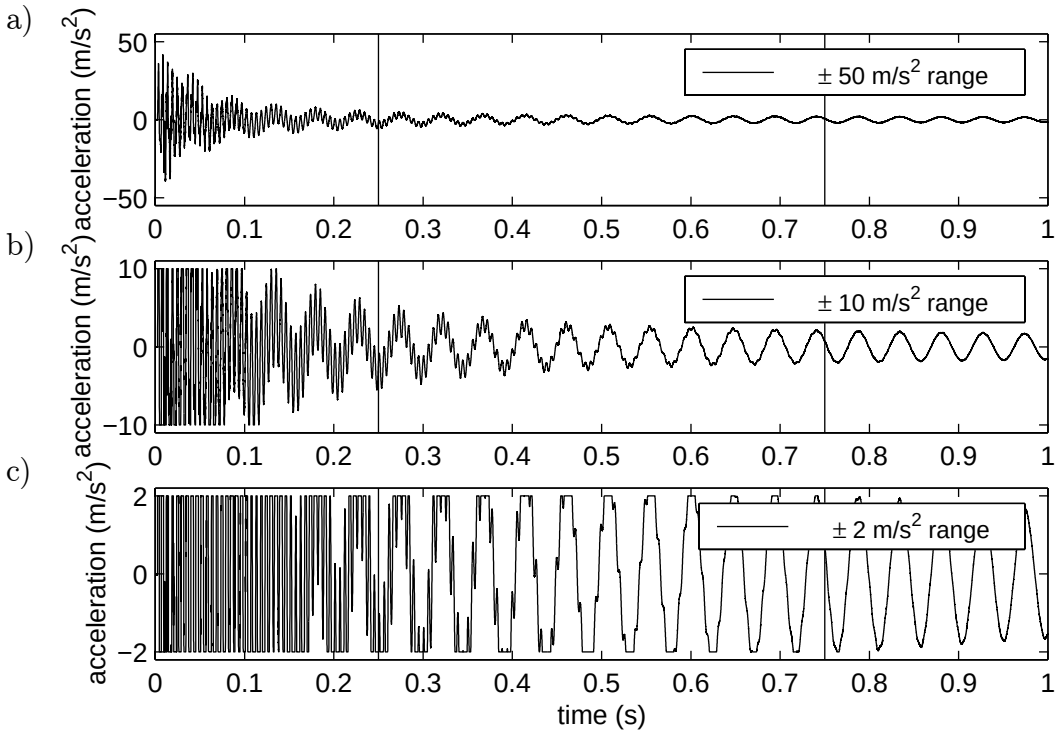

Figure 8.11: Vibration signal for each sensitivity ranges

recorded. Clearly, clipping of the signal when the acceleration goes out of range will lead to a reduction in the amplitude of the frequency peaks, which may alter the positions of the peaks due to a change in the interaction of the side-lobes corresponding to the various modes. This can be seen if a 0.5 s sample of the signal centred at 0.5 s (indicated by vertical lines in figure 8.11) is examined in the frequency domain. Figure 8.12 shows the frequency domain estimation. It can be seen that, as expected, the ± 50 m/s^2 and the ± 10 m/s^2 range signals have the same frequency content. However the ± 2 m/s^2 range signal, which was clipped for about half the window width, has significantly lower fundamental and third mode amplitudes. Therefore, it was necessary to consider all three signals to build up an accurate picture of the time-frequency relationship. This was done by combining the time-frequency distributions of the three signals.

The first step was to define regions over which each signal may be considered accurate. The beginning of the region for the ± 50 m/s^2 range signal was taken to be at $t = 0$. For the other two signals the beginning was when clipping had ended. This point was defined as the maximum time-point at which the magnitude of the signal exceeds

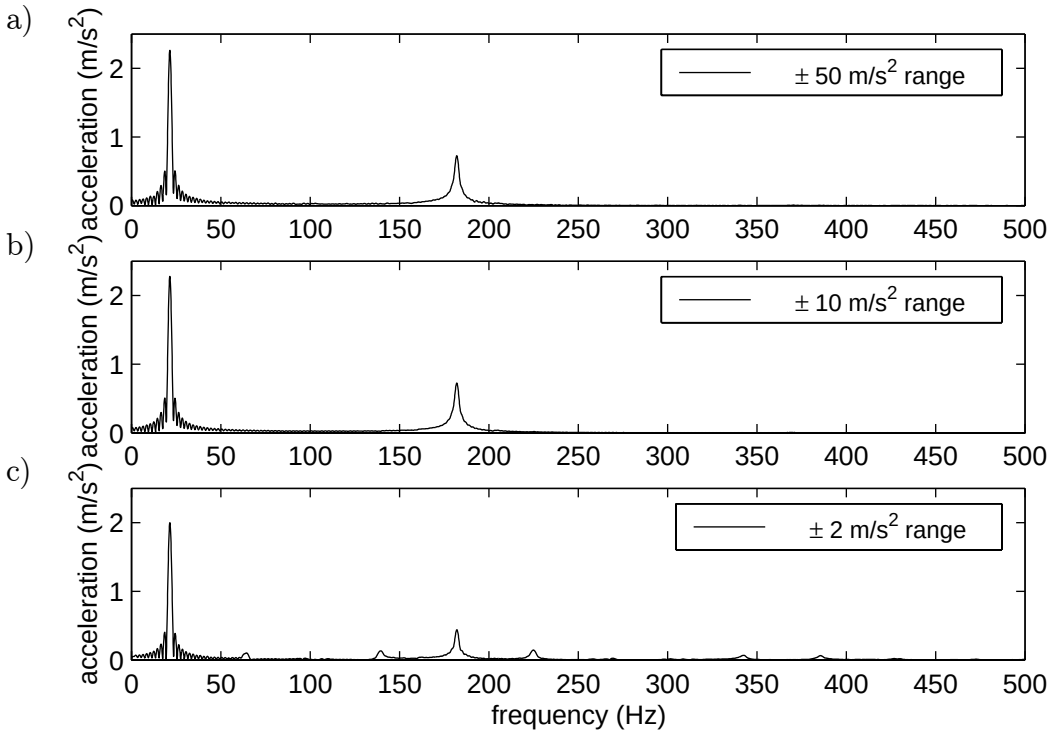

Figure 8.12: Vibration signal lasting 0.5 s centred at 0.5 s in the frequency domain for each sensitivity range

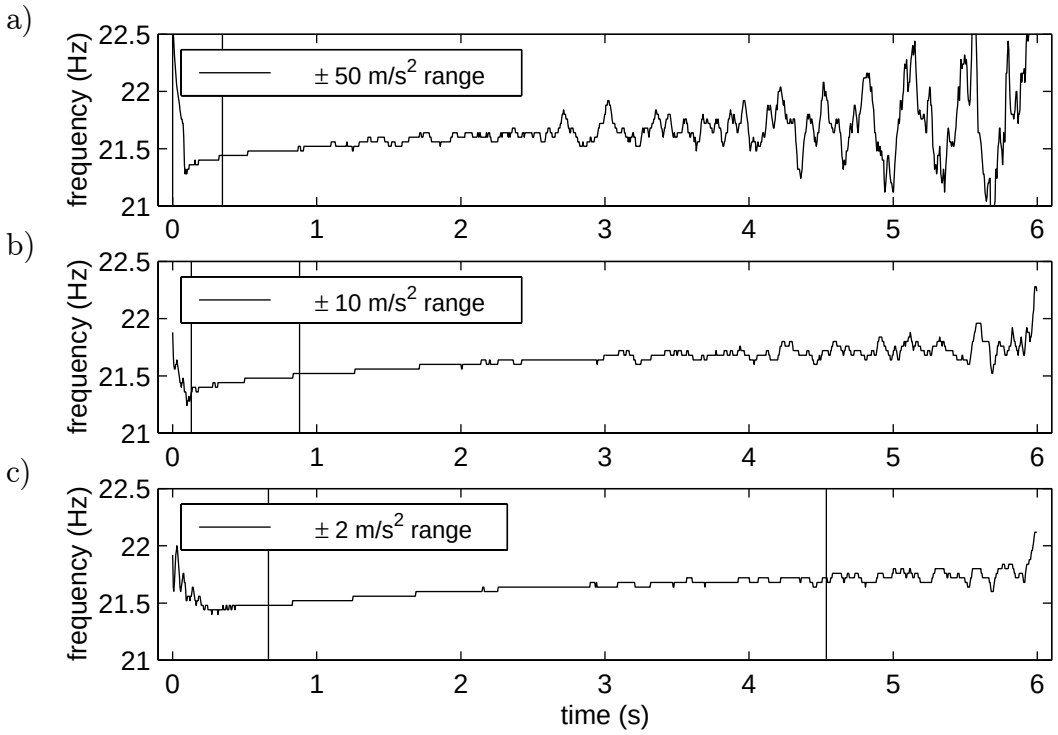

Figure 8.13: Time-frequency plots with valid regions for each sensitivity range

2040 bins (the signal goes out of range at bins 2047 and −2048). The point was found before decimation, since any higher frequency components that are removed during the filtering will contribute to the clipping. The end of the accurate region for the ±2 m/s^2 range signal was taken as being when the amplitude had decayed to an unacceptably low level at which quantisation effects during digitisation become significant. The level selected was ±100 bins. This was done after decimation to ensure that any higher frequencies did not contribute to the amplitude of the signal at this point. The ends of the regions for the other two signals are taken to be at either 50 time-steps after the point where the next more sensitive signal region begins, or when the signal level falls below ±100 bins, whichever was earlier.

Secondly, it was necessary to combine the signals. This was done by averaging the frequency estimation at each data point over the signals which were within their acceptable time range. Figure 8.13 shows the time-frequency estimations for all three sensitivity ranges for an undamaged vibration test with vertical lines indicating the beginning and end of the valid regions. Figure 8.14 shows the resultant combined signal.

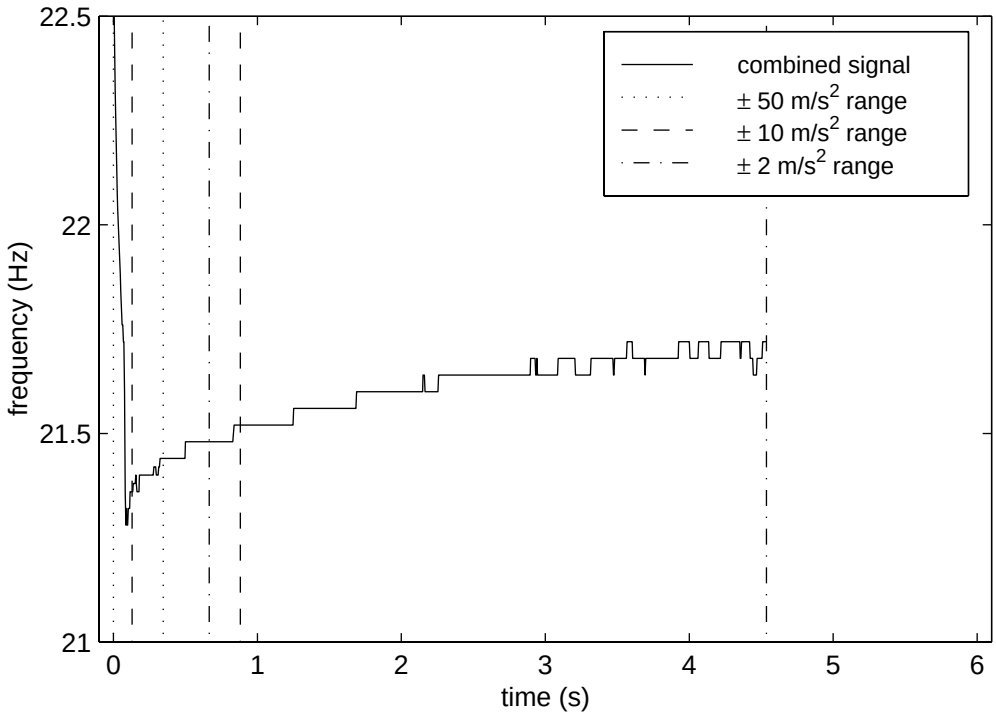

Figure 8.14: Time-frequency relationship using the combined signal

8.2.5 Assessing the Various Time-Frequency Methods

The assessment of the various time-frequency methods described in chapter 3 will be based on a window width in time (or pseudo-time signal for the bilinear distributions) of 0.164 s, the optimum width for the DFT moving window (see section 8.2.3).

As has been seen in section 8.2.2, the vibration signal consists almost entirely of the fundamental mode, higher modes having died away in the first 0.5 s. Therefore, firstly, the fundamental frequency estimation given by each of the methods will be compared using the combination of all three signals of varying sensitivity. A brief comparison of the estimation of the higher modes using the ± 50 m/s^2 range signal will then follow.

The Fundamental Frequency

Before the calculation of the time-frequency characteristics, the vibration signals were decimated to a sample frequency of 25000/108 Hz and converted to analytic form. For the distributions with windows in the time domain, the beginning and end of the signal was zero padded by half the window width to allow a estimation of the frequency at

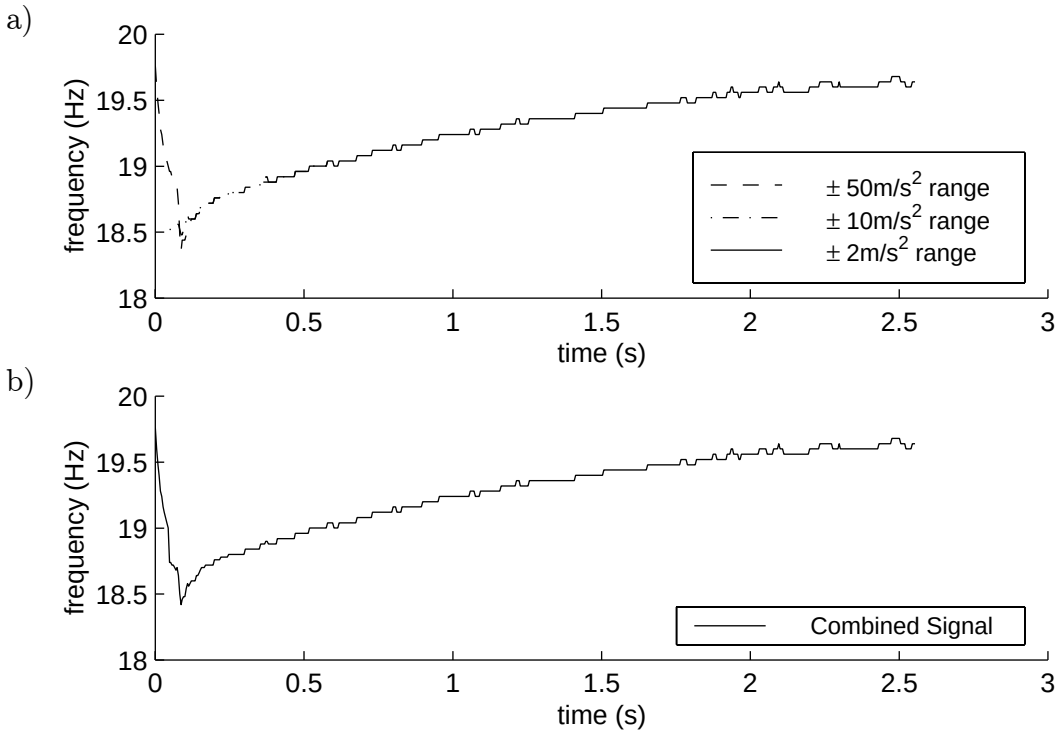

Figure 8.15: Fundamental frequency estimation using DFT moving window, a) separate and b) combined signals

every time-point (as explained in section 3.6.1). The fundamental frequency was then found by looking at the peaks in the time-frequency relationship. A vibration signal recorded at damage level 2 for the mid-span of the beam was used. Figure 8.15 shows the variation of the fundamental frequency with time using the DFT moving window, for each of the three sensitivities and the combination of the three using the valid regions of each. It should be noted that there is a slight step introduced to the time-frequency relationship at approximately 0.06 s when the combined signal is generated. This is due to differing estimations of the frequency depending on which signal is used at this time. This difference is probably due, in turn, to the uncertainties in the estimation of frequencies within the first half window width in time of the signal.

With the DFT moving window (and the other methods with windows in the time or pseudo-time domain), the finite width of the time domain window causes the frequency estimation for time-points at the beginning and end of the signal to be based on fewer non-zero points, as discussed in section 3.6.1. For example, when the moving window

was positioned at time 0 the window spanned −0.082 s to 0.082 s. However, since data are only known after time 0, the first half of the window was assumed to be zeros. This leads to greater uncertainty in the estimation due to a convolution with a wider sinc function than would be expected for the given time window width. The effect reduces with time until 0.082 s, when there will be no zero padding needed to fill the time window. This effect coupled with the fact that, initially, the magnitude of the third mode was far larger than the fundamental mode, probably explains the estimation of an initial decrease in the fundamental frequency. It should also be noted that the conversion to the analytic form of the signal creates some end effects which may affect the initial frequency estimation.

The other time-frequency estimation methods discussed in section 3 are now compared to the combined time-frequency relationship using the DFT moving window. Figure 8.16a shows the peaks in the time-frequency estimation using the AR moving window for the three sensitivity ranges in their valid regions, along with the DFT moving window fundamental frequency estimation for comparison. The AR model used four poles. The fundamental frequency estimation using the AR moving window was very similar to that using the DFT moving window although it was slightly noisier, especially towards the end of the signal. This is possibly because of the additional step to calculate the model coefficients involved when using the AR moving window rather than the DFT moving window. This extra step may add to the noise present in the signal.

Figure 8.16b shows the estimation with the wavelet transform using a window width of 8 Hz. Again the estimation of the fundamental frequency was very similar to the DFT moving window estimation, with the noticeable exception of the first 0.15 s. The problem of the time window initially containing zero padding is eliminated when the wavelet transform is used, since the moving window is in the frequency domain rather than the time domain. However, the wavelet estimation will also be in error, since, as shown in section 3.7.3, towards either end of the time signal the wavelet transform incorrectly predicts the amplitude of the oscillation due to applying the window in frequency. Therefore, up to 0.082 s, more confidence must be placed in the wavelet estimation. In the 0.082 s to 0.15 s region it is likely that the DFT moving window is closer to the correct frequency, since the whole of the time window will contain actual

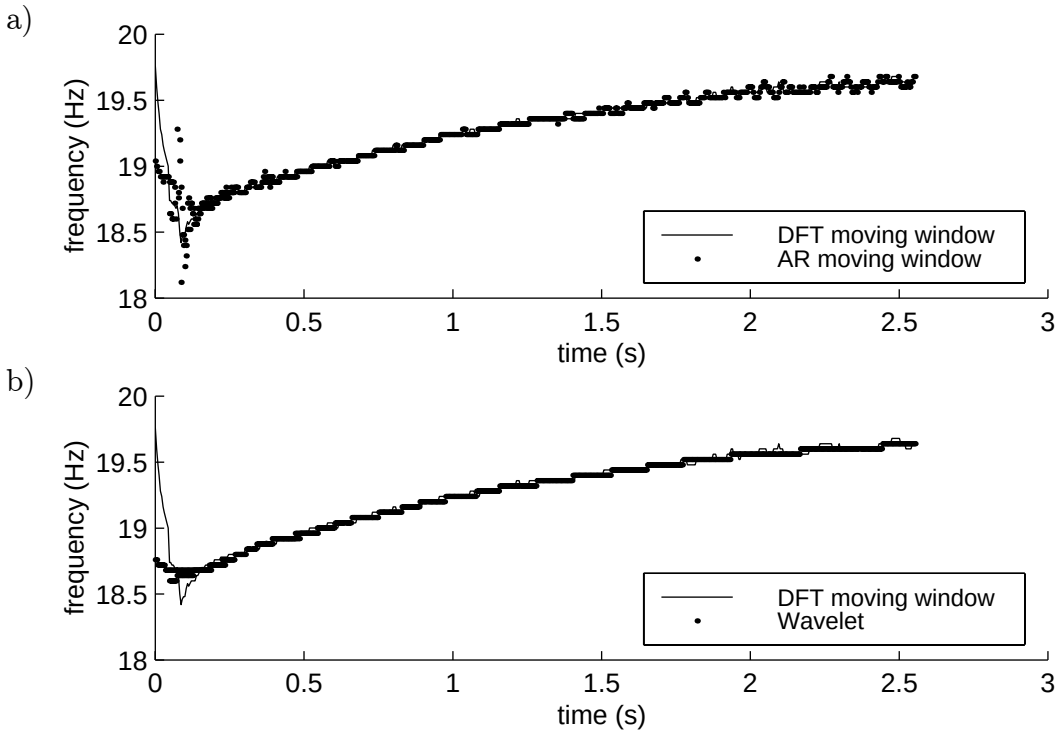

Figure 8.16: Fundamental frequency estimation using a) the AR moving window and b) the wavelet transforms

signal rather than zeros and the wavelet transform will still be affected to some degree by the loss of higher frequency amplitude information. This is demonstrated later, in figure 8.23b, which shows that the wavelet transform predicts the maximum amplitude of oscillation at about 0.133 s.

Figure 8.17a shows the fundamental frequency estimation using the Wigner-Ville distribution. As with the examples in section 3.8.1, the fundamental frequency predicted using the WV distribution is flatter than the estimation using the other methods. This is because of the wide effective time window (due to the finite length of the time signal rather than an imposed window), which leads to the low frequency at the beginning of the signal influencing the estimation of the frequency at later points. It should be noted that the signal used to generate the time-frequency distribution is 6 s long, therefore the initial lower instantaneous frequency of the signal will affect the frequency estimation over all time within the valid region. It is only after 3 s that the initial time-points will not be used to generate the bilinear form of the signal. For example, at 4 s after excitation the bilinear signal will be made up of signal information contained over the

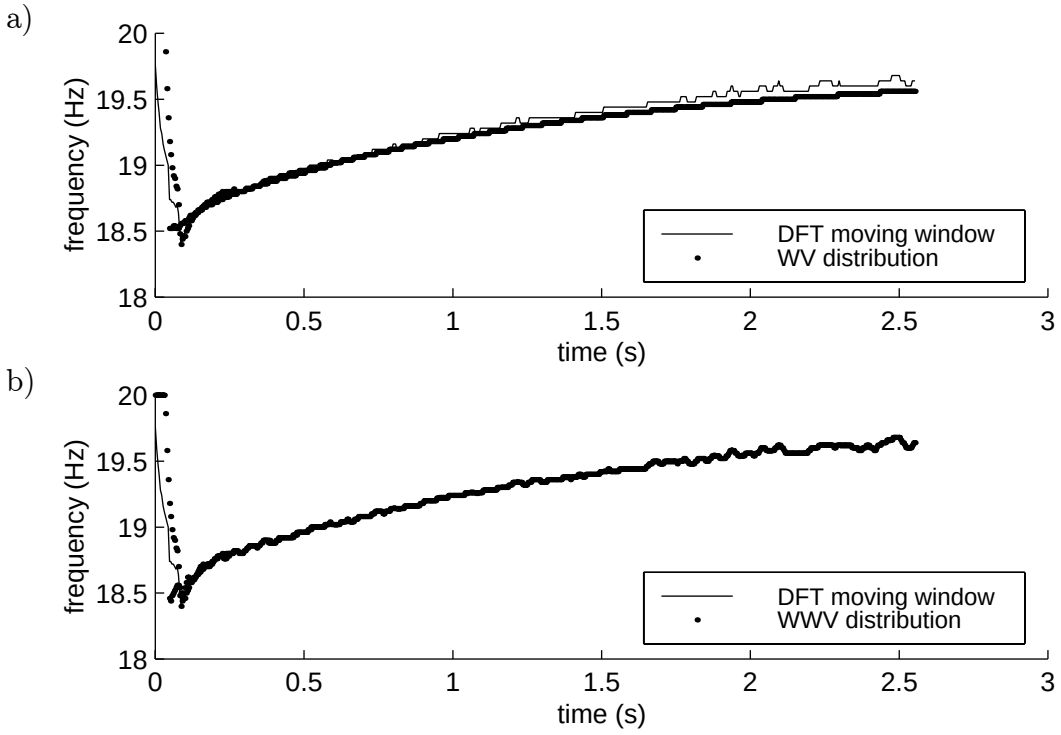

Figure 8.17: Fundamental frequency estimation using a) the WV and b) the WWV distributions

range $2 < t < 6$ s, since the signal at a time-point before $t = 2$ s is multiplied by the signal at a time-point after $t = 6$ (which is taken to be 0) in the transformation into pseudo-time (equation 3.64).

Figure 8.17b shows the estimation using the windowed Wigner-Ville distribution. The effect of applying the time windowing to the WV in this case is to limit the influence of the initial lower frequencies. Due to the windowing, the instantaneous frequency at time t may only affect the frequency estimation over the range of $t-0.082$ to $t+0.082$ s. The estimation of the fundamental frequency is very similar to that using the DFT moving window.

Finally figure 8.18a shows the estimation using the modified exponential distribution. Again, this is very similar to the DFT moving window estimation.

In summary, the fundamental frequency estimations, which employs the valid zones for each sensitivity range, are very similar using either the DFT moving window, the wavelet transform, the WWV distribution or the ME distribution, as can be seen in

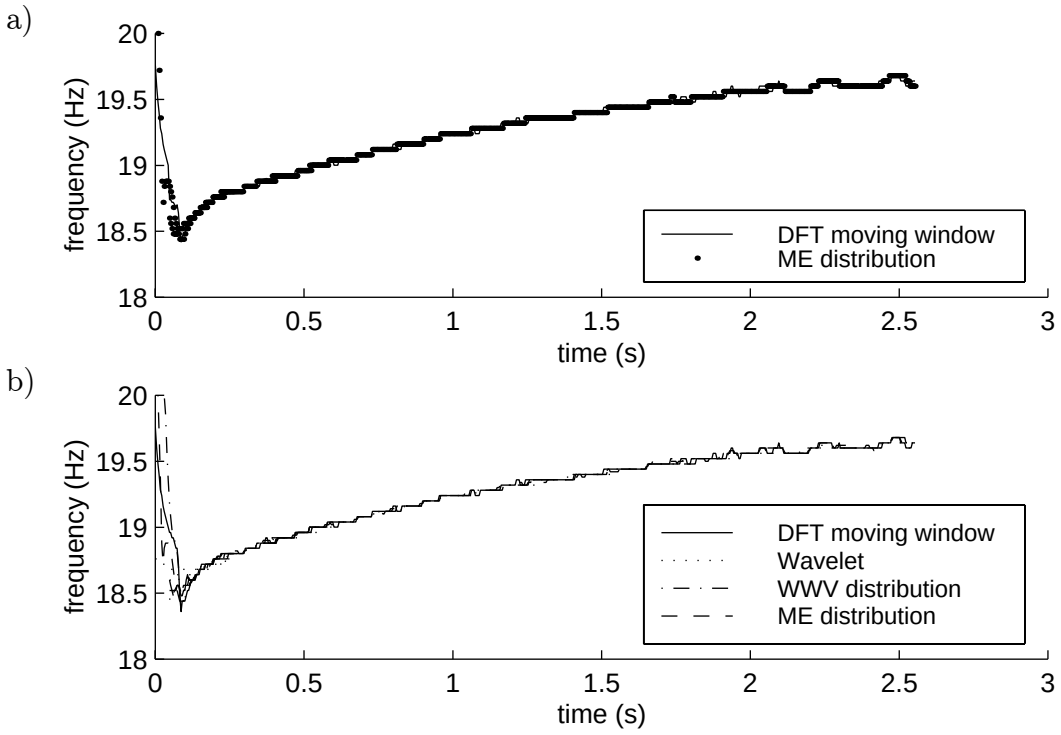

Figure 8.18: Fundamental frequency estimation using a) the ME distribution and b) a comparison of several time-frequency estimation methods

figure 8.18b. If the AR model is used within a moving window very similar results are also obtained, only the estimation is noisier. The WV distribution estimation is poor due to the influence of the low instantaneous frequencies at the start of the signal over the rest of time within the valid regions. Therefore, since it is computationally fastest, the DFT moving window will be used to predict the instantaneous fundamental frequency. The initially better estimation by the wavelet transform is unimportant for the data analysis, as it has already been shown that the supports move for the first 0.5 s and so these data cannot be relied upon.

Higher Modes

The second and third modes are not of direct interest since they have almost completely decayed away by 0.5 s, the time at which the beam may be assumed to be simply-supported. However, it is interesting to look at how the various distributions perform when calculating these modes. Figure 8.19 shows the effect of applying the moving window DFT to the first second of a signal for damage level 2 at the quarter-span point. The contour lines for each plot are based on the region within the plot, so the contour line for a certain magnitude may not be compared across plots. Figure 8.20 shows the frequency content of the signal over the whole 1 s period. These plots show that the second mode was too small to allow the frequency to be found with any confidence. Therefore the comparison of various methods concentrates on the third mode using the first second of the mid-span signal at damage level 2. The signal sample frequency after decimation was 25000/18 Hz. This gives a Nyquist frequency of 694.5 Hz. When it is noted that the maximum frequency content for the WV and the WWV distributions is a quarter of the sampling frequency, the maximum frequency after filtering for these distributions is 347.2 Hz.

Figure 8.21 shows the estimation of the first and third modes using the DFT moving window. The contour lines show that, initially, the amplitudes of both modes increases. Clearly this is not the case, but is an artefact of the zero padding, as has been explained earlier. Therefore, at time-points before 0.082 s (the half-width of the time window), the amplitude of the estimation can only be compared over frequency for particular time-points. It is possible to scale the predicted amplitude to take the zero padding into

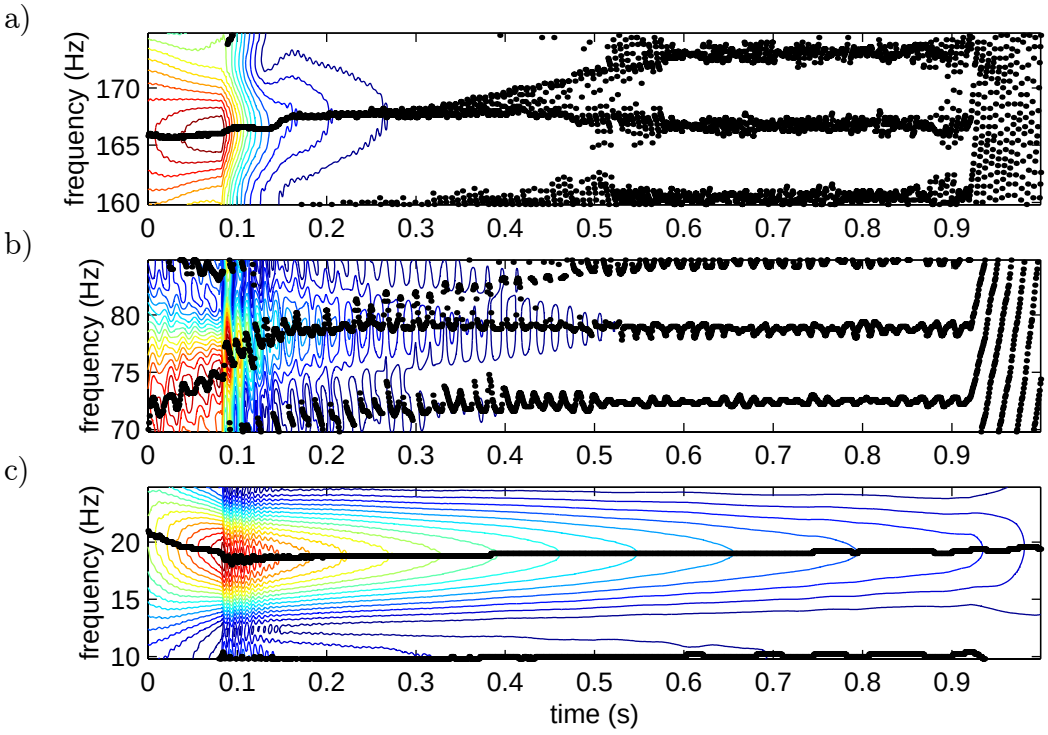

Figure 8.19: Time-frequency characteristics at the quarter-span point for the beam 6, damage level 2 using the DFT moving window for a) the third, b) the second and c) the first mode

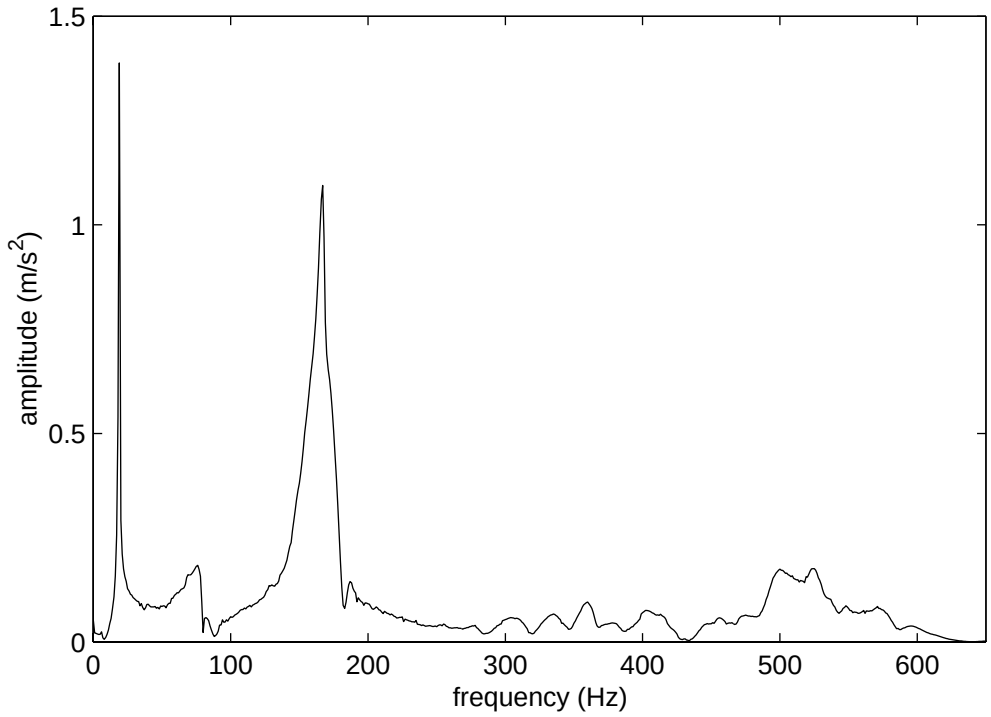

Figure 8.20: Frequency content of the first 1 s of signal at the quarter-span point

account. However this is not done here as it is less clear how this may be achieved with the ME distribution. It is clear that after around 0.2 s the amplitude of the third mode is too small to allow the frequency to be tracked, although it is likely that before 0.2 s the side-lobe interferes with the frequency estimation of the third mode. The moving window using the AR model with 10 poles, figure 8.22, predicts a very similar third mode characteristic, but a noisier fundamental mode estimation. Fewer poles reduce the noise in the region of the fundamental frequency but lead to a worse estimation of the third mode. Figure 8.23 shows the estimation of the fundamental and third modes using the wavelet transform with a window width of 4 Hz. The elimination of the problem of zero padding the time window present in the time windowed distributions suggests that the frequency estimations over the first 0.082 s are likely to be superior to those derived using the other distributions. However, the agreement with the estimations for the frequency of the third mode using AR and DFT moving windows for later times is poor.

The WWV distribution for the signal is shown in figure 8.24. There are more side-

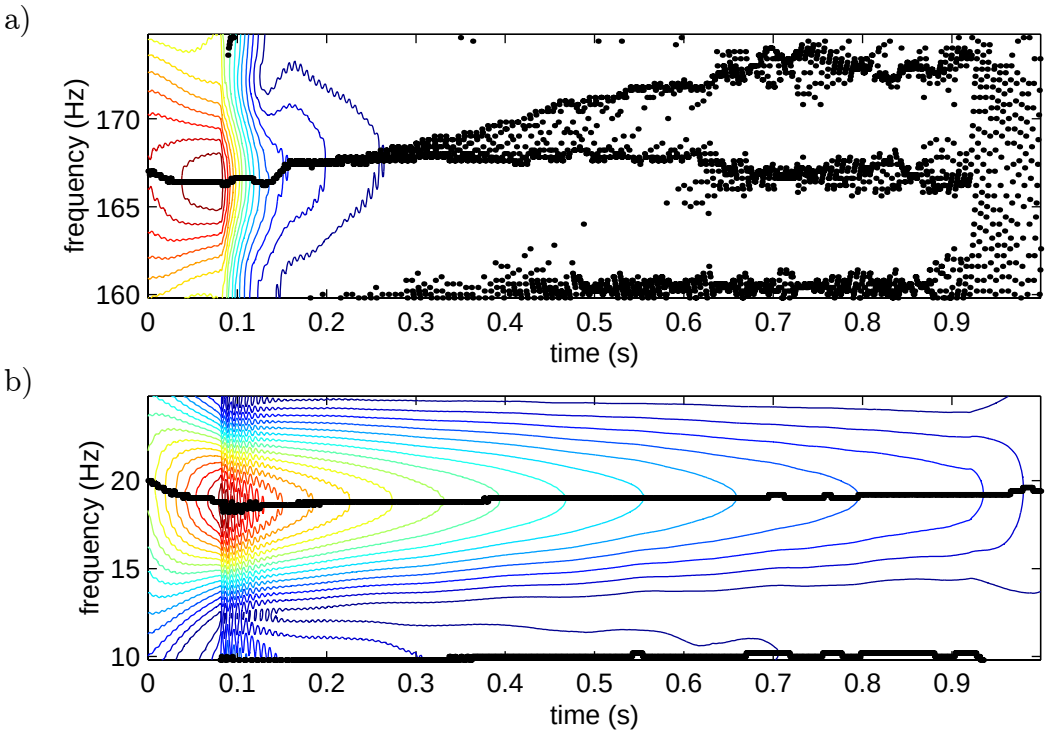

Figure 8.21: Time-frequency characteristics at the mid-span point for the beam 6, damage level 2 using the DFT moving window for a) the third and b) the first mode

lobes than with the other distributions. However this is due to the fact that the bilinear signal is used. As was explained on page 78, the equation for $P_{\text{wwv}}(k, m/2)$ is the DFT of $R_{\text{wwv}}(k, n)$, therefore the frequency calculated for bin m in the discrete Fourier transform corresponds to bin $m/2$ in the time-frequency distribution. This effectively compresses the width of the peaks of the sinc function (which is convolved with the frequency content because of the windowing in pseudo-time) by a factor of two. This is shown in the contours of the fundamental frequency, which are far narrower than for the other distributions and thus permitting better confidence in the estimation, but with the knock-on effect of having closely spaced side-lobe peaks. This effect is not present in the ME distribution (figure 8.25) which uses the anti-alias version of the bilinear signal.

It should be noted that the amplitude of the Cohen distributions decays more quickly than the moving window distributions, as the signal is entered into the calculation of the pseudo-time signal twice and so predicts an energy rather than an amplitude.

Although the distributions predict broadly similar behaviour for the third mode,

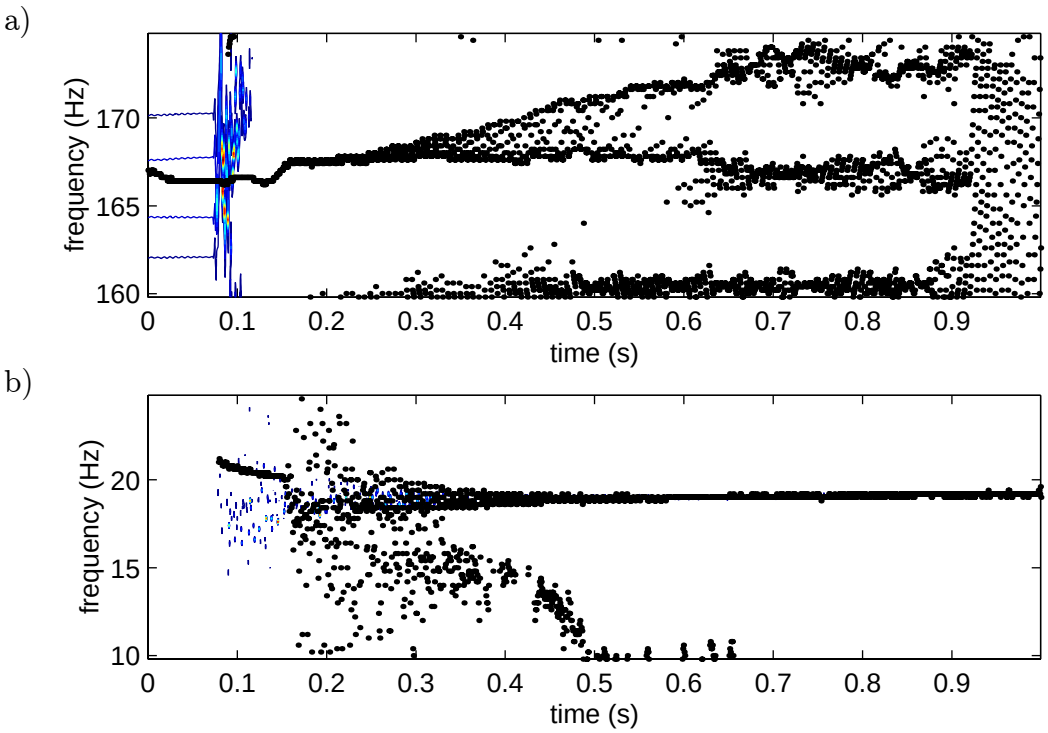

Figure 8.22: Time-frequency characteristics at the mid-span point for the beam 6, damage level 2 using a moving window with a 10 pole AR model for a) the third and b) the first mode

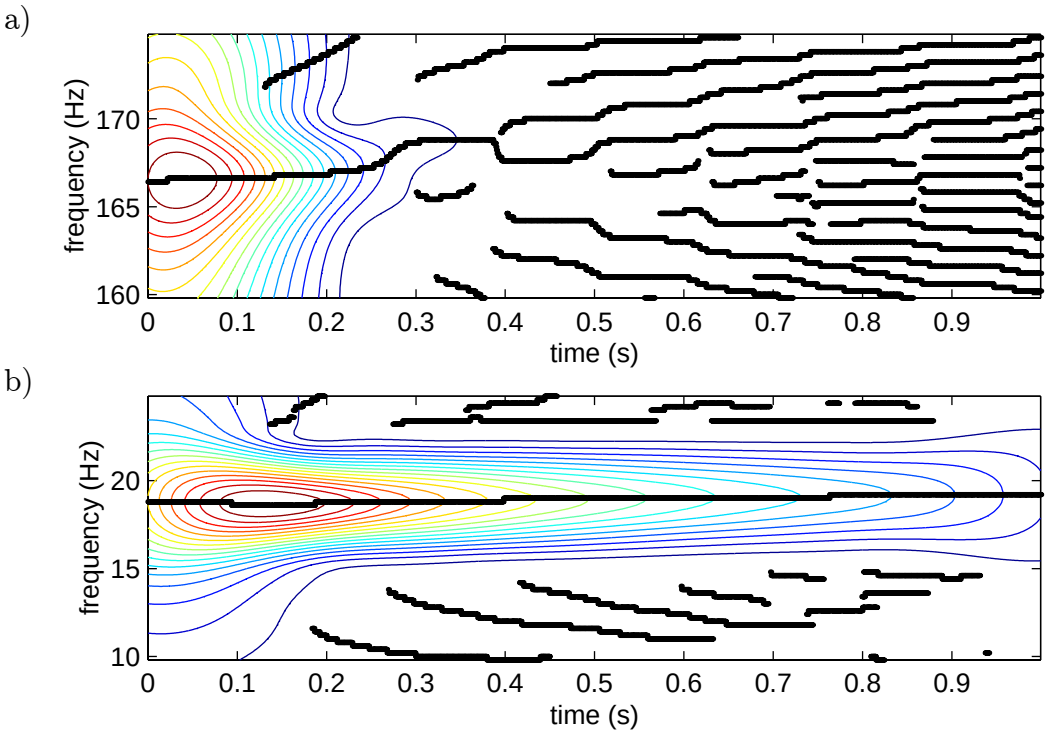

Figure 8.23: Time-frequency characteristics at the mid-span point for the beam 6, damage level 2 using the wavelet transform for a) the third and b) the first mode

the predictions are not the same. One method of assessing the effect of side-lobes on the frequency estimation is to look at the change in the estimation with a change in window width. This will produce a combination of two effects; firstly, a change in the width of the peaks in the sinc function which allows the assessment of side-lobe interference with the predicted frequencies, and secondly a change in the "averaging" of the instantaneous frequencies of the signal over the time window. Figure 8.26 shows the DFT moving window estimation using a 50% shorter time window. It clearly shows that the estimation of the time-frequency relationship for the third mode was altered by the change in window width. Therefore little confidence may be attached to this estimation. In contrast, the fundamental frequency estimation remains almost unchanged, with the exception of the first half window width in time.

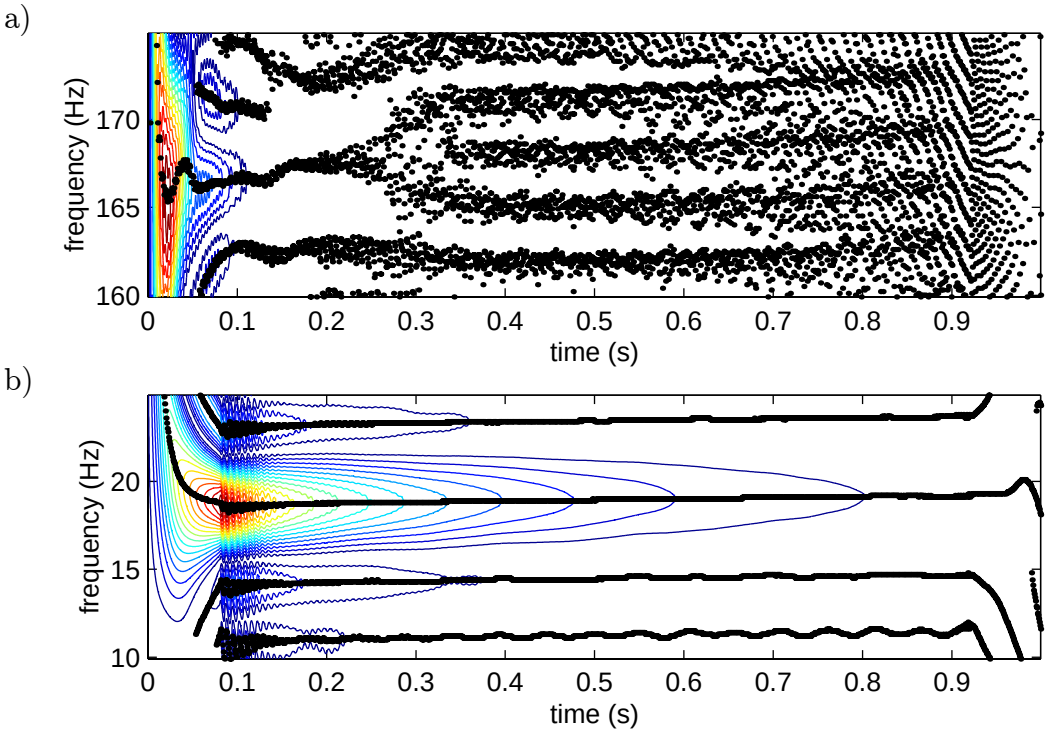

Figure 8.24: Time-frequency characteristics at the mid-span point for the beam 6, damage level 2 using the WWV distribution for a) the third and b) the first mode

Summary

The impulse response signal at the central accelerometer was examined using the DFT moving window with a window width of 0.164 s. The signal was decimated to a sample frequency of approximately 230 Hz. The time-frequency relationship for the fundamental mode was made up of the three signals of different sensitivity with a small overlap between the signals which were averaged in the combined relationship.

Since only the fundamental mode is of interest, the quarter-span acceleration signals were not used. The first 0.5 s of the signal was discarded since the second and third modes are present over this time and the beam may not be considered to be simply-supported. In section 8.2.2 it was stated that the results would be easier to interpret if only the fundamental mode is present. The significance of the higher modes being present during the first 0.5 s is discussed further in the next section.

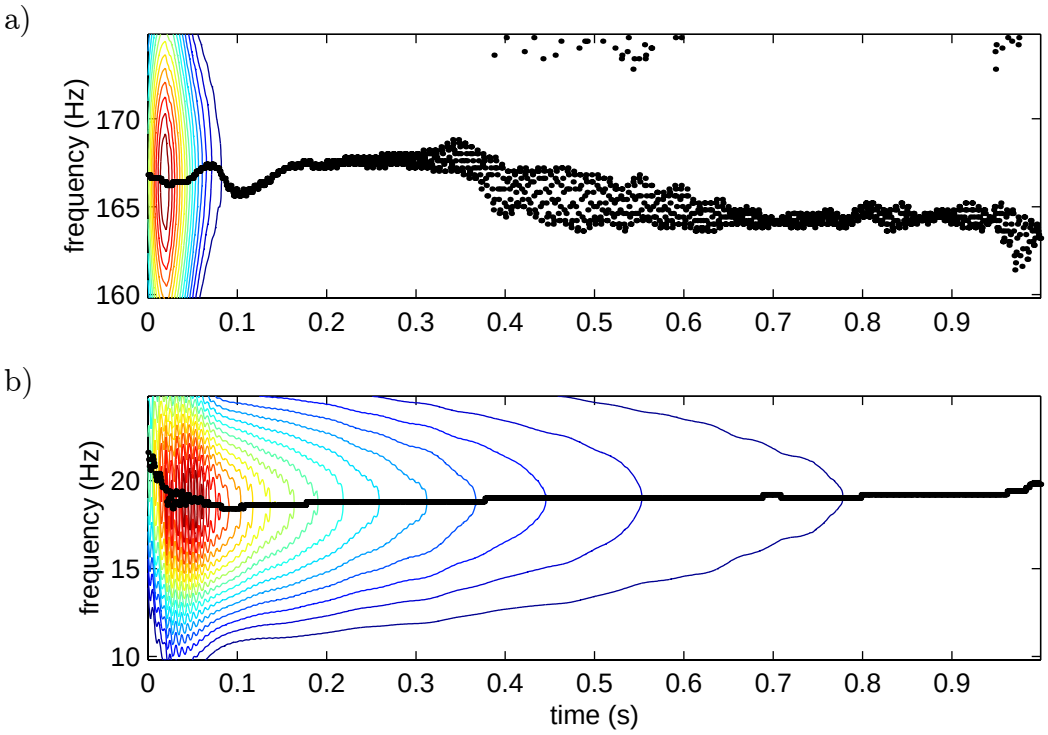

Figure 8.25: Time-frequency characteristics at the mid-span point for the beam 6, damage level 2 using the ME distribution for a) the third and b) the first mode

8.2.6 Signal Amplitude

The drawback with using the time-frequency relationship to assess changes in non-linearity with increasing damage is that damage affects the damping properties of the beam (Casas and Aparicio [15] and Salawu and Williams [98]). In section 5.2, the possible non-linear crack mechanisms were mainly due to frictional effects, so it follows that increased damage which would alter these frictional effects would also alter the damping (either linearly or non-linearly). It is therefore useful to plot the instantaneous frequency against the amplitude of oscillation rather than against time. It has already been stated that after around 0.5 s the vibration consists almost entirely of the fundamental mode, therefore the (displacement) amplitude of the vibration relates to the amplitude of the fundamental mode. It has been shown by several authors that damage does not significantly affect the mode shapes (see for example Das *et al.* [26]). Therefore, the maximum curvature over an oscillation may be related to the maximum amplitude over that oscillation.

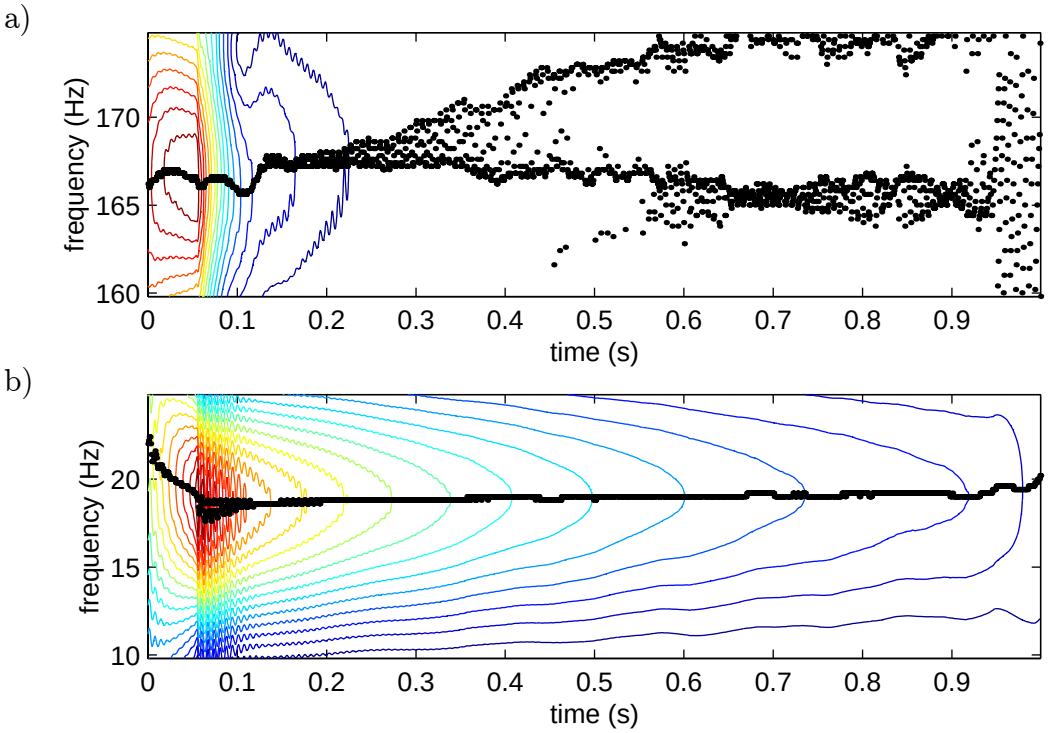

Figure 8.26: Time-frequency characteristics at the mid-span point for beam 6, damage level 2 using the DFT moving window, for a) the third and b) the first mode, with the window reduced to 2/3 normal size

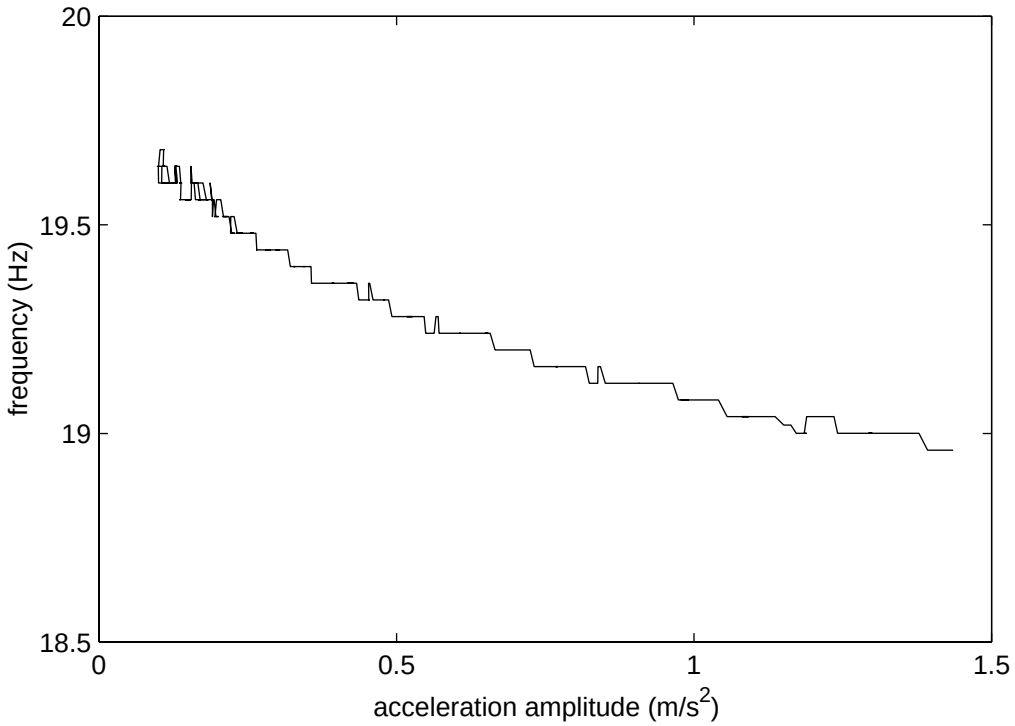

Figure 8.27: Amplitude-frequency characteristics of beam 6, damage level 2

The amplitude of the acceleration of the vibration is calculated by taking the magnitude of the analytic signal. The three different resolution signals are combined into one in the same way as for the fundamental frequency estimations. If it assumed that over any one cycle the vibration is sinusoidal, it is then possible to convert the magnitude of the acceleration to a displacement using the instantaneous frequency estimation.

Figure 8.27 shows the amplitude-frequency plot for an impact response of beam 6 at damage level 2 using the combined signal. It is plotted for time-points greater than 0.5 s so that effects due to higher modes and movement of supports are minimised.

8.2.7 Damping

Following on from the previous section, as damage alters the damping properties of the beam, it is possible that damping could be used as an indicator of non-linearity in the vibration response. If the beam stiffness properties are linear, it is expected that the decay is exponential. Therefore, a plot of the amplitude on a logarithmic scale against time would produce a straight line. Figure 8.28 shows this plot for an impact response

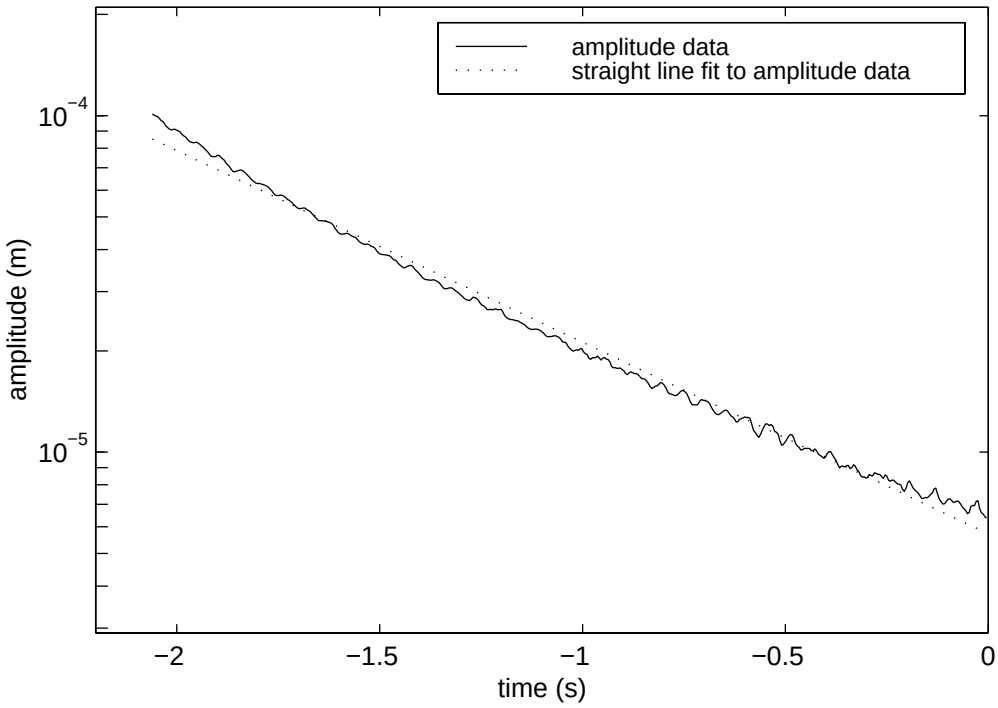

Figure 8.28: Damping characteristics for beam 6, damage level 2

of beam 6 at damage level 2 using the combined signal. The line has a clear curve which indicates some non-linearity in the beam behaviour. The time axis is shifted so that the point where the amplitude falls below 100 bins for the most sensitive range (the end of the valid region for this signal) is at 0 s. This will allow compensation for any variation in hammer impact force when several tests are plotted.

8.2.8 Averaging Several Impacts

To produce more reliable trends averaging over several impacts must occur. The averaging was performed on the combined signal.

For the time-frequency plots, the time axis was shifted for each test so that the end point of the valid region of the most sensitive signal was at time zero. Then the frequency was averaged at each time-point across the tests. Figure 8.29a shows the individual plots and the resulting averaged plots for six tests for beam 6 in its undamaged state.

For the amplitude-time plots, the displacement amplitude was calculated from the acceleration amplitude and the instantaneous frequency, then this was averaged across

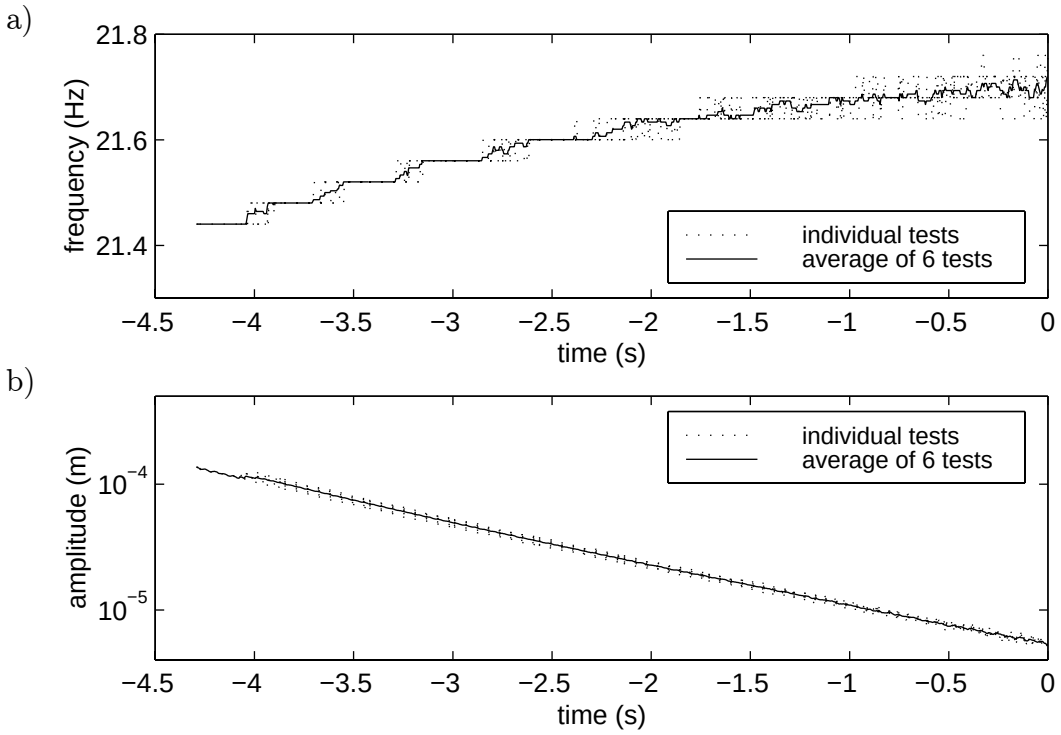

Figure 8.29: Averaging a) the frequency and b) the amplitude trends over time for six tests, beam 6, undamaged

the tests for each point along the shifted time scale. Figure 8.29b shows the individual and the average plots.

For the case of the amplitude-frequency plots, the averaging had a slight complication. Both the frequencies and the acceleration amplitudes were known at specific time bins. Therefore, it was necessary to interpolate the frequency over the amplitude range to generate a vector of frequencies at specific amplitudes. Then it was possible to average the frequency over each acceleration amplitude point. The displacement amplitude could then be calculated using the averaged acceleration amplitude and the averaged instantaneous frequency. An example of this is shown in figure 8.30.

8.3 Vibration Tests: Analysis

It is now possible to analyse the fundamental time-frequency trends predicted using the DFT moving window. For each damage level, the average of six tests will be used.

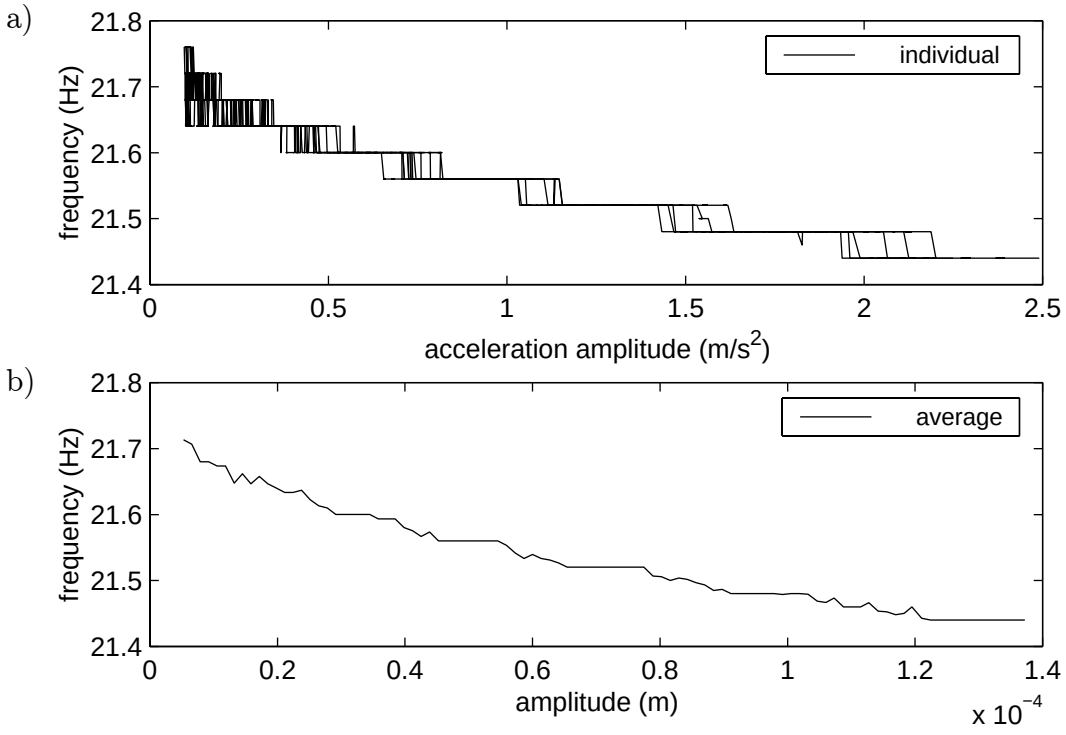

Figure 8.30: Amplitude-frequency relationship for a) individual tests and b) average of six tests, beam 6, undamaged

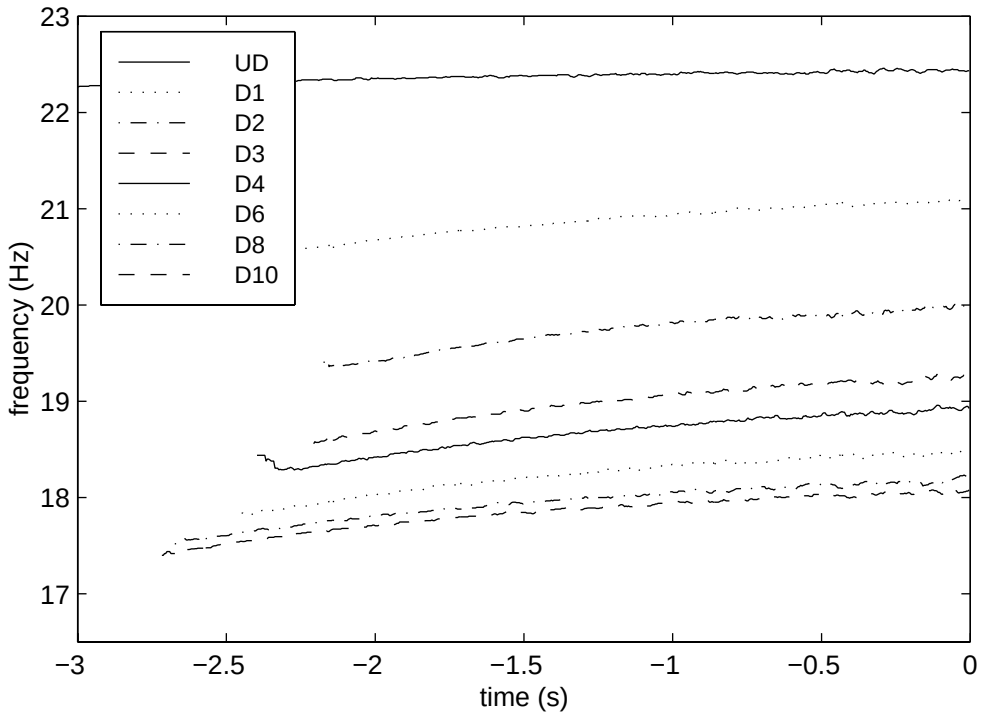

Figure 8.31: Comparison of time-frequency relationships for beam 5

8.3.1 Time-Frequency Relationship

Figure 8.31 shows the averaged time-frequency characteristics of the combined vibration signal of beam 5 for increasing damage levels. Some of the higher damage levels have been omitted for clarity. There is a clear drop in natural frequency at every damage level, which is consistent with published work on damage detection using changes in frequency assuming linear behaviour (see, for example, Eccles *et al.* [30]). The undamaged beam has some non-linear behaviour, and initially with increasing damage there appears to be a rise in the non-linearity indicated by a steeper gradient. However, above damage level 3 this trend appears to reverse and the non-linear effects reduce. The same trend is present in beam 6, shown in figure 8.32.

8.3.2 Frequency-Amplitude Relationship

It has already been mentioned that damage changes the damping characteristics of the beam. To remove the effect of a change in damping from the vibration characteristics, the fundamental frequency estimation can be plotted against amplitude which relates

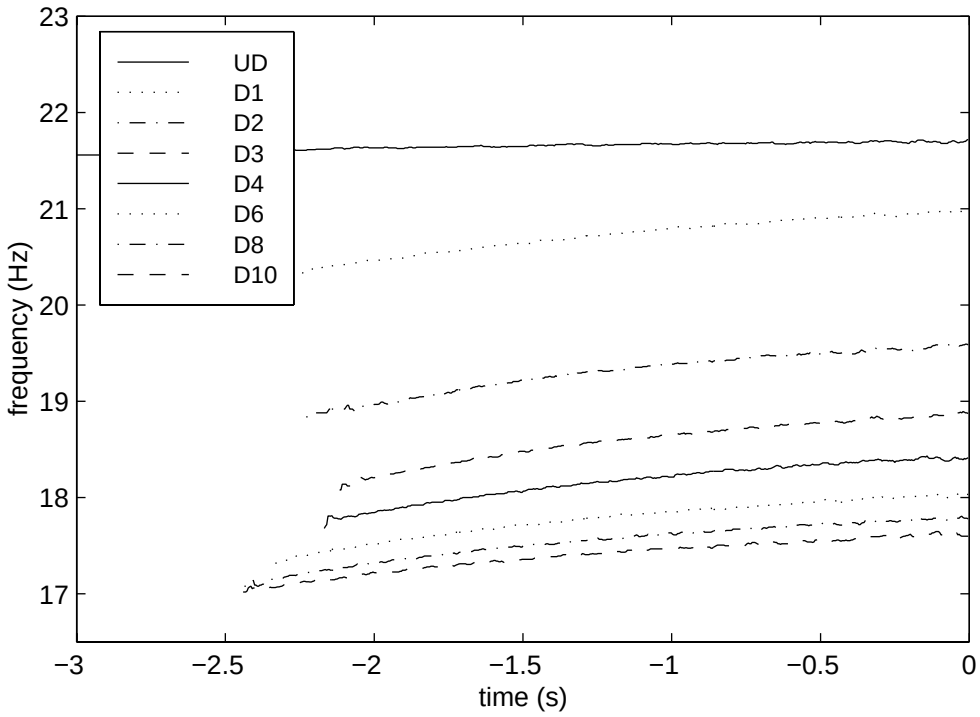

Figure 8.32: Comparison of time-frequency relationships for beam 6

more directly to curvature of the beam. Figures 8.33 and 8.34 show the amplitude-frequency characteristics of beam 5 and beam 6 respectively for increasing damage. However it is difficult to see the changes in any non-linear behaviour because of the changes in the overall frequency at each damage level.

To aid the comparison of non-linearity for different damage levels, the overall change in frequency must be removed. This was done by subtracting the final frequency (the instantaneous frequency at the end of the valid region of the most sensitive signal) from the instantaneous frequency. The relationships are plotted in figures 8.35 and 8.36 for beams 5 and 6 respectively. Figure 8.35a demonstrates that there was a large increase in non-linearity when the beam was loaded to the first damage level. Then there was a slight increase with subsequent damage levels up to level 3. Figure 8.35b shows that above damage level 3 there was a reduction in non-linearity with damage of similar magnitude to the increases from damage level 1 to 3. Damage level 3 is plotted on both graphs for comparison. The trend is very similar for beam 6, figure 8.36.

For beam 6 an additional damage level, mid-way between undamaged and damage

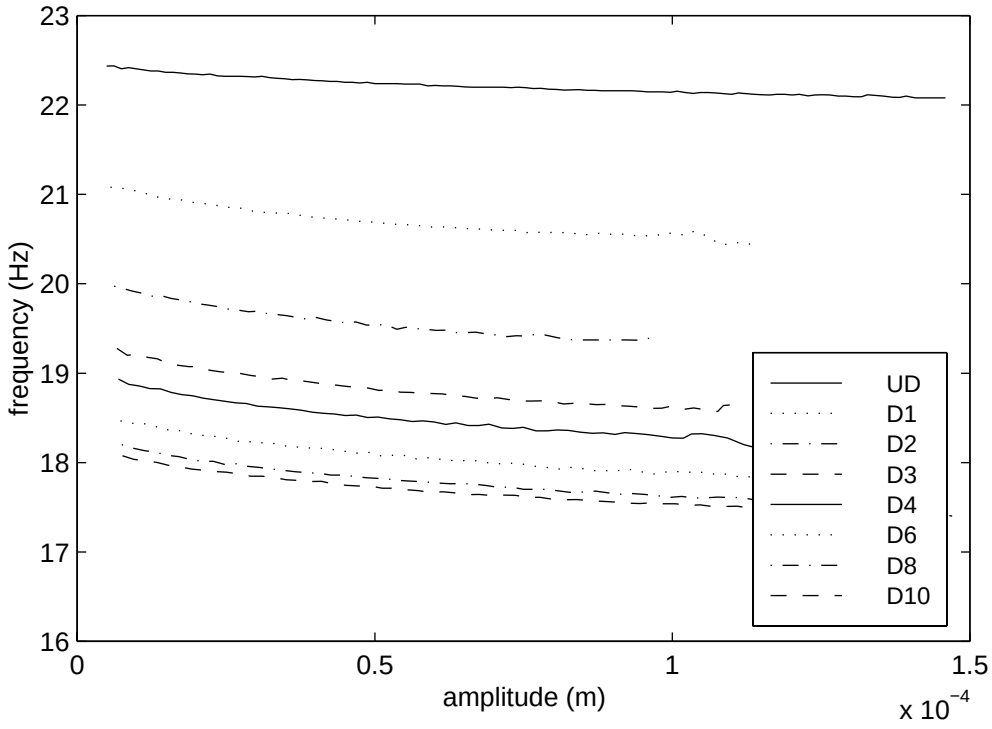

Figure 8.33: Comparison of frequency-amplitude relationships for beam 5

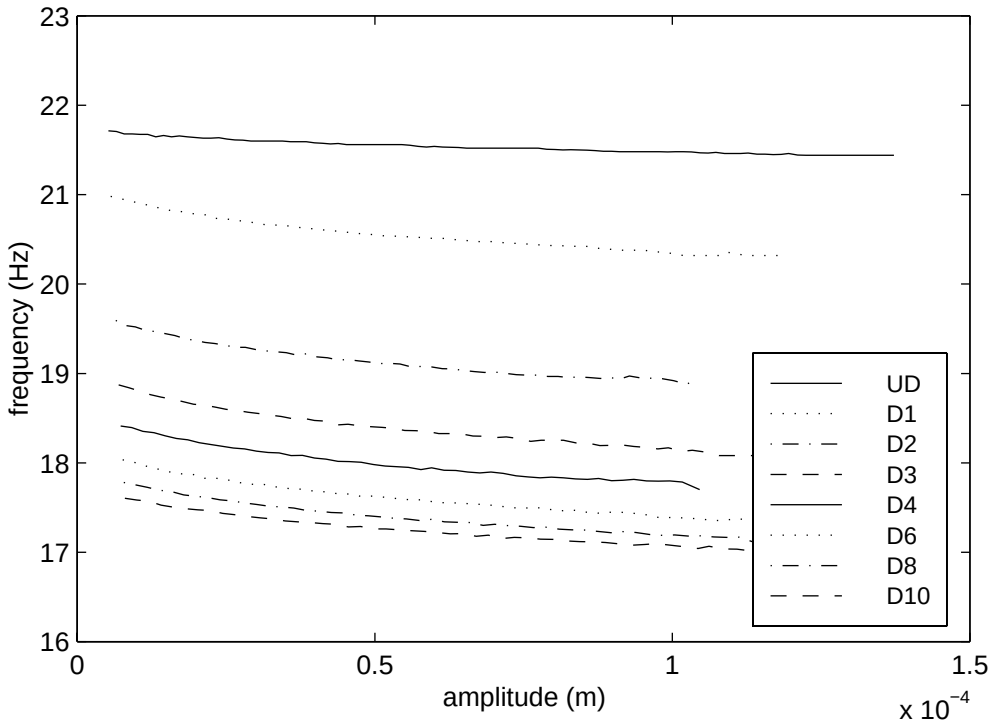

Figure 8.34: Comparison of frequency-amplitude relationships for beam 6

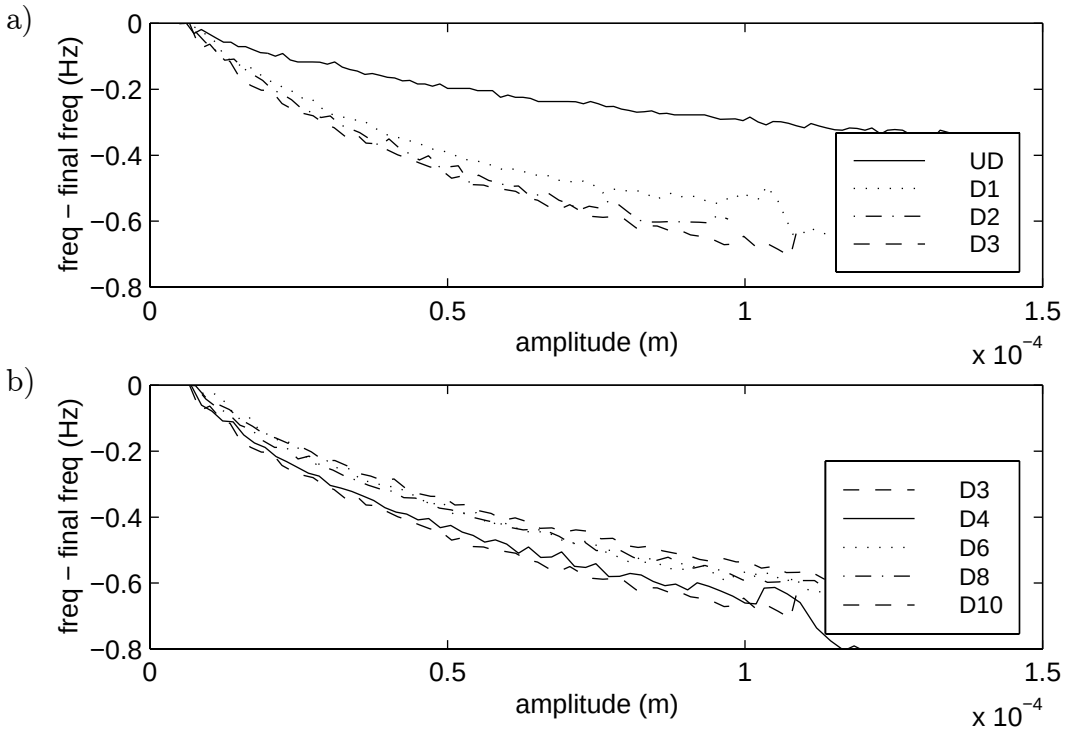

Figure 8.35: Comparison of the non-linear amplitude-frequency relationships for beam 5

level 1 (i.e. a load of 750 N) was added, labelled damage level 0.5. Figure 8.37 shows this additional damage level, indicating that the sudden change in non-linearity occurs between damage levels 0.5 and 1.

For completeness, the final frequencies for both beams are plotted in figure 8.38. They demonstrate the initially rapid change in natural frequency which then starts to level off for increasing damage, as reported in studies which assume linear behaviour, such as Eccles *et al.* [30].

8.3.3 Damping

These changes in non-linearity with damage are confirmed if changes in damping are inspected. Figures 8.39 and 8.40 show amplitude plotted on a logarithmic scale against time. Any change in the overall gradient is due to a change in overall damping which would show up using linear analysis. An increase in non-linearity is indicated by an increase in curvature of the line which demonstrated an increased rate of change in

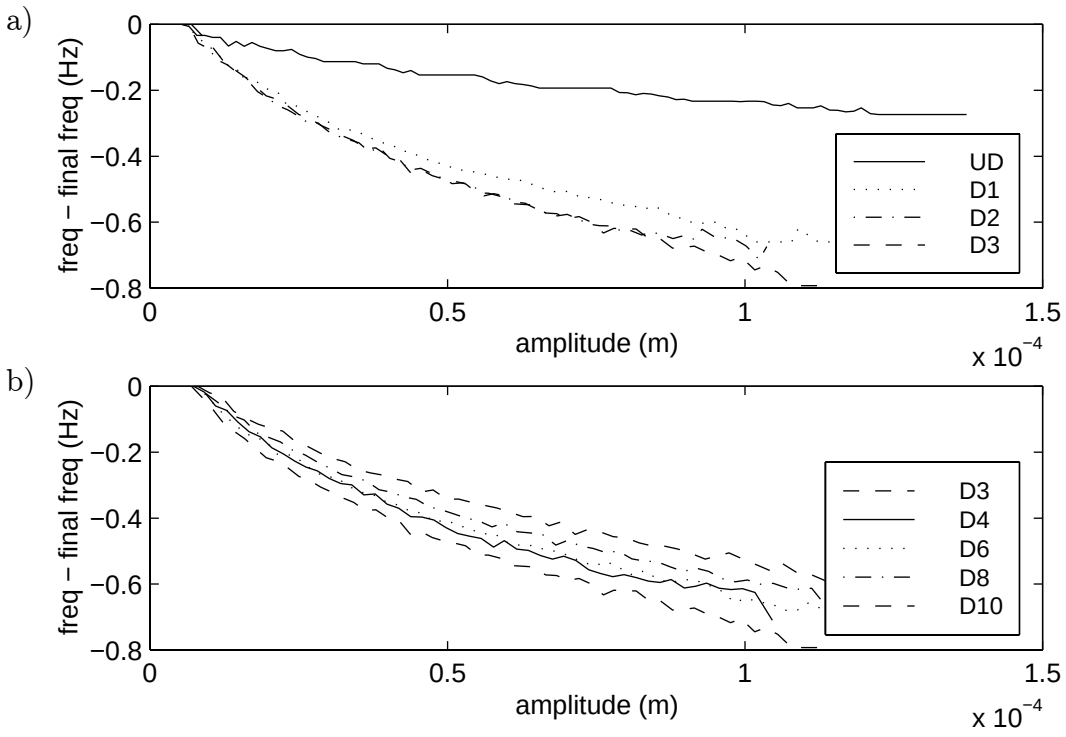

Figure 8.36: Comparison of the non-linear amplitude-frequency relationships for beam 6

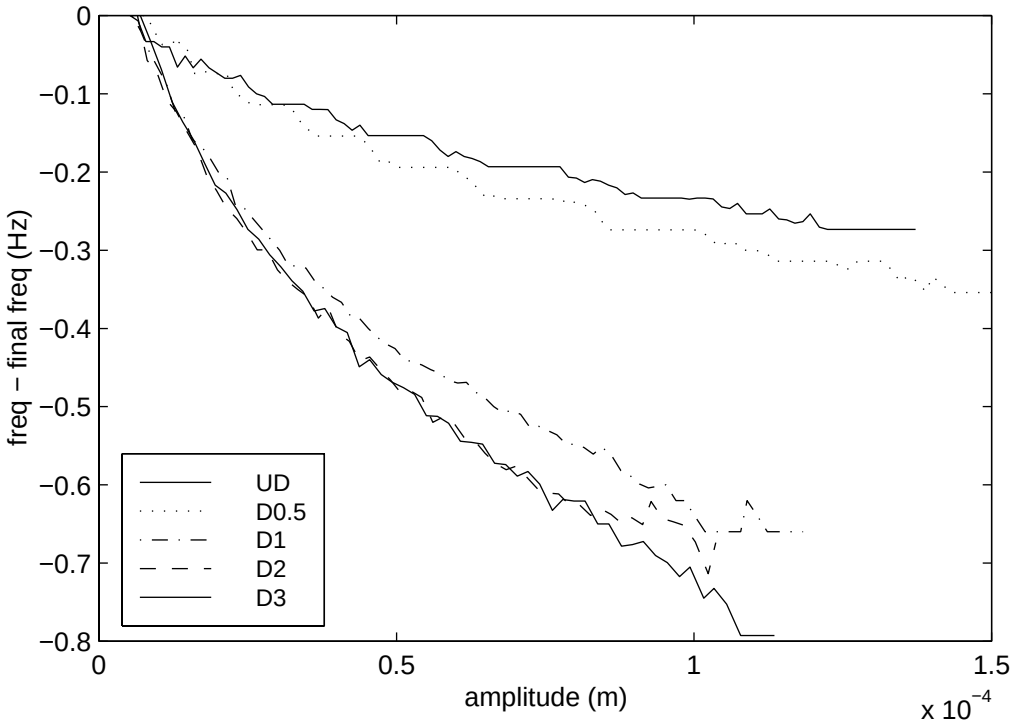

Figure 8.37: Damage level 0.5, beam 6

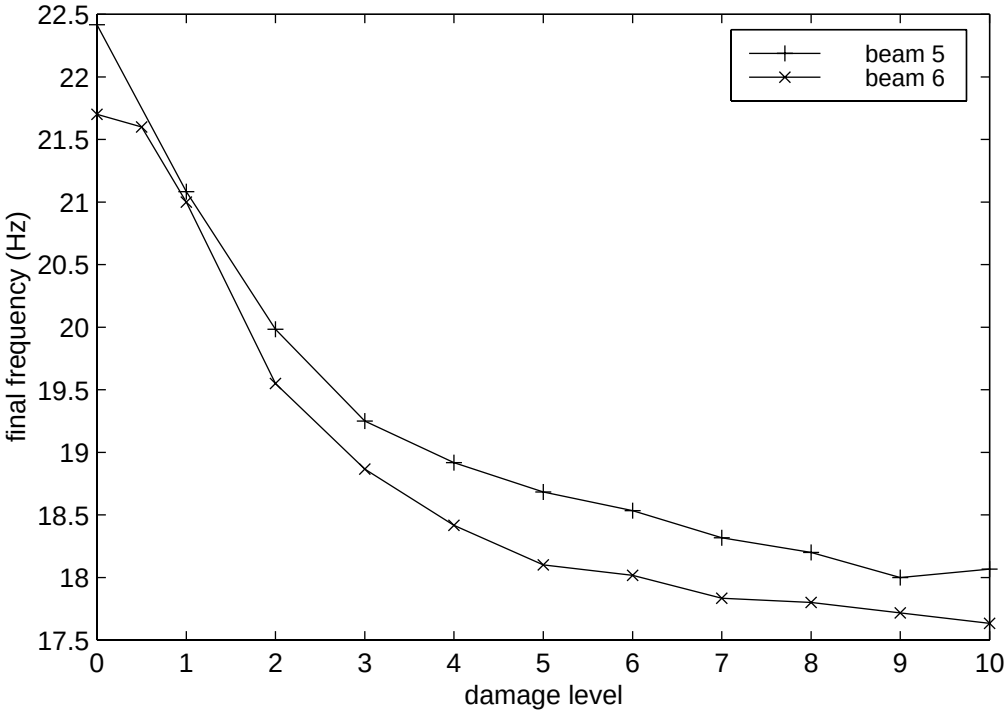

Figure 8.38: Change in final frequency with increasing damage

damping over time (and amplitude).

Summary

The vibration tests confirmed that there is a change in non-linearity with damage. The change is greatest over the first damage level and after the third damage level there is a reversal in the trend and a slight reduction in non-linearity with further damage.

8.4 Static Load Tests: Processing

The aim of the static load tests was to demonstrate a method of measuring the static moment-rotation hysteresis loop for different levels of loading and at different damage levels. This would allow the modelling of the crack behaviour using the model developed in chapter 4, if it is assumed that the static moment-rotation relationship is the same as the dynamic relationship.

To summarise the static load tests described in section 7.2.3, the beam was statically loaded in cycles to allow the moment-rotation hysteresis loop to be calculated. The

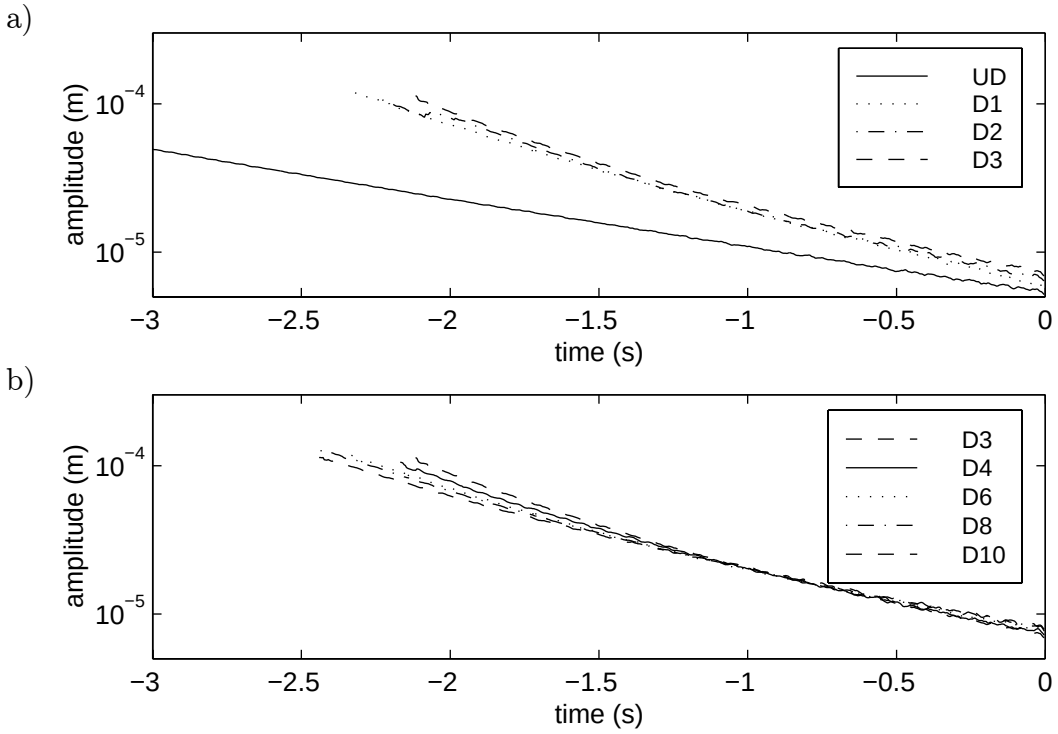

Figure 8.39: Comparison of the damping properties for beam 5

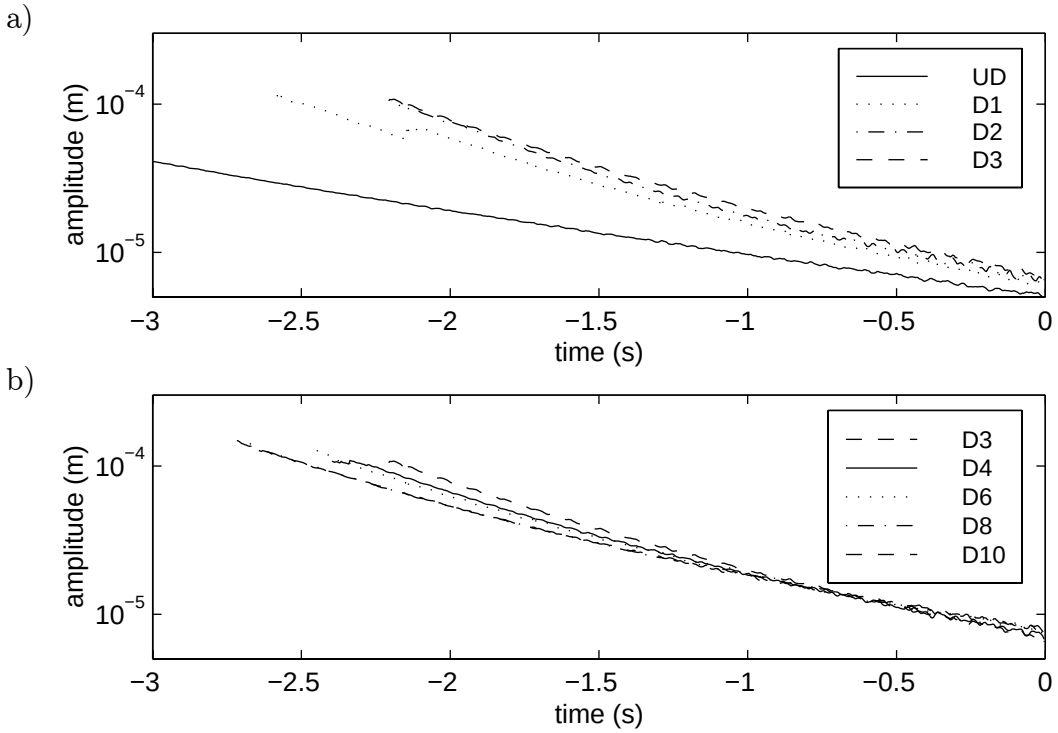

Figure 8.40: Comparison of the damping properties for beam 6

load was applied 120 mm off mid-span in both the positive and negative directions by applying weights in steps of 10 kg. Strain was measured at the top and bottom surfaces of the beam using the vibrating wire strain gauges described in chapter 6, with a gauge length of 117 mm centred at the mid-span of the beam.

Throughout the processing of this data it will be assumed that the planes 58.5 mm (i.e. at the gauge anchors) either side of the mid-span remain plane throughout the static load tests. This assumption is needed to allow the strains to be related to rotation of the beam. To justify this assumption further tests with more vibrating wire strain gauges positioned at the mid-section of the beam at differing heights must be performed. Alternatively, the vibrating wire strain gauges must be modified so that an 80 mm gauge length may be used, since cracks form at a spacing of approximately 80 mm, the spacing of the shear stirrups. (With the current design the anchor bolts would obstruct the positioning of the coil if an 80 mm gauge length was used).

The frequencies measured utilising the vibrating wires were converted to strain measurements and corrected for temperature effects, as described in sections 6.1.1 and 6.1.2, using the gauge factor $G = 1.259 \times 10^{-9}$ measured in the calibration tests (section 6.5). There may therefore be a slight linear error in the scale of the strains measured if this gauge factor is slightly inaccurate. However what is really of interest is the shape of the hysteresis loop rather than exact strains.

For beam 6, the ± 40 kg load cycles were performed in the steps shown in figure 8.41. A positive load is defined as a load applied downwards. Figure 8.41b shows the lower strain gauge data for these load points for beam 5 at damage level 1. Test 1 has been used as the zero-strain datum point from which the strains for the other load points are measured. Tensile strain is defined as positive. The loops are followed in the clockwise direction. The first two points do not follow the hysteresis loop since the beam is initially in the equilibrium position. The plots in this section will consist of the data from test 3 to test 19 using test 1 as the datum zero-strain point.

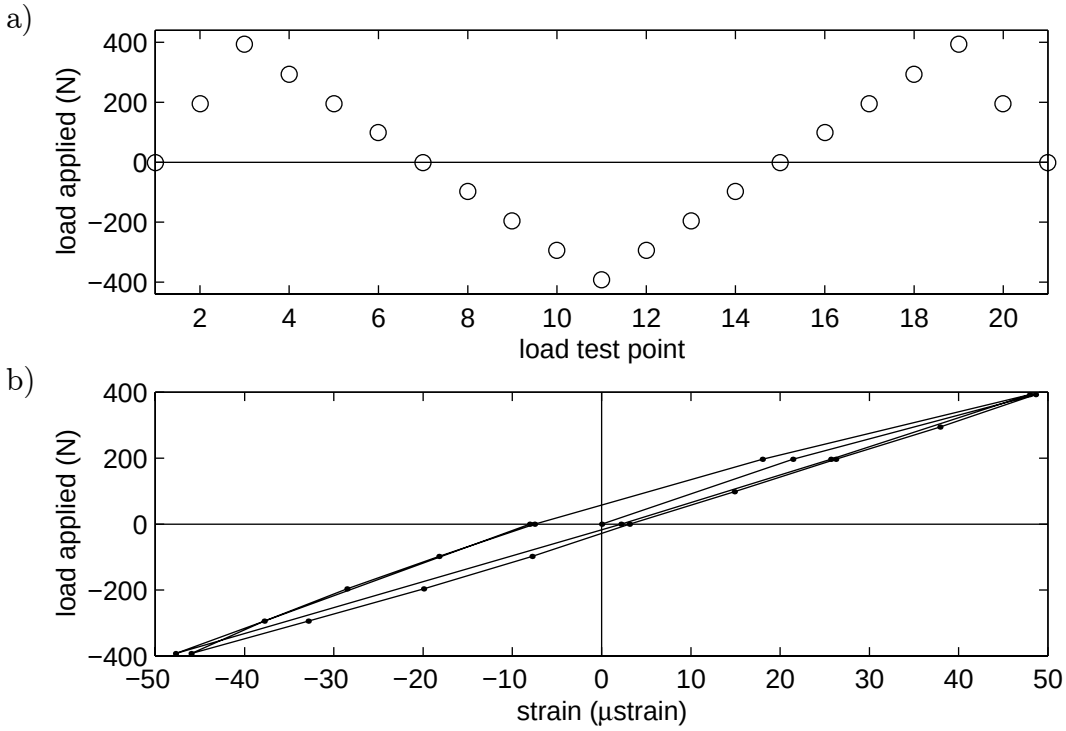

Figure 8.41: Static load tests; a) data points and b) an example of the resulting hysteresis loop

8.4.1 Recovery

The static load tests on beam 5 will not be used in the analysis. This is because it was found that the strain measurements were dependent on the time between the damage loading and the static load tests. Figure 8.42a shows the strain measured using the lower strain gauge for two load cycles performed 4 hours after the beam was loaded to damage level 9 and unloaded. It is clear that there is a gradual compression of the beam's lower surface over the gauge length in the results during the time over which the tests were performed. This would be consistent with the crack gradually closing after the load applied to damage the beam has been removed. In contrast, figure 8.42b shows the results for an identical test performed 72 hours after the damage was inflicted. It is clear that the recovery of the beam has ceased by this time. Figure 8.43 shows the same plots for the top strain gauge and demonstrates that the recovery due to concrete expansion at the top gauge is less pronounced than the compressive recovery at the bottom gauge. The loops are followed in the anti-clockwise direction for the top gauge.

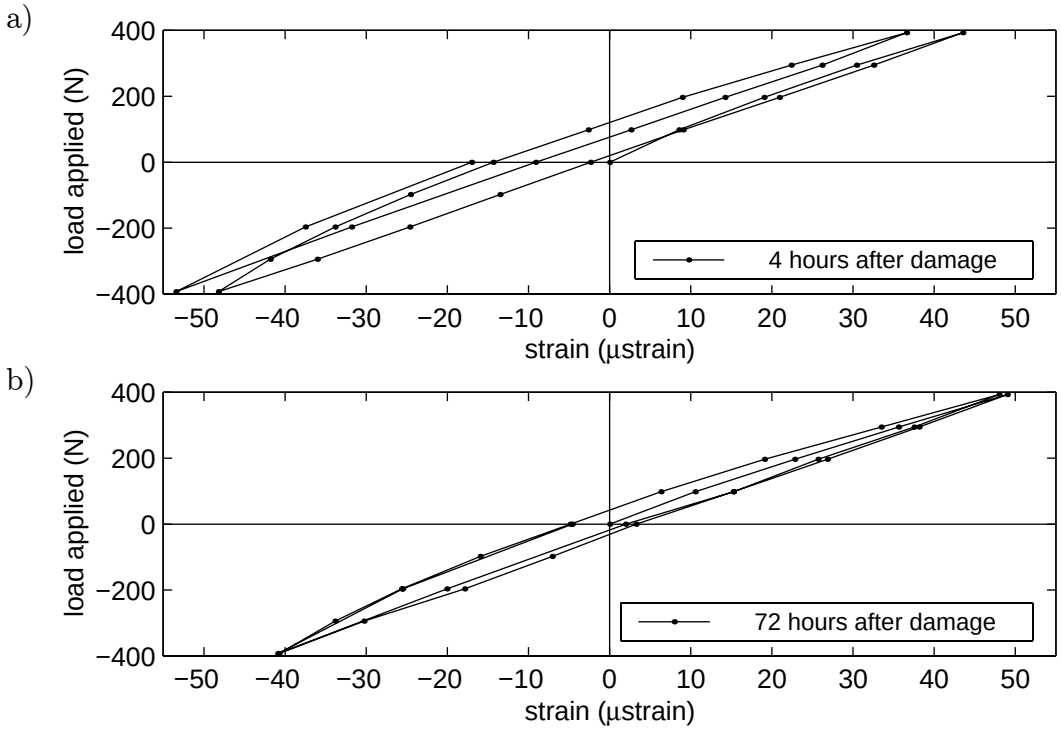

Figure 8.42: Recovery of the beam after damage has been inflicted, bottom gauge, tested at a) 4 hours and b) 72 hours after damage

If it is assumed that the test at each load level takes roughly the same time, it is possible to correct crudely for the recovery over the time the tests took place. Taking the time between each load level test to be Δt then the corrected strain, ϵ_c, may be written as:

$$\epsilon_c = \epsilon + \alpha \Delta t (n-1) \tag{8.1}$$

where n is the test number and α is the strain recovery rate. The time between static load tests, Δt, is approximately 130 s. Figure 8.44a shows the corrected data for the bottom gauge for tests conducted 4 hours after damage loading using a strain recovery rate of $\alpha = 0.0035$ μstrain/s. The strain-load relationship now resembles that measured 72 hours after the damage was inflicted, albeit shifted in strain by about -4 μstrain. Figure 8.44b shows the corrected data for the top gauge using $\alpha = -0.0004$ μstrain/s.

There is no detectable change in the time-frequency relationships generated from

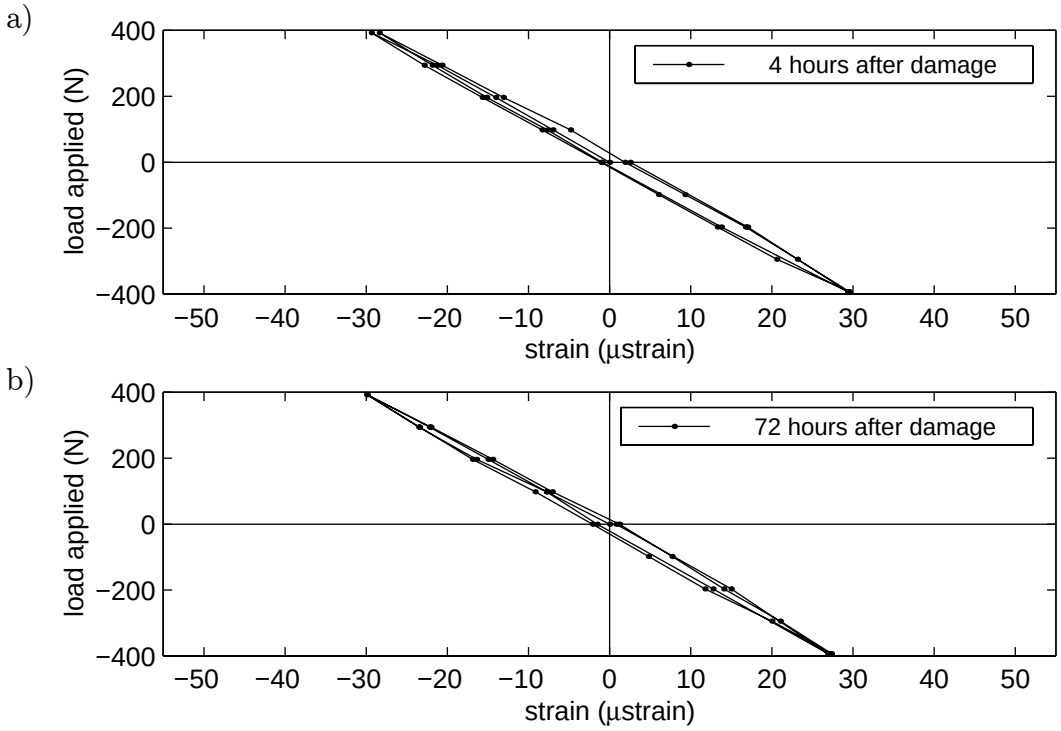

Figure 8.43: Recovery of the beam after damage has been inflicted, top gauge, tested at a) 4 hours and b) 72 hours after damage

vibration tests taken over this time.

For beam 6, to overcome the problem of the recovery affecting the strain measurements, static load tests were conducted 16 hours after damage loading.

8.4.2 Moment-Strain Relationship and Neutral Axis Position

The loads are applied 0.12 m off mid-span, so the moment may be related to the load using:

$$M = 0.64F \tag{8.2}$$

where F is the load applied. Figures 8.45a and 8.45b show the strain-moment relationship at damage level 1 for the top and bottom gauges respectively. Moment is defined as positive for positive loads, i.e. sagging occurs when positive moments are applied.

The strain data from the top and bottom gauges may be used to calculate the neutral axis position. As stated in section 7.2.3, the top and bottom gauges were positioned 7 mm and 98 mm from the top of the beam respectively. It follows that the neutral-axis

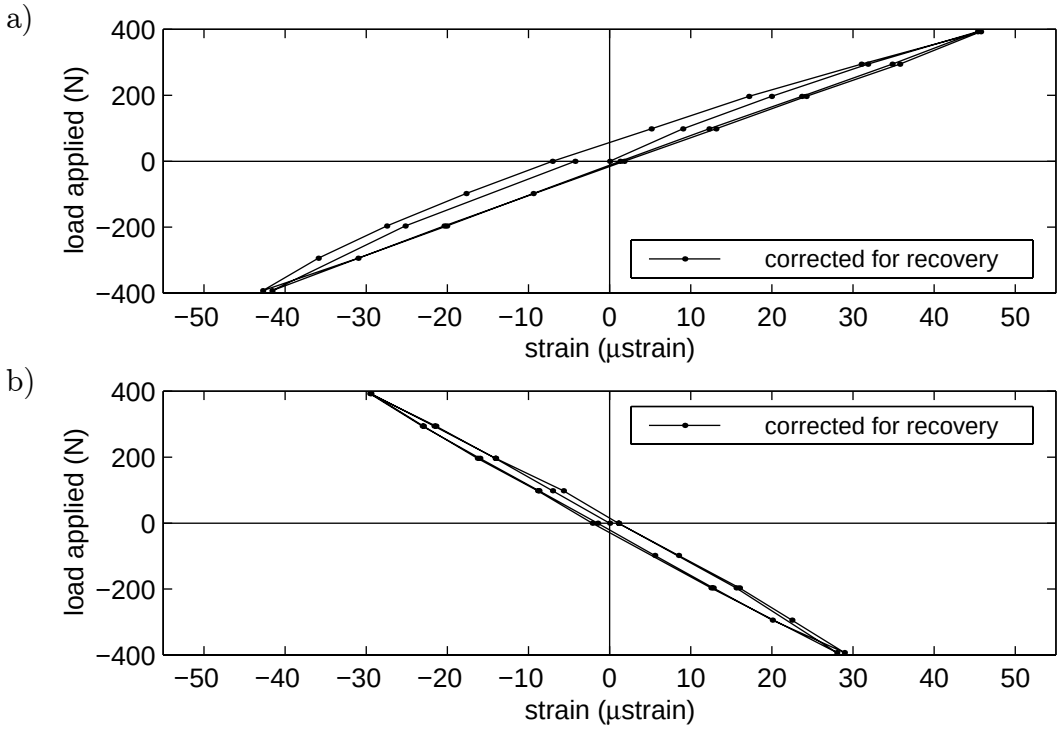

Figure 8.44: Strain-load relationship after recovery correction for a) the bottom gauge and b) the top gauge

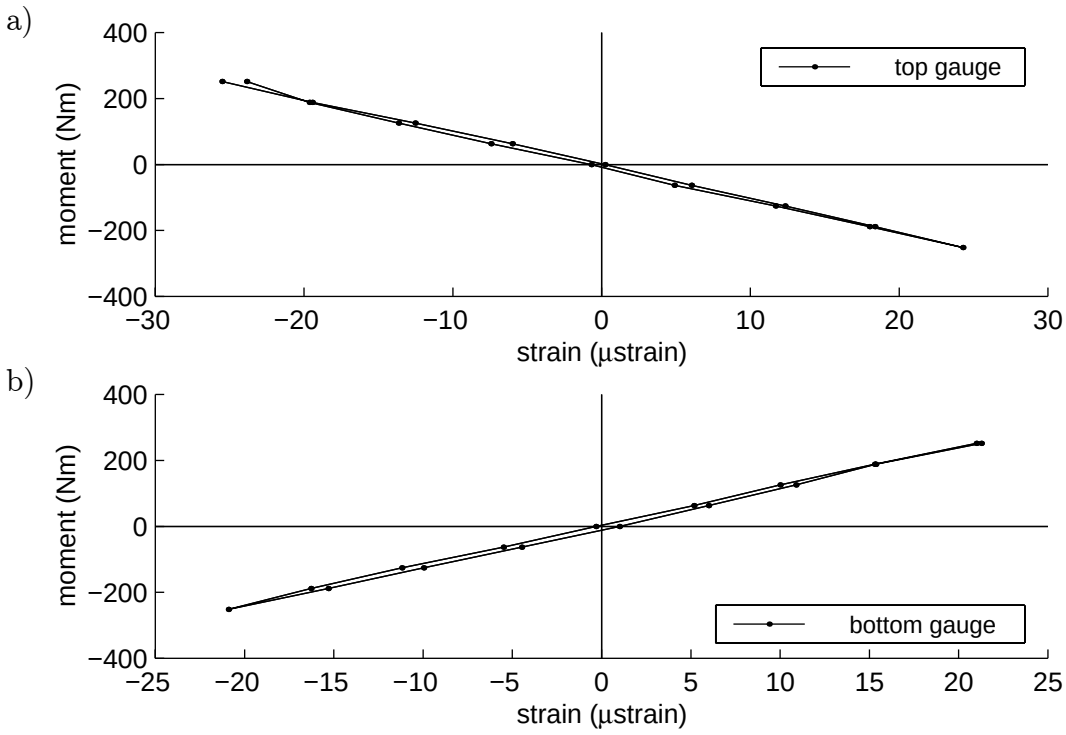

Figure 8.45: Moment-strain relationship for a) the top gauge and b) the bottom gauge

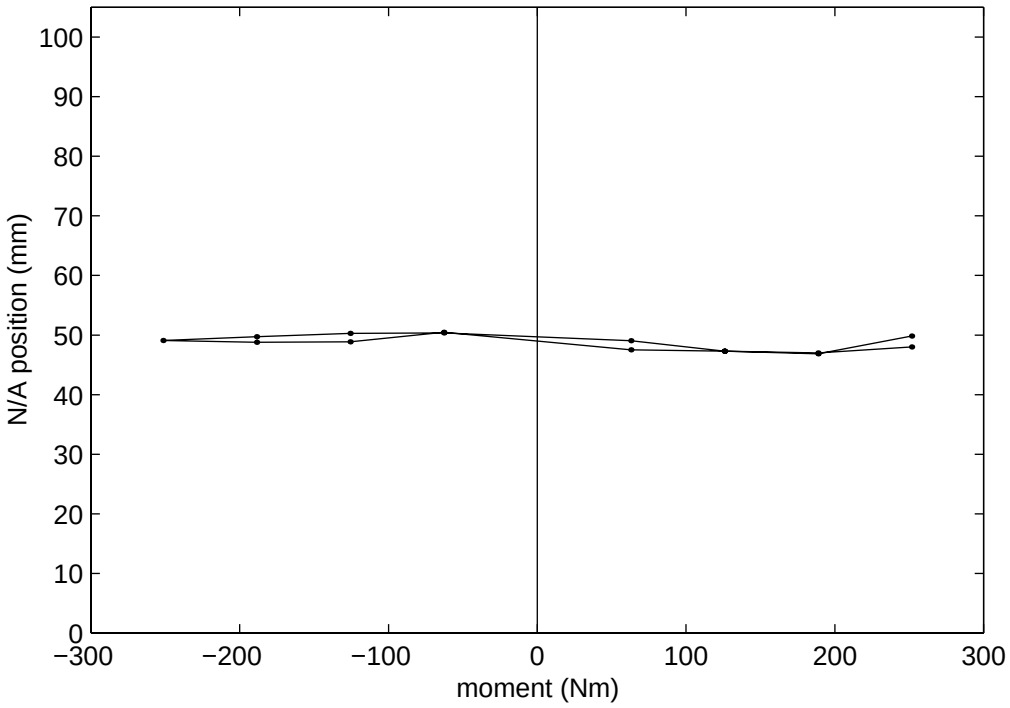

Figure 8.46: Neutral-axis height for damage level 1

height, x, (measured from the bottom of the beam) is given by:

$$x = \frac{0.007\epsilon_t - 0.098\epsilon_b}{\epsilon_t - \epsilon_b} \tag{8.3}$$

where ϵ_t and ϵ_b are the strains at the top and bottom gauge positions respectively. Figure 8.46 shows the neutral-axis height for damage level 1 over the range of applied moments, where on the y-axis 0 mm relates to the bottom and 105 mm relates to the top of the beam. It can be seen the neutral-axis height remains at approximately the same height over the whole range of moments.

8.4.3 Moment-Rotation Relationship

Using the plane sections remain plane assumption discussed on page 199, the rotation of the plane 58.5 mm to one side of the mid-span calculated relative to the plane 58.5 mm to the other side of the mid-span, $\Delta\theta$, may be expressed as:

$$\Delta\theta = \frac{l}{h}(\epsilon_t - \epsilon_b) \tag{8.4}$$

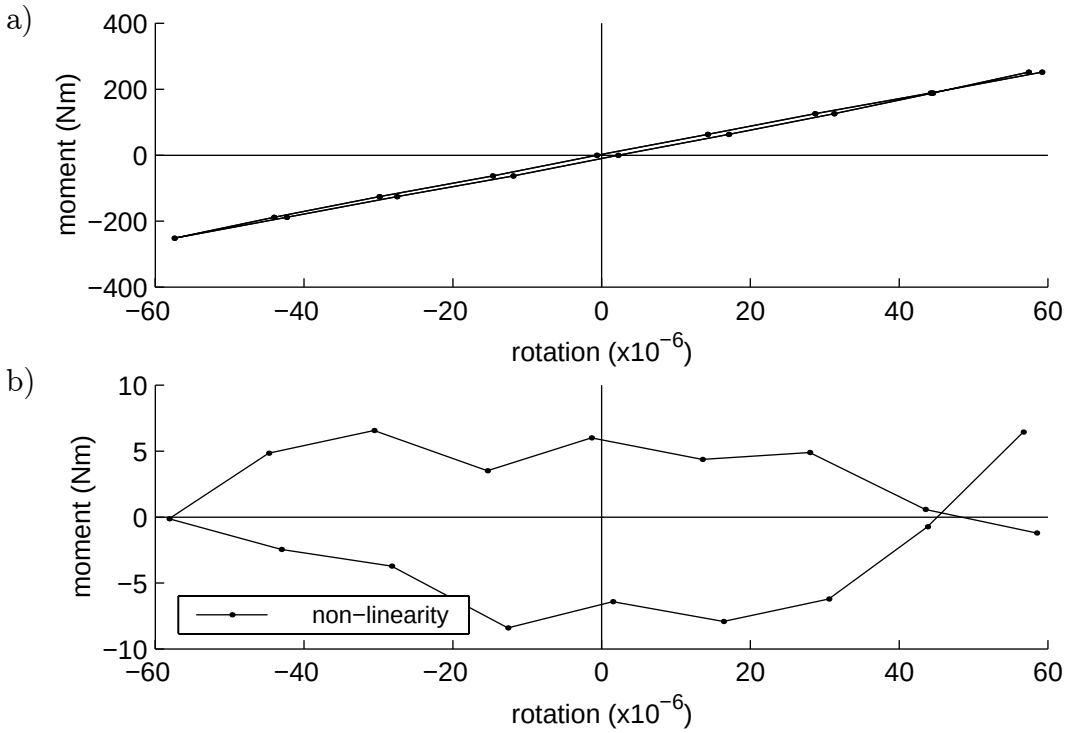

Figure 8.47: Moment-rotation relationship, a) including linear behaviour and b) once linear behaviour has been removed, damage level 1

where l is the vibrating wire gauge length and h is the vertical distance between the two gauges. Rotation is defined as positive when the moment is positive. Figure 8.47a shows the moment-rotation relationship for damage level 1.

To make the moment-rotation hysteresis loop clearer, a straight line fit to the data may be subtracted from it. If the behaviour is assumed to be linear, then a straight line would be fitted to the data to find the stiffness of the section. By subtracting from the behaviour this straight line fit, the behaviour due to non-linearities may be plotted. There are two complications with this procedure. Firstly, it is not clear whether the error between the fit and the data should be minimised in the x-direction or the y-direction. Any uncertainty in the measurements is in the rotation data (x-direction error), however, it is usual to fit a line to moment-rotation data to minimise the error in moments (y-direction error). In this case it was decided to minimise error in the y-direction since the strain at a certain moment is expected to vary, depending on whether the moment is increasing or decreasing. Hence, it can not wholly be attributed to an

error in the strain data. However, the change in the result was only very slight if the error was minimised in the x-direction. The second problem is whether to force the line through the origin. If the behaviour is approximated to a linear relationship then the line fit must be through the origin. However, the zero-strain point for each gauge is based on only one test (consisting of nine excitations). If the beam was not quite in the equilibrium position when the strain at this data point was measured, the error will affect the whole of the data set. It was therefore decided to fit the line to the data without forcing it through the origin and then to shift the axis in the x-direction so that the straight line goes through the origin. It should therefore be noted that the non-linear data may have a slight y-axis shift error. This error is not important here, since it is the change in the shape and relative size of the hysteresis loops at different damage levels which is of interest.

Figure 8.48 shows a schematic plot of a hysteresis loop and indicates the energy required to move from one point on the curve to another for the case where the moment is increasing and where it is decreasing. By subtracting the linear behaviour from the moment-rotation hysteresis loop, the area under the resulting curve represents the energy "spent" to overcome the friction non-linearities.

Figure 8.47b shows the hysteresis loop for damage level 1 once the linear relationship has been removed. The equation of the line fit was:

$$M = 4.32 \times 10^6 \Delta\theta - 2.9731 \tag{8.5}$$

giving a linear rotation stiffness of 4.32×10^6 Nm and a shift of the rotation axis to the right by 0.68×10^{-6}. The predicted non-linear hysteresis loop is not very smooth, however this is understandable if the sensitivity of the moment estimation to a 1 μstrain error in strain measurement at one of the gauges is considered. A change of 1 μstrain in one gauge would relate to a change in rotation of 1.29×10^{-6} (equation 8.4). The new moment remaining once the linear behaviour has been removed is given by:

$$M_{nl} = M - 4.32 \times 10^6 (\Delta\theta + 1.29 \times 10^{-6}) - 2.9731 \tag{8.6}$$

Therefore, if there is a 1 μstrain error in the estimation of the strain for one of the gauges the resultant vertical shift of the data point on the non-linear hysteresis loop plot is of magnitude 5.6 Nm (there will also be a horizontal shift of magnitude 1.29×10^{-6}).

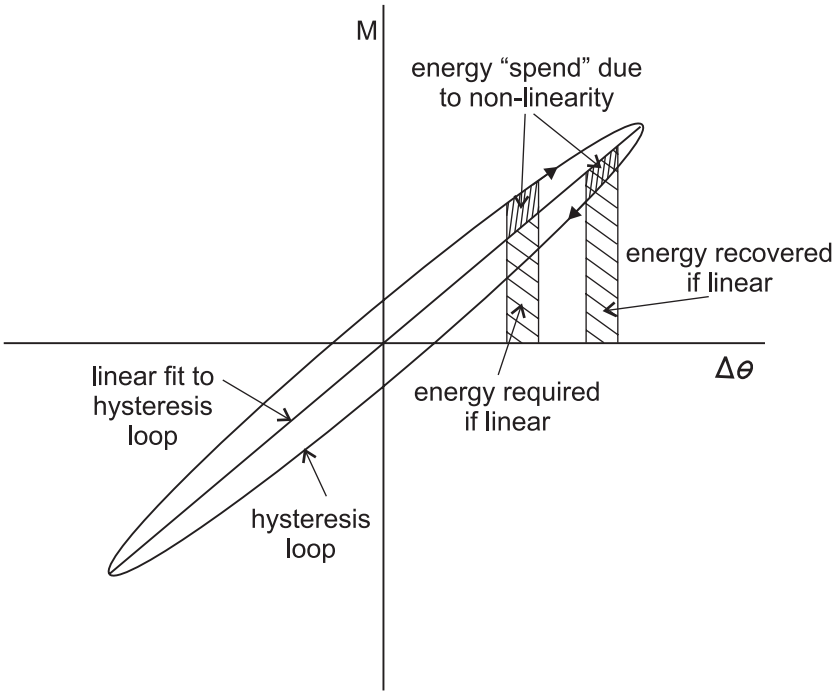

Figure 8.48: Schematic of hysteresis loop

As was explained in section 7.2.3, for each damage level three load cycles were conducted, over the ranges ±40 kg, ±30 kg and ±20 kg. Figure 8.49 shows the hysteresis loops for all three cycles for damage level 1 and figure 8.50 shows the loops once the straight line fit has been removed. The gradient of the line fits were 4.32×10^6 Nm, 4.37×10^6 Nm and 4.39×10^6 Nm for the ±40 kg, ±30 kg and ±20 kg cycles respectively, which shows a gradual reduction in global stiffness as the load cycle increases.

8.4.4 Beam Deflection

From the LVDT data taken at the mid-span of the beam, it is possible to assess the amplitude of vibration that produces a comparable relative rotation over the vibrating wire gauge length to that produced during the static load test.

Assuming that the fundamental mode shape is a sinusoid and is unaffected by damage, as has been suggested by Das *et al.* [26], the relative rotation of the plane 58.5 mm one side of the mid-span to the plane 58.5 mm to the other side of the mid-span can be derived, using the small angle assumption:

$$\Delta\theta = -ly \tag{8.7}$$

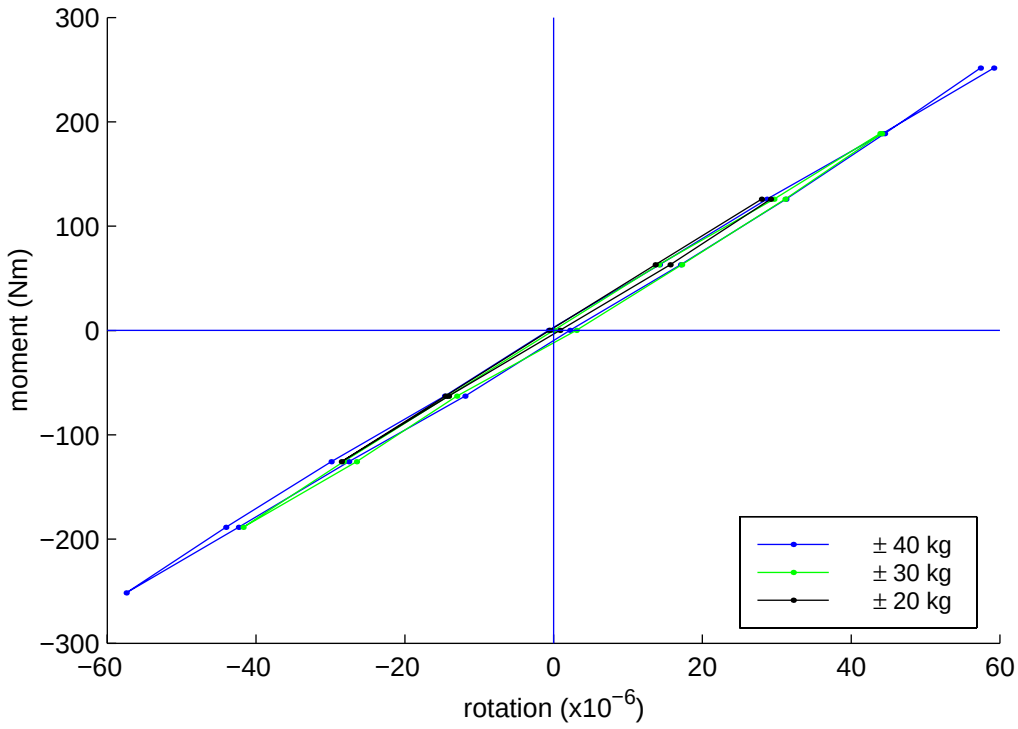

Figure 8.49: Hysteresis loops for different load ranges, damage level 1

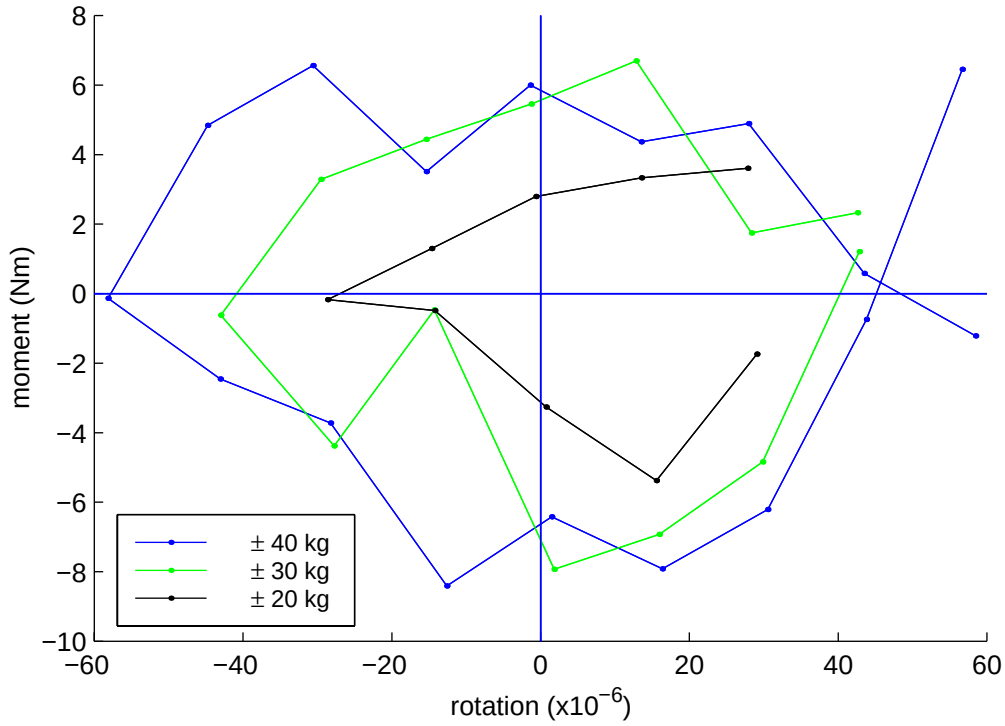

Figure 8.50: Hysteresis loops for different load ranges after linear fit has been removed, damage level 1

where l is the vibrating wire gauge length and y is the amplitude of oscillation.

This may be compared to the rotation-deflection relationship for static loading. If the beam is assumed to behave linearly, then:

$$\Delta\theta = \frac{-12l}{L^2 + 2Ld - 2d^2} y \tag{8.8}$$

where L is the span of the beam and d is the distance from the mid-span at which the load is applied ($d = 0.12$ m).

This means that if a deflection of y_s is measured at the mid-span during the static load test, then the relative rotation over the gauge length is comparable to a vibration of magnitude y_d:

$$y_d = \frac{12}{L^2 + 2Ld - 2d^2} y_s = 1.42 y_s \tag{8.9}$$

For damage level 1 the central deflections when +40 kg and −40 kg were applied were 0.036 mm and −0.036 mm respectively. The ±40 kg load cycle therefore corresponds approximately to a vibration of 0.051 mm.

8.5 Static Load Tests: Analysis

Using the analysis methods described in the previous section, the effects of damage may be assessed.

It is first necessary to stress that the tests were loading tests. A better comparison of how damage affects the moment-rotation relationship would be to examine hysteresis loops which have the same maximum relative rotation. However, this would involve considerable complication to the experiments, as the load would have to be applied and the rotation calculated using the strain gauges before further load could be added, until the rotation reaches its maximum value.

8.5.1 Neutral Axis Position

The neutral-axis remains broadly constant over the hysteresis loop, as was shown for damage level 1 and the ±40 kg loop in figure 8.46. Figure 8.51 shows the mean neutral-axis height for various damage levels and for each magnitude of hysteresis loop. As

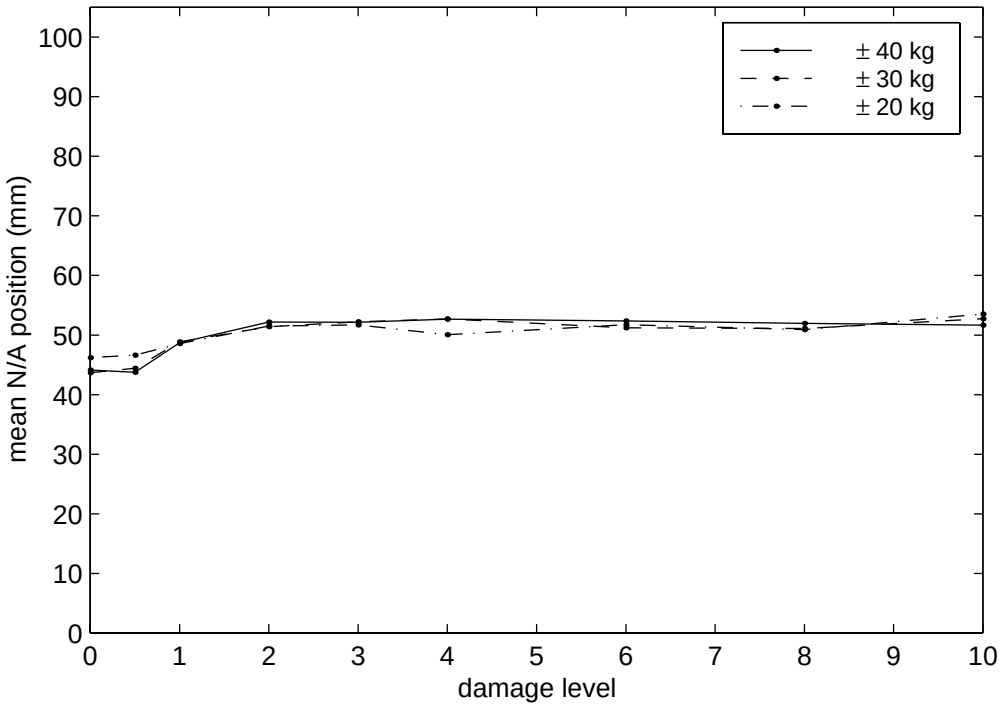

Figure 8.51: Average neutral-axis height during static load tests

with figure 8.46, 0 mm and 105 mm correspond to the bottom and top of the beam respectively. Figure 8.51 shows that at any particular damage level, the neutral-axis height remains approximately the same regardless of the magnitude of the hysteresis loop. For damage levels 2 and above the neutral-axis may be taken to be constant. However, the height of the neutral-axis is different to that during damage loading (in the region of 72 mm from the bottom of the beam).

8.5.2 Moment-Rotation Relationship

Figure 8.52 shows the moment-rotation relationships for various damage levels using the data from the ±40 kg load tests. Damage level 3 is plotted on both graphs to aid comparison. It can be seen that after damage level 3 there is far less reduction in overall stiffness for increased damage. If the behaviour is taken to be linear, then, by means of a straight line fit, the stiffness for the section for the different damage levels may be calculated. This is shown in figure 8.53 along with the linear stiffness fits for the ±30 kg and ±20 kg load tests. Figure 8.53 confirms the reduction in the rate of decrease

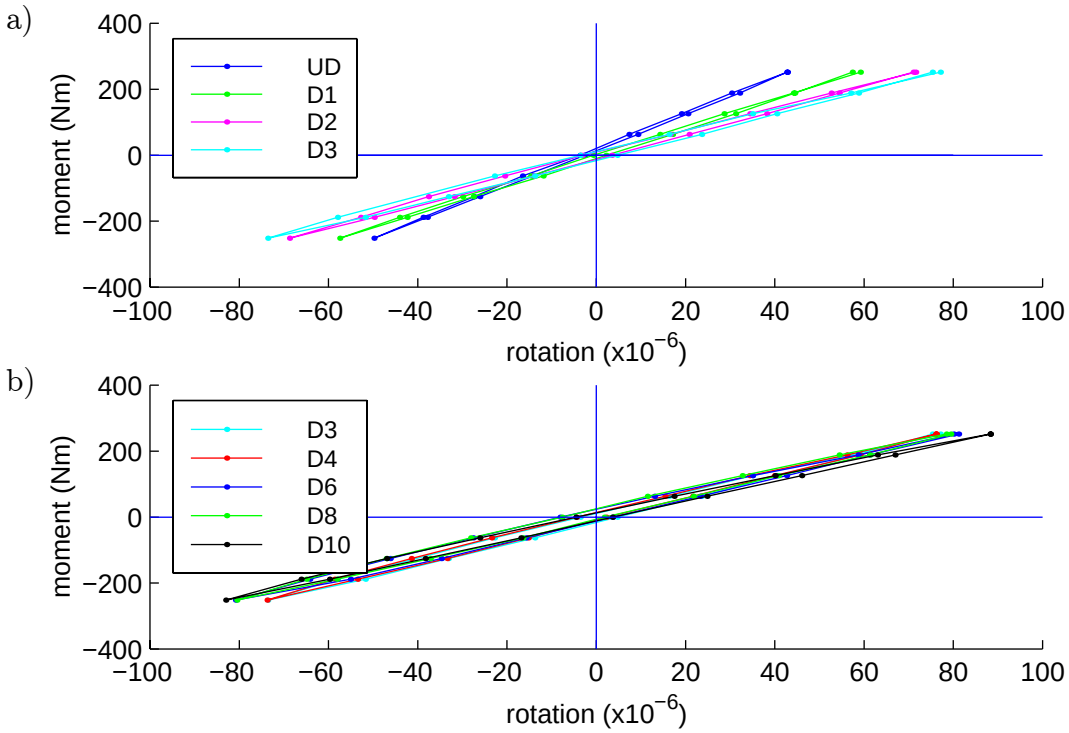

Figure 8.52: Moment-rotation relationships for the ±40 kg load tests

in overall stiffness with damage observed in figure 8.52, with the exception of damage level 10 where there is a significant drop in stiffness due to the additional loading. It also demonstrates that there is, at each damage level, an increase in overall stiffness for hysteresis loops with lower maximum load.

As described in section 8.4.3, if the linear approximation to the hysteresis loop is subtracted from the loop, then it is easier to see the non-linear effects. These are shown in figure 8.54 for the ±40 kg load tests at the various damage levels plotted in figure 8.52. Figure 8.54b shows that for the higher damage levels there is a slight increase in the magnitude of the non-linear stiffness properties of the beam, with the exception of the highest damage level, D10, where there is a flattening off of the hysteresis loop on its lower side, corresponding to the part of the test where the moment is being reduced. This would suggest that for the highest damage level there is a reduction of frictional effects as the crack closes. It must be stressed that these loops are for a fixed maximum load applied, so are not directly comparable when considering the moment-rotation behaviour for a certain amplitude of vibration or for a certain maximum rotation. It

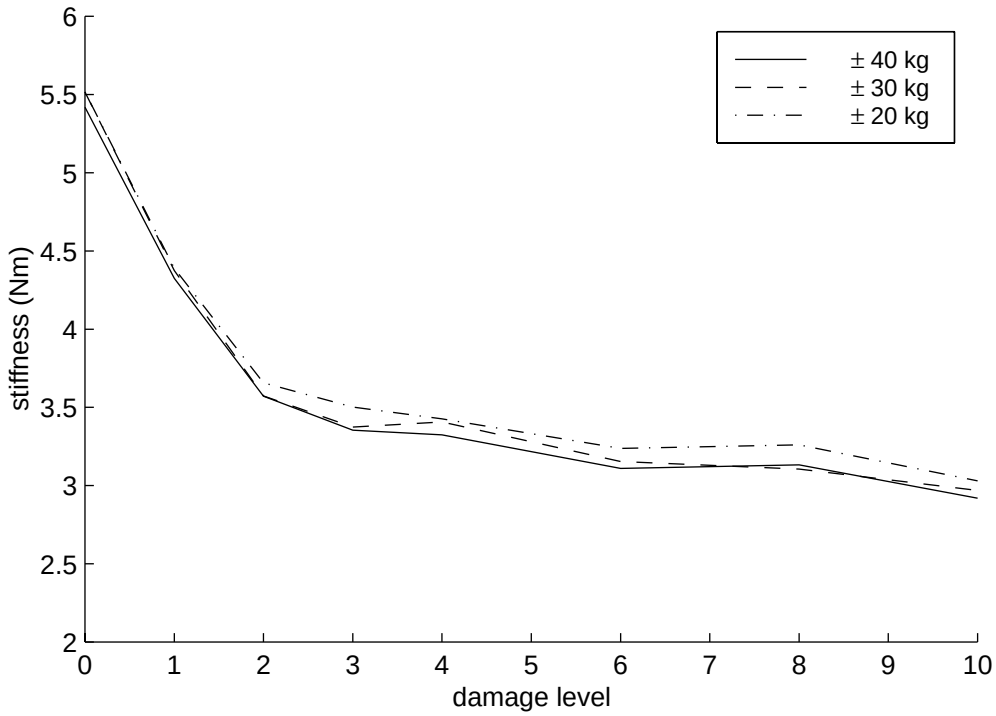

Figure 8.53: Stiffness relationships for the ±40 kg load tests

must also be noted that the static moment-rotation tests measure the stiffness properties locally around the mid-span point, whereas vibration tests will be affected by stiffness changes all over the whole length of the beam, although those changes nearer the mid-span will affect the frequency most. However, for the comparison of damage levels 3 to 10, the ±40 kg load tests are a good approximation to a comparison of the hysteresis loops for a given maximum rotation since the stiffness change with damage over this range is small.

8.5.3 Displacement

Figure 8.55 shows the maximum displacement of the mid-span of the beam for various damage levels for the ±40 kg, ±30 kg and ±20 kg load tests. Also plotted are the corresponding maximum relative rotations of the section over which the vibrating wire strain gauges are placed (calculated using the linear fit to the moment-rotation relationship and the maximum moment applied). This figure demonstrates that the maximum displacement at mid-span may be related simply to the maximum relative rotation by

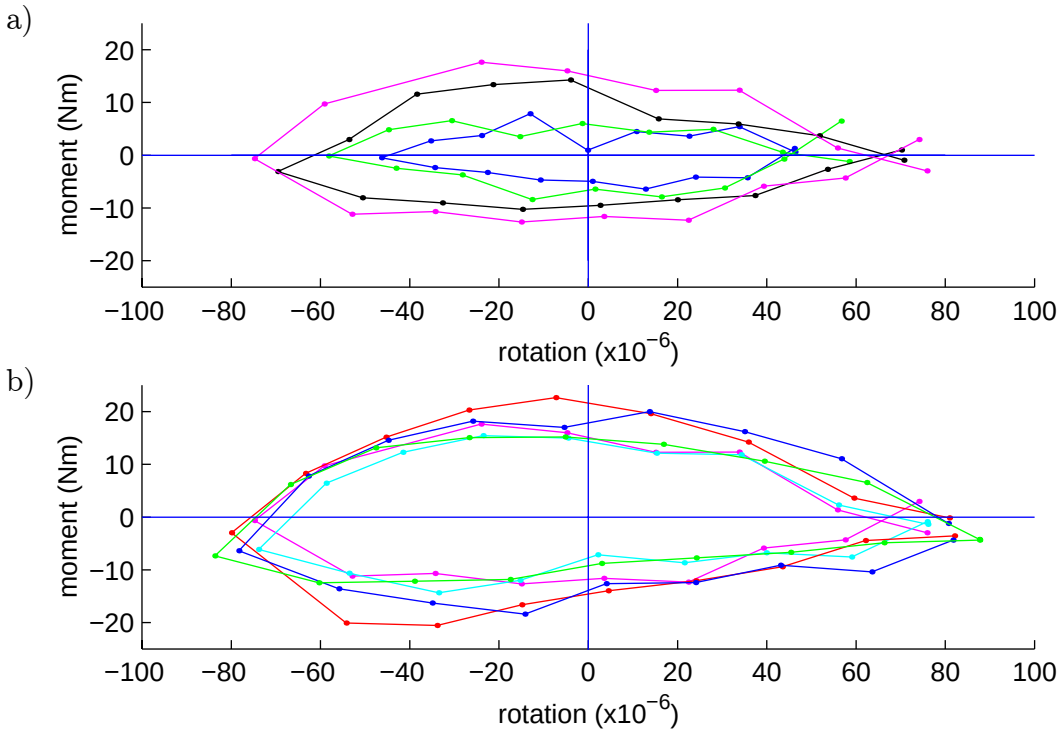

Figure 8.54: Hysteresis for the ±40 kg load tests

applying a scaling factor. It is therefore proposed that, for future tests, rather than cycling the load applied over a fixed load range, it should be cycled over a fixed displacement range by incrementing the load until the maximum or minimum displacement level is reached. This would allow comparison of hysteresis loops of approximately the same maximum relative rotation.

8.5.4 Summary and Experimental Improvements

These static load tests have demonstrated a way of measuring the static moment-rotation relationship over a short section of the beam, which may then be used in the model presented in chapter 4 to aid understanding of the beam behaviour.

The tests have demonstrated that at low damage level the stiffness of the beam decreases rapidly with damage, but above damage level 3 the stiffness change with increasing damage is small. By removing the linear stiffness from the moment-rotation relationships, it has been shown that for differing levels of damage above damage level 3 there is little change in the size of the hysteresis loops for load cycles over a range

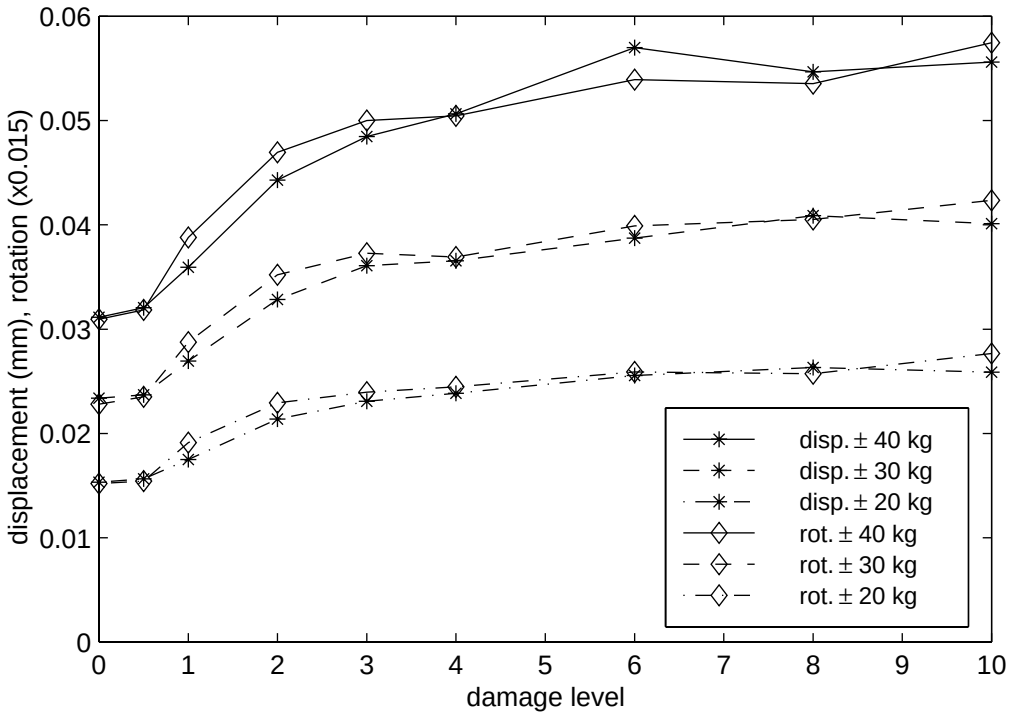

Figure 8.55: Maximum displacement at mid-span

of ±40 kg. However, the shape of the hysteresis loop at damage level 10 is flatter as the moment applied decreases. This suggests that, when loading to this damage level, a breakdown of the frictional effects present at lower damage levels during crack-closure has occurred.

It has also been shown that the relationship between damage level and the maximum displacement at mid-span and between damage level and the maximum relative rotation over the length of the vibrating wire strain gauges, exhibit the same properties. It is therefore possible to predict approximately the maximum relative rotation by measuring and scaling the displacement at mid-span. The scaling factor for beam 6 was found by minimising the error between the displacement and the scaled relative rotation over the various damage levels. This result will allow static load tests over fixed displacements (and therefore relative rotation) rather than fixed load levels to be performed, which will permit better comparison between the non-linear characteristics at differing damage levels.

It is envisaged that future work will include:

- Modifications to the vibrating wire strain gauges to allow a gauge length of 100 mm. This will allow an easier comparison to damage loading strains recorded using a Demec gauge.

- A test with additional vibrating wire strain gauges to check the assumption that the vertical planes at either end of the gauges remain plane during the load tests.

- Tests at different damage levels over a fixed range of displacement (rather than over a fixed range of load) to allow easier comparison of the moment-rotation characteristics using hysteresis loops of fixed maximum relative rotation.

Ideally, these tests would be performed on a modified beam with a stirrup spacing of 100 mm to ensure that the crack spacing matches the Demec gauge length.

The static load test results will be used in the next chapter along with the damage load test results to assess the non-linear crack mechanisms proposed in chapter 5.

Chapter 9

Assessment of Possible Non-Linear Mechanisms

Four possible mechanisms which may cause the non-linear vibration characteristics have been identified in chapter 5. They are the non-linear behaviour of concrete in compression, slip between the steel and the concrete, slip in the concrete across the crack due to matrix aggregate interaction and crack closure leading to a bilinear stiffness characteristic (off-centred due to self-weight). Some of these mechanisms may now be assessed using the experimental results presented in the last chapter.

9.1 Bilinear Mechanism

The bilinear mechanism was proposed as a possible cause of the non-linear behaviour of the reinforced concrete beam exhibited during the vibration tests. The mechanism represents the idea that the crack is either in a closed or an open state depending on the curvature of the beam, and within these two states the stiffness of the section is constant.

Once the beam has been damage loaded and unloaded, there is a residual strain over the cracked region. This was demonstrated using Demec strain gauge readings in the last chapter. Figures 8.1 and 8.2 show the strains over the cracked region during damage loading and once the damage load has been removed. It can be seen that at the lower surface of the beam the residual strain after loading was in the region of 180 μstrain

for damage level 2 and 450 μstrain for damage level 8. To assess whether the crack closes during each cycle of a vibration test, these residual strains must be compared to the maximum strains experienced at the lower surface of the beam during the vibration tests.

During the $\pm$40 kg static load tests, the maximum strains measured over the vibrating wire gauge length for these two damage levels were in the order of 70 μstrain and 80 μstrain respectively. This demonstrates that the crack remained open during the $\pm$40 kg static load test at both damage levels. To relate the static load tests to the vibration tests it is necessary to consider the deflection of the beam. It was shown in section 8.5.3 that the maximum mid-span deflection was in the order of 0.044 mm for damagge level 2 and 0.055 mm for damage level 8 (see figure 8.55). As described in section 8.4.4, the amplitude of oscillation at which a comparable relative rotation of the beam over the length of the vibrating wire strain gauges occurs may now be found. These amplitudes of oscillation are 0.0625 mm and 0.0781 mm respectively. Assuming that the neutral-axis height is the same for the vibration tests and the static load tests, this means that, at amplitudes of 0.0625 mm and 0.0781 mm, the strains at the lower surface of the beam were approximately 70 μstrain for damage level 2 and 80 μstrain for damage level 8.

Figures 8.34 and 8.35 show that the maximum vibration amplitude was in the order of 0.1 mm. Assuming that the strain-displacement relationship is broadly linear, this would mean that the maximum strains during the vibration tests were in the order of 110 μstrain and 100 μstrain, i.e around 60% and 20% of the residual strain, for damage levels 2 and 8 respectively. It is therefore very unlikely that the crack closed during the vibration tests, which would require that the maximum strain during the test exceeds the residual strain.

This analysis indicates that complete crack closure does not occur during the vibration tests and so indicates that the simple fatigue crack representation of damage discussed in section 5.2.1 is not a useful model for these reinforced concrete beams. This does not mean, however, that there is no change in stresses over the cracked concrete. It is possible that the cracked concrete stresses will alter during the vibration because of frictional forces due to matrix-aggregate interaction. This type of mechanism was

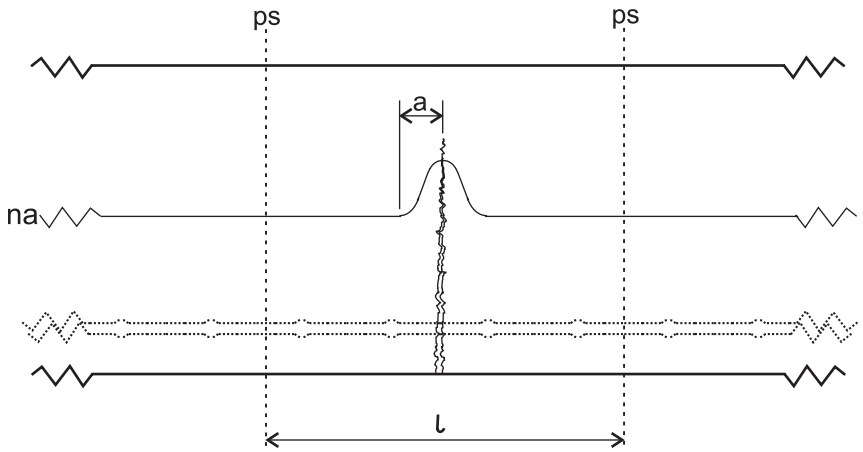

Figure 9.1: Concrete cracked region

explained in section 5.2.3 and is addressed in the next section.

9.2 Non-Linearity in the Cracked Concrete

The possibility that the non-linear vibration characteristic is dominated by the non-linearity in the behaviour of cracked concrete is now examined. A simple model is used to assess the significance of the cracked concrete strength in the overall stiffness of the beam, since, if this effect is very small, the non-linearities in the behaviour will not be detectable. Damage level 4 is selected for consideration.

Figure 9.1 shows the concrete beam in the cracked region. The neutral-axis is expected to rise near to the crack since, at the crack, less tensile stress will be carried by the concrete than at an uncracked region, because the stiffness of the concrete will be reduced.

The first step is to calculate the concrete strength in the cracked region. The assumptions made to allow this to be done simply are:

- At a distance of 0.05 m either side of the crack, plane sections remain plane (indicated ps). This is at the location of the Demec pips and the approximate location of the vibrating wire anchors.

- There is only one crack in this region, a realistic assumption for the first few damage levels.

- During damage loading, all the concrete deformation in the tensile region takes place across the crack.

- The transfer of load across the crack is governed by the model suggested by Rots *et al.* (summarised in [49]) and others (for example Farag and Leach [33]).

The concrete crack strength at any position along the crack is a function of the maximum crack width, w_m, experienced at that position, which can be calculated using the Demec strain readings during loading to damage level 4. Given this information, a failure stress σ_f can be found using experimental results from Cornelissen *et al.* (see p49 [49]). The model suggested by Rots *et al.* states that, provided this crack width is not exceeded, subsequent behaviour will be governed by:

$$\frac{w}{\sigma} = \frac{w_m}{\sigma_f} \tag{9.1}$$

It should be noted that this eliminates the non-linear effects since there is no hysteresis loop. However, this is acceptable for this calculation, which aims to establish whether the cracked concrete strength contributes significantly to the stiffness of the cracked region, and not whether the non-linearities in the cracked concrete strength result in non-linear vibration behaviour.

A way of dividing the beam into a region influenced by the crack and a region that is not is now discussed. On moving away from the crack to either side, there will be a stress transfer from the steel to the concrete. This transfer will be achieved by slip of the steel relative to the concrete. The point where there is no further stress transfer is defined as a distance a away from the crack. Beyond this distance there will be no further slip and no further change in neutral-axis height, as shown in figure 9.1. At these positions and at the crack (due to symmetry) plane sections will remain plane, so stresses can be calculated. Therefore, it was decided to approximate the effect of the cracked concrete by assuming that: The beam may be split into two regions; region 1 where the concrete has retained its full tensile strength and region 2 where the concrete takes the cracked concrete strength. The transition from one region to the other, rather than being gradual over distance a, is taken to be a step change at distance $a/2$ from the crack on either side, (see figure 9.2.)

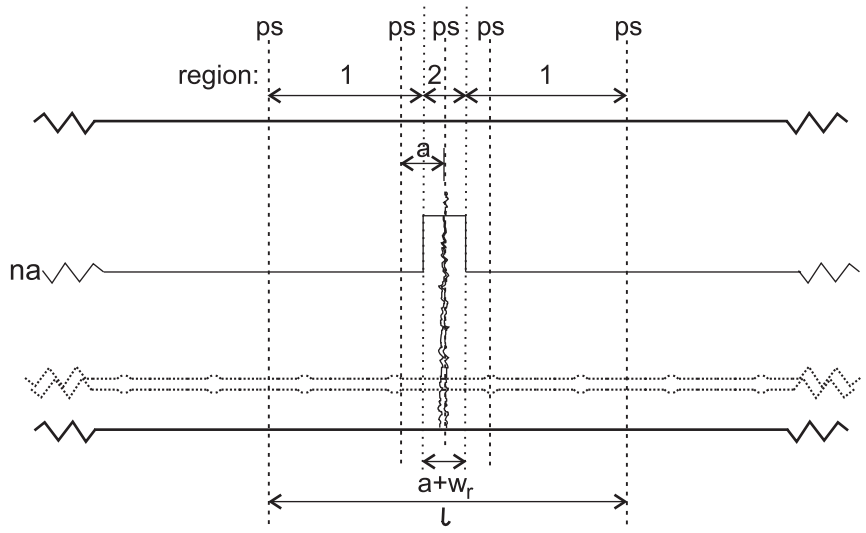

Figure 9.2: Modelling the concrete cracked region

As a result of this assumption, in the model there is a step change in neutral-axis height and in the stresses in the concrete and steel. Region 1, the uncracked region, where there is no slip between the steel and concrete, has a total length $l-a-w_r$, where w_r is the residual crack width after damage loading at the lower surface of the beam. However, w_r is very small so the length may be taken as $l-a$. Region 2, the cracked region with stresses based on the plane section through the crack, is of length $a+w_r$, but taken to be a.

Further assumptions required to calculate the stresses in the concrete simply are:

- The uncracked concrete Young's modulus in tension and compression (E_0) is assumed to be constant during the small amplitude vibration and is calculated using the equation in the BS 8110 code [13].

- The moment is constant over the length l, since l is short in comparison to the length of the beam.

It is now possible to write equations for the beam. A summary of some of the notation used is shown in figure 9.3. Region 1 is considered first. The forces in the concrete over the compressive region, the tensile region and the force in the steel may be written as:

$$F_{cc1} = \frac{E_0 x_1 b \epsilon_{c1}}{2} \tag{9.2}$$

$$F_{ct1} = \frac{E_0(d - x_1)b\epsilon_{t1}}{2} \tag{9.3}$$

$$F_{s1} = E_s A_s \left(\frac{d_s - x_1}{d - x_1}\right)\epsilon_{t1} \tag{9.4}$$

respectively, where b is the width of the beam, A_s is the cross-sectional area of the steel, ϵ_{c1} is the maximum compressive strain in region 1, ϵ_{t1} is the maximum tensile strain in region 1, and E_s is the Young's modulus of the steel. Since plane sections remain plane at either end of both the regions 1, the strains may be related:

$$\epsilon_{c1} = \frac{x_1}{d - x_1}\epsilon_{t1} \tag{9.5}$$

For equilibrium there must be no net axial force, therefore:

$$F_{cc1} = F_{ct1} + F_{s1} \tag{9.6}$$

Rearranging equations 9.2 to 9.6, it is possible to calculate the neutral-axis height:

$$x_1 = \frac{E_0 bd^2 + 2E_s A_s d_s}{2E_0 bd + 2E_s A_s} \tag{9.7}$$

Finally, in this region the moment may be calculated:

$$M = F_{s1}\left(d_s - \frac{x_1}{3}\right) + F_{ct1}\left(\frac{2d}{3}\right) \tag{9.8}$$

using equations 9.3 and 9.4, this can be expressed as a constant multiplied by a strain:

$$M = \alpha\epsilon_{t1} \tag{9.9}$$

where:

$$\alpha = E_s A_s \left(\frac{d_s - x_1}{d - x_1}\right)\left(d_s - \frac{x_1}{3}\right) + \frac{E_0 db}{3}(d - x_1) \tag{9.10}$$

The equations for region 2 are based on the plane section through the crack which remains plane due to symmetry. Most of the equations for the cracked region, region 2, take a similar form to those for region 1 (with the exception of the equation for the tensile force in the cracked concrete F_{ct2} and the moment equation which will be dealt with later):

$$F_{cc2} = \frac{E_0 x_2 b\epsilon_{c2}}{2} \tag{9.11}$$

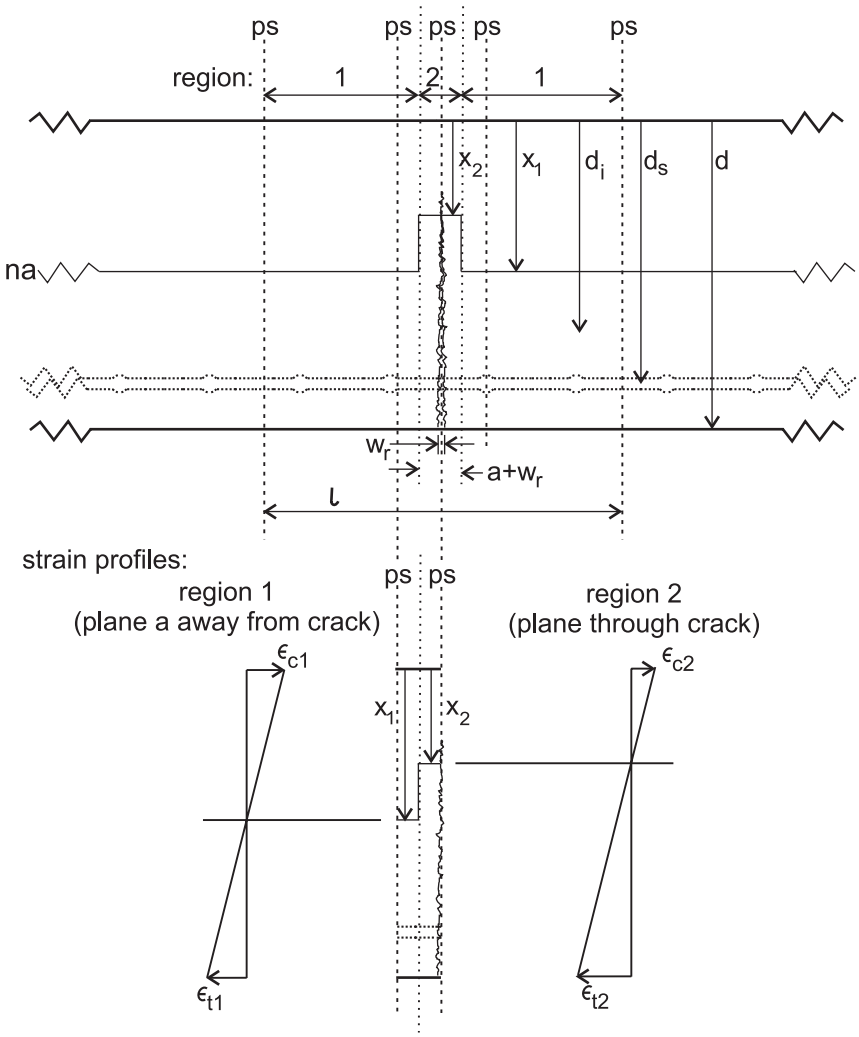

Figure 9.3: Model notation

$$F_{s2} = E_s A_s \left(\frac{d_s - x_2}{d - x_2} \right) \epsilon_{t2} \tag{9.12}$$

where ϵ_{c2} is the maximum compressive strain in region 2 and ϵ_{t2} is the maximum tensile strain in region 2. At the plane section the strains may be related:

$$\epsilon_{c2} = \frac{x_2}{d - x_2} \epsilon_{t2} \tag{9.13}$$

and for equilibrium there must be no net axial force, therefore:

$$F_{cc2} = F_{ct2} + F_{s2} \tag{9.14}$$

This time the location of the centroid of the tensile concrete force is not obvious, since the stiffness of the concrete in tension over the crack is not constant. The moment is therefore written as:

$$M = F_{s2} \left(d_s - \frac{x_2}{3} \right) + M_{ct2} \tag{9.15}$$

where M_{ct2} is the moment exerted by the cracked concrete about an axis $x_2/3$ from the top of the beam (the location of the compressive concrete force). To calculate the force carried by the cracked concrete, rather than integrating over the depth below the neutral-axis, the beam is split into discrete steps and a summation is performed. Using equation 9.1 for the cracked concrete strength, the stress at a distance d_i from the top of the beam may be written:

$$\sigma_i = \frac{\sigma_{fi}}{w_{mi}} a \epsilon_{t2i} \tag{9.16}$$

where the subscript i refers to the position a distance d_i from the top of the beam, σ_{fi} is the failure stress of the crack when the crack width is at a maximum during damage loading, w_{mi}, and ϵ_{t2i} is the strain in the tensile region at this position. The total tensile force carried by the concrete is therefore:

$$F_{ct2} = \sum_i A \frac{\sigma_{fi}}{w_{mi}} \left(\frac{d_i - x_2}{d - x_2} \right) a \epsilon_{t2} \tag{9.17}$$

where A is the area of each discrete step. The moment generated by the cracked concrete at a position d_i from the top of the beam may be written as:

$$M_{ct2} = \sum_i A \frac{\sigma_{fi}}{w_{mi}} \left(\frac{d_i - x_2}{d - x_2} \right) a \epsilon_{t2} \left(d_i - \frac{x_2}{3} \right) \tag{9.18}$$

Unfortunately, it is only possible to express the neutral-axis height in terms of the length of the slip region a, rather than expressing it exclusively in terms of the fundamental beam properties as was the case in region 1:

$$x_2(a) = \frac{\sqrt{(\gamma_a a + E_s A_s)^2 + 2E_0 b\,(\gamma_b a + E_s A_s d_s)} - (\gamma_a a + E_s A_s)}{E_0 b} \tag{9.19}$$

where γ_a and γ_b are functions of the maximum crack width during loading, so will change with damage but not during a vibration test:

$$\gamma_a = A \sum_i \frac{\sigma_{fi}}{w_{mi}} \tag{9.20}$$

$$\gamma_b = A \sum_i \frac{\sigma_{fi} d_i}{w_{mi}} \tag{9.21}$$

It is then possible to express the moment in terms of strain and the neutral-axis position (itself a function of a):

$$M = \beta\,(x_2(a))\,\epsilon_{t2} \tag{9.22}$$

where:

$$\beta\,(x_2(a)) = E_s A_s \left(\frac{d_s - x_2}{d - x_2}\right)\left(d_s - \frac{x_2}{3}\right) + \left(\gamma_c - \frac{4}{3}\gamma_b x_2 + \frac{1}{3}\gamma_a x_2^2\right)\left(\frac{a}{d - x_2}\right) \tag{9.23}$$

and:

$$\gamma_c = A \sum_i \frac{\sigma_{fi} d_i^2}{w_{mi}} \tag{9.24}$$

It should be noted that if the cracked strength of the concrete was ignored, all but the first term in the equation for β would disappear.

The interaction between the two regions must now be considered in order to find a relationship for a in terms of M and the overall maximum strains over the length l, ϵ_{to} and ϵ_{co}. First it is necessary to find a way of modelling the stress transfer between the cracked and the uncracked regions. There are numerous reports of experiments on the local stress-slip relationship under repeated load (for example Edwards and Yannopoulos [31], Morita and Kaku [65], Ismail and Jirsa [45] and Perry and Jundi [82]). However, their work concentrates on repeated loading up to a large stress which inflicts increasing damage to the bond every cycle, whereas the conditions for this calculation are that the beam was loaded up to a large stress during damage loading and then during the vibration tests there was repeated loading, but only at very low stresses. The Comité

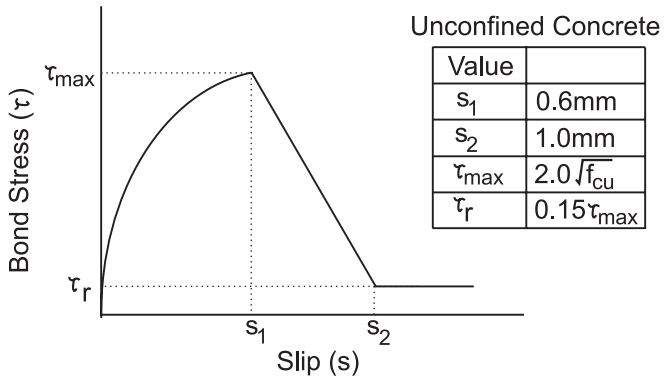

Figure 9.4: Bond stress - slip relationship for monotonic loading (after CEB, see [49])

Euro-International du Béton (CEB) (see [49]) suggested a mathematical approximation to the bond stress-slip relationship. This is shown in figure 9.4, along with typical values for unconfined concrete with good bond conditions. The approximate relationship consists of an initial rapid growth in bond stress modelled by the equation:

$$\tau = \tau_{max} \left(\frac{s}{s_1} \right)^{0.4} \tag{9.25}$$

where τ is the bond stress and s is the corresponding slip, followed by a region of constant stress before a linear decrease in stress with increasing slip. They also report that if the peak bond stress during cyclic loading does not exceed 70-80% of the monotonic maximum bond stress, then the bond stress against slip relationship is unaffected for up to 10 cycles. The slip at which the monotonic maximum bond stress first occurs is in the region of 0.6 mm. If damage level 4 is considered, the maximum crack width at the steel is in the region of 0.1 mm, using the Demec strain readings and assuming that all the strain occurs at the crack. Therefore, it can be assumed that the slip relationship during vibration testing follows the monotonic loading curve.

It is now theoretically possible to consider the strains at the crack and at a distance a away from the crack and write the differential equations at a position x for the crack:

$$\frac{\mathrm{d}s(x)}{\mathrm{d}x} = \epsilon_s - \epsilon_c \tag{9.26}$$

$$\frac{\mathrm{d}F(x)}{\mathrm{d}x} = C\tau(x) \tag{9.27}$$

where F is the force in the steel at x from the crack and C is the circumference of the steel bar. However, this results in two mathematically difficult differential equations once the

expressions for the strains have been included. In addition, the strain distribution in the concrete at the steel height in this region is unclear and so assumptions would have to be made to progress. It was therefore decided to consider the following two extreme cases in order to assess the significance of the crack strength on the behaviour of the beam. The two extremes are:

1. The bond stress is small and so slip is only limited by the reinforcing bar rib spacing.

2. The bond stress takes the value τ_{max}.

In assuming either extreme, any non-linearity due to the stress-slip relationship will be altered. However the aim of this calculation is to assess the significance of the crack strength rather than to model the non-linear behaviour of the beam. For extreme 1, the slip distance a is simply set to half the rib spacing, 5 mm, (assuming the crack is mid-way between two ribs). For extreme 2, the slip distance must be calculated using the assumption that the beam may be represented as two regions and expressing the total force transfer in the steel between the two regions in terms of the bond stress and the steel surface area:

$$a = \frac{F_{s2} - F_{s1}}{\tau_{max} C} = \frac{E_s A_s M}{\tau_{max} C} \left[\frac{1}{\beta} \left(\frac{d_s - x_2}{d - x_2} \right) - \frac{1}{\alpha} \left(\frac{d_s - x_1}{d - x_1} \right) \right] \tag{9.28}$$

Finally, using compatibility conditions, the overall strains for the section l long may be expressed as:

$$\epsilon_{to} = \frac{l-a}{l} \epsilon_{t1} + \frac{a}{l} \epsilon_{t2} = \frac{M}{l} \left(\frac{l-a}{\alpha} + \frac{a}{\beta} \right) \tag{9.29}$$

$$\epsilon_{co} = \frac{l-a}{l} \epsilon_{c1} + \frac{a}{l} \epsilon_{c2} = \frac{M}{l} \left[\left(\frac{l-a}{\alpha} \right) \left(\frac{x_1}{d - x_1} \right) + \left(\frac{a}{\beta} \right) \left(\frac{x_2}{d - x_2} \right) \right] \tag{9.30}$$

from which the change in rotation from one end of the section relative to the other may be calculated as:

$$\Delta\theta = \frac{l}{d} \left(\epsilon_{co} + \epsilon_{to} \right) \tag{9.31}$$

Solution of these equations, for a certain applied moment M, is done iteratively using the following routine:

1. Calculate x_1 and α using equations 9.7 and 9.10.

2. Pick an initial value of a.

3. Calculate x_2 using equations 9.19, 9.20 and 9.21.

4. Calculate β using equations 9.23 and 9.24.

5. Calculate a using either extreme 1 or extreme 2 condition.

6. Calculate if the difference between the new value of a and the old one is below an acceptable error. If the error is too large, return to step 2.

7. Calculate the overall strains ϵ_{to} and ϵ_{co} using equations 9.29 and 9.30 and the relative rotation over the section using 9.31.

This scheme was implemented in Matlab using the beam properties in table 7.1, the undamaged Young's modulus for the concrete, and the bond properties in figure 9.4. Figures 9.5a and 9.5b show the moment against relative rotation for the section for extreme 1 and extreme 2 respectively for both the case where the cracked concrete strength is included (labelled inc. ccs) and when it is ignored (labelled exc. ccs). Figure 9.6 shows the maximum tensile and compressive strains for both including and excluding the cracked concrete strength and both extremes. Figure 9.7 shows the increase in relative rotation when the cracked concrete strength is excluded from the calculation for both extremes. The results clearly show that at both extremes the effect of including the cracked concrete strength is minimal, so suggesting that any non-linear mechanism due to friction between the crack surfaces will not play a significant part in the non-linearity present during the vibration tests or the hysteresis present in the static load tests. As mentioned before, due to the crude approximation using the two extremes in the bond stress against slip relationship, no conclusion can be made about the non-linearity resulting from this relationship using this model. A detailed non-linear finite element model would be required.

It should be noted that this model cannot be directly compared to the experimental data. Figure 9.6 shows that the relative rotation is approximately 4×10^{-5} when a moment of 250 Nm is applied. Figure 8.52 shows that at damage level 4 the relative rotation measured using the vibrating wire strain gauges is approximately 8×10^{-5} when

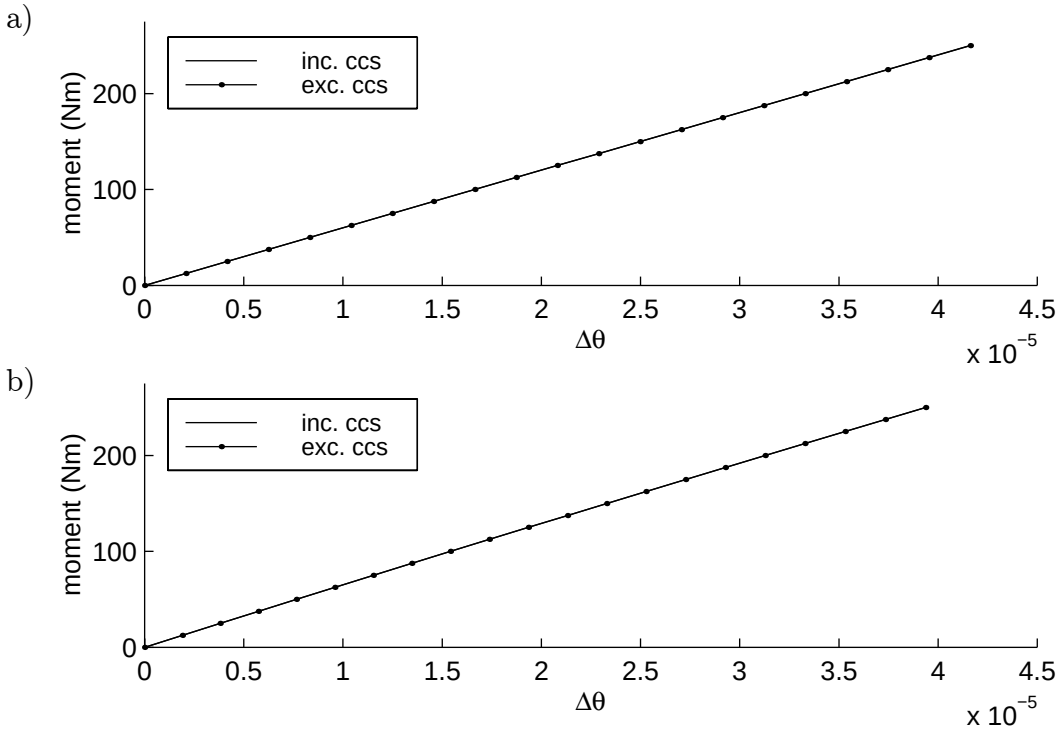

Figure 9.5: Moment - relative rotation relationship for a) extreme 1 and b) extreme 2

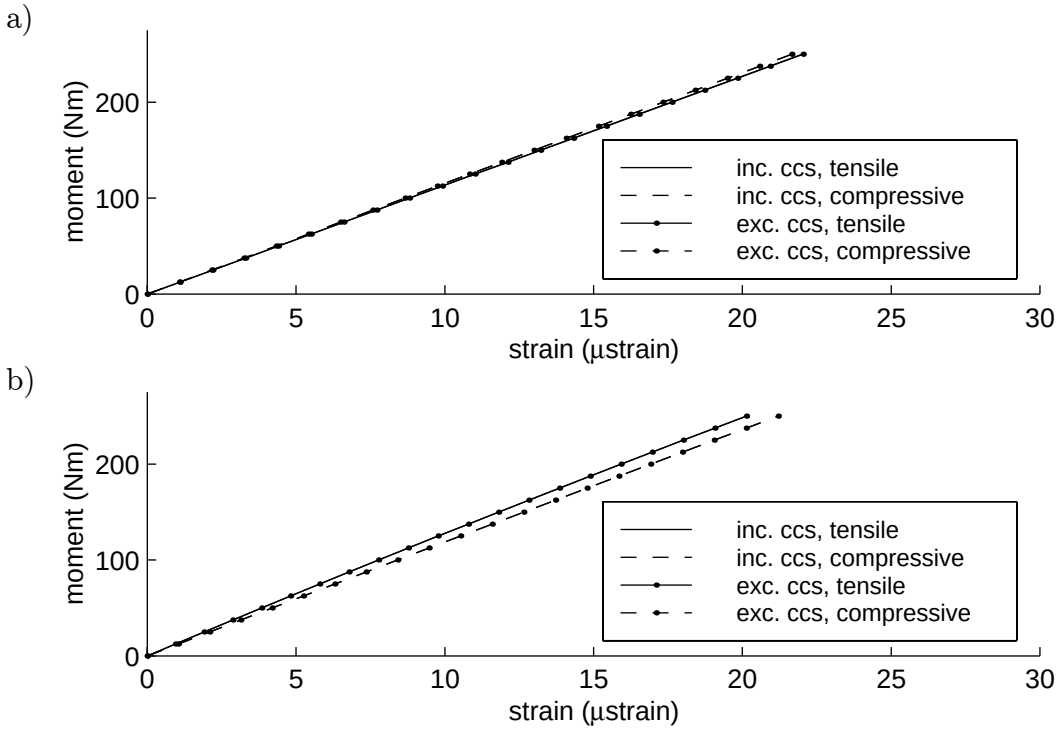

Figure 9.6: Moment - maximum strain relationship for a) extreme 1 and b) extreme 2

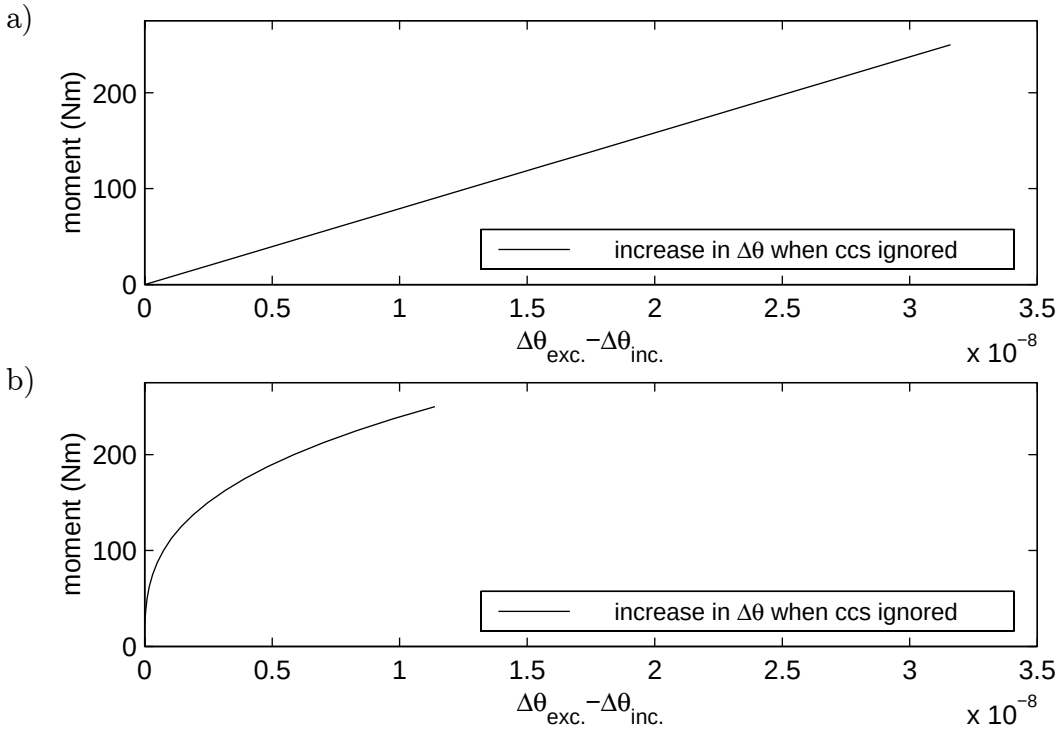

Figure 9.7: Difference between the relative rotation when the cracked concrete strength is excluded and when it is included for a) extreme 1 and b) extreme 2

a moment of 250 Nm is applied. The main reason for this factor of 2 error in the model is almost certainly that the Young's modulus of the uncracked concrete was taken to be the unloaded Young's modulus. However by damage level 4 the beam has been loaded and unloaded four times in progressively larger cycles. The concrete at the top surface of the beam had experienced compressive strains up to around 740 μstrain and tensile strains (averaged over the cracked region) up to around 1300 μstrain during the damage loading (see figure 8.1). This loading will have had the effect of reducing the Young's modulus of the uncracked concrete (see, for example, Park and Pauley [80]). Therefore, by using the undamaged concrete Young's modulus in the model, it must be expected that the relative rotation for a given moment will be smaller than the measured value. In fact, the relative rotation predicted using the model is very similar to the measured values for the undamaged beam. If the Young's modulus of the concrete is reduced, to account for the damage loading, the effect of the cracked concrete strength on the stiffness of the beam is still negligible.

9.3 The Bond between the Concrete and Steel

Further tests are required to assess what effect the bond between the concrete and steel has on the vibration behaviour of the damaged beam. It is proposed that attempts be made to cast a beam with a region where there is no bond strength between the concrete and the steel. The difficulty with this is that it is unclear whether, during the vibration tests, the slip is confined to the region between the ribs on the reinforcing bars or whether the damage loading is sufficient to cause some damage to the concrete surrounding the ribs, which would allow them to slip relative to the concrete. If the slip during the vibration tests is confined to the region between the ribs, a beam could be cast with oiled reinforcing bars. This would remove the concrete-steel bond between the ribs, but allow the ribs to act in their usual way. The removal of any effects due to the ribs moving during the vibration testing is more difficult, as any alteration to the bond between the ribs and the concrete will significantly alter the behaviour of the beam during damage loading. Ribs could be removed over a short section prior to casting. However during the comparison of the resultant vibration behaviour with that

of a standard beam, it must be remembered that the behaviour at certain damage levels will not be directly comparable. The testing would only allow an assessment of any overall effect on the changes in the non-linear vibration characteristics with increased damage.

9.4 Summary

In summary, the experiments discussed in chapters 7 and 8 have allowed an assessment of two of the possible non-linear mechanisms proposed in chapter 5.

The vibrating wire strain gauge measurements along with the Demec strain measurements have indicated that the bilinear mechanism representing the crack opening and closing during each oscillation is not a realistic mechanism for the beams tested. This is because the residual strain over the cracked region is not exceeded during the vibration tests.

A model of the region over which the crack occurs in conjunction with the experimental data has demonstrated that the strength of the cracked concrete is not likely to have a significant effect on the stiffness of the beam. Therefore, the frictional behaviour generated by the matrix-aggregate interaction is not thought to contribute to the non-linear vibration behaviour. Future experimental work is planned to confirm this finding. Static load tests will be conducted on a beam with a pre-cast steel plate inserted as described in section 7.1.1 to simulate a smooth crack. This plate will be positioned slightly off-centre. Strain measurements will be taken over the region of the plate and over a region the same distance the other side of the mid-span, in order to allow a direct comparison of the behaviour of the beam with and without the cracked concrete stiffness contribution.

Further experimental work is required to assess the other two mechanisms suggested in chapter 5. It is suggested that experimental tests on modified reinforced concrete beams would aid understanding of the slip behaviour. Detailed modelling will be required to make an assessment of whether the inherent non-linearity of concrete in compression contributes to the non-linear vibration behaviour of the beam.

Chapter 10

Conclusions and Further Work

10.1 Conclusions

A literature review has revealed that much work has been conducted on the use of vibration tests to detect damage in reinforced concrete bridges. Almost all of this work has assumed that the vibrations are linear, i.e. the vibration characteristics are not dependent on amplitude of oscillation. Problems with sensitivity, fluctuations in modal properties with temperature and a need to have undamaged modal data have not been overcome. In contrast, very little work has been reported on the non-linear vibration properties of concrete bridges. An investigation into the possibility of using non-linear vibration characteristics to detect damage in reinforced concrete bridges has been presented here.

A time-stepping model has been derived to aid the understanding of non-linear crack mechanisms present in damaged beams. The model is based on the idea that the mass and inertia of the beam may be approximated by point masses and inertias at discrete points, and shear distortion and bending stiffness may be represented using rotational and transverse springs between rigid blocks. The advantage of this method over other methods of modelling cracked vibrating beams is that it is capable of modelling non-linear crack mechanisms without the assumption that the vibration is dominated by the fundamental mode (an assumption which ensures that crack compliance will cycle at the same frequency as the beam vibration). The model has been verified theoretically for linear vibration behaviour. The natural frequencies and mode shapes for the first

three modes, derived from acceleration data generated using the model, compared well to theoretical values with an error of less than 0.1% if 20 or more blocks were used and only a 0.6% error when a 10 block representation was used. Non-linear damage is modelled by altering the spring stiffness at each time-step depending on the curvature of the beam at that time. The model's capabilities of predicting the non-linear behaviour have been demonstrated using a cantilever beam with a non-linear element, which resulted in a localised stiffening of the beam when the curvature exceeded a threshold value.

To detect the non-linearities present in impact excitation vibration signals, the time-frequency distribution (and hence the amplitude-frequency relationship) of the signal is needed. Several time-frequency distribution estimation tools have been discussed including the discrete Fourier transform moving window, the auto-regressive model moving window, harmonic wavelets and examples of the Cohen class of bilinear time-frequency distributions. A detailed investigation into these various distribution estimators has been conducted to assess which is most suitable for analysing the vibration signals generated during tests on reinforced concrete beams to detect changes in frequency with time. It was found for these signals, which consisted almost entirely of the fundamental mode, that using either the discrete Fourier transform (DFT) moving window, the wavelet transform, the windowed Wigner-Ville distribution or the modified exponential distribution gave very similar time-frequency estimations for the fundamental mode. Due to its relative simplicity the DFT moving window was therefore selected to analyse experimental results.

The vibration experiments consisted of impact excitation tests conducted on two reinforced concrete beams with low natural frequencies. Damage was induced using three-point loading. There were 10 damage levels before failure (which was defined as the point where the beam was unable to sustain any additional load and occurred at a load just below that corresponding to the 11th damage level). Methods of combining data from the acceleration data recorded at several sensitivity levels and techniques for averaging the non-linear characteristics over several impact tests have been proposed. Since the signals consisted almost entirely of the fundamental mode, a method of converting the time-frequency relationship to an amplitude-frequency relationship, which it was argued gave a better comparison over varying damage levels as it eliminated changes

due to damping, has been presented. These vibration tests confirmed that there is a change in non-linear vibration behaviour with damage. Unfortunatly, the change is greatest over the first damage level and after the third damage level there is a reversal in the trend and a slight reduction in non-linearity with further damage. Therefore, this method of detecting damage is unlikely to be suitable for reinforced concrete bridges, however may be useful in detecting low levels of cracking in special structures where very high levels of structural integrity are required.

In addition to the vibration tests, static load tests were also conducted on the beams. Strain was measured at the upper and lower surfaces on the beam across a crack using vibrating wire strain gauges. These data were used to calculate the moment-relative rotation properties of the beam over the length of the strain gauges. These experiments were performed to demonstrate a method of finding the moment-rotation relationship which represents a section of cracked concrete. This moment-rotation relationship could then be used in conjunction with the model to allow better understanding of the non-linear damage mechanism exhibited during the vibration tests.

Several possible non-linear crack mechanisms have been discussed, namely the bi-linear crack closure mechanism and mechanisms due to the non-linear behaviour of concrete in compression, relative slip between the reinforcing bar and the concrete on either side of the crack, and matrix-aggregate interaction over the crack surface. Strain measurements taken during the static load tests and during damage loading have been used to indicate that the bilinear mechanism representing the crack opening and closing during each oscillation is not a realistic mechanism for the beams tested. A model of the region over which the crack occurs, in conjunction with the experimental data, has demonstrated that the strength of the cracked concrete is not likely to have a significant effect on the stiffness of the beam. Therefore, the frictional behaviour generated by the matrix-aggregate interaction is not thought to contribute to the non-linear vibration behaviour.

To summarise, the major conclusions are:

- Studying non-linearities in the response to impact excitation is unlikely to be a useful damage detection tool for concrete bridges.

- Since the strength of the non-linear behaviour varies significantly for very low levels of damage (up to 27% of the failure load) it may be of use to detect damage in structures requiring very high levels of structural integrity.
- The DFT moving window has been shown to be the most efficient method of analysing the impact excitation vibration signals.
- The crack closure mechanism is not a realistic mechanism for cracked concrete.
- The stiffness of the cracked concrete is insignificant in comparison with the overall stiffness of the beam therefore the matrix-aggregate interaction mechanism cannot explain the non-linear behaviour of the damaged beam.

10.2 Further Work

It is suggested that forced excitation vibration tests should be performed. These will allow the assessment of non-linearities by inspecting super-harmonics present in the response. This technique may prove to be more sensitive than the method of examining the amplitude-frequency relationship for impact excitation tests employed here, since averaging over many cycles would be possible.

To improve the method of measuring the moment-relative rotation relationship using static load tests, it is recommended that modifications be made to the vibrating wire strain gauges and to the beam. It would be easier to analyse the results if the vibrating wire strain gauges were modified to allow a gauge length of 100 mm. This would permit direct comparison with the Demec strain measurements taken during damage loading. Ideally the tests would be performed on a modified beam with a stirrup spacing of 100 mm to ensure that the crack spacing also matches the Demec gauge length, therefore ensuring that the vertical planes on which the anchor points of the strain gauges are located remain plane during loading. It has been shown that the maximum relative rotation over the gauge length and the maximum mid-span displacement display similar characteristics (albeit scaled) over varying damage. Therefore tests at different damage levels over a fixed range of displacement (rather than over a fixed range of load) should be

conducted. This would allow easier comparison of the moment-rotation characteristics using hysteresis loops of fixed maximum relative rotation.

Once the improved static load tests have been conducted, the moment-relative rotation characteristics over the cracked region may be used in conjunction with the time-stepping model to understand further the non-linear vibration of the cracked beam.

Additional work is required to assess the possible non-linear damage mechanisms. To confirm the conclusion, drawn from a model of the cracked concrete region, that the increase in stiffness due to cracked concrete strength is insignificant compared to the overall stiffness of a section of cracked concrete beam, it is proposed that static load tests on a beam with a pre-cast plate be conducted. This plate would simulate a smooth crack and, by comparing the stiffness characteristics over the smooth crack region with that over a normal cracked region, would allow the assessment of the stiffness contribution due to cracked concrete strength. Vibration tests would also aid this assessment.

Tests are also required to assess what effect the bond between the concrete and steel has on the vibration behaviour of the damaged beam. These tests would consist of static load tests and vibration tests on another modified beam. It is suggested that a beam be cast with oiled reinforcing bars to examine the effects of bond slip between the reinforcing bar ribs by removing any slip resistance. Additional tests may be necessary to determine whether the slip extends to the ribs moving relative to the concrete during the vibration tests. This would require the testing of a beam with the ribs removed around a localised crack region.

Detailed modelling must be conducted to make an assessment of whether the non-linearity of concrete in compression contributes to the non-linear vibration behaviour of the beam.

References

[1] M. Abdel Wahab and G. De Roeck 1997, Structural Engineering International 4, 266–270. Effect of temperature on dynamic system parameters of a highway bridge.

[2] S. Alampalli, G. Fu and E.W. Dillon 1997, Journal of Structural Engineering 123, No. 2, 237–245. Signal versus noise in damage detection by experimental modal analysis.

[3] D. Armon, Y. Ben-Haim and S. Braun 1994, Mechanical Systems and Signal Processing 8, No. 1, 81–91. Crack detection in beams by rank-ordering of eigenfrequency shifts.

[4] H. Aoyama 1964, Proceedings of the International Symposium on the Flexural Mechanics of Reinforced Concrete ASCE-ACI, 183–212. Moment-curvature characteristics of reinforced concrete members subjected to axial load and reversal of bending.

[5] A. Ayoub and F.C. Filippou 1999, Journal of Structural Engineering 125, No. 6, 661–671. Mixed formulation of bond-slip problems under cyclic loads.

[6] I. Ballo 1998, Journal of Sound and Vibration 217, No. 2, 321–333. Non-linear effects of vibration of a continuous transverse cracked slender shaft.

[7] J.R. Billing 1984, Canadian Journal of Civil Engineering 11, 833–843. Dynamic loading and testing of bridges in Ontario.

[8] P. Bonato, R. Ceravolo, A. De Stefano and M. Knaflitz 1997, Mechanical Systems and Signal Processing 11, No. 4, 509–527. Bilinear time-frequency transformations in the analysis of damaged structures.

[9] A.P. Bovsunovsky and V.V. Matveev 2000, Journal of Sound and Vibration 235, No. 3, 415–434. Analytical approach to the determination of dynamic characteristics of a beam with a closing crack.

[10] R.N. Bracewell 1986, The Fourier Transform and its Applications, 2nd Edition, McGraw-Hill.

[11] B. Bresler and V. Bertero 1968, Proceedings of ASCE: Journal of the Structural Division 94, No. 6, 1567–1590. Behaviour of reinforced concrete under repeated load.

[12] E.O. Brigham 1974, The Fast Fourier Transform, Prentice-Hall.

[13] British Standard 1997, BS 8110: Structural Use of Concrete, Part 1. Code of Practice for Design and Construction, BSI.

[14] P. Cawley and R.D. Adams 1979, Journal of Strain Analysis 14, No. 2, 49–57. The location of defects in structures from measurements of natural frequency.

[15] J.R. Casas and A.C. Aparicio 1994, Journal of Structural Engineering 120, No. 8, 2437–2450. Structural damage identification from dynamic-test data.

[16] T.D. Chaudhari and S.K. Maiti 1999, Engineering Fracture Mechanics 63, 425–445. Modelling of transverse vibration of beam of linearly variable depth with edge crack.

[17] R.S. Chen 1999, Journal of Sound and Vibration 221, No. 2, 325–333. A novel numerical method for evaluating the natural vibration frequency of a bending bar considering rotary inertia and shear effect.

[18] W.Y. Chen and G.R. Stegen 1974, Journal of Geophysical Research 79, No. 20, 3019–3022. Experiments with maximum entropy spectra of sinusoids.

[19] S.M. Cheng, X.J. Wu, W. Wallace and A.S.J. Swamidas 1999, Journal of Sound and Vibration 225, No. 1, 201–208. Vibrational response of a beam with a breathing crack.

[20] H.I. Choi and W.J. Williams 1989, IEEE Transactions on Acoustics, Speech and Signal Processing 37, No. 6, 862–871. Improved time-frequency representation of multicomponent signals using exponential kernels.

[21] L. Cohen 1988, Journal of Mathematical Physics 7, 2180–2183. Generalized phase-space distribution functions.

[22] L. Cohen 1989, Proceedings of the IEEE 77, No. 7, 941–981. Time-frequency distributions - a review.

[23] W.B. Collis, P.R. White and J.K. Hammond 1998, Mechanical Systems and Signal Processing 12, No. 3, 375–394. Higher-order spectra: the bispectrum and trispectrum.

[24] R.W. Clough and J. Penzien 1975, Dynamics of Structures, McGraw-Hill.

[25] P.C. Das, N.C. Davidson and C. Colla 1995, Institution of Structural Engineers Seminar: Analysis and Testing of Bridges. Potential applications of NDT methods for bridge assessment and monitoring.

[26] P.C. Das, J.S. Owen, B.J. Eccles, M.A. Woodings and B.S. Choo 1997, 76th Annual Meeting of the Transportation Research Board, Washington DC. The role of dynamic testing in the assessment of bridges.

[27] A.D. Dimarogonas and S.A. Paipetis 1983, Analytical Methods in Rotor Dynamics, Elsevier Applied Science.

[28] S.W. Doebling, C.R. Farrar and M.B. Prime 1998, The Shock and Vibration Digest 30, No. 2, 91–105. A summary review of vibration-based damage identification methods.

[29] B.J. Eccles, J.S. Owen, B.S. Choo and M.A. Wooding 1999, 4th Conference of the European Association of Structural Dynamics (EURODYN), 357–364. Non-linear vibrations of cracked reinforced concrete beams.

[30] B.J. Eccles, J.S. Owen, M.A. Woodings and B.S. Choo 1997, Structural Faults and Repair Conference, Edinburgh. A proposed new approach to full life qualitative bridge assessment.

[31] A.D. Edwards and P.J. Yannopoulos 1978, Magazine of Concrete Research 30, No. 103, 62–72. Local bond-stress-slip relationships under repeated loading.

[32] G. Eilbracht and M. Link 1995, International Symposium on Non-Destructive Testing in Civil Engineering (NDT-CE) 26, 327–334. Identification of crack parameters in concrete beams using modal test data.

[33] H.M. Farag and P. Leach 1996, International Journal for Numerical Methods in Engineering 39, 2111–2129. Material modelling for transient dynamic analysis of reinforced concrete structures.

[34] C.R. Farrar and G.H. James III 1997, Journal of Sound and Vibration 205, No. 1, 1–18. System identification from ambient vibration measurements on a bridge.

[35] C.R. Farrar and D.A. Jauregui 1998, Smart Materials and Structures, No. 7, 704–719. Comparative study of damage identification algorithms applied to a bridge; 1, experimental.

[36] C.R. Farrar and D.A. Jauregui 1998, Smart Materials and Structures, No. 7, 720–731. Comparative study of damage identification algorithms applied to a bridge; 2, numerical study.

[37] A.J. Felber, C.E. Ventura and S.F. Stiemer 1993, EDI Experimental Dynamics Ltd. Queensborough bridge ambient vibration study.

[38] J. Fernández-Sáez, L. Rubio and C. Navarro 1999, Journal of Sound and Vibration 225, No. 2, 345–352. Approximate calculation of the fundamental frequency for bending vibrations of cracked beams.

[39] Gage Technique International Ltd 1999, Vibrating Wire Strain Gauge Technical Specification.

[40] A. Goldsmith 1999, Fourth Year Undergraduate Project Report, Department of Engineering Science, University of Oxford. Damage detection in concrete beams using vibration measurements.

[41] P. Gudmundson 1983, Journal of the Mechanics and Physics of Solids 31, No. 4, 329–345. The dynamic behaviour of slender structures with cross-sectional cracks.

[42] P.R. Gutowski, E.A. Robinson and S. Treitel 1978, IEEE Transactions in Geoscience and Electronics GE-16, 80–84. Spectral estimation: fact or fiction.

[43] S.S. Haykin (Editor) 1979, Nonlinear Methods of Spectral Analysis, Springer-Verlag.

[44] J.L Humar and A.M. Kashif 1993, Canadian Journal of Civil Engineering 20, 287–298. Dynamic response of bridges under travelling loads.

[45] M.A.F. Ismail and J.O. Jirsa 1972, American Concrete Institute Journal, 334–343. Bond deterioration in reinforced concrete subject to low cycle loads.

[46] J. Jeong and W.J. Williams 1992, IEEE Transactions on Signal Processing 40, No. 11, 2757–2765. Alias-free generalized discrete-time time-frequency distributions.

[47] S.M. Kay and S.L. Marple Jr. 1981, Proceedings of the IEEE 69, No. 11, 1380–1419. Spectrum analysis - a modern perspective.

[48] M. Kisa and J. Brandon 2000, Journal of Sound and Vibration 238, No. 1, 1–18. The effects of closure of cracks on the dynamics of a cracked cantilever beam.

[49] G. König and H. Duda 1996, RC Elements under Cyclic Loading: State of the Art Report, Thomas Telford.

[50] C. Krämer, C.A.M. De Smet and G. De Roeck 1999, Proceedings of the International Modal Analysis Conference (IMAC) 17, 1023–1029. Z24 bridge damage detection tests.

[51] C. Krämer , C.A.M. De Smet and B. Peeters 1999, Proceedings of the International Modal Analysis Conference (IMAC) 17, 1030–1034. Comparison of ambient and forced vibration testing of civil engineering structures.

[52] E. Kreyszig 1988, Advanced Engineering Mathematics, 6th Edition, J Wiley and Son.

[53] L.A. Lutz 1970, American Concrete Institute Journal, October, 778–787. Analysis of stresses in concrete near a reinforcing bar due to bond and transverse cracking.

[54] J. Maeck, M. Abdel Wahab, B. Peeters, G. De Roeck, J. De Visscher, W.P. De Wilde, J.-M. Ndambi and J. Vantomme 2000, Engineering Structures 22, 1339–1349. Damage identification in reinforced concrete structures by dynamic stiffness determination.

[55] J. Maeck, M. Abdel Wahab and G. De Roeck 1999, Proceeding of the International Modal Analysis Conference (IMAC) 17, 1289–1295. Damage localization in reinforced concrete beams by dynamic stiffness determination.

[56] J.R. Maguire and R.T. Severn 1987, Proceedings of the Institution of Civil Engineers Part 2 83, 769–784. Assessing the dynamic properties of prototype structures by hammer testing.

[57] M.A. Mahmoud, M. Abu Zaid and S. Al Harashani 1999, Communications in Numerical Methods in Engineering 15, 709–715. Numerical frequency analysis of uniform beam with a transverse crack.

[58] J. Makhoul 1975, Procedures of the IEEE 63, 561–580. Linear prediction: a tutorial review.

[59] Matlab 2000, Signal Processing Toolbox User's Guide, The Math Works.

[60] D.F. Mazurek and J.T. DeWolf 1990, Journal of Structural Engineering 116, No. 9, 2532–2549. Experimental study of bridge monitoring techniques.

[61] A. Messina, E.J. Williams and T. Contursi 1998, Journal of Sound and Vibration 216, No. 5, 791–808. Structural damage detection by a sensitivity and statistical-based method.

[62] MGS Geosense Ltd. 2000, Vibrating Wire Strain Gauges (2000 Series).

[63] G. Monti, F.C. Filippou and E. Spacone 1997, Journal of Structural Engineering 123, No. 5, 614–623. Finite element for anchored bars under cyclic load reversals.

[64] A. Morassi 2001, Journal of Sound and Vibration 242, No. 4, 577–596. Identification of a crack in a rod based on changes in a pair of natural frequencies.

[65] S. Morita and T. Kaku 1973, IABSE Symposium on the Resistance and Ultimate Deformation of Structures, The Report of the Working Commissions 13, 221–227. Local bond stress-slip relationship under repeated loading.

[66] B.P. Nandwana and S.K. Maiti 1997, Journal of Sound and Vibration 203, No. 3, 435–446. Detection of the location and size of a crack in stepped cantilever beams based on measurements of natural frequencies.

[67] Y. Narkis 1994, Journal of Sound and Vibration 172, No. 4, 549–558. Identification of crack location in vibrating simply supported beams.

[68] S.A. Neild, P.D. McFadden and M.S. Williams 2001, Journal of Sound and Vibration 239, No. 1, 99–121. A discrete model of a vibrating beam using a time-stepping approach.

[69] M. Nelkon and P. Parker 1987, Advanced Level Physics, 6th Edition, Heinemann Educational.

[70] A.M. Neville 1981, Properties of Concrete, 3rd Edition, Longman Scientific and Technical Series.

[71] D.E. Newland 1993, An introduction to Random Vibrations, Spectral & Wavelet Analysis, 3rd Edition, Prentice Hall.

[72] D.E. Newland 1999, Journal of Vibration and Acoustics 121, 149–155. Ridge and phase identification in the frequency analysis of transient signals by harmonic wavelets.

[73] C.L. Nikias and A.P. Petropulu 1993, Higher-Order Spectra Analysis: a nonlinear signal processing framework, Prentice Hall Signal Processing Series.

[74] A.V. Oppenheim, A.S. Willsky and I.T. Young 1983, Signals and Systems, Prentice Hall Signal Processing Series.

[75] J.S. Owen 2001, Civil Engineering Colloquium, University of Oxford, February 23th. Structural health monitoring of bridges.

[76] J.S. Owen and B.S. Choo 1998, University of Nottingham Report No. SR98006. The use of dynamic testing methods for bridge assessment and monitoring (draft).

[77] J.S. Owen, B.J. Eccles, B.S. Choo and M.A. Woodings 2001, Engineering Structures 23, 521–536. The application of auto-regressive time series modelling for the time-frequency analysis of civil engineering structures.

[78] A.K. Pandey, M. Biswas and M.M. Samman 1991, Journal of Sound and Vibration 145, No. 2, 321–332. Damage detection from changes in curvature mode shapes.

[79] A. Papoulis 1982, Signal Analysis, McGraw-Hill.

[80] R. Park and T. Pauley 1975, Reinforced Concrete Structures, Wiley-Interscience.

[81] P. Paultre, O. Chaallal and J. Proulx 1992, Canadian Journal of Civil Engineering 19, 260–278. Bridge dynamics and dynamic amplification factors - a review of analytical and experimental findings.

[82] E.S. Perry and N. Jundi 1969, American Concrete Institute Journal, May, 377–380. Pullout bond stress distribution under static and dynamic repeated loading.

[83] M. Petyt 1990, Introduction to Finite Element Vibration Analysis, Cambridge University Press.

[84] B.A.D. Piombo, A. Fasana, S. Marchesiello and M. Ruzzene 2000, Mechanical Systems and Signal Processing 14, No. 1, 75–89. Modelling and identification of the dynamic response of a supported bridge.

[85] D.S. Prakash Rao, M.G. Tamhankar and S.P. Sharma 1983, Materials and Construction 16, No. 96, 457–466. Literature survey on in situ testing of concrete bridges.

[86] W.H. Press, B.P. Flannery, S.A. Teukolsky and W.T. Vetterling 1988, Numerical Recipes in C: The Art of Scientific Computing, Cambridge University Press.

[87] N. Pugno, C. Surace and R. Ruotola 2000, Journal of Sound and Vibration 235, No. 5, 749–762. Evaluation of the non-linear dynamic response to harmonic excitation of a beam with several breathing cracks.

[88] G.-L. Qian, S.-N. Gu and J.-S. Jiang 1990, Journal of Sound and Vibration 138, No. 2, 233–243. The dynamic behaviour and crack detection of a beam with a crack.

[89] M. Raghavendrachar and A.E. Aktan 1992, Journal of Structural Engineering 118, No. 8, 2186–2203. Flexibility by multireference impact testing for bridge diagnostics.

[90] R.B. Randall 1987, Frequency Analysis, 3rd Edition, Brüel and Kjær.

[91] C.P. Ratcliffe 1997, Journal of Sound and Vibration 204, No. 3, 505–517. Damage detection using a modified Laplacian operator on mode shape data.

[92] A. Rivola and P.R. White 1998, Journal of Sound and Vibration 216, No. 5, 889–910. Bispectral analysis of the bilinear oscillator with application to the detection of fatigue cracks.

[93] P.F. Rizos, N. Aspragathos and A.D. Dimarogonas 1990, Journal of Sound and Vibration 138, No. 3, 381–388. Identification of crack location and magnitude in a cantilever beam from the vibration modes.

[94] G.P. Roberts 1995, The Institution of Structural Engineers, Analysis and Testing of Bridges Seminar. Recent experience in dynamic monitoring of a multi-span bridge.

[95] H.J. Salane and J.W. Baldwin Jr. 1990, Journal of Structural Engineering 116, No. 7, 2008–2021. Identification of modal properties of bridges.

[96] O.S. Salawu 1997, Engineering Structures 19, No. 9, 718–723. Detection of structural damage through changes in frequency: a review.

[97] O.S. Salawu 1997, Canadian Journal of Civil Engineering 24, 218–228. Assessment of bridges: use of dynamic testing.

[98] O.S. Salawu and C. Williams 1995, Journal of Structural Engineering 121, No. 2, 161–173. Bridge assessment using forced-vibration testing.

[99] O.S. Salawu and C. Williams 1995, Engineering Structures 17, No. 2, 113–121. Review of full-scale dynamic testing of bridge structures.

[100] R. Shepherd and R.J. Aves 1973, Proceedings of the Institution of Civil Engineers March, 191–210. Impact factors for simple concrete bridges.

[101] E.I. Shifrin and R. Ruotolo 1999, Journal of Sound and Vibration 222, No. 3, 409–423. Natural frequencies of a beam with an arbitrary number of cracks.

[102] W.J. Staszewski 1997, Journal of Sound and Vibration 203, No. 2, 283–305. Identification of damping in MDOF systems using time-scale decomposition.

[103] W.J. Staszewski 1998, Journal of Sound and Vibration 214, No. 4, 639–658. Identification of non-linear systems using multi-scale ridges and skeletons of the wavelet transform.

[104] J.N. Sundermeyer and R.L. Weaver 1995, Journal of Sound and Vibration 183, No. 5, 857–871. On crack identification and characterization in a beam by non-linear vibration analysis.

[105] D.C. Teychenné, R.E. Franklin and H. Erntroy 1975, Design of normal concrete mixes, Department of the Environment, HMSO.

[106] S.K. Thyagarajan, M.J. Schulz, P.F. Pai and J. Chung 1998, Journal of Sound and Vibration 210, No. 1, 162–170. Detecting structural damage using frequency response functions.

[107] J. Todd (Editor) 1962, Survey of Numerical Analysis, McGraw-Hill.

[108] F.S. Tse, I.E. Morse and R.T. Hinkle 1978, Mechanical Vibrations: Theory and Applications (2nd Edition), Allyn and Bacon Inc.

[109] S.L. Tsyfansky and V.I. Beresnevich 2000, Journal of Sound and Vibration 236, No. 1, 49–60. Non-linear vibration method for detection of fatigue cracks in aircraft wings.

[110] T.J. Ulrych and T.N. Bishop 1975, Review of Geophysics and Space Physics 13, 183–200. Maximum entropy spectral analysis and autoregressive decomposition.

[111] K. Van Den Abeele and J. De Visscher 2000, Cement and Concrete Research 30, 1453–1464. Damage assessment in reinforced concrete using spectral and temporal nonlinear vibration techniques.

[112] H.S. Ward 1984, Journal of Engineering Structures 110, No. 10, 2487–2498. Traffic generated vibrations and bridge integrity.

[113] W. Weaver, S. Timoshenko and D.H. Young 1990, Vibration Problems in Engineering, 5th Edition, Wiley.

[114] D.M. Williams 1996, Undergraduate Fourth Year Project Report, Department of Engineering Science, University of Oxford. Damage detection within reinforced concrete beams using vibration characteristics.

[115] K. Worden and G.R. Tomlinson 2001, Philosophical Transactions of the Royal Society A 359, 113–130. Nonlinearity in experimental model analysis.

[116] D.Z. Yankelevsky 1985, Journal of Structural Engineering 111, No. 7, 1533–1542. New finite element for bond-slip analysis.

[117] G.T. Zheng and P.D. McFadden 1999, Journal of Vibration and Acoustics 121, 328–333. A time-frequency distribution for analysis of signals with transient components and its application to vibration analysis.

Appendix A

The Auto-Regression Method

The equations used to calculate the coefficients in the auto-regression method, based on the Burg algorithm and the Levinson-Durbin recursive algorithm are presented here (see Kay and Marple [47], Ulrych and Bishop [110] and Makhoul [58]). The method calculates the coefficients for increasing numbers of poles until the desired number of poles, M, is reached.

Initially for the data vector x which is of length N, the forward prediction error and the backward prediction error are given as:

$$f_{0,i} = x_i, \quad b_{0,i} = x_i \tag{A.1}$$

where the subscript notation is the i^{th} point in the sequence when 0 poles are used in the model. The modelling error is:

$$\sigma_0^2 = \sum_{k=1}^{N} \frac{(x_k^* x)}{N} \tag{A.2}$$

where x^* is the complex conjugate of x.

Then for increasing values of m from 1 to the desired number of poles M, the coefficients $a_{m,1}, a_{m,2} \ldots a_{m,m}$, and the modelling error σ_m^2 may be calculated using:

$$n_m = -2 \sum_{k=1}^{N-m} b_{m-1,k}^* f_{m-1,k+1} \tag{A.3}$$

$$d_m = \sum_{k=1}^{N-m} f_{m-1,k+1}^* f_{m-1,k+1} + b_{m-1,k}^* b_{m-1,k} \tag{A.4}$$

$$a_{m,m} = \frac{n_m}{d_m} \tag{A.5}$$

$$a_{m,i} = a_{m-1,i} + a_{m,m}a^*_{m-1,m-i} \qquad \text{for } i = 1 \text{ to } m-1 \tag{A.6}$$

$$f_{m,i} = f_{m-1,i+1} + a_{m,m}b_{m-1,i} \qquad \text{for } i = 1 \text{ to } N-m-1 \tag{A.7}$$

$$b_{m,i} = b_{m-1,i} + a^*_{m,m}f_{m-1,i+1} \qquad \text{for } i = 1 \text{ to } N-m-1 \tag{A.8}$$

It should be noted that it is not necessary to calculate $f_{m,i}$ and $b_{m,i}$ for $i \geq N-m$ as the vectors are only used in the summations to find n_{m+1} and d_{m+1} which on the next loop use only values up to $i = N-m$.

$$\sigma^2_m = \sigma^2_{m-1}(1 - a^*_{m,m}a_{m,m}) \tag{A.9}$$

As stated in the auto-regression section, $a_{m,0} = 1$ no matter what number of poles is used.